Phase Decompositions In Iron-rich Iron-nickel Alloys At Low Temperatures (less Than Or Equal To 450 Degrees C).

Order Number 9130021

Phase decompositions in Fe-rich Fe-Ni alloys at low temperatures ($\leq$450°C)

Zhang, Jing, Ph.D.

Lehigh University, 1991

U·M·I
300 N. Zeeb Rd.
Ann Arbor, MI 48106

PHASE DECOMPOSITIONS IN Fe-RICH Fe-Ni ALLOYS AT LOW TEMPERATURES (≤450°C)

by

JING ZHANG

A Dissertation
Presented to the Graduate Committee
of Lehigh University
in Candidacy for the Degree of
Doctor of Philosophy
in the
Department of Materials Science and Engineering

Lehigh University
March 1991

CERTIFICATE OF APPROVAL

Approved and recommended for acceptance as a dissertation in partial fulfillment of the requirements for the degree of Doctor of Philosophy.

3/28/91
(date)

Professor in Charge

Accepted: 3/28/91
(date)

Special committee directing
the doctoral work of
Mr. Jing Zhang

Chairman: J. I. Goldstein

D. B. Williams

K. C. Russell

R. S. Clarke, Jr.

H. M. Chan

ACKNOWLEDGEMENTS

I would like to express my sincere appreciation to my advisers, Dr. J.I. Goldstein and Dr. D.B. Williams for their constant guidance and support throughout my Ph.D study. Sincere appreciation is also extended to the other members of my committee: Dr. K.C. Russell, Dr. R.S. Clarke, Jr., and Dr. H.M. Chan, especially to Dr. Russell for his interest in this project and his suggestions which helped to translate the data into a good story. Special thanks are due to Dr. Clarke and the Smithsonian Institution for providing the meteorite samples. I am particularly grateful to Dr. J.R. Michael for his willingness and skill in assisting me with the VG STEM at Homer Research Laboratory, Bethlehem Steel Corporation. Gratitude is also extended to Dr. C.E. Lyman for his help with the VG STEM.

This work was supported financially by NASA through Grant NAG 9-45 and is sincerely acknowledged. The atom probe work in this study was sponsored by the Division of Materials Science, U.S. Department of Energy, under contract DE-AC05-84OR21400 with Martin Marietta Energy System, Inc. and through the SHaRE program under contract DE-AC05-76ORO0033. I would like to thank Dr. M.K. Miller of Metal and Ceramics Division, Oak Ridge National Laboratory, for his help with the atom probe work. My stay in Oak Ridge National Laboratory was a great learning experience.

Thanks are due to Dave Ackland, Dave Calvert, and Jim Kerner for their efforts to keep the electron optical instruments running smoothly, to Arlan Benscoter for keeping the polishing lab organized, to Dee Dee Pressler and Robert Walch for photographic assistance. Thanks are also due to Gina Kline and Maxine Mattie for their secretarial work and for their help to fill those confusing and constantly

changing forms.

My graduate study at Lehigh would not have been an exciting and enjoyable one without my fellow graduate students. I have learned a great deal from them: from Saikumar, John Sutliff and John Hunt about the computers, from Jim Ciulik and Jeff Reoder about the "dirty work" of metallurgy (furnaces etc.), from JD French about correct English, from Brian Smith about NBA ..... I have enjoyed many good discussions with Kamal Soni and Mike Zemyan. Particularly, I want to thank Vinayak Dravid who, for many years, was my only company working in Whitaker Lab during the late night/early morning hours.

I also appreciate the company and the friendship of the members of the Chinese community at Lehigh, BZ Zhou, Ping Peng, Jie Chen, Zhao, Tao Liu, Zhu etc., of course many of them look and sound the same to the non-Chinese people.

Finally, I would like to thank my parents. Their support and encouragement from the other side of the Earth is very important to me. Perhaps more importantly, it is they who have taught me to do what I believe to be the right things.

TABLE OF CONTENTS

LIST OF TABLES

LIST OF FIGURES

ABSTRACT

The phase transformations in Fe-rich Fe-Ni and P saturated Fe-Ni alloys at <450°C were investigated using analytical electron microscopy and atom probe/field-ion microscopy techniques. Martensitic and austenitic Fe-Ni alloys of 15 to 44 wt% Ni and Fe-Ni-P alloys of the same Ni composition with 0.2-0.3 wt% P were isothermally heat treated (300 to 450°C) and analyzed. Iron meteorites, two octahedrites which contain decomposed Fe-Ni martensite regions and one high Ni ataxite which has an austenitic (fcc) structure, were also analyzed.

In the octahedrites (Carlton and Grant), the decomposed martensite regions which have 9~10 wt% Ni have a stable two phase structure in which the $L1_0$ ordered FeNi precipitate phase is in equilibrium with a bcc matrix phase (4~5 wt% Ni). The decomposed martensite regions which have >15 wt% Ni are composed of the $L1_0$ ordered FeNi precipitates and a bcc matrix of ~12 wt% Ni. This higher matrix Ni composition in the high Ni martensite regions is attributed to the very fine microstructure of these regions which are composed of ~10 nm wide intragranular disc-shaped precipitates. The decomposed martensite alloys have a two phase structure with fcc precipitates in a bcc matrix. The morphology of this structure is similar to that of the decomposed martensite regions in the meteorites. No ordering was observed in the precipitates containing 50 to 57 wt% Ni formed below the ordering temperature (320°C). Stable and metastable phase equilibria in the Fe-Ni and Fe-Ni(P) alloys formed by the martensite decomposition below 450°C were established according to a consistent interpretation of the compositional data obtained from both the meteorites and the alloys. The differences in the phase equilibrium conditions between the meteorites and the alloys were explained by the mechanism and kinetics of the phase transformations occurred. The formation of the plessite structure was explained based on the results of this study and the current Fe-Ni phase diagram.

The microstructure of the high Ni ataxite (Santa Catharina) was determined. It is a two phase structure composed of an $L1_0$ ordered FeNi island phase and a low Ni fcc honeycomb phase. This two phase honeycomb structure is formed by low temperature (<400°C) spinodal decomposition. The implications of the structure of Santa Catharina to the Fe-Ni phase diagram are discussed.

1. INTRODUCTION

The Fe-Ni alloy system has attracted research interest for several decades. Not only is Fe-Ni the basic constituent of a class of important structural materials, but more importantly, it has some unique characteristics. First, iron meteorites are mainly composed of Fe-Ni phases. A very unique and complicated microstructure has developed in the iron meteorites during the extremely slow cooling process that these meteorites experienced (estimated cooling rate 1-100 K/10^6 yrs). An understanding of the iron meteorite microstructure will provide valuable information about the thermal history of our Solar System in which the meteorites evolved. The phase transformations through which the complex microstructure of iron meteorites were formed include martensite formation and decomposition, spinodal decomposition, and ordering. The microstructure of iron meteorites that formed at low temperatures cannot be completely duplicated in the laboratory. From the metallurgical point of view, a study of the iron meteorite structure will give a better understanding of phase transformation processes that occur in transition metal systems at temperatures less than 0.3 of the melting point (T_m).

Second, an invar alloy forms at a composition Fe-35%Ni. The Fe-Ni Invar alloy has an approximately zero thermal expansion coefficient over several hundred degrees above room temperature. It has been shown recently that Fe-Ni alloys exhibit a remarkable resistance to neutron and heavy ion irradiation induced dimension changes (Brager and Garner, 1985). It is believed that these exceptional macroscopic properties of the invar alloy are the result of the complex interplay of the phase decomposition and the magnetic transition at low temperatures ($<0.5T_m$). Therefore, there is great interest in understanding the phase transformation and phase stability of Fe-Ni alloys at temperatures below $0.5T_m$.

Surprisingly, an alloy system as fundamental and important as Fe-Ni is not very well understood, especially the phase transformations at low temperatures ($<0.3T_m$). One of the major difficulties of studying the low temperature behavior of the Fe-Ni system is the very low diffusivity of the system. The scale of the microstructural features formed in Fe-Ni alloys at low temperatures is often 10 nm or less. The analytical electron microscope (AEM), in which ~2 nm spatial resolution

for chemical analysis has recently been achieved, is a very useful technique to investigate such small scale features.

The purpose of this study was to investigate the phase decomposition and the resulting phase equilibria of the Fe-rich portion (<50% Ni) of the Fe-Ni alloy system. Since it has been shown that P has a significant effect on the iron meteorite structure formed at high temperatures, Fe-Ni alloys with saturated P contents were also investigated. The major analytical technique used in this study to characterize the structure and composition of the meteorites and the laboratory alloys was the AEM. The field ion microscopy/atom probe (FIMAP) was also used in an attempt to detect atomic scale phase separation below the detection limit of the AEM.

In this investigation, both iron meteorite specimens and long-term heat treated laboratory alloys were studied. The study of iron meteorites is mainly focused on the microstructures of decomposed martensite regions which have not been characterized previously. The study of decomposed martensitic Fe-Ni and Fe-Ni(P) alloys will help to understand the nature of the low temperature martensite decomposition process and will help to interpret the formation of the iron meteorite structure.

A high Ni (35%) iron meteorite was also studied. The study of this meteorite, along with the investigation of high Ni austenitic alloys, was aimed at understanding the magnetically induced low temperature (≤400°C) spinodal decomposition and the proposed high temperature (~600°C) spinodal decomposition (Russell and Garner, 1990).

The emphasis of this study is the quantitative characterization of the microstructure of the iron meteorites and the laboratory Fe-Ni and Fe-Ni-P alloys which were designed to parallel certain structural features of the iron meteorites. Based on the quantitative structural and chemical information obtained in this study, the fundamental metallurgical behavior of Fe-Ni alloys and the formation of iron meteorite structures are better understood.

Previous research work on the physical metallurgy of Fe-Ni alloys and on the relevant background for the phase transformations and analytical techniques employed in this study is briefly discussed in the next section.

2. BACKGROUND

2.1 Pertinent Phase Transformation Theories

2.1.1 Nucleation and Growth of Precipitates

When a single phase (α) solid solution becomes supersaturated (α') and is in a two phase field due to a temperature change, the most common mechanism through which the metastable α' phase is transformed into a stable $\alpha+\beta$ two phase mixture is nucleation and growth. The necessity for nucleation is shown in Fig. 2.1. The volume free energy will decrease by the formation of the precipitate phase β. However, the strain energy and the interfacial energy introduced by forming the β phase in the α matrix will increase the free energy of the system. It can be shown that there is a critical size of the β phase at which the free energy increase due to the strain and the interfacial energy reaches a maximum. Any β embryo which is larger than the critical size is able to grow larger because the free energy of the system will be decreased. The curves in Fig. 2.1 are calculated by assuming a spherical embryo and neglecting the strain energy effect. The critical size of the embryo, in this case, is defined by the critical radius r^*. The maximum increase of the free energy due to the initial formation of the β embryo (ΔG^*) is the energy barrier for nucleation.

The energy barrier for nucleation can be significantly reduced if the nucleation occurs at structural defects, such as grain corners and boundaries or dislocations, because the formation of the precipitate phase will annihilate these defects and lower the total free energy of the system. Therefore, nucleation is usually heterogeneous. The driving force for nucleation is provided by supersaturation or undercooling. For a small driving force, the nucleation can only occur at the highest energetically favorable sites such as grain corners and boundaries. If the driving force is large enough, the nucleation will also occur in less energetically favorable sites such as dislocations and vacancies.

The growth of a nucleus requires a positive driving force across the precipitate/matrix interface (α/β) $\Delta\mu_B^i$ as shown in Fig. 2.2b. The interface velocity v is given by: (Porter and Easterling, 1981)

$$v = M \, \Delta\mu_B^i / V_m \qquad (2\text{-}1\text{-}1)$$

where M is the interface mobility and V_m is the molar volume of the precipitate (β)

phase. For an ideal solution,

$$\Delta\mu_B^i = RT \ln(X_i/X_e) \qquad (2\text{-}1\text{-}2)$$

where X_i and X_e is the real and the equilibrium interface composition respectively.

If M is very large, $\Delta\mu_B^i$ can be very small i.e. $X_i \approx X_e$. In this case, the interface movement (growth) is as fast as the solute atoms are brought to the interface through diffusion. The growth is under diffusion control. If M is small, a positive $\Delta\mu_B^i$ is required so that a dynamic balance is established at the interface between the solute fluxes toward the interface and across the interface. The growth is then under mixed control. On the other extreme, if M is very small, X_i is close to its maximum possible value, X_0. The growth is under interface control.

In a crystalline solid, different interfaces have very different mobilities. The shape of a precipitate is greatly affected by the different mobility (growth rate) of the interfaces surrounding the precipitate. The interfaces which have low mobility usually grow through the ledge mechanism. Detailed discussion about various aspects of the nucleation and growth can be found in many physical metallurgy text books (Christian, 1965; Martin and Doherty, 1976a; Porter and Easterling, 1981).

2.1.2 Spinodal Decomposition

There are special situations in phase transformations where there is no barrier for nucleation. A classic example is spinodal decomposition. When a single phase (α) of composition X_0 is cooled into a miscibility gap at T_2, as shown in Fig. 2.3, the free energy curve of the α phase has a negative curvature at X_0,

$$\frac{d^2G}{dX^2} < 0$$

The α phase is unstable because any small fluctuation in composition will reduce the free energy of the system, and therefore, will proceed until a stable two phase $\alpha_1(X_1)+\alpha_2(X_2)$ structure forms. Fig. 2.4a and 2.4b are schematic composition profiles of the two phase structure in various stages of the transformation showing the difference between the nucleation and growth mechanism and the spinodal mechanism. The rate of spinodal decomposition is controlled by the interdiffusion coefficient.

Spinodal decomposition was discussed in detail by Cahn (1961, 1968). After considering the strain energy and the interfacial energy introduced by the decomposition, Cahn has shown that the free energy change due to the formation of a composition fluctuation is:

$$\Delta G = [\frac{d^2G}{dX^2} + \frac{2K}{\lambda^2} + 2\eta^2 E' V_m] \cdot \frac{(\Delta X)^2}{2} \qquad (2\text{-}1\text{-}3)$$

where ΔX and λ is the amplitude and the wave-length of the composition fluctuation. K is a proportionality factor giving the contribution of the interfacial variation at certain ΔX and λ.

$$\eta = \frac{1}{a}(\frac{da}{dX}) ; \qquad E' = \frac{E}{1-\nu}$$

where a is the lattice parameter, E is the Young's modulus and ν is the poisson's ratio.

The significance of Equation 2-1-3 is that it gives the criterion for spinodal decomposition to occur in a solid i.e.

$$|-\frac{d^2G}{dX^2}| > \frac{2K}{\lambda^2} + 2\eta^2 E' V_m \qquad (2\text{-}1\text{-}4)$$

It also gives the minimum possible wave-length that can be formed by spinodal decomposition i.e.

$$\lambda_{min}^2 > \frac{2K}{-(\frac{d^2G}{dX^2} + 2\eta^2 E' V_m)} \qquad (2\text{-}1\text{-}5)$$

If the term in the parentheses is greater than zero, Equation 2-1-5 is not valid. This means that the strain energy is too large for spinodal decomposition to occur.

2.2 Iron Meteorite Structures

The study of the Fe-Ni alloy system has historically been connected with the study of iron meteorites. Iron meteorites are composed of Fe, Ni and small amounts of other elements (<1 wt%) such as Co, P, S, C etc. (Buchwald, 1975a). The thermal history of iron meteorites is very complicated. However, it is known that the last stage in which the present phases were formed was a continuous cooling process in

the meteorite parent bodies from >900°C to a low temperature (ambient temperature depending on the size and the orbit of the parent body). The cooling rate was very slow, typically 1-100 K/10^6 yrs. Extensive information about meteorite evolution and parent body cooling rate can be found in the literature (Goldstein and Short, 1971; Wasson et al., 1980; Rasmussen, 1981; Wasson, 1985).

Due to the extremely slow cooling rate, iron meteorites have unique microstructures which contain useful information about the evolution of the solar system, as well as the metallurgical behavior of the Fe-Ni system. Since the solubility limits of P, S, and C in Fe-Ni phases are very low at low temperatures, most of the P, S, and C is found in phosphide, sulphide, and carbide precipitates which form during cooling. The Fe-Ni phases of iron meteorites indicate, at least to a first order approximation, the phase equilibria of the Fe-Ni binary system at low temperatures. In turn, the understanding of the Fe-Ni system has helped to explain the formation of the microstructures of iron meteorites.

2.2.1 Classification of Iron Meteorites

The iron meteorites are historically classified on the basis of their microstructure when a polished section is examined by a hand lens. There are three major groups of iron meteorites, octahedrites, hexahedrites, and ataxites (Buchwald, 1975b). In the first group, the octahedrites, a Widmanstätten pattern can be observed. The Widmanstätten pattern was formed by nucleation and growth of bcc ferrite (α) plates in a single crystal fcc austenite (γ) matrix. In the meteoritical terminology, the bcc α(Fe,Ni) is called kamacite and the fcc γ(Fe,Ni) is called taenite. Fig. 2.5 shows a typical polished section of an octahedrite showing the Widmanstätten structure. The Ni content of the octahedrites varies from ~6 wt% to ~18 wt%. The octahedrites are further classified based on the width of the kamacite plate, also known as the Widmanstätten band width. Generally, the higher the Ni content, the finer is the band width.

The second group, hexahedrites, has a microstructure containing large equiaxed single crystals of kamacite. The Ni content of hexahedrites is usually <6 wt%. The third group, ataxites, has a very fine microstructure which can not be seen with the unaided eye. The Ni content of the ataxites is usually higher than 15 wt%.

Most ataxites have a fine Widmanstätten structure visible in the optical microscope.

The above classification includes most of the iron meteorites found so far. However, some iron meteorites do not seem to belong to any of these classes and they are collectively called "anomalous". Among these anomalous irons, a few have more than 30 wt% Ni and an fcc single crystal structure.

The chemical classification of iron meteorites is based on the trace element (Ga, Ge, and Ir etc.) content relative to the Ni content (Wasson, 1967; Goldstein, 1969; Scott and Wasson, 1975). Accurate determination of the Ni, Ga, Ge, and Ir composition of each iron meteorite shows that there are 13 distinct groups. In 4-dimensional composition space (Ni, Ga, Ge, Ir), each group forms a very compact and well defined cluster. An example is shown in Fig. 2.6 by plotting the Ga (or Ge) content vs. Ni content on a log-log plot. The thirteen natural groups can be clearly seen. There is an arbitrary criterion which states that five or more similar meteorites are required to form a group. Those irons which do not have more than four brothers/sisters, and do not fit in any of the 13 groups, again are put in a special group called "anomalous".

It is believed that the chemical classification is "genetic", that is, the meteorites of the same group were originally from the same parent body. The structural classification and chemical classification correlate and agree with each other quite well. The meteorites of the same chemical group show similar structure, and those of the same structural group are most likely to belong to the same chemical group. The meteorites which are classified as "anomalous" in the structural scheme are often found in the chemical classification of "anomalous". However, the two classifications do not have a one-to-one correspondence. They give different information about the meteorites and are usually used together.

2.2.2 Widmanstätten Pattern Formation

The formation of the Widmanstätten pattern can be understood based on the established high temperature portion of the Fe-Ni phase diagram (Fig. 2.10) (Goldstein and Ogilvie, 1965a). In the composition range of the octahedrites, the meteorites were single phase taenite above a temperature of ~750°C. As they cooled down through the two phase region, kamacite precipitated and grew on the {111}

planes of the taenite. The characteristic structure of the Widmanstätten pattern is due to the simultaneous growth of kamacite plates along all crystallographically equivalent planes of the taenite (fcc{111}). The taenite phase between the kamacite plates is generally called retained taenite.

The Widmanstätten plates in meteorites were at the equilibrium Ni content during the growth down to a certain temperature which was primarily determined by the cooling rate. According to the numerical simulation of the diffusion controlled Widmanstätten plate growth (see Fig. 2.7), this temperature is most likely to be ~500°C for most octahedrites. Above ~500°C, the Ni content of kamacite increases with cooling, and the kamacite growth was controlled by Ni diffusion in the taenite and the kamacite. The diffusion rate of Ni in kamacite is relatively fast. Under equilibrium conditions, the width of the kamacite plates is determined by the bulk Ni content and cooling rate. For the meteorites of lower Ni content, kamacite nucleated at higher temperature and grew wider than for the meteorites of higher Ni. If the Ni content is very high, the kamacite nucleates at or below ~500°C and the amount of growth is very small. This low growth rate explains why the ataxites have very fine kamacite plates or needles. The effect of cooling rate on the Widmanstätten pattern growth is important. Meteorites of similar Ni content which cool faster will have less time for kamacite growth, and therefore, have narrower kamacite band widths.

Although the Widmanstätten band width is primarily determined by the bulk Ni content of the meteorite and the cooling rate, the effect of P content is also important. First of all, it was shown that P greatly enhanced the Ni diffusion in both kamacite and taenite (Narayan and Goldstein, 1984a). Secondly, P formed phosphides at high temperatures. The taenite/phosphide interfaces served as nucleation sites for kamacite so the presence of P effectively increased the nucleation rate and temperature. In fact, kamacite nucleated only at taenite/phosphide interfaces in laboratory alloys (Narayan and Goldstein, 1984b). The formation of the Widmanstätten pattern is more accurately understood based on the Fe-Ni-P ternary phase diagram (Goldstein and Doan, 1972).

Below ~500°C, further growth of kamacite plates is still controlled by the Ni diffusion rate in taenite due to the lower Ni diffusion rate in taenite. The kamacite growth is much slower. More Ni is piled up in the taenite near the kamacite/taenite

interface and a Ni composition gradient is developed in the taenite. Different phase transformations take place in the taenite phase upon further cooling resulting in a complicated microstructure which is discussed in the next section.

A plot of Ni composition profiles at different temperatures during the Widmanstätten growth is shown in Fig. 2.7. This plot is obtained by numerically simulating the diffusion controlled growth of kamacite based on the current knowledge of the diffusion coefficients and the phase diagram (Saikumar and Goldstein, 1988; Reuter et al., 1988). The composition profiles show the equilibrium growth at high temperatures and the development of the Ni composition gradient at low temperatures.

2.2.3 Microstructure of Retained Taenite

As the kamacite phase grows, the Ni content of taenite increases according to the equilibrium $\alpha+\gamma/\gamma$ phase boundary (see Fig. 2.10). As temperature decreases the Ni diffusion rate in taenite is no longer able to keep up and equilibrium is no longer maintained in the meteorite. At what temperature this happens varies from region to region in a meteorite depending on the distance between the adjacent kamacite phases (impingement effect). However, this temperature can be as high as ~700°C based on the fact that a 8 to 9 wt% Ni composition is observed in the center of many retained taenite regions. In this case, a Ni composition gradient will form in the taenite phase with the kamacite/taenite interface at or close to the equilibrium Ni composition and the center region of the taenite phase remains at the original Ni composition of the meteorite.

As cooling continues to below 500°C, Ni piles up in taenite regions close to the kamacite/taenite interface due to the slower diffusion rate of the γ phase. The so-called "M" shaped Ni composition profile is formed. The highest Ni composition in the "M" profile is about 50 wt% Ni according to the AEM study of Reuter et al. (1988). The lowest Ni composition in the "M" profile varies with the width of the retained taenite region and has a minimum Ni which is the original Ni composition of the meteorite.

The retained taenite does not remain in solid solution as cooling continues, instead, a very complicated microstructure is developed. The microstructure of the

retained taenite varies with its local average Ni composition. Each distinct structural region is named according to its appearance in nital etched section in the light optical microscope. An optical micrograph of typical retained taenite is shown in Fig. 4.5 and a half "M" shaped profile measured by the EPMA is shown in Fig. 4.6. The spatial resolution of the EPMA is about 1 μm which is not enough to reveal the interface composition in such a steep composition gradient. The narrow rim next to the kamacite plates is named clear taenite 1 (CT1) because of its bright intensity. The next region showing a grey intensity is named cloudy zone (CZ). The next region which shows a similar contrast to CT1 is clear taenite 2 (CT2). Next to CT2 is the martensite region because some apparent martensite plates intruding into the CT2 can be clearly seen. The regions inside the CT2 are collectively called plessite. In this study, we will use the word "plessite" strictly for the central regions of the retained taenite, not including CT1, CZ, and CT2. A review of previous research on each structural region is given below.

Peterson et al. (1977) and Albertsen et al. (1978) first found that an $L1_0$ ordered FeNi (γ') phase existed in the CT1 region of Cape York iron meteorite (IIIA) using Mössbauer spectroscopy and X-ray diffraction. They later found the same ordered phase in a number of meteorites (Toluca, Carlton, Dayton) using the same techniques. Clarke and Scott (1980) examined optically over 40 meteorites in which this $L1_0$ ordered FeNi phase was present. Their method was to look at the optical anisotropy of this phase resulting from the tetragonal ordering. The Ni composition was also measured using the EPMA. They named the phase tetrataenite because the Bravais lattice of the $L1_0$ ordered phase was tetragonal.

The application of electron microscopy allowed more detailed study of the structure and composition of tetrataenite. Individual domains and antiphase boundaries were observed. By overlapping the centered dark field (CDF) images from each variant of the tetrataenite, it was shown that the entire CT1 region was the tetrataenite phase (Mehta et al., 1980, Reuter et al., 1984). Using EDS X-ray analysis, the Ni composition across the CT1 region was measured as 52 wt% at the kamacite interface, decreasing to 45 wt% near the CZ with an increasing number of antiphase domain boundaries. The ordered domains ranged in size from about 650 nm to 15 nm (Reuter et al., 1988).

The structure of CZ can only be observed by TEM or FEG-HRSEM. The two phase structure, with globular island phase in a honeycomb phase, was first revealed by Scott (1973). However, there are contradictory experimental results about the identities of the two phases. The early studies by Scott (1973) and Lin et al. (1977) using conventional TEM showed that the two phases in CZ were interpenetrating α and γ single crystals. The more recent studies using various techniques showed that the island phase was tetrataenite with a Ni composition of about 51±2.8 wt%. The discrepancy conceerned the identity of the honeycomb phase. Albertsen et al. (1983) found a low Ni fcc phase in the CZ region of a number of meteorites belonging to various groups using Mössbauer spectroscopy. Novotny et al. (1982) and Reuter et al. (1984) showed that the honeycomb phase of CZ had a bcc structure using the electron diffraction technique. Reuter et al. (1984) measured the Ni composition of the honeycomb phase of Estherville stony iron meteorite as 11.7±0.5 wt%. According to this Ni composition and the observed bcc structure, they concluded that the honeycomb phase was martensite. They also concluded that the CZ was formed through spinodal decomposition of the fcc taenite phase and that the martensite transformation occurred in the low Ni honeycomb phase.

It seems that the discrepancy was related to the analytical technique. The Mössbauer spectroscopy did not have adequate spatial resolution to locate the phase. The specimen preparation technique of intense etching used by Albertsen et al. (1983) etched away any bcc phase, and could not separate CZ from CT2. On the other hand, the AEM analyses were mostly performed in CZ regions near the CT1. The only measured honeycomb composition was of Estherville, a meteorite with a very slow cooling rate and a well developed CZ structure. Therefore, it is still necessary to conduct AEM analysis on CZ regions near the CT2.

The CT2 region was originally thought to be single crystal fcc phase containing 30 to 25 wt% Ni. Recently, Reuter et al. (1988) observed ordering diffraction spots of fcc phase from the CT2 region of the Dayton meteorite. The CDF imaging showed <10 nm sized ordered domains. The electron diffraction technique could not identify whether the ordering was $L1_0$ type or $L1_2$ type. The very small size of the ordered domains prevented detailed AEM analysis. Therefore, whether the ordering was due to the nucleation of FeNi ($L1_0$) or the nucleation of Fe_3Ni ($L1_2$) was not confirmed.

Atom probe work by Miller and Russell (1988) showed that the Ni composition fluctuation in a 28 wt% Ni region (possibly CT2) of Cape York meteorite was ~50 wt% to ~15 wt%. This suggested that the ordered phase in the CT2 region was FeNi rather than Fe_3Ni.

There is an ataxite, Twin City meteorite (30 wt% Ni), which consists entirely of the CT2 structure. Reuter et al. (1988) observed the same ordering spots in the electron diffraction pattern as those from the CT2 region of Dayton meteorite. Miller and Russell (1990) also studied Twin City using the atom probe. They found that the composition fluctuation was from ~50 wt% Ni to ~15 wt% Ni with a periodicity of about 70 nm. The high Ni clusters were about 2 nm in size.

In the optical microscope, plessite shows progressive continuous stages of internal decomposition. The plessite microstructure is quite arbitrarily divided into duplex plessite and black plessite. The duplex plessite refers to the coarser two phase structure in the central region of plessite which can be resolved by an optical microscope. The black plessite refers to the regions between the CT2 and duplex plessite which appear black, and can not be clearly resolved by the optical microscope. The duplex plessite forms in those octahedrites which have relatively low bulk Ni content. For the higher Ni octahedrites, the entire plessite structure is very fine and is often black plessite.

Massalski et al. (1966) first systematically discussed the possible mechanisms of plessite formation. They assumed that the two phase structure of the duplex plessite was equilibrium $\alpha+\gamma$ and the structure of the black plessite was martensite. The $\alpha+\gamma$ two phase structure could be formed through different phase transformations, either $\gamma \rightarrow \alpha+\gamma$, or $\gamma \rightarrow \alpha_2 \rightarrow \alpha+\gamma$. Lin et al. (1977, 1979) observed black and duplex plessite for the first time using the TEM. They found that the black plessite consisted of martensite and decomposed martensite. The two phases in the duplex plessite were also a martensite decomposition product in which γ phase nucleated in the α matrix. Due to instrumental limitations no accurate chemical data for the plessite has been obtained.

2.2.4 High Ni Anomalous Iron Meteorite: Santa Catharina

Santa Catharina is one of the few anomalous iron meteorites which has more

than 30 wt% Ni. The early studies of its origin, chemistry and microscopic features have been summarized by Buchwald (1975c). The 2-10cm diameter γ grains are randomly oriented to each other. The bulk Ni content of Santa Catharina is generally agreed to be 35wt%. Lovering and Parry (1962) first found the evidence of phase decomposition in Santa Catharina, long before the nature of the cloudy zone was revealed. In their thermomagnetic analysis, they interpreted the thermomagnetic curve of Santa Catharina by assuming the existence of two phases of 24±2wt% and 55±2wt% Ni respectively. No microscopic correspondence was presented. The microscopic observations by different authors on polished sections of Santa Catharina had shown basically the same morphology. A typical polished, unetched section of the meteorite is shown in Fig. 2.8. Different from the octahedrites, two irregular shaped blocky regions of about 10 to 100 μm in dimension interpenetrating each other can be seen without etching. They are traditionally called "dark" and "light" regions according to their appearance in the LOM and SEM BSE images. The relative abundance of the two regions varies from place to place in the meteorite. Lovering and Andersen (1965) first determined the composition of dark and light regions using EPMA. They found that the light region has 31.8wt% Ni and 67.3wt% Fe with less than 1 wt% of all other elements and that the dark region has 45.2wt% Ni, 46.1wt% Fe and 8.4wt% O (25at%). The oxygen content increased to about 17wt% (42at%) at the area close to the cracks in the meteorite. The abundance of oxygen was due to the terrestrial weathering. Bowles et al. (1978), Jago (1979), and Saito and Takeda (1988) agreed with the result that there is a major oxygen containing region in the Santa Catharina. However Danon et al. (1977) reported an EPMA analysis with 51-50wt% Ni, 49-48wt% Fe and only 1-2wt% O detected in the dark region. The composition of the light region reported by Danon et al. (1977) was about the same as that of the other authors but with a more heterogeneous Ni range from 26 to 31wt% Ni. They claimed that their sample was taken from the metal part of the Santa Catharina while other investigators were looking at oxidized pieces. There is a problem in their paper which they did not explain. Since the electron backscattering coefficient increases monotonically with the atomic number the area of higher Ni should be brighter in the BSE image. However in their BSE image, the dark region was identified as the high Ni region.

More discrepancies about the microstructure of Santa Catharina have arisen after tetrataenite was found in the meteorite. The tetrataenite, i.e. $L1_0$ ordered FeNi phase, was found in Santa Catharina by Bowles et al. (1978) using x-ray diffraction and by Danon et al. (1977) using Mössbauer spectroscopy and x-ray diffraction. The characteristic asymmetric six peak Mössbauer spectrum detected in Santa Catharina was identical to that in the octahedrites and in the irradiated Fe-Ni Invar alloys. X-ray diffraction showed <100> peaks which indicated the existence of long range ordering. Bowles et al. (1978) concluded that the dark region consisted of a dispersion of particles of Fe_2NiO_4 in an ordered 53 at% Ni taenite (tetrataenite) and the light region was fcc taenite of 30.7 at% Ni. They could detect the spinel (Fe_2NiO_4) particles by electron microscopy in the extraction replicas. They also found that the spinel peaks appeared in X-ray diffraction patterns after the sample was heated at 575K for one hour. They attributed the absence of the spinel peaks in the non-heated samples to the incoherent scattering of the randomly oriented small spinel grains. Scorzelli and Danon (1985) did not find any evidence of oxide in their X-ray diffraction and Mössbauer spectra. The strong central peak in the Mössbauer spectra was interpreted as due to a paramagnetic phase. They concluded that the light region was the low Ni paramagnetic phase and the dark region was the tetrataenite. By comparing the relative intensities of the peaks in the Mössbauer spectra, they estimated that about 50% of the Fe-Ni phase of Santa Catharina was tetrataenite.

Jago et al. (1982) observed the Santa Catharina meteorite using TEM. The 10 nm scale duplex structure they found in both dark and light regions was very similar to the cloudy zone in the octahedrites. The selected area diffraction patterns were quite complicated and tetrataenite was identified from the SAD pattern. There were weak reflections due to another phase which disappeared after annealing the sample at 200°C for 15 min. Jago et al. (1982) concluded that this phase was formed by shock induced lattice reorientation. Some of the diffraction spots were first interpreted as due to γ phase but later as Fe_2NiO_4. There were still some unexplained extra reflections. Based on their Mössbauer spectroscopy and TEM observations, Jago et al. (1982) concluded that the equilibrium state of Fe35%Ni alloy was γ+FeNi. They also discussed the possibility of a miscibility gap and a spinodal decomposition at low temperature in the Fe-Ni system.

The Santa Catharina meteorite has attracted considerable attention from researchers outside the field of meteoritics because the nominal bulk Ni composition of Santa Catharina is the same as that of the Fe-Ni Invar alloy. One can study the equilibrium phases of the Invar-type alloys by using this meteorite since the meteorite cooled very slowly. The equilibrium state of these Invar-type alloys cannot be obtained in laboratories because of the extremely slow diffusion rate of Ni in the Fe-Ni system at low temperatures. In fact Santa Catharina is called a natural 'Invar specimen' and has been compared with artificial alloys which were irradiated with high energy electrons in an attempt to enhance the Ni diffusion rate (Danon et al. 1980).

2.3 Fe-Ni Alloy System

The phase equilibria of the Fe-Ni alloy system in the high temperature range (>500°C) are well known. Fig. 2.9 shows an Fe-Ni phase diagram assessed by Kubaschewski (1982). The $\alpha/\alpha+\gamma$ and $\alpha+\gamma/\gamma$ phase boundaries were first determined by Owen and Sully, (1939) and Oven and Liu (1949). They used the x-ray diffraction technique to determine the phases that existed in a series alloys of composition 2 to 3 at% different from each other. These alloys (<1 to 60 at% Ni) were quenched from 1000°C in water and then aged at various temperatures for up to several hundred days. By determining the structure of each alloy, whether it was single phase α or γ, or an $\alpha+\gamma$ two phase mixture, the boundaries of the $\alpha+\gamma$ region were determined. The major source of uncertainty of this method was that the x-ray lines from α and γ phase were severely diffused or broadened because the lattice was highly distorted by the martensite transformation. Goldstein and Ogilvie (1965b) determined the boundaries of the two phase region using the EPMA technique. Martensite alloys were aged in the two phase field for various time to form γ precipitates in an α matrix. The compositions of the precipitate and the matrix were measured using EPMA. These compositions gave the tie-line for the two phase region. This method was limited by the spatial resolution of compositional analysis of EPMA (~1 μm). Therefore, the boundaries of the two region were determined down to 500°C, a temperature where >1 μm precipitates were formed in maximum practical aging time. Romig and Goldstein (1980) extended the boundaries of the two phase region to lower

temperatures (300°C) using the same experimental approach used by Goldstein and Ogilvie but performing the analysis with a STEM which has a higher spatial resolution for compositional analysis. The results of Romig and Goldstein (1980) as well as the results of Goldstein and Ogilvie (1965b) at higher temperatures, are shown in Fig. 2.10. The martensite start temperature (M_s) measured by Kaufman and Cohen (1956) is also shown in this phase diagram.

The $\alpha/\alpha+\gamma$ and $\alpha+\gamma/\gamma$ phase boundaries determined using different methods are quite consistent in high temperature range (900°C to 500°C). However, uncertainty arises at lower temperatures. Owen and Sully (1939) noted that the phase equilibria at low temperatures seemed to be unusual and varied among alloys which had been cooled down or heated up to the final aging temperature. The phase diagram determined by Romig and Goldstein can not explain the microstructures observed in iron meteorites which had apparently undergone further phase transformations at lower temperatures. The low temperature phase diagram will be discussed in more detail in section 2.3.3.

The Fe-Ni-P (0-30 wt% Ni, 0-16 wt% P) ternary phase diagram was first systematically studied by Doan and Goldstein (1970). Isothermal sections from 1100°C to 550°C were determined by measuring the compositions of each phase of alloys heat treated in both two phase and three phase field at corresponding temperatures. In general, the addition of P to Fe-Ni alloys lowers the melting point of the alloy. A phosphide phase, $(Fe,Ni)_3P$, is formed with an $\alpha(Fe)+Fe_3P$ eutectic point between 1060 and 1010°C. The study of Doan and Goldstein (1970) was extended by Romig and Goldstein (1980) to lower temperatures using the AEM. Isothermal sections from 700°C to 300°C were constructed. It had been shown that the addition of P narrowed the $\alpha+\gamma$ two phase field. The alloys in the three phase field which were used in the low temperature study had martensite structure before the heat treatment. However, for the alloys heat treated at higher temperatures, it was possible that the martensite alloys were transformed to austenite first. Therefore, the precipitation process could be different, either γ and phosphide (Ph) in an α matrix or α and Ph in a γ matrix. This is not a problem for the binary Fe-Ni alloys because that α will not nucleate in γ within the practical time limit of laboratory heat treatment (Narayan and Goldstein, 1984a). It seems that at relatively

high temperatures, 700°C for example, different phase transformation sequences will not affect the final phase equilibria. The compositions of the α precipitates and the γ matrix in the alloy continuously cooled to 700°C (Narayan and Goldstein, 1984b) were quite consistent with the compositions of the γ precipitates and the α matrix in the 700°C isothermally heat treated martensite alloy (Romig and Goldstein, 1980).

2.3.1 Diffusion in Fe-Ni and Fe-Ni-P Alloys

The interdiffusion coefficients of the Fe-Ni system were measured by many groups (Wells and Mehl, 1941; Goldstein et al, 1965; Ustad and Sorum, 1973; Ganessan et al., 1984). Most of these authors measured the concentration gradient in the diffusion couples using EPMA. Since at least ten independent data points are needed in the measured composition profile and the spatial resolution of the EPMA is about 1 μm, a 10 μm wide diffusion zone is required for a good EPMA analysis. Therefore, only the diffusion coefficient data above ~800°C for the γ phase and above ~700°C for the α phase could be accurately measured using the maximum practical diffusion time. The high temperature data reported in the literature differ by almost two orders of magnitude. Dean and Goldstein (1986) measured the interdiffusion coefficients of both γ and α phases in the temperature range from 900 to 550°C using the AEM which can analyze a much narrower diffusion zone due to its higher spatial resolution for compositional analysis when compared to EPMA. The imaging ability of the TEM/AEM instrument also makes it possible to eliminate the grain boundary diffusion effect by properly choosing the analysis regions. Their measurements were in agreement with the extrapolated values from the high temperature data of Goldstein et al. (1965), which were the lowest diffusion coefficients among all available data measured at the same temperature. Therefore, Dean and Goldstein (1986) concluded that the higher diffusion coefficients of other researchers were due to grain boundary diffusion instead of pure lattice diffusion.

The interdiffusion coefficients of the Fe-Ni-P system were first studied by Heyward and Goldstein (1973). They measured the diffusion coefficients of the α and the γ phase in the temperature range from 1200°C to 900°C by measuring the composition gradients of the diffusion couples using EPMA. They found that the addition of P in both the α and the γ phase increases the major diffusion coefficients.

In the γ, adding 1.7 at% P to an alloy of constant Ni content increases D_{NiNi} by a factor of ten. The P diffusion is much faster than the Ni diffusion. The ratio of the cross coefficients to the major coefficients is very small and negligible although the values of the cross coefficients were not determined due to the large experimental uncertainty. The ternary diffusion coefficients from 900 to 550°C were measured by Dean and Goldstein (1986) using the AEM. Saikumar and Goldstein (1988) summarized both binary and ternary data of the interdiffusion coefficients and gave the equations of the diffusion coefficient as a function of temperature and Ni or P content for both the α and γ phase.

Diffusion in Fe-Ni and Fe-Ni-P martensite phase (α_2) was studied by Romig and Goldstein (1981). In the decomposed (α+γ) martensite alloys that they used to determine the phase diagram, the Ni composition profiles of precipitate and matrix were measured. By assuming interface equilibrium and diffusion-controlled precipitate growth, Romig and Goldstein numerically simulated the composition profile in these alloys. For each temperature, the diffusion coefficient of the α_2 phase was determined by matching the simulated composition profile with the experimentally measured one since the diffusion coefficient was the only variable. The diffusion coefficients measured by Romig and Goldstein (1981) show that the diffusion in the martensite phase is much faster than in the γ and α phase. At temperatures, below 400°C, unusually large diffusion coefficients which required a much lower activation energy were calculated. These large diffusion coefficients were attributed to a high density of defects in the martensite phase, the major diffusion path at low temperatures.

Diffusion coefficients of all three phases at selected temperatures are listed in table 2-1. The data are calculated using the equations given by Saikumar and Goldstein (1988), and Romig and Goldstein (1981). There are relatively large errors in the data for the martensite phase due to its heterogeneous structure.

2.3.2 Invar Alloy

The Fe-35at% Ni invar alloy has an almost zero thermal expansion coefficient over a wide temperature range above room temperature. The discovery of the Invar alloy by the Swiss physist Guillaume (1897) won him the 1920 Nobel Prize in physics,

a year before Einstein got his for the explanation of the photoelectric effect, and probably benefitted the Swiss watch industry a great deal. The Fe-Ni and Fe-Ni based Invar alloys are technologically important today with their applications in nuclear reactors, gas turbine engines, and calibration instruments which need temperature stability.

It is interesting that the mechanism which is responsible for the Invar behavior is still not fully understood. It is generally believed that the Invar effect is due to the strong coupling of the magnetic transformation and composition ordering (or decomposition). As shown in Fig. 2.9, the composition range from 30 to 50 pct Ni and temperature range from 200 to 500°C is a magnetic transition zone and chemical ordering may also occur. Research on the Invar effect has been active for many years. A recent book edited by Russell and Smith (1990) gives an excellent source to look at the vast and in-depth nature of these investigations. In this section, some experimental work on the Invar alloy concerning the possible phase decomposition, which is related to the study of high Ni iron meteorites, is discussed.

The commercial Fe-Ni Invar alloys are made by annealing the alloy at about 800°C and quenching to room temperature. The current high temperature phase diagram (Fig.2.10) does not provide any reason for using this procedure because a single phase region is present at 35% Ni and 800°C. However, anomalous behavior was found in many physical properties in this temperature and composition range. Among these physical properties are: magnetization and Curie temperature; lattice parameter (Asano, 1969; Kachi and Asano, 1969); residual electrical resistivity at 4.2K (Kondorsky and Sedov, 1960); thermoelectric power relative to Pt (Tanji et al., 1978); elastic constants (Hausch and Warlimont, 1971; 1973). The anomalous behavior of the above physical properties suggest that a phase decomposition occurs in the 30 to 50% Ni Fe-Ni alloys. However, neither direct observation of structural decomposition nor direct measurement of chemical inhomogeneity has been made in laboratory alloys because the fcc γ phase is retained in this composition range due to the extremely slow diffusion.

As mentioned previously, the extremely slow diffusion rate excludes any possibility of reproducing the low temperature phases by conventional metallurgical method. However the diffusivity can be greatly enhanced by using high energy

particles to irradiate the specimen so that the equilibrium states can be reached in a reasonable time. The detailed discussion about the physical process and the applications of the irradiation can be found in the literatures (Bleiberg and Bennet, 1977; Peterson and Harkness, 1976; Russell, 1984; Garner and Perrin, 1985).

Chamberod et al. (1979) studied electron irradiation effects on the Fe-Ni alloys. They irradiated the 26 to 50 at% Ni alloys with 2 MeV electrons in the temperature range from 80°C to 500°C. The irradiated specimens were examined by X-ray diffraction, Mössbauer spectroscopy and electron microscopy. The Mössbauer spectroscopy showed that the alloys of 30 to 40 at% Ni decomposed into two phases, one Fe-rich and another Ni-rich. Both phases had an fcc structure and the same lattice parameter. The Ni-rich phase had an AuCu superlattice structure as determined by detailed analysis of the Mössbauer spectra. The diffraction techniques also revealed the superlattice reflection. The 42 to 50 at% alloys did not decompose, however ordering did occur. The relative intensities of the FeNi peaks in the Mössbauer spectra showed that the ordered FeNi phase was better developed in the 40 at% Ni alloy than in the 50 at% Ni alloy. They concluded that the phase separation tendency of the 30-40 at% alloys enhanced the ordering process.

Morita et al. (1984) measured the Curie temperature variation of the electron irradiated Fe-Ni alloys. The Curie temperature of the 33-40 at% alloy were apparently increased by the electron irradiation but the Curie temperature of the 40-60 at% Ni alloys appeared to be almost constant. This again suggested that the phase decomposition occurred in the 30-40 at% Ni range and the high Ni phase had a Ni content of 40-60 at%.

The critical ordering temperature of the 35-50 wt% Ni alloys was determined by Reuter (1986). The experiment was performed on thin film samples using the high voltage electron microscope (HVEM) by in-situ irradiation and observation. It was found that the critical ordering temperature decreased from 320°C at 50 wt% Ni to 290°C at 35 wt% Ni. Various possible experimental errors were discussed by Reuter and the total error was estimated to be 10-15°C. It was difficult to observe the structures of the irradiated alloys microscopically because of radiation damage to the specimen. Nevertheless Reuter estimated that the ordered domains in the electron irradiated alloys were approximately 10 nm in size using CDF imaging in the TEM.

The high temperature neutron and self-ion irradiation resulted in another kind of phase decomposition for the Fe-Ni and Fe-Ni-Cr alloys (Dodd et al., 1986; Garner et al., 1986). Garner et al. (1986) irradiated the Fe-35%Ni alloy with neutron and Ni^+ ions in the temperature range from 450°C to 725°C. A cellular structure on a 100nm scale was observed with TEM after the sample was electropolished at room temperature. The cellular structure was revealed by preferential etching of the low Ni areas. The Ni composition fluctuation was also detected by EDS on the properly electropolished specimens which did not show the cellular structure. The Ni composition variation was between 25% and 50% in the specimen irradiated at 550 to 600°C. The composition fluctuation could be detected at temperatures as high as 725°C. The micro-invariants which had different Ni composition did not show any kind of phase boundary contrast in the TEM images. However, they apparently aligned along certain crystallographic directions, most probably <100>. Similar cellular structures had been observed on Fe-35%Ni-7~15%Cr alloys using the same experimental conditions. The structure and the Ni composition fluctuation were not affected by the Cr content and the Cr only acted as a substitute for the Fe.

The intensity of the irradiation that Garner et al. (1986) applied to the Fe-Ni and Fe-Ni-Cr alloys was quite high, being 10 to 50 DPA compared with 0.2 DPA of the electron irradiation. Many other processes could occur under such a high level irradiation. Russell and Garner (1991) discussed many possibilities of the irradiation-induced structural and compositional variations. They believed that the decomposition occurred in the irradiation experiments revealed the intrinsic property of the Fe-Ni alloy system. The effect of the irradiation was merely to enhance the diffusion so that the equilibrium state could be reached.

2.3.3 Low Temperature Fe-Ni Phase Diagram

Many versions of the low temperature phase diagram have been proposed by different research groups based on their experimental or theoretical work. At the Fe-rich side of the phase diagram the $\alpha/\alpha+\gamma$ and the $\alpha+\gamma/\gamma$ phase boundaries were established experimentally by Romig and Goldstein (1980) down to 300°C. On the Ni-rich side, the $L1_2$ ordered fcc phase was first detected by Leech and Sykes (1939) using X-ray diffraction. Vandeen and Woude (1981) determined the phase diagram

around the critical ordering temperature of $FeNi_3$ using Mössbauer spectroscopy. They found a first order transformation with a maximum critical ordering temperature of 516°C at 73 at% Ni.

An eutectoid reaction was incorporated by Heumann and Karsten (1963) suggesting that at low temperatures the α and $FeNi_3$ were in equilibrium. They determined the $\alpha+FeNi_3/FeNi_3$ boundary and the eutectoid point which was at 345°C and 52 at% Ni. It is worth noting that they used a chemical metallurgy method to prepare the sample and the final samples contained up to 0.2 wt% C. Combining the above data, Kubaschewski (1982) constructed a complete Fe-Ni phase diagram shown in Fig. 2.9. The FeNi and Fe_3Ni phase were also incorporated in Kubaschewski's diagram under the eutectoid temperature in the two phase field. These two phases were drawn in dashed lines and accompanied by a question mark indicating that no solid experimental evidence was available.

However, the existence of the ordered FeNi phase has been established in meteorites (section 2.2.3) and the critical ordering temperatures were measured by high energy particle irradiation experiments (section 2.3.2). Rossiter and Jago (1984) proposed a phase diagram including the ordered FeNi phase as shown in Fig. 2.11. The critical ordering temperatures that they accepted were 320°C at 50 at% Ni and 350°C at 52 at% Ni. Therefore two eutectoid points were introduced with $\alpha+FeNi$ and $FeNi+FeNi_3$ in equilibrium respectively. They suggested that the cloudy zone in the iron meteorites could be either $\alpha+FeNi$ or $\gamma+FeNi$ depending on whether true equilibrium had been achieved. To account for their experimental evidence, Chamberod et al. (1979) suggested a phase diagram including both FeNi and Fe_3Ni phases as shown in Fig. 2.12. The most distinctive feature of their phase diagram was a peritectoid reaction at 400°C and 25 at% Ni to form Fe_3Ni. It should be pointed out that this diagram can not explain the structure of the iron meteorites.

There were attempts to calculate the Fe-Ni phase diagram thermodynamically. The thermodynamic calculations are very useful but they usually need something to start with such as the existing phases and their structures. Also many thermodynamic parameters need to be calibrated according to the known parts of the phase diagram. Recently, major progress has been made by Chuang et al. (1986) in showing the interplay of the chemical and magnetic contributions to the stability of

phase equilibria of Fe-Ni alloys. They calculated the Fe-Ni phase diagram by taking into account the magnetic effect on the Gibbs free energy. The magnetic contribution is large enough to change the free energy curve in a system which shows rapidly changing Curie temperature vs. composition so that a miscibility gap will form. Such a miscibility gap, as well as the associated spinodal, has been predicted by Chuang et al. (1986) for Fe-Ni alloy system. Their calculated phase diagram is shown in Fig. 2.13. Since they used Kubaschewski's phase diagram to establish the thermodynamic functions which they needed for the calculation, this diagram is basically the same as that of Kubaschewski (1982) except for the miscibility gap and the resulting $\alpha+\gamma_2$ two phase field, the monotectoid reaction, and the tricritical point at 494°C.

Since the experimental evidence from both iron meteorites and Invar alloys indicated some kind of phase decomposition, the magnetically induced miscibility gap has been accepted by Reuter et al. (1989) in constructing a new phase diagram. Reuter et al.'s phase diagram is shown in Fig. 2.14. The FeNi phase joins the γ phase congruently at 462°C and 47at% Ni. The critical ordering temperature of the FeNi phase is 320°C. The boundaries of the miscibility gap and the spinodal decomposition area are determined from the analytical data of the iron meteorites and HVEM in-situ irradiation experiments. The authors extended the FeNi phase to the disordered γ phase field because no $\alpha/FeNi_3$ equilibrium has been observed in iron meteorites. The Fe_3Ni phase is left out because experimental evidence, especially the atom probe work by Miller and Russell (1988; 1989), shows that the Fe_3Ni phase does not exist in the iron meteorites. The diagram of Reuter et al. (1989) actually combines the features of the Rossiter's diagram (Fig. 2.11) and Chuang's diagram (Fig. 2.13). It is consistent with the currently available experimental results of the meteorites.

Another miscibility gap has been proposed by Russell and Garner (1991) to account for the experimental evidence for a high temperature phase decomposition. Russell and Garner's phase diagram is shown in Fig. 2.15. A high temperature miscibility gap and a spinodal were proposed. They argued that the large scale composition fluctuation which occurred in the neutron irradiated alloys and the reported large scale two phase structure of the Santa Catharina meteorite could not be formed by the low temperature decomposition. Their high temperature miscibility gap suggests that the 35% Ni alloy decomposes into 25% and 50% phases at 550°C.

To explain the other experimental evidence which showed much finer scale decomposition products they did not exclude the existence of the low temperature magnetically induced miscibility gap.

The differences between these phase diagrams are mainly about how to interpret the experimentally observed phase decomposition in the composition range of 25-50% Ni. So many different analytical techniques were employed to investigate alloys which had undergone so many different treatments, that it is important to judge just what are the equilibrium features of the system and what are the non-equilibrium features which occur under certain conditions.

2.3.4 Structure of Fe-Ni Martensite

Two types of martensite are formed in the Fe-Ni alloys. The lath martensite, sometimes called massive martensite, is formed in alloys containing less than 29 at% Ni (Bryans et al., 1969). The most dominating morphological feature of the lath martensite is the blocks. As shown in Fig. 2.16, each block is composed of many parallel laths which have the same orientation and are separated by low-angle boundaries and a high density of dislocations (Marder and Marder, 1969). Several blocks which are separated by high-angle boundaries form a packet. Bryans et al. showed that the blocks in the lath martensite formed in a self-accommodating fashion and homogeneous deformation is often associated with the transformation. The interface between pairs of self-accommodating blocks is usually undistorted. The M_s temperature of the Fe-Ni lath martensite, as measured by Kaufman and Cohen (1956), is from 525°C at 9.5 at% Ni to about 0°C at 29 at% Ni.

Plate martensite is formed in alloys containing more than 29 at% Ni and is characterized by acicular plates with midribs. Adjacent plates do not form parallel to one another. The plates which are the first to form tend to span their parent austenite grains, limiting the size of plates that subsequently form. The effect of this partitioning of the austenite is to provide a large range of plate sizes in the plate martensite. Between the already formed plates is the austenite in which new martensite plates will form upon further cooling. The fine structure of the plate martensite consists in part of fine parallel twins (Kelly and Nutting, 1960). A dislocation fine structure consisting of parallel arrays of screw dislocations is found

to coexist with the fine twins in the plates of Fe-Ni martensite (Krauss and Pitsch, 1965).

The fundamental reason for the morphological transition from lath to plate martensite is not well understood. Krauss and Marder (1971) discussed the effect of alloying elements on the morphological transition and pointed out that the plate martensite only formed in alloy systems in which the alloying elements stabilized the austenite. They further suggested that the effect of alloying elements was to decrease the M_S to the temperature range in which the preferred plastic deformation mechanism was twinning. Therefore, phenomenologically, the lath to plate transition can be related to the M_S temperature.

2.4 Analytical Electron Microscopy

The modern analytical electron microscope (AEM) is a powerful instrument in materials research because of its ability to yield structural and chemical information with very high spatial resolution (~0.2 nm for imaging and ~2 nm for chemical analysis) in thin foil specimens. While having inherited the full imaging and diffraction capability of the traditional transmission electron microscope (TEM), AEM incorporates X-ray energy dispersive spectrometer (EDS) and electron energy loss spectrometer (EELS) so that almost every element in the periodic table can now be quantitatively analyzed and correlated with certain structural features. In this study, the AEM was utilized as the major analytical technique. The pertinent techniques and limitations are discussed in this section.

2.4.1 Quantitative EDS X-ray Microanalysis in Thin Foils

Quantitative EDS X-ray microanalysis in AEM uses a ratio technique which was first proposed by Cliff and Lorimer (1975). This technique relates the ratio of the concentration of elements present in the specimen to the intensity ratio of the characteristic X-ray counts collected:

$$\frac{C_A}{C_B} = k_{AB}\frac{I_A}{I_B} \qquad (2\text{-}4\text{-}1)$$

where C is the concentration of the element in wt%, I is the characteristic peak intensity, A and B are the elements present in the specimen. k_{AB} is a proportionality factor termed the Cliff-Lorimer k-factor which accounts for the difference in generation and collection of the characteristic X-rays between element A and B. For a specific characteristic X-ray line i being analyzed (i=K_α, L_α etc)

$$(k_{AB})_i = \frac{(Q_i \omega_i a_i \varepsilon_i)_B / A_B}{(Q_i \omega_i a_i \varepsilon_i)_A / A_A} \qquad (2\text{-}4\text{-}2)$$

where A is atomic weight, Q_i, ω_i, a_i, and ε_i are the ionization cross section, the fluorescence yield, the ratio of intensities of i line and its line family, and the EDS detector efficiency for element i respectively. The k-factors are usually measured experimentally on a specimen of known composition. They can also be calculated from Equation 2-4-2. However, many parameters required by Equation 2-4-2 have not been, or cannot be, measured or calculated to such level so that the accuracy of the calculated k-factors are comparable to those of experimentally determined k factors.

To use Equation 2-4-1, an assumption must be made that the specimen is "infinitely thin" so that absorption and fluorescence effects are negligible. Practically, a thin-film criterion is established which states that the specimen is considered to be "infinitely" thin if the calculated absorption and fluorescence corrections on x-ray intensity ratio are less than the statistical error of the peak X-ray counts (Goldstein et al., 1986). The thin-film criterion is not an absolute quantity but a relative value which needs to be determined for different specimens and analytical conditions. If the absorption effect is not negligible, the intensity ratio in Equation 2-4-1 must be corrected. The correction factor A equals:

$$A = \frac{\int_0^{t_0} \phi_B(\rho t) \exp[-\mu/\rho|^{B}_{spec} (\rho t) \csc\alpha] \, dt}{\int_0^{t_0} \phi_A(\rho t) \exp[-\mu/\rho|^{A}_{spec} (\rho t) \csc\alpha] \, dt} \qquad (2\text{-}4\text{-}3)$$

where $\phi_i(\rho t)$ is the depth distribution of X-ray generation of element i (i=A,B), $\mu/\rho|^{i}_{spec}$ is the X-ray mass absorption coefficient of the element i for the specimen,

t_0 is the specimen thickness, and α is the X-ray take-off angle. Usually in thin foils the absorption correction factor takes a simpler form: (Goldstein et al., 1977)

$$A = \frac{\mu/\varrho\,|^{A}_{spec}}{\mu/\varrho\,|^{B}_{spec}} \cdot \frac{1-\exp[-\mu/\varrho\,|^{B}_{spec}(\varrho t)\csc\alpha]}{1-\exp[-\mu/\varrho\,|^{A}_{spec}(\varrho t)\csc\alpha]} \qquad (2\text{-}4\text{-}4)$$

The accuracy of the absorption correction depends on the accuracy of the specimen thickness measurement. The fluorescence correction in most specimens is usually small so that it can be ignored safely at the current accuracy level.

Recently, Horita et al. (1987) suggested an approach to obtain the composition ratio or k-factor at zero thickness without an absorption correction. The approach is based on the fact that in a certain thickness range the logarithm of the intensity ratio is approximately proportional to the specimen thickness. This linear relationship can be obtained by assuming that $t=t_0/2$ in Equation 2-4-3 i.e. assuming all X-rays were generated in the middle of the specimen instead in a uniform distribution within the entire thickness range ($\phi(\varrho t)=1$). One can then plot the logarithm of the intensity ratio vs thickness in the appropriate linear range and extrapolate the log-ratio to zero thickness. The beauty of this method is that it does not require absolute accuracy in specimen thickness measurement since the value of t only affects the slope, not the intersection of this linear extrapolation with the zero thickness. This allows the use of relatively inaccurate thickness measurement methods such as the contamination spot method so long as the method consistently overestimates or underestimates the thickness. Even more convenient, since x-ray counts are propotional to thickness before absorption is severe, no measurement of thickness is needed.

The error introduced in this assumption is determined by specimen thickness and mass absorption coefficients of the specimen. Any chemical variation on the specimen surface will result in large errors in k factor determined by this method. Therefore, the applicability of this method must be carefully verified for each specific specimen according to the absorption coefficients of all elements in the specimen, the linear range, the accuracy required, and the surface conditions of the specimen.

2.4.2 Other Important Factors in Quantitative EDS Analysis

The first problem which should be considered is the precision of the analysis. This is described by the analytical sensitivity (ΔC) and the minimum detectability limit (D_L). The analytical sensitivity is the ability to tell the difference between two peaks which are almost equal. The minimum detectability limit is the ability to tell a peak from the background. Both of them are governed by x-ray counting statistics (Goldstein et al. 1981).

$$\Delta C = \sqrt{2}\ \frac{(t_{n-1}^{1-\alpha})S_C}{\sqrt{n}\ \bar{N}}\ C \qquad (2\text{-}4\text{-}5)$$

$$D_L = \sqrt{2}\ \frac{t_{n-1}^{1-\alpha}\ S_c}{\sqrt{n}\ (\bar{N} - \bar{N_B})}\ C \qquad (2\text{-}4\text{-}6)$$

where $\bar{N}$ and S_c is the average x-ray counts and the standard deviation of n measurement, $\bar{N}$ is the average background counts, C is the concentration of the sample used, and $t_{n-1}^{1-\alpha}$ is the student t factor for n measurements at $1-\alpha$ confidence level. In general, the higher the peak counts and peak to background ratio, the better are the analytical sensitivity and minimum detectability limit.

The above discussion is valid for any analysis which involves counting statistics. In AEM quantitative X-ray microanalysis it is most important to consider the achievable analytical sensitivity and minimum detectability limit at a specific spatial resolution because there is a trade-off between the spatial resolution and the analytical sensitivity.

The spatial resolution of AEM EDS analysis is determined by the electron probe size: d, and the electron beam broadening in the specimen: b. Traditionally, the spatial resolution is defined as: (Goldstein et al., 1977)

$$R_{max} = \sqrt{d^2+b^2} \tag{2-4-7}$$

Recently, Michael et al. (1990) suggested that the spatial resolution is more accurately defined by:

$$R = \frac{d+\sqrt{d^2+b^2}}{2} \tag{2-4-8}$$

or for a planar interface, by:

$$R = \frac{d+\sqrt{d^2+b^2}}{2\sqrt{2}} \tag{2-4-9}$$

The definition of spatial resolution is schematically shown in Fig. 2.17.

There are many models to estimate the amount of beam broadening in the specimen. The simplest one is the single scattering model originally proposed by Goldstein et al. (1977) and revised by Reed (1982). The equation is:

$$b = 721\times10^{-5}\ \frac{Z}{E_0}\left(\frac{\rho}{A}\right)^{1/2} t^{3/2} \tag{2-4-10}$$

where A is the atomic weight, Z is the atomic number, E_0 is the accelerating voltage in keV, ρ is the density in g/cm^3, and t is the specimen thickness in cm. The numerical factor in Equation 2-4-10 is obtained by assuming that 90% of the electrons scattered are within a cone of diameter b. Therefore, to use spatial resolution equations involving the quadrature sum, the d parameter which contains 90% of the electrons in the incident probe should be used (Michael and Williams, 1987).

For quantitative analysis, the electron probe size is best defined by its diameter containing 90% of the total incident electrons (90% probe size). In the ideal case, i.e. the electron probe intensity is a Gaussian distribution, the 90% probe size is close to the full width at tenth maximum (FWTM) of the Gaussian peak (FWTM contains 94% of the intensity under a Gaussian peak). Due to the presence of spherical aberration in the practical electron optical systems a non-Gaussian electron probe will appreciably increase the 90% probe size although it may not increase the full width at half maximum (FWHM) of the probe. Whether a Gaussian probe can be obtained

depends on the size of final limiting aperture, focusing condition of the probe forming lens, and the actual probe size formed. Although the electron probe characteristics are fixed for a specific instrument, the operator does have control of aperture size and should always measure the 90% probe size if the accurate knowledge of spatial resolution is desired.

In the present electron optical systems, the smaller probe size, the less beam current is contained in the probe. An attempt to improve spatial resolution by using a smaller probe or analyzing a thinner specimen region will result in less X-ray counts being generated, and hence a poorer analytical sensitivity or minimum detectability limit. A major improvement in spatial resolution and/or analytical sensitivity can be achieved by using a field emission gun (FEG) as the electron source. Due to a much higher brightness of the FEG, a much smaller probe size can be used to perform analysis in very thin specimen regions while retaining the current level of analytical sensitivity (Lyman and Michael, 1987; Goldstein et al., 1990). Using high accelerating voltages will also improve the spatial resolution and analytical sensitivity because this will increase the brightness of the thermionic electron source, decrease the beam broadening, and increase the peak to background ratio of generated X-rays. However, the use of the FEG has a more dramatic effect.

Another problem is the stray radiation induced artefact obtained in x-ray spectra, also known as the "hole-count" problem. This problem arises because the illumination system of AEM can not fully converge all electrons into the probe. The stray electrons along with the hard x-rays that they generate in the microscope column and the beam limiting apertures are able to reach the entire specimen and excite x-rays (Williams, 1984). These x-rays are collected indiscriminately along with x-rays generated from the region of interest. Although, in modern AEMs, the intensity of stray radiation is extremely small compared to the total number of electrons in the probe, the x-rays that they generate can be quite significant in some situations. This is due to the fact that the stray radiation will be more likely to excite x-rays in bulk materials (such as grid bars and the rim of a self-supporting disc) but the electron probe will be exciting x-rays in thin specimen regions. There is a practical lower limit in terms of x-ray counting rate obtained from the region of interest below which the analysis will be highly inaccurate because of the stray

radiation effect (Lyman et al., 1989). In general, the higher the intensity of stray radiation and the more bulk materials in the sample area, the higher this lower limit will be.

Using an appropriate final beam limiting aperture and minimizing the amount of thick materials in the specimen stage will reduce the stray radiation effect. However, from an operator's point of view, it is very important to characterize the effect of stray irradiation for specimens of different nature to estimate how thin a specimen region can be analyzed accurately.

Another problem in x-ray analysis is the problem of specimen geometry and specimen drift. Both of these factors may degrade the spatial resolution. For example, if the electron beam is placed on a small precipitate to analyze its composition, this precipitate should be through specimen thickness and it should not move relative to the probe during the x-ray measurement. To optimize the specimen geometry at the analyzing point, one still relies on the operator's TEM experience. However, recent developments in computer controlled digital STEM imaging has allowed much better control over the specimen drift. A computer program controls the specimen drift more objectively and more precisely.

2.4.3 Application of EELS

Electron energy loss spectroscopy (EELS) is a versatile analytical technique. An EELS spectrum contains not only information about the chemical composition (inner shell ionizations) but also electronic structure information (pre-edge and post-edge fine structures) of the specimen (Egerton, 1986). Analytically, EELS detects the primary event (ionization of atoms) and an EELS spectrometer can collect most of the transmitted electrons. Therefore, it is an intrinsically more sensitive technique. However, since electrons which are scattered more than once by the specimen only contribute to the background of the spectra, EELS requires very thin specimens. Moreover, in an ionization event, energy loss of an electron can be any value from the ionization energy up to the total incident energy. This fact, combined with the plural scattering, makes an EELS spectrum very complicated. To extract quantitative information from such a spectrum is not a trivial matter. In this section, only two relatively simple applications of EELS will be discussed. They are qualitative analysis

of light elements and specimen thickness determination.

Compared to X-ray analysis, EELS has an advantage because it can identify the presence of light elements. Due to the absorption effect, the lowest energy characteristic X-ray which can be detected is that from Na for an EDS detector with a Be window. For an ultra-thin window detector, the lowest atomic number element detectable is B. There is a more fundamental reason why EELS is more suitable for light element analysis, that is, the fluorescence yield ϖ decreases dramatically with decreasing atomic number Z. For example, only 1 out of 500 C K shell ionizations will produce characteristic X-rays (Williams, 1984). These low energy X-rays are heavily absorbed by the specimen itself and, even with a window-less detector, by the Au film and Si dead layer of the EDS detector. Since EELS is not affected by fluorescence yield and absorption problems, it can more effectively detect the presence of light elements.

As discussed in a previous sections, knowing the local specimen thickness is very important to quantitative EDS X-ray microanalysis. EELS is an effective and convenient method to measure the local specimen thickness because there is a very simple relationship between the specimen thickness and the ratio between zero-energy-loss electrons and total incident electrons: (Joy et al., 1979)

$$\frac{t}{\lambda} = \ln\frac{I_T}{I_0} \qquad (2\text{-}4\text{-}11)$$

where t is the specimen thickness, I_0 is the number of zero-energy-loss electrons (intensity of zero-loss peak), and I_T is the total number of incident electrons (intensity of whole spectrum). λ is the total inelastic mean free path of the electrons in the specimen. It is a function of the average atomic number of the specimen (Z) and the accelerating voltage (E_0). Equation 2-4-11 is rigorously correct if the spectrum is collected over all scattering angles. Since the EELS spectrometer can only collect electrons emerged from the specimen in a certain angular range, λ is also a function of semi-collection angle of the spectrometer β. It has been shown that λ is not a function of specimen thickness up to $t \approx 4.5\lambda$ (Leapman, 1984). Based on Equation 2-4-11, EELS can give a very accurate measurement of relative specimen thickness t/λ. If the $\lambda(E_0,Z,\beta)$ is known, the specimen thickness can be accurately determined.

The total inelastic mean free path λ can be related to the total cross-section of inelastic scattering σ:

$$\lambda = \frac{A}{\sigma \rho N_0} \qquad (2\text{-}4\text{-}12)$$

where A is the atomic weight, ρ is the density of the specimen, and N_0 is Avogadro's constant. Rigorous calculations using quantum mechanics predict a small oscillatory component to the Z-dependence of σ. However, the term A/ρ varies with Z in the same manner as σ, therefore λ is a relatively smooth function, decreasing as Z increases. Therefore, it is possible to obtain an equation for λ as a function of t and E_0 by fitting a limited number of experimentally measured values of λ.

Malis et al. (1988) measured λ in eleven different inorganic materials of known thickness. The data were fitted to a power function. The final equation that they derived is:

$$\lambda = \frac{106 F E_0}{E_m \ln(2\beta E_0 / E_m)} \qquad (2\text{-}4\text{-}13)$$

$$E_m = 7.6 Z^{0.36}$$

where E_m is the average energy loss in eV, E_0 is the accelerating voltage in keV, and β is the semi-collection angle of the spectrometer in mrad. F is the relativistic factor which is defined by:

$$F = \frac{1+(E_0/1022)}{1+(E_0/511)^2} \qquad (2\text{-}4\text{-}14)$$

Malis et al. suggested that Equation 2-4-13 is likely to yield a more accurate value of λ if β is chosen to be larger than α (semi-convergence angle of the incident beam) but less than the smallest Bragg scattering. The term $2E_0/E_m$ in the logarithm term is an approximation which will yield ~10% error in an energy range up to 150 keV and larger error for higher accelerating voltages. But its effect on λ is not so large because it is in the logarithm term. The accuracy of λ determined by Equation 2-4-11 is $\leq$20% relative according to the estimation by Malis et al. (1988). The major source of error is the thickness measurement in their study. By employing more accurate thickness

measurement techniques on more materials, it is possible to obtain a better fit of the λ equation. Nevertheless, a 20% error is good enough for most microanalysis purposes at the present time. Compared to other thickness measurement methods currently used in AEM, the EELS technique has a comparable accuracy and is obviously superior in terms of convenience, sensitivity, and consistency.

2.4.4 Artifacts due to Thin Foil Specimen Preparation

Whether the thin foil specimens which are produced by severe chemical or physical reactions (chemical thinning, electropolishing, ion-beam milling) represent the characteristic structural and chemical features of the bulk materials has long been a question in TEM/AEM analysis. Although this problem has not been completely solved, a positive answer is widely accepted largely due to the great success of TEM/AEM technique in solving real materials science problems. However, as with the development of modern AEM, it is desirable to perform EDS x-ray analysis in very thin specimens (10-20 nm) to achieve high spatial resolution. At the same time, EELS analysis must be performed in very thin specimen regions. Obviously, any surface layers introduced in specimen preparation processes will have a much larger effect on the specimen composition for a 10 nm thin foil than for a 100 nm thin foil. This gives rise to new concerns about the artifacts due to specimen preparation, most importantly the composition variations in very thin foils.

The surface layer can be formed by various mechanisms in different specimen preparation techniques, such as the differential etching in chemical thinning, the surface redeposition or surface leaching in electropolishing, the differential sputtering in ion-beam milling etc. The redeposition problem was reported in the Al-Cu system where a surface layer of Cu was formed during electropolishing (Thompsom et al., 1977). A similar problem was found in the Al-Zn and the Al-Ag systems with both electropolishing and ion-beam milling (Morris, 1977). Contrary to common perception, ion-beam milling does not have lesser problems than electropolishing. Reuter et al. (1986) found that the "ion-beam cleaned" specimens had a thicker surface oxide layer than freshly jet-polished specimens in Fe-35wt% Ni alloy.

Clearly, this problem is material dependent and specimen preparation technique dependent. However, it can be easily detected by measuring the x-ray

intensity ratio as a function of thickness. The characteristics of surface deposition are that the x-ray intensity ratio shows an enrichment of one element at the thinnest region of the specimen and that the enrichment can not be explained by an absorption effect at different thickness regions. To avoid this problem using the traditional specimen preparation techniques, many trial-and-error type experiments are needed. Different combinations of electrolyte and polishing conditions, different ion source and beam energy may have to be used to ensure that the chemistry of the thin foil has not been changed. An alternative method is to clean the specimen surface by using the ion-beam in a UHV environment after the thinning process (Fraser and McCathy, 1982).

Recently, more mechanically oriented specimen preparation techniques such as ultramicrotoming and dimpling have been developed to avoid the composition variation in thin foils (Malis, 1989). Microtoming is a relatively old technique which has been used in organic and soft materials for a long time. With the improvement of instrumentation, it has been shown that the technique produces good thin foils of very hard materials. Surprisingly, thin foils of many hard materials obtained by ultramicrotoming do not have a severely deformed structure as one would expect (Malis, 1988). The key to the successful ultramicrotoming of hard material is to make a very fine tip from the material and protect the tip with an appropriate mount. Certainly, ultramicrotoming is a very promising technique for producing artifact-free thin foils for AEM chemical analysis.

Another trend to minimize artifacts is to mechanically polish the specimen until it is very thin or even perforated. It was reported that thin regions were obtained in a Si specimen using dimple-to-perforation technique (Ivey and Piercy, 1988). Whether the thin regions produced by the direct dimpling method are suitable for high spatial resolution chemical analysis is uncertain, however, dimpling the specimen to <5 μm and finishing with low angle ion-beam milling is definitely an effective technique to minimize the artifacts (Anderson, 1990).

2.4.5 Principle of Atom Probe

The atom probe combines an ultrahigh-resolution field-ion microscope (FIM) with a mass spectrometer. The field-ion microscope is capable of producing images

of the surface of the specimen in which each distinct point in the image is an individual atom. The mass spectrometer is used to analyze the specimen chemically with single atom sensitivity for all elements. The basic configuration of an atom probe is shown schematically in Fig. 2.18 (Miller, 1987).

To obtain an FIM image, a small amount of inert imaging gas is introduced into the ultrahigh vacuum chamber and then a positive DC voltage is applied to the needle-shaped specimen. At a certain voltage, depending on the sharpness of the specimen, the electric field on the tip of the specimen is high enough to ionize the imaging gas atoms. The positive gas ions will be repelled from the specimen and travel along the direction normal to the tip surface. An FIM image is formed when these ions hit a phosphor screen placed in front of the tip. The FIM image is a projection of the atomic arrangement on a semi-spherical surface on a two dimensional plane.

When the voltage on the specimen is increased to a certain level, the atoms on the surface will be evaporated. The field evaporation process is the basic physical process of the atom probe chemical analysis. Practically, a voltage pulse of a 300 ps to 20 ns with an amplitude of a fraction of the DC voltage is applied on the specimen. The evaporated ions which pass through the aperture on the FIM screen are collected by the mass spectrometer. For the time-of-flight atom probe, the mass/charge ratio of these ions is calculated based on the known kinetic energy and the flight time of these ions. The mass resolution of the modern atom probe is good enough to detect all the isotopes.

An often used analysis method is the random area analysis. This approach is used to analyze specimens which have a high-volume-fraction microstructure that is very small and shows little contrast between the phases. In this method, a cylinder of atoms is collected sequentially from the specimen without regard to any feature in the FIM image. The composition may be determined by simply dividing the ion-by-ion data into blocks containing equal number of ions. However, if the particles are smaller than the effective area defined by the aperture or if a particle is only partially cut by the cylinder of analysis, the true composition will not be measured. Various statistical methods are usually used to detect any clustering or ordering which might exist in the ion-by-ion data, and therefore, the specimen (Miller and Smith, 1989).

3. EXPERIMENTAL

3.1 Design of the Experiments

The basic idea of this experimental work was to investigate the microstructure of various Fe-Ni and Fe-Ni (P-saturated) specimens which have undergone phase transformations at various temperatures. The specimens include both iron meteorites which were slowly cooled over millions of years and laboratory alloys which were isothermally heat treated. By characterizing the microstructure and chemistry of these specimens using AEM and other techniques, the phase transformations and phase equilibria of Fe-Ni and Fe-Ni (P saturated) system at low temperatures (≤450°C) will be better understood. The complex microstructures of the iron meteorites will also be better explained.

It should be emphasized that the investigations of the iron meteorites and laboratory alloys are closely related and complementary to each other. First of all, the iron meteorites are not a purely binary system and their thermal history is relatively complicated. But they were cooled for a very long time and equilibrium has been achieved at least at the 100 nm scale. (Although the "M" shape profile in the plessite is a non-equilibrium feature, local equilibrium must have been achieved in most of the distinct structural regions.) Contrary to the iron meteorites, laboratory alloys have a well controlled chemical composition and thermal history. They can not be fully equilibrated due to limited heat treatment time. Therefore, a correct understanding of the Fe-Ni and Fe-Ni (P) system must be able to consistently explain the microstructures formed in both laboratory alloys and iron meteorites.

The application of various AEM techniques for structural and chemical characterization is critical to this experimental work because the microstructures of the iron meteorites and laboratory alloys which were formed by low temperature phase transformations are very fine due to the very low diffusivity of the system.

3.1.1 Decomposed Martensitic Alloys

A group of alloys was designed to investigate the phase equilibria at low temperatures through martensite decomposition during isothermal heat treatment.

In addition to the phase equilibria, these alloys would also give information about the mechanism of the martensite decomposition at various temperatures and Ni compositions. The nominal compositions and heat treatment temperatures of this group of alloys are listed in table 3-1. These alloys are also shown in the current Fe-Ni binary phase diagram proposed by Reuter et al. (Fig. 3.1) They are distributed in the $\alpha+\gamma$ two phase region and α+FeNi region, within or outside the proposed miscibility gap. The ternary decomposed martensitic alloys closely resemble the plessite structure of the octahedrites. The binary alloys would help to show the effect of P if there is any.

The heat treatment time was estimated based on Romig's earlier work (Romig and Goldstein, 1981). According to Romig's measured diffusion coefficients of martensitic Fe-Ni alloys, the width of the precipitates phase would be ~200 nm at 450°C and ~50 nm at 300°C for a one year isothermal heat treatment. Although the diffusivity of Ni in the martensite is much higher than that of the austenite, the decomposed martensite alloys are still not equilibrated. Interfacial equilibrium is assumed so that the analytical results from these unequilibrated alloys can be used to determine the phase equilibria.

3.1.2 Austenitic Alloys

The Fe-Ni alloys which contain more than 30 wt% Ni will not transform to martensite even at liquid nitrogen temperature. To directly investigate the two proposed miscibility gaps and spinodal decompositions, a set of austenite Fe-Ni and Fe-Ni(P) alloys was made. The nominal Ni concentrations and heat treatment temperatures of these alloys are listed in table 3-2. They are also shown in Fig. 3.1. The 35 wt% Ni (the Invar composition) 650°C alloy was in the high temperature spinodal decomposition region proposed by Russell and Garner (1991) based on the neutron irradiation experiments. (see Fig. 2.15) The diffusion coefficient of Ni in the austenite phase at 650°C is $\sim 10^{-17}$ cm^2/sec. Therefore, if the miscibility gap does exist at 650°C, a phase separation on the 100 nm scale is expected for a six month heat treatment time. The 44 wt% Ni alloys are inside the spinodal decomposition region proposed by Chuang et al. (1986) and Reuter et al. (1989). If the high temperature diffusion data are extrapolated to low temperatures, the diffusion coefficients are 10^{-22}

cm^2/sec at 400°C and 10^{-27} cm^2/sec at 300°C. This diffusivity does not allow significant coarsening to occur within practical heat treatment time. However, since the spinodal decomposition has no barrier for transformation, it is worth trying to see if the phase separation due to spinodal decomposition will occur. The scale of the decomposition will be so fine that the chemical analysis may have to be done with the field ion microscope/atom probe. This low temperature spinodal decomposition has been observed in the iron meteorites. Whether and how the presence of P will affect the spinodal decomposition as it does in Widmanstätten pattern formation can be investigated by comparing the analytical results of binary and ternary alloys.

3.1.3 Iron Meteorites

Selected iron meteorite specimens, both octahedrites and high Ni anomalous meteorite, were studied. The study of octahedrites was focused on the plessite, a two phase structure at different microstructural scales formed through martensite decomposition. The martensite decomposition started at different temperatures in different regions of plessite depending on the local average Ni composition. The lower Ni regions transformed to martensite, and decomposed at higher temperatures forming the coarser duplex plessite structure. The higher Ni regions transformed into martensite, and decomposed at lower temperatures forming the finer black plessite structure. The investigation of plessite is like examining various alloy specimens of different Ni compositions and different decomposition start temperatures. The analytical results on the plessite structure will be compared with those on the decomposed martensitic alloys.

Two octahedrites were chosen for study. The first one is the Grant meteorite. It belongs to the chemical group IIIB and has a bulk Ni composition of ~9 wt%. (see Table 3-3) There are large areas of plessite including a coarse duplex plessite present in Grant due to this relatively low Ni concentration. The second meteorite is Carlton. It belongs to the chemical group IIIC and has a relatively high bulk Ni composition of ~13 wt%. Therefore, the plessite structure of Carlton is finer and mostly a mixture of duplex and black plessite. The CT1 and CZ regions of Carlton have been thoroughly investigated previously (Reuter et al. 1989). So the study on the plessite of Carlton would give a complete analysis of the entire retained taenite region of the

octahedrite (across the whole "M-shape" profile).

The high Ni meteorites have cooled directly into the miscibility gap. This is a different transformation path from that of the high Ni regions in the octahedrites (see section 2.2.3). The high Ni regions in the octahedrites have formed below 450 to 400°C. One high Ni iron meteorite, Santa Catharina, was studied. The Santa Catharina meteorite has a bulk Ni composition of ~35 wt%. It is listed as "anomalous" in both structural and chemical classification. Its bulk Ni composition is inside both proposed miscibility gaps and has the nominal composition of the Invar alloy. As discussed in the background section, there are conflicting interpretations of how the microstructure of Santa Catharina has developed. The comparison between the analytical results of Santa Catharina and those of ~35 wt% Ni regions of octahedrites would separate any microstructure components formed by high temperature and low temperature phase transformations.

3.2 Alloy Preparation

3.2.1 Melting and Homogenization

All the laboratory alloys were made from high purity Fe and Ni rods, 5 mm in diameter, and high purity P. The chemical analyses of the materials, as provided by the supplier, Johnson Matthey Inc., are listed in table 3-4. Fe and Ni rods were cut and weighed to yield a melt of about 10 gm for each alloy. The P in lump form was broken and a piece of the appropriate weight was used to make the Fe-P master alloy. Only the approximate composition was needed and the composition was adjusted by changing the weight of Fe.

The Fe-Ni binary alloys were melted using a vacuum induction furnace (Lepel 30kW high frequency generator). The metals were placed in an alumina crucible (Coors porcelain Co.) and the crucible was placed inside the induction coils in the vacuum chamber. The vacuum before melting was $5\text{-}8\times10^{-6}$ torr or better. The crucible was slowly heated to prevent breaking due to thermal shock. The molten metal was held in the liquid state for at least 30 seconds, then slowly cooled to room temperature in vacuum.

To make the ternary alloys, a Fe-P master alloy was made first. This alloy was

melted under atmospheric pressure in an Ar environment using another induction melting unit. The alumina crucible holding the weighed Fe and P was placed inside a quartz melting chamber, as schematically shown in Fig. 3.2. The chamber was flushed with Ar gas for half an hour before the melting started. The melting and cooling took place in the same Ar environment but with a reduced flow rate. The current in the induction coil was rapidly increased to achieve fast melting of the metal. The molten metal was able to cover the P before any substantial evaporation of P occurred so that the composition was close to the target composition of ~2 wt%. Because of the rapid melting, the crucible was always broken. This master alloy was then homogenized at 1000°C (below the eutectic temperature) for 7 days to ensure a uniform alloy. The average composition of the master alloy was analyzed by means of wet chemistry. The result is listed in Table 3-5. The P content of this alloy was slightly larger than the solubility limit of P in α-Fe at 1000°C. Therefore, it was examined metallographically and analyzed using an EPMA. The result showed that there were Fe_3P precipitates, less than 5 μm in size, uniformly distributed throughout the alloy. The composition of the precipitate and the matrix was homogeneous.

All ternary alloys were made from this master alloy and the Fe, Ni rods. The P content was more accurately controlled by using the master alloy due to the minimized P loss. The melting set up for the ternary alloys was the same as that used for the master alloy except that the heating was much slower to prevent the crucible from breaking.

All the Fe-Ni and Fe-Ni-P alloys were homogenized in the single austenite phase region at 1200°C. Each alloy was placed in a quartz tube with a piece of tantalum foil as an oxygen absorber. The tubes were repeatedly evacuated and refilled with Ar gas, and eventually sealed. These tubes were placed in a horizontal furnace for 7-10 days. After homogenization, the alloys were quenched by crushing the tubes in cold water and then the alloys were removed into liquid nitrogen. Despite the protection procedures that were taken, the surface of these alloys was oxidized. However, the oxidation was only on the surface of the ingot as shiny metal was observed after grinding off the thin surface oxide layer.

3.2.2 Homogeneity Analysis and Structure Observation

Each homogenized alloy was mounted, polished, and etched for metallographic examination using a light optical microscope. The martensite alloys were also observed using the SEM. The homogeneity of each alloy was analyzed using WDS X-ray analysis in an EPMA. The level, and the range of homogeneity of each alloy was calculated using the following equations: (Goldstein et al. 1981)

$$W_{1-\alpha} = \pm C \frac{t_{n-1}^{1-\alpha} S_c}{\sqrt{n}\,\bar{N}} \tag{3-2-1}$$

$$\frac{W_{1-\alpha}}{C} = \pm \frac{t_{n-1}^{1-\alpha} S_c}{\sqrt{n}\,\bar{N}} \times 100\% \tag{3-2-2}$$

where $W_{1-\alpha}$ and $W_{1-\alpha}/C$ are the homogeneity range and level respectively of the element of interest at a 1-α confidence level. C is the average concentration of the element of interest, n is the number of measurements performed, $\bar{N}$ is the average number of x ray peak counts for n measurements. $t_{n-1}^{1-\alpha}$ is the student t value which is a function of n and the confidence level 1-α. S_c is the standard deviation which is given by:

$$S_c = \sqrt{\sum_{i=1}^{n} \frac{(N_i - \bar{N})^2}{(n-1)}} \tag{3-2-3}$$

In this study, at least 16 measurements were made on random positions for each alloy specimen. An alloy was considered to be homogeneous if the homogeneity level of Ni was less than 1% at 99% confidence level. This criterion was consistent with the accuracy which was routinely obtained with WDS X-ray analysis in the EPMA.

A straightforward labeling system was adopted to specify each alloy. For example, alloy FN25 means that the alloy contains Fe and Ni, and its nominal Ni composition is 25 wt%; alloy FNP30 means that the alloy contains Fe, Ni and P, and

its nominal Ni composition is 30 wt%; and so on.

3.2.3 Heat Treatment

Each homogeneous alloy was cut into a few 3 mm diameter rods using a Servomet spark machine (Metals Research Ltd.) and into small pieces using a diamond plate low speed saw (Buehler Ltd.). These alloys were separately sealed in quartz tubes using the same procedure as that for alloy homogenization. The isothermal heat treatment was conducted in the horizontal tube furnaces (800 watts, Applied Test Systems, Inc.). The temperature controlling unit was a microprocessor controller (LFE model 2000) which was able to control the temperature fluctuation within ±1°C around the preset temperature. The temperature of the sample was measured by placing a thermocouple next to the tube. The thermocouple was a K type and connected to an Omega HH-52 hand held digital thermometer. The accuracy of the thermocouple was ±2.2°C and the accuracy of the thermometer was 0.1%+0.7°C (manufacturer's quote). Therefore, the temperature of the isothermal heat treatment was accurate to ±4°C and varied within ±1°C. The quartz tubes were placed in the uniform temperature zone in the middle of the furnaces.

The same labeling system as that for the homogeneous alloys was used. The alloys which had the same composition but a different heat treatment temperature were distinguished by a three digit number in front of the label. This three digit number was the heat treatment temperature in celsius. All the alloys specimens and their heat treatment temperatures and time period are listed in table 3-6. When the heat treatment finished, the alloys were quenched into water.

3.3 Sample Preparation for Analysis

3.3.1 Bulk Samples for SEM/EPMA

The same preparation procedures for the bulk sample SEM/EPMA analysis were used for both iron meteorites and laboratory alloys. A specimen was mounted, ground with SiC paper, and polished with 6 μm diamond paste, 1 μm alumina powder and finally 0.05 μm silica. The sample was then etched with 1% nital for various times, usually less than ten seconds for the optical microscope observation and a little longer for SEM observation. The samples for compositional analysis using EPMA

were not etched. The SEM and EPMA samples were coated with carbon after polishing using a vacuum evaporator (Denton Vacuum DV-502).

3.3.2 Thin Foil Samples for AEM

The heat treated alloy specimens were in the form of 3 mm diameter rods. These rods were cut into discs using the diamond plate saw. The discs were ground down and finished with 6 μm diamond paste polishing. The thickness of the discs after polishing was 50-100 μm. The principal thinning technique used was double-jet electropolishing. The electrolyte was 2% perchloric acid in ethanol. The polishing condition was 110 V and -40°C for which a polishing current of about 25 mA was obtained. The double-jet polisher used was a Fischione model 120.

For binary alloys, this method usually gave good polishing and a large thin area, although the high Ni precipitate phase was always thicker than the low Ni matrix phase. Sometimes the matrix phase was completely polished away on the edge of the specimen. This facilitated the accurate composition analysis of the fine precipitates. Ion-milling the specimen using 4-5 kV Ar ions at low incidence angle for a few minutes eliminated the thickness differences.

Very rarely did the electropolishing yield good thin areas in ternary alloys. One of the reasons is probably that there were many bubbles in the ternary alloy formed in the melting and solidification process. These bubbles were observed in the optical microscope and SEM. They could result in premature perforation. Therefore, most of the ternary alloy specimens were ion-beam thinned for 1-2 hrs (Gatan model 600 dual ion miller) after electropolishing. The thinning condition was 5 kV, 15° incident angle, 0.5 mA gun current, and room temperature stage. During the last five minutes, the voltage was dropped to 4 kV.

The preparation of iron meteorite AEM specimens was more difficult because the meteorites do not have a uniform microstructure. The perforation had to be in exactly the right place to observe the desired regions of the meteorite. Therefore, each 3 mm disc had to be treated individually. The octahedrite was first cut into thin sheet (~0.5 mm thick) using the diamond plate saw. The relatively smooth surface of the sheet was briefly etched with 1% nital. This revealed the Widmanstätten plate and the plessite areas of the octahedrite. The 3 mm disc was cut from the sheet using the

spark machine with a certain structural feature (plessite for example) being carefully aligned in the middle of the disc. The disc was ground and polished, and then etched again and observed with the SEM so that the microstructure in the center of each disc was known. If only a small area in the center of the disc had the structure of interest, the disc was dimpled down to ~10 μm (Gatan model 656 dimple grinder) and then ion-beam thinned. If a relatively large area in the center had the structure of interest, the disc was electropolished. The electropolishing condition was the same as that for the laboratory alloys. In either case, if the initial perforation was not at a desired area, further ion-beam milling was performed until an area of interest was thin enough, or the specimen was discarded.

3.4 Analysis

3.4.1 SEM and EPMA

The morphology of the plessite of the octahedrites, the martensite alloys, and the decomposed martensite alloys was observed using scanning electron microscopy (SEM). The low Ni phase on the surface of these specimens was preferentially etched and the surface topography showed the size and distribution of the precipitates. To observe the surface topography, the secondary electron imaging (SEI) mode of the SEM was used and the typical operating voltage was 20 kV.

An ETEC SEM with a W filament and a JEOL 840F SEM with an FEG were utilized. The spatial resolution of SEI of the ETEC SEM was 10-20 nm which was sufficient for observing microstructures of the alloys heat treated above 350°C and the coarser part of the plessite. The spatial resolution of the FEG JEOL SEM was much higher (~2 nm) due to its ability to form a very fine probe with high probe current. The alloys decomposed at 350°C which had a characteristic microstructure of ~10 nm wide precipitates were observed using this microscope. The black plessite, which was close to the CT2/martensite boundary in the plessite region was also observed with this microscope. Due to the high brightness gun, the JEOL SEM can operate at significantly lower voltages, as low as a few hundred eV. There are many advantages of the low voltage SEM. However, for the purposes of this study, traditional medium voltage was sufficient and 10 kV to 25 kV was used.

The backscattered electron imaging mode of SEM was used to obtain

information on the composition variation of the Santa Catharina meteorite due to oxidation. In this case, the sample was not etched so that the compositional contrast was maximized.

A JEOL 733 electron probe microanalyser (EPMA) equipped with three wave length dispersive spectrometers and a Tracor Northern TN2000 computer control system was used for chemical analysis of bulk specimens. The data were processed (commonly known as ZAF correction) using Bastin's $\phi(\rho z)$ method (Bastin et al., 1984). The $\phi(\rho z)$ program along with the EPMA automation program were all contained in a software package called Sandia Task.

For the homogeneity analysis of the laboratory alloys in which Fe, Ni, and P were analyzed, the instrumental conditions were 15-20 kV accelerating voltage, 20-40 nA beam current. These yielded a precision of <1% relative within a counting time of up to 40 sec for each measurement. Pure metallic Fe and Ni were used as the Fe and Ni standard. A Schreibersite, $(Fe,Ni)_3P$, precipitate which contained 15.9 wt% P was used as the P standard.

A different instrumental condition was used for the oxygen analysis in the Santa Catharina meteorite. The accelerating voltage was reduced to 10 kV to minimize the absorption of oxygen X-rays by the specimen. Larger beam currents of ~100 nA and longer counting time up to 100 seconds were used to get more peak X-ray counts. A high purity, stoichiometric single crystal TiO_2 was used as the oxygen standard. The difference in absorption correction between this standard and the specimen (Fe,Ni,O) was very small so the error in the absorption correction was minimized. A pure iron oxide would be ideal for a standard, but practically it was more difficult to ensure the purity and stoichiometry of the iron oxides. A stearate (STE) crystal was used in the WDS of the EPMA to detect oxygen X-rays. An energy window was set for the single channel analyzer to prevent any higher order diffraction of higher energy X-rays from being counted as oxygen X-rays.

3.4.2 Analytical Electron Microscopes

Three analytical electron microscopes, two TEM/STEMs and one dedicated STEM, were used in this study. They were a Philips EM400T AEM equipped with an EDAX Li-drifted Si EDS detector and a Gatan 606 serial collection EELS (SEELS)

controlled by a Tracor Norther TN2000 multi-channel analyzer (MCA)/computer system, a Philips EM430 AEM equipped with a LINK intrinsic Ge EDS detector and a Gatan 666 parallel collection EELS (PEELS) controlled by a LINK AN10000 MCA/computer system, and a VG HB501 STEM equipped with a LINK Li-drifted Si EDS detector and a VG SEELS controlled by a LINK AN10000 MCA/computer system. The VG HB501 STEM is in the Homer Research Laboratory, Bethlehem Steel Corporation. The electron source was an LaB_6 filament for both Philips AEMs and a cold field emission gun for the VG STEM. The highest accelerating voltage was used for each microscope i.e 120 kV for the EM400T AEM, 300 kV for the EM430T AEM, and 100 kV for the HB501 STEM.

The beam current was measured for most analyses. For the Philips AEMs, the beam current was measured by using a double tilt holder, electrically insulated from the microscope column and connected to a picoammeter (Keithley 480). The holder was pulled back so that the electron beam would hit the Al coated holder instead of the specimen. The true beam current was calculated by multiplying the reading of the picoammeter by a backscattering correction factor of Al. The beam current varied greatly from one filament to another. The typical beam current measured during a time span of one year and of several filaments are listed in Table 3-7. The normal filament saturation and bias were used. The difference in the beam current is due to the varying filament conditions.

For the VG STEM, the beam current was measured by inserting a beam stopper, which is made of Mo, into the column. The beam current reading from the nanoammeter was then corrected for the backscattering of Mo. The typical beam current is 0.2 nA to 0.8 nA for the 50 μm virtual objective aperture (VOA) and 1 nm (FWHM) probe size.

It has been shown that the size and the alignment of the final probe-forming aperture determines the shape of the electron probe (Michael, 1988). For the VG STEM, this aperture is the VOA. The optimum VOA size and probe size settings, which are listed in the previous paragraph, were determined by Michael (1988) and were used in this study.

For the Philips AEMs, the size and shape of the probe in STEM mode were measured for different probe size settings and C2 aperture size combinations. This

was done by imaging the probe directly on a photographic plate and measuring the intensity profile of the probe image on the photographic plate with a densitometer (LKB 2222-020 UltraScan XL laser densitometer). Very high magnification and short exposure time was used so that the intensity is controlled to be within the linear range of the plate. To image the electron probe, beam scanning was stopped and the microscope imaging system was switched from diffraction mode to image mode so that, instead of a scan raster, a magnified probe image was obtained on the microscope viewing screen. The objective focus was changed slightly to obtain a focused probe image. The error introduced in the probe diameter by varying the objective focusing length was minimal.

Typical probe images and the measured densitometer profiles are shown in Fig. 3.3 through Fig. 3.6. The FWTM and FWHM probe size was measured from these profiles. The results are listed in Table 3-8. These measurements show the FWTM probe sizes are strongly affected by the size of C2 aperture, although the FWHM probe sizes are quite consistent with the manufacturer's numbers. If the C2 aperture is too large, the electron probe will still have a tail at the optimum focusing conditions (Fig. 3.5). For a small C2 aperture and small probe size, it is possible that the best condition for STEM imaging (Gaussian image plane, Fig. 3.4f) and for microanalysis (disc of minimum confusion, Fig. 3.4e) can be distinguished. In the Gaussian image plane, a probe with smallest FWHM diameter is formed but with a tail. In the disc of minimum confusion, a probe of Gaussian shape is formed but with slightly larger FWHM diameter than that of the probe formed on the Gaussian image plane. For a small C2 aperture and larger probe sizes, one optimum focusing condition exists for both STEM imaging and microanalysis (Fig. 3.4a,c). In summary, the measured FWTM of the probe is larger than the calculated value for a Gaussian peak, FWHMx1.82, for the 70 μm C2 aperture used in the EM400T. The larger FWTM probe size shows that the electron probe has a broad tail. For the EM430T with a 50 um C2 aperture, the electron probes are approximately Gaussian.

The technique to obtain a STEM probe image on the viewing screen was also used as a means to align the C2 aperture more accurately. This is very critical for obtaining a Gaussian probe without tails. A probe which is off the center of the C2 aperture will not form a true Gaussian shaped probe and will elongate in different

directions when the objective lens focusing condition changes. It turns out that the alignment of the C2 aperture cannot be perfectly done by the standard procedures using the control knobs on the Philips STEM box. It is much better if the final fine adjustment of the C2 aperture is made by moving the C2 aperture while watching the image of both the aperture and the probe on the viewing screen.

The hole-counts of all three microscopes were measured experimentally on the Fe-Ni specimens with the same instrumental conditions as those used for analysis. The results have shown that the hole-counts from an Fe-Ni specimen are negligible ($\leq$0.1%) for the three microscopes when the analysis is performed in the specimen area of typical thickness, e.g 10-20 nm for the VG STEM and 40-100 nm for the Philips AEMs. Therefore, the hole-counts were not considered in the quantification process of each spectrum in this study.

For the specimen thickness range stated above, the absorption of Ni K x-rays by the specimen is also insignificant (<3%). Therefore, the absorption correction was not performed for Fe and Ni quantitation unless specified. The absorption effect is large for the P K x-ray in Fe-Ni-P specimens. The absorption correction was performed for spectrum precessing which involved P quantification. The absorption coefficients of Heinrich (Goldstein et al. 1981) were used in the absorption correction.

The specimen thickness was measured when it was necessary, using the x-ray count method. A calibration curve of x-ray counts/pA collected in the 0-10 keV range on an Fe-25wt%Ni specimen for a fixed time vs the specimen thickness was made for each microscope. To make these curves, the specimen thickness was measured using the EELS log-ratio method and the equation for total mean free path of inelastically scattered electrons formulated by Malis et al. (1988). This method gives a consistent, convenient, and on-the-spot-of-analysis measurement of specimen thickness. The estimated accuracy of this method (20% relative) is not as good as the that of CBED method reported in literature. However, the accuracy of CBED method would be much worse for the Fe-Ni specimen because, first, it is very difficult to set up the desired two beam condition on the magnetic specimen, and secondly, the high density defects and strain in the martensitic specimen result in few and less well defined fringes in the CBED discs. Fig 3.7 shows the calibration curves for the three microscopes.

Other precautions which were taken to ensure the accuracy of EDS x-ray analysis include: (1) the specimen was always kept in the horizontal position (0° tilt, 20° take-off angle); (2) through thickness precipitates and interfaces perpendicular to the specimen surface were chosen for the analysis. These were done to the best that TEM imaging would allow; (3) interfaces which were oriented parallel to the EDS detector axis were chosen for analysis.

The specimen drift was corrected manually for the EM400T AEM. This is an important factor which limits the practically achievable spatial resolution of the EM400T AEM. The specimen drift correction was done much more accurately for the HB501 STEM and the EM430T AEM by using a computer controlled digital imaging system. The software provided in LINK AN10000 is called "tracking analyser". The procedures of this drift correction program are: first a digital STEM image of the area around the point to be analyzed is taken and memorized; then a reference point which is any recognizable feature in the image is specified and its coordinates are memorized along with the coordinates of the analyzing point; during the analysis, the computer will stop the acquisition periodically according to a pre-set time interval and take a new digital image of the same area; then the new image is compared with the previous image and any specimen drift will be recognized by the movement of the reference point; the computer will correspondingly move the electron beam so the analysis will continue at the same analyzing point.

The spatial resolutions of EDS analysis obtained in this study are typically 30-50 nm for the EM400T AEM, 10 nm for the EM430T AEM, and 2 nm for the HB501 STEM when the experimental conditions and procedures discussed in this section are used.

3.4.3 Determination of Cliff-Lorimer k factors

A very important aspect of EDS x-ray microanalysis in the AEM is to determine the k factor. The most practical and reliable way to determine the k factors is to measure the I_A/I_B ratio experimentally on a specimen of known composition (C_A, C_B). This is particularly true if low energy x-ray lines are going to be used. For low energy x-ray lines, absorption by the EDS detector not only varies significantly among individual detectors but also varies with time for the same detector.

In this study, both k_{NiFe} and k_{PFe} were determined experimentally for each instrument that was used. The determination of k_{NiFe} was done on the laboratory alloy whose composition was measured using the EPMA. The k_{NiFe} determined in this study has shown little variation from either the theoretically calculated value or the experimental values previously determined in this laboratory. The experimental k_{NiFe} values are 1.14, 1.09, and 1.05 for the EM400T at 120 KV, HB501 at 100kV, and EM430T at 300 kV respectively with a precision of <1% relative.

The determination of k_{PFe} is more complicated due to the low energy nature of P K_α x-rays as well as an artifact introduced in the specimen preparation process. The specimen which was used was an Fe-8.8wt%P alloy. This composition is close to the eutectic composition of α-Fe(P)+Fe_3P which is at about 10.5 wt% P. The alloy was homogenized at 600°C for 96 hours and water quenched. The composition of the P-rich phase was measured using the EPMA. The P composition is 16.0±0.44 wt% at the 99% confidence level and is the Fe_3P phase of which the stoichiometric composition is 15.6 wt%. The Fe_3P phase was used to determine the k_{PFe}.

The alloy was cut into discs 3 mm in diameter and ground to about 70 μm thickness. It was then dimpled to a thickness of <5 μm and ion-beam thinned. A plot of measured Fe K_α/P K_α peak intensity ratio on a logarithmic scale as a function of specimen thickness is shown in Fig. 3.8. The specimen thickness was measured using the EELS log-ratio technique. Theoretically, this plot should be a straight line with a positive slope due to the absorption effect. The y-intercept is the I_{Fe}/I_P at zero thickness. However, this curve increases sharply at the thin specimen thickness which shows a loss of P at the thin regions. Therefore, the extrapolation method developed by Horita et al (1986) can not be be used in this case.

The absorption corrected I_{Fe}/I_P data are also plotted in the same figure for several data points in the relatively thick regions. They show a reasonably good horizontal line which is consistent with a properly applied absorption correction. The k_{PFe}, which is determined using the value of the thickest region, is 0.84. The statistical error of this value is about 1% relative at the 99% confidence level. However, a larger error is expected due to the error introduced by specimen composition variation and the absorption correction.

The observed P loss on the surface of the Fe_3P specimen is a result of the

differential sputtering rate of Fe and P atoms by the Ar ions. The IBT condition used for this specimen was 4.5 kV accelerating voltage, 0.5 mA/gun, and 13° incidence angle. A much worse situation was found for a sample which was not dimpled and ion-beam thinned from a thickness of about 50 μm. The I_{Fe}/I_P vs thickness plot of this specimen is shown in Fig. 3.9. The effect of accelerating voltage, beam current and incident angle on the P loss is not clear.

3.4.4 Error of the AEM Analysis

It is assumed that the systematic errors which could exist in quantitative EDS x-ray microanalysis are minimized after the procedures discussed in the two previous sections are followed. In this section, errors due to the statistical nature of the x-ray generation and collection process are dealt with, i.e the precision of the analysis.

From Equation 2-4-1, the statistical error comes from the errors in the k factor, peak counts of element A (I_A) and element B (I_B). The k factors are usually determined on a uniform alloy and the counts collected can be very large. Therefore, the statistical error in the k factor can be usually neglected. In fact, the error in the k factors determined in this study are all ≤1%. Only the error in I_A and I_B need to be considered. For a single analysis, the relative error of I_A is approximately:

$$\sigma_A = \frac{\sqrt{I_A}}{I_A} \qquad (3\text{-}4\text{-}1)$$

The total relative error of I_A and I_B is:

$$\sigma = \sqrt{\sigma_A^2 + \sigma_B^2} \qquad (3\text{-}4\text{-}2)$$

The $(I_A)^{1/2}$ is the standard deviation and the background counts are neglected. In this study, the error of a datum point is determined by 2σ unless specified. The 2σ represents a 95% confidence level as a Gaussian distribution is usually assumed.

In AEM thin foil analysis, the counts collected from the same phase will be very different due to the local thickness variation. Therefore, the standard deviation equation for multiple measurements, Equation 3-2-3, can not be used directly. However, if the standard deviation is approximately calculated by $(\bar{N})^{1/2}$, the error can

be estimated by:

$$\Sigma = \frac{t_{n-1}^{1-\alpha}}{\sqrt{n}} \frac{\sqrt{\bar{N}}}{\bar{N}} \qquad (3\text{-}4\text{-}3)$$

for n measurements on the same phase. Therefore, the precision of the precipitate composition can be improved by analysing many precipitates of the same composition, although the counting time for one precipitate is limited by contamination and specimen drift.

3.4.5 Atom Probe Field-ion Microscope

The atom probe used in this study was the Oak Ridge National Laboratory Atom Probe which is an energy compensated time-of-flight atom probe. The basic units of the ORNL atom probe (vacuum vessel, mass spectrometer etc.) are provided by VG Inc. (VG FIM-100). The electronic system and the computer controlled data acquisition and processing system were modified and built in ORNL by Dr. M.K. Miller.

The instrumental conditions used in this study were: imaging gas for field-ion microscope (FIM), Ne; tip temperature, 70K; diameter of the aperture on FIM viewing screen, 2 mm; the distance from the tip to the screen, 5.5 cm; tip voltage (DC), 4 to 18 kV; pulse voltage, 20% of the DC voltage; background vacuum pressure for the analysis, $<2\times10^{-11}$ mbar; Ne gas pressure for FIM imaging, $2\text{-}3\times10^{-5}$ mbar.

4. RESULTS

4.1 As-Quenched Microstructure and Compositional Homogeneity of the Laboratory Alloys

The optical micrographs and SEM SE images of the quenched laboratory alloys are shown in Fig. 4.1 through Fig. 4.4. Typical Fe-Ni martensite microstructures were formed in the alloys below 30 wt% Ni. The martensite in 15 and 25 wt% Ni alloys is lath martensite and that in 30 wt% Ni alloy is plate martensite. There is no difference in terms of martensite structure between the binary alloys and their ternary counterparts when observed by LOM and SEM. The 35 wt% and 44 wt% Ni alloys retain the austenitic structure after quenching. The grain size is on the order of a tenth of a millimeter.

The Ni composition (Ni and P composition for the ternary alloys) and chemical homogeneity measured by the EPMA of each alloy are listed in table 4-1.

4.2 Plessite in Octahedrites

4.2.1 Grant

Fig. 4.5 is a LOM image of a typical plessite region of Grant. It contains the duplex plessite, which has a coarse two phase structure with the precipitates >200 nm wide, and the black plessite which is apparently martensite and finely decomposed martensite. A Ni composition profile from a kamacite plate to the center of a plessite region, measured using the EPMA, is shown in Fig. 4.6. This is half of so-called M-shaped profile. The microstructure of the duplex plessite region is coarse compared to the ~1 μm^3 electron-specimen interaction volume so that significant data scattering occurs.

Fig. 4.7 is an SEM SE image of the duplex plessite region, a region containing approximately 10 wt% Ni. The less heavily etched phase is the high Ni precipitate phase. The precipitates were formed along the original martensite lath boundaries. From the morphology of the precipitates, the original martensite blocks are clearly seen (see Fig. 4.1c). A TEM BF image of such a precipitate in Grant and the SAD patterns from both the precipitate and the matrix are shown in Fig. 4.8. The precipitate phase has the fcc structure and the matrix phase has the bcc structure.

The fcc{111} plane of the precipitates is exactly parallel to the bcc{110} plane of the matrix. However, the fcc{110} plane is not exactly parallel to either the bcc{100} or the bcc{111} plane. Therefore, the orientation relationship can be either Nishiyama-Wasserman (N-W) or Kurdjumov-Sachs (K-S). More detailed discussions about the orientation relationship will be given in the discussion section. No ordering is observed in the precipitates using electron diffraction. However, fcc (111) twinning is observed in many of these precipitates. TEM BF and CDF images and an SAD pattern of the fcc (111) twin in a precipitate are shown in Fig. 4.9. Fig. 4.10 shows an EDS Ni composition profile across one precipitate in the DP region. The Ni composition of the precipitate is 50.7±1.1 wt% and that of the matrix 4.1±0.4 wt%, the same equilibrium compositions as those measured for the kamacite/CT1 interface in a number of iron meteorites (Reuter et al, 1988).

In the black plessite region (20 to 25 wt% Ni), the decomposed martensite has a different microstructure from that in the duplex plessite. The martensite formed in this Ni composition range is plate martensite instead of the lath martensite. The precipitates are nucleated within the original martensite plate. This is shown by an SEM image in Fig. 4.11a. The intragranular precipitates are formed along all crystallographically equivalent directions of the martensite matrix. The SEM image shows that martensite next to the CT2 region (~25~27 wt%) is also decomposed but on a very fine scale (see Fig. 4.11b).

The region of 10 to 20 wt% Ni is a transition zone in which both interganular and intragranular precipitates are formed. The sizes of these precipitates vary with the average local Ni content of the region from ~100 nm at the regions close to the duplex plessite to <10 nm at regions near the CT2. Fig. 4.12 shows TEM BF images of precipitates of various sizes in the black plessite region. An EDS Ni composition profile across a very fine precipitate (~20 nm wide) in a 17 wt% Ni region is shown in Fig. 4.13. The precipitate has 56.4±2.9 wt% Ni and the matrix 10.3±0.8 wt%. The Ni contents in both phases are significantly higher that those of the intergranular precipitates found in the DP region. The structure of these fine precipitates is fcc and no ordering, which is an indication of the presence of the tetrataenite, is observed. The orientation relationship could not be determined accurately because these precipitates are misoriented slightly with respect to each other in a highly strained

and defect-rich matrix. However, the electron diffraction shows that the orientation relationship is N-W and/or K-S type. (see discussion)

The CT2 region of the Grant is a single crystal fcc phase. The small ordered domains of the ordered phase which were observed in some other iron meteorites are not observed in Grant. Instead, many fcc twins are observed. Fig. 4.14 shows a set of TEM images, a diffraction pattern and its indexing from the fcc (111) twin observed in the CT2 of Grant. The Ni composition of this region is 27.4±1.2 wt%. No compositional variation is detected in the region using the EM400T AEM. The Grant meteorite is known to be heavily shocked. The twinning observed in the CT2 region of Grant is evidence of shock-induced plastic deformation. More evidence for shock is observed in the kamacite region of Grant. Under normal circumstances, kamacite has a single crystal bcc structure. However, when the pressure increases above 130 kbar, α-Fe (bcc) will transformed into ε-Fe (hcp). As the pressure decreases, ε-Fe will transform back to α-Fe. Both transformations occur through a shear mechanism which breaks down the original single crystal structure and results in a high density of defects. Fig. 4.15 shows TEM images and an SAD pattern of a typical kamacite region of Grant. The BF image shows the existence of a high density of dislocations. The two small grains which are shown in the two CDF images have a bcc (112) twin orientation relationship to each other.

4.2.2 Carlton

The bulk Ni composition of Carlton is about 13wt%, much higher than that of Grant. Therefore, the central region of the plessite of Carlton does not show the typical duplex plessite structure i.e. large intergranular precipitates. A half M-shaped Ni composition profile measured using the EPMA is shown in Fig. 4.16. Fig. 4.17 show SEM images of the central plessite regions of Carlton. Both intergranular and intragranular precipitates exist which are apparently formed by martensite decomposition.

The intergranular precipitates in the central region of the plessite, which are much larger in size (>200 nm wide), have the $L1_0$ ordered fcc structure with a domain size of about 90 nm. TEM images and a CBED pattern of such a precipitate are shown in Fig. 4.18. Fig. 4.19 shows a TEM image of a ~13 wt% Ni area and the EDS

composition profile across one precipitate in this area. The Ni composition of the precipitate and the matrix is 56.2±3.4 wt% and 5.2±0.5 wt% respectively.

The martensite close to the CT2 region which has an average Ni composition of 25 to 27 wt% is also decomposed. The precipitates formed in the high Ni martensite region are predominantly intragranular ones with a very small width, <10 nm as shown in Fig. 4.20. The precipitates formed in the high Ni martensite regions near the CT2 also have the $L1_0$ ordered fcc structure. Fig. 4.21 shows an SAD pattern and the CDF of a decomposed martensite/CT2 interface region. The Ni composition of CT2 at the interface is 28.1±0.9 wt% as measured by the AEM. The average Ni composition of the decomposed martensite in a ~0.3 μm diameter area next to the interface is ~26 wt% as measured with EDS in the AEM. The very fine precipitates in the decomposed martensite near CT2 are formed in the matrix with their fcc{111} planes parallel to the matrix bcc{110} planes. The fcc {111} plane is also the habit plane of the precipitates as shown by the streaking in the diffraction pattern (Fig. 4.21b). The precipitates formed on different bcc{110} planes are misoriented with respect to each other by ~10° resulting in a complicated diffraction pattern and a very weak ordering spot. An EDS Ni composition profile across a fine intragranular precipitate (~15 nm wide) in an 18 wt% Ni area is shown in Fig. 4.22. The average Ni composition of the area (18 wt%) was measured on the thin film specimen using a scanning beam in the STEM. The Ni composition of the precipitate and the matrix is 60.1±1.6 wt% and 9.4±0.5 wt% respectively. Both these compositions are significantly different from those of larger intergranular precipitates (see Fig. 4.20b).

In the plessite region of Carlton, small (<0.5 μm wide) kamacite precipitates are observed. These α precipitates were probably formed at relatively low temperatures and did not have a chance to grow into a Widmanstätten pattern before the surrounding matrix was transformed to martensite. Such α precipitates are characterized by a platelet which has a bcc structure and is surrounded by a high Ni rim. Fig. 4.23 is a TEM BF image and fcc(111) CDF image of such an α plate. The Ni composition profile across the α precipitate is shown in Fig. 4.24. It should be noted that the high Ni phase which surrounds the α precipitate is the ordered FeNi and is in equilibrium with kamacite of ~4 wt% Ni and with martensite of ~10 wt% Ni.

The structure and composition of the cloudy zone of Carlton are very similar

to those of the Estherville stony iron meteorite as measured by Reuter et al. (Reuter et al., 1984). Fig. 4.25 shows a TEM image and an SAD pattern of a CZ region of Carlton. This diffraction pattern, as indexed in Fig. 4.25c, is composed of the fcc<110> zone, bcc<111> zone, and associated double diffraction spots. Therefore, the orientation relationship is close to K-S relationship. The island phase has 52.5±1.0 wt% Ni, as measured using the HB501 STEM, and the $L1_0$ ordered fcc structure and, therefore, is FeNi. The honeycomb phase has a bcc structure. The CDF images show that the globular island phase overlaps in most areas indicating that the honeycomb phase is in thin layers between the globular island phase. The composition of the honeycomb phase is more difficult to analyze due to the geometry of the phase. The lowest Ni composition of the honeycomb phase measured at the edge of the specimen is 12.2±0.7 wt% using the HB501 STEM. Therefore, the structure of the honeycomb phase of CZ in Carlton is martensite.

4.3 High Ni Anomalous Iron Meteorite: Santa Catharina

4.3.1 BM#52283 Sample (also known as USNM#6293 sample)

The non-etched section of the BM sample does not show any microstructure in the metal region when observed optically. Fig. 4.26 is a backscattered electron image of a non-etched section of the BM sample. It shows several oriented dark platelets and many bright bands forming a network structure. The dark platelets have a lower average atomic number. Small precipitates were observed in etched sections of the sample as shown in the SEM secondary electron image (Fig. 4.27). These precipitates are typically 0.1 μm to 0.5 μm wide and show a similar shape and distribution to those dark platelets observed in SEM BSE images on polished sections (Fig. 4.26). The results of the chemical analysis of 40 positions in the matrix using the EPMA are 28.2±0.5 wt% Ni, 0.03±0.01 wt% P, and remainder Fe. This is a homogeneous sample and its Ni composition is significantly lower than the other Santa Catharina samples.

TEM analysis of this sample shows that it is a single crystal with an fcc structure. Superlattice diffraction spots of the fcc structure are observed in electron diffraction patterns, as shown in Fig. 4.28b. The superlattice spots are due to the presence of ordered FeNi, tetrataenite. Fig. 4.28a is a TEM dark field image from a {100} superlattice diffraction spot. The size of the ordered domains is very small,

<10nm. Small α (bcc-kamacite) precipitates <100nm in size are also observed. EDS analysis using the EM400T with a Be window detector shows that the composition of the precipitates observed in Fig. 4.27 is 20.3±0.9 wt% (31.9 at%) P, 23.0±1.0 wt% (19.1 at%) Ni and remainder Fe. Electron diffraction shows that these P-rich precipitates are not $(Fe,Ni)_3P$ or any known phosphate phase.

4.3.2 USNM#3043 Sample:

This sample has the characteristic structure of most of Santa Catharina samples. Dark and light regions can be observed optically on the non-etched section as shown in Fig. 4.29. The distribution of the two kinds of regions does not seem to show any correlation with the presence of cracks. The size and distribution of the two kinds of regions vary considerably from place to place in the meteorite. Fig. 4.30a shows an optical photograph of an etched section of the USNM#3043 sample. The original light regions have mostly turned brown (grey in black/white figures) and show the small phosphorus-rich precipitates similar to those observed in the BM#52283 sample. The brown color observed in the light regions after etching is very similar to the cloudy border observed in the octahedrites. The original dark regions are less affected by etching (1% nital). A BSE image of the non-etched section is shown in Fig. 4.30b. The regions that appear dark optically are also dark in the BSE image indicating that the dark regions have a lower average atomic number. The compositions of the dark and light region were measured using EPMA away from the vicinity of the cracks. The dark region contains 48±2.2 wt% Ni, 8.6±0.93 wt% O, and remainder Fe. The light region contains 34.9±0.4 wt% Ni and <0.15 wt% O (detection limit). Phosphorus was not analyzed in this sample. The large error of the data obtained in the dark region shows that the region is not homogeneous on the micron scale. The presence of 7 to 12 wt% O lowers the average atomic number. This is the reason why the dark region is dark in SEM BSE image. The light region is homogeneous on a scale similar to the BM#52283 sample, although its Ni content is 7wt% higher than the BM sample.

The AEM was used to reveal the structure on the submicron to nanometer scale. Fig. 4.31a is a TEM image of the sample. The upper right part of this image is from the region that appears dark in the BSE image and shows a two phase

structure. The two phase structure can be described as an island phase surrounded by a honeycomb phase. This structure looks very similar to the cloudy zone structure of the octahedrites. The average composition of ~100 nm diameter areas from this two phase region was measured using EDS and its Fe to Ni ratio is about one indicating that it is the dark region observed optically. The diffraction pattern from the two phase region in the upper right part of Fig. 4.31a and its indexing are shown in Fig. 4.31b. The pattern is composed of a) an ordered fcc phase; b) another fcc phase of which the lattice parameter is more than two times larger than the ordered fcc phase; c) double diffraction of the two phases. The ordered fcc phase is tetrataenite. EELS spectra were obtained from this kind of region and exhibit a clear oxygen K edge along with the Fe-$L_{2,3}$, and Ni-$L_{2,3}$ edges (Fig. 4.32a). Therefore the second fcc phase is an oxide and from its lattice parameter it can either be Fe_2NiO_4 or Fe_3O_4. The oxide in this region is most probably a Ni-rich oxide as the Fe and Ni ratio measured in this region is close to one.

The CDF images taken from the diffraction spots of the ordered fcc metal phase and the oxide phase are shown in Fig. 4.31c and d respectively. From Fig. 4.31d, it is clear that the oxide phase exists as very fine particles (<5 nm) and associates with the honeycomb phase of the two phase structure.

The diffraction pattern from the lower left part of Fig. 4.31a shows diffraction spots from a single phase fcc structure and the ordering. The composition of a ~100 nm diameter area, measured using EDS in the AEM, is 35 wt% Ni and 65 wt% Fe. EELS spectra obtained from the same regions do not show the presence of oxygen (Fig 4.32b). The composition of this region on a 100 nm scale is consistent with the composition of the light region. If the thin specimen is tilted away from strong diffraction conditions, a cloudy zone structure of the same scale as that in the oxide-containing regions can also be observed as shown in Fig. 4.33a. Fig. 4.33b and c are SAD patterns taken from the dark and light region respectively. The ordering, and therefore the tetrataenite, is present in both dark and light regions. The oxide is only present in the dark regions. The morphology of this two phase structure observed in both oxidized (dark in the optical and BSE) and non-oxidized (light in the optical and BSE images) regions is the same as the cloudy zone structure of the octahedrites. The bcc diffraction spots, which have been observed in the low Ni

honeycomb phase of the CZ of some mesosiderites and octahedrites (Reuter et al., 1988), is not observed in Santa Catharina. A more detailed discussion of the microstructure of Santa Catharina is given by Zhang et al. (Zhang et al., 1990).

4.4 Decomposed Martensitic Alloys

4.4.1 Alloys Heat Treated at 450°C

The martensite alloys isothermally heat treated at 450°C for 60 days decomposed into two phases, an fcc precipitate phase (γ) in a bcc matrix phase (α or α_2). Fig. 4.34 shows the SEM SE images of the 450FN15 and the 450FN25 alloy. The precipitates are nucleated along the original martensite block or lath boundaries in both alloys. There are many more precipitates in the 25 wt% Ni alloy than in the 15 wt% Ni alloy. However, the typical size of the precipitates is slightly larger in the 15 wt% Ni alloy than in the 25 wt% Ni alloy. A TEM BF image of the 450FN15 alloy is shown in Fig. 4.35. The Ni composition of the precipitates is 39.7±0.8 wt% as measured using EDS in the AEM. EDS Ni composition profiles of this alloy are shown in Fig. 4.36. The composition of the matrix has not reached equilibrium. The Ni composition of the matrix away from the precipitates is still at the bulk alloy composition (15 wt%) and a composition gradient exists toward the precipitate/matrix interface. The lowest Ni composition, approximately 7.6±0.9 wt%, is measured at a grain boundary connecting two precipitates (A-B in Fig. 4.36b).

Fig. 4.37 gives a TEM BF image of the 450FN25 alloy. In this alloy, the precipitates are formed in almost all the original martensite lath boundaries. The Ni composition profile across a precipitate is shown in Fig. 4.38. The precipitate and matrix Ni composition is 39.6±1.3 wt% and 9.4±0.5 wt% respectively.

The precipitate distribution in the 450FNP15 alloy is the same as that of the 450FN15 alloy and there is no appreciable difference in the size of the precipitates between the two alloys as shown by comparing Fig. 4.39, an SEM SE image of the 450FNP15 alloy, with Fig. 4.34. The Ni composition of precipitates and matrix in the 450FNP15 alloy is 39.2±0.5 wt% and 12.2±0.7 wt% respectively. A Ni composition profile across a precipitate in this alloy is shown in Fig. 4.40.

4.4.2 Alloys Heat Treated at 400°C

Fig. 4.41a-f are SEM SE images of the binary and ternary alloys of different Ni compositions heat treated at 400°C for 362 days. The precipitates in the 400FN15 alloy have a very similar morphology to those of the 450FN15. Fig. 4.42 shows TEM images of the 400FN15 alloy. The precipitates have the fcc structure and the matrix has the bcc structure. The heat treatment time of this alloy was six times longer than that of the 450FN15 alloy. The slightly smaller precipitate size in 400FN15 indicates that the diffusion coefficient decreases by a factor greater than six for the 50°C temperature change if the transformation is diffusion controlled. The Ni composition profile across a precipitate in the 400FN15 alloy is shown in Fig.4.43. The measured precipitate and matrix Ni composition is 48.2±1.3 and 8.5±0.6 wt% respectively.

The precipitates in the 400FN25 alloy also have a similar morphology to that of the 450FN25 alloy. Fig. 4.44 is a TEM BF image of the 400FN25 alloy. The fcc the precipitates are formed in the bcc matrix along all the original martensite lath boundaries. The Ni composition of the precipitates is 50.6±1.5 wt%. The matrix compositions measured using the high spatial resolution STEM show an interesting phenomenon. As shown in Fig. 4.45a, the matrix composition between two precipitates only ~25 nm apart is ~9 wt%. However, the Ni composition of a wide matrix area in equilibrium with a precipitate is ~12 wt% and no Ni composition gradient toward the interface is measured at a spatial resolution of ~2 nm (Fig. 4.45b). It appears that the impingement of the diffusion field not only affects the matrix composition away from the interface but also the interface composition itself. A Ni composition profile of this alloy measured using the EM400T AEM is shown in Fig. 4.45c. The matrix composition listed in Table 4-2 is the lowest composition measured using each instrument.

The morphology of the precipitates in the 400FN30 alloy is quite different from that of the lower Ni composition alloys (see Fig. 4.41). This is because the original martensite structure is different. The martensite formed in the 30 wt% Ni alloy is plate martensite while that formed in the lower Ni alloys is lath martensite. Fig. 4.46 is a TEM BF image showing the precipitate distribution in the 400FN30 alloy. A Ni composition profile across a precipitate is shown in Fig. 4.47. The measured Ni composition of the precipitate and matrix is 50.9±1.7 and 9.3±0.5 wt% respectively.

The ternary alloys show a similar morphology of the decomposed martensite structure when compared to their binary counterparts of the same Ni content. Since the solubility limit of P in both fcc (γ) and bcc (α) Fe-Ni is very low at the low temperatures, the ternary alloys in this study (0.2-0.3 wt% P) are in the three phase field. Fig. 4.48 shows an SAD and CBED pattern and a BF image of a phosphide precipitate in the 400FNP15 alloy. The crystal structure of the phosphide precipitate can be uniquely determined by indexing the SAD pattern combined with information from the HOLZ rings in the CBED pattern. The phosphide precipitate in the ternary alloy is the $(Fe,Ni)_3P$ phase which has a space group of $I\bar{4}$ with a_0=0.9056 nm and c_0=0.4471 nm. The Ni and P composition was analyzed using EDS in the AEM. Fig. 4.49a,b show the composition profiles across the phosphide and γ precipitate. The absorption-corrected data were used in the plot. The Ni content of the phosphide is 45.1±2.3 wt%. The P content of the phosphides shown in Figs. 4.49a and b is 16.1±1.1 wt% and 14.7±1.1 wt% respectively. P contents lower than the stoichiometric value are measured in many phosphide precipitates. This lower P content measurement is most likely due to P loss in ion-beam thinned thin foil specimens; the same problem that has been encountered in k_{PFe} determination. The P solubility limit in the α and γ phase at this temperature is below the detectability limit of the AEM under the instrumental conditions used in this study (~0.2 wt%). The measured P compositions of α and γ phases (zero in most cases) shown in Figs. 4.49a,b do not have any significance statistically. The Ni composition of the bcc matrix (α) and fcc precipitate (γ) is 12.7±0.6 wt% and 48.7±2.7 wt% respectively.

Fig. 4.50 shows a TEM BF image of the 400FNP25 alloy and a Ni composition profile across a γ precipitate in this alloy. The precipitate and the matrix composition is 46.9±1.1 wt% and 13.9±0.7 wt% Ni respectively. The matrix composition is higher than that measured in the 400FNP15 alloy. The possible reason for the higher matrix Ni composition in the 25 wt% Ni alloys than in the 15 wt% Ni alloys will be discussed in the Discussion section.

4.4.3 Alloys Heat Treated at 370°C and 350°C

The alloys heat treated at 370°C for 275 days and at 350°C for 400 days have a similar decomposed martensite structure to those of the 400°C alloys, except for the

smaller precipitate size (see Fig. 4.51 and Fig. 4.52). The precipitates in the 15 wt% and the 25 wt% Ni alloys are formed along the original martensite block and lath boundaries. In the 15 wt% Ni alloy, not only the size of precipitates is smaller, but the number of precipitates is noticeably less than that of the alloys heat treated at higher temperatures. In the 25 wt% Ni alloy, the precipitates saturate all the original martensite block and lath boundaries. The precipitates in the 30 wt% Ni alloy are formed inside the original martensite plates along all crystallographically equivalent directions. The ternary alloys do not show any significant difference from their binary counterpart in terms of size and distribution of the precipitates.

Fig. 4.53 shows TEM images of fcc precipitates in the 370FN15 alloy. Interfacial dislocations are observed in the CDF image indicating the precipitate has a semi-coherent interface with the matrix grain on one side. The orientation relationship is either K-S or N-W. The Ni composition profile across this precipitate is shown in Fig. 4.54. The Ni composition of the precipitate is 50.9±1.7 wt%. Most areas of the matrix still remain at the original Ni content, 15 wt%. A small composition gradient is measured in the matrix of Fig. 4.54 and the extrapolated interface composition with the precipitate is 9.1±0.5 wt% Ni.

Fig. 4.55 shows a TEM BF image of the 370FN25 alloy. A Ni composition profile across a precipitate in this alloy is shown in Fig. 4.56. The precipitate composition is 49.8±3.9 wt% Ni, consistent with that measured in the 370FN15 alloy. However, the matrix composition of the 370FN25 alloy is higher than that measured in the 370FN15 and the 370FN30 alloys. This problem of higher matrix composition in the 25 wt% Ni alloys will be discussed later.

Figs. 4.57a-c are TEM images and a diffraction pattern of the 370FN30 alloy. The SAD pattern is composed of a [110] zone axis pattern of the fcc precipitates and diffraction spots of a non-zone axis orientation of the bcc matrix. Very weak streaking is observed along the fcc {111} directions indicating the habit plane of the precipitates is fcc{111}. The streaking is due to the shape-effect of the precipitates. Some discrete, weak diffraction spots are also observed. These spots are due to double diffraction between the matrix and the precipitate diffraction. A Ni composition profile across the precipitates in the 370FN30 alloy is shown in Fig. 4.58. The precipitate and matrix composition is 52.7±2.2 and 12.4±0.7 wt% Ni respectively.

Fig. 4.59 shows a TEM BF image of a γ precipitate of the 350FN15 alloy. The Ni composition profile across the precipitate in this alloy is shown in Fig. 4.60. The composition of the precipitate is 52.0±1.7 wt% Ni and the extrapolated precipitate/matrix interface composition is 10.0±0.7 wt% Ni on the right hand side of the precipitate. Fig. 4.61 is a TEM image of the 350FN25 alloy. The precipitates in this alloy are very difficult to analyze using the thermonic source TEM/AEM instrument although the apparent width of the precipitates is comparable to that of the 350FN30 alloy. The reason why the 25 wt% Ni alloys are more difficult to analyze will be discussed later in more detail.

Figs. 4.62a-c give TEM images and an SAD pattern of the 350FN30 alloy. The diffraction pattern is composed of fcc {111}, {200} and bcc {110} diffraction spots. Visible streaks are present and the major diffraction spots are splitting into several spots. The streaking is due to the thin plate nature of the precipitates and the direction of the streaking gives the habit plane of the precipitates i.e. fcc {111}. The splitting of the major diffraction spots shows that the precipitates are misoriented with respect to each other and the matrix is highly distorted. The CDF image from one fcc(111) diffraction spot shows that, although the fcc diffraction spots seemingly form an fcc [110] zone axis pattern, the major diffraction spots of this "zone axis pattern" are actually from different precipitates. Fig. 4.63 shows Ni composition profiles across the precipitates in the 350FN30 alloy. In this alloy, a much lower matrix Ni composition was measured (5.6±0.7 wt%) in some locations between the precipitates. However, the matrix Ni composition near the precipitate/matrix interface in the other region is about 10 wt% (Fig. 4.63b). The Ni composition is more consistent for the precipitates, at 52.0±2.8 wt%.

Fig. 4.64 is a TEM image of the 370FNP25 alloy. A Ni composition profile across a precipitate in this alloy is shown in Fig. 4.65. The precipitate and matrix composition is 49.1±1.5 and 12.2±0.6 wt% Ni respectively. Fig. 4.66 is a TEM BF and CDF image of the 350FNP30 alloy showing the similar morphology of the precipitates to the 350FN30 alloy. The precipitates are formed inside the original martensite plate along all bcc {110} planes. An SAD pattern of the 350FNP30 alloy and its indexing are shown in Fig. 4.67. The pattern is a bcc[100] zone axis pattern with some strong fcc {111} and {200} diffraction spots and their double diffraction maxima. Fig. 4.68

shows a Ni composition profile across a precipitate. This measurement was made using the EM400T AEM with manual specimen drift correction. However, the precipitate composition of this alloy was separately measured on an electropolished specimen in which the matrix phase was all polished away at the edge of the specimen. Therefore, the precipitate composition was measured accurately as 50.2±2.6 wt% Ni. The Ni composition of the matrix could well be lower than the measured value (17.1±1.2 wt%).

4.4.4 Alloys Heat treated at 300°C

Fig. 4.69 shows the SEM SE images of the 25 wt% Ni and the 30 wt% Ni binary and ternary alloys heat treated at 300°C for 372 days. The precipitates again show a very similar morphology to that in the alloys of the same Ni composition but heat treated at higher temperatures. However, they have a smaller precipitate width, about 10 nm. The apparent size difference of precipitates that formed in the martensite lath boundaries between the 300FN25 and 300FNP25 alloy is an etching effect. The difference in the precipitate size is actually much smaller for these two alloys.

Figs. 4.70a-c are TEM BF and CDF images and an SAD pattern of the 300FN30 alloy. The SAD pattern is a bcc[100] zone axis pattern which is from the matrix. This pattern is essentially the same as that in Fig. 4.64 but the fcc diffraction spots are much weaker for this pattern. The streaks, which are stronger than those observed in the higher temperature alloys, are along the bcc {110} directions indicating that the habit plane of the precipitates which is fcc {111} is parallel to the bcc {110}. The fringes observed in the TEM images are most likely Moiré fringes. The Moiré fringes are formed by the lattice mismatch and distortion between two coherent crystals. This is an indication that the initial stage of the high Ni fcc precipitation in the bcc matrix is coherent. A Ni composition profile across the precipitate in this alloy is shown in Fig. 4.71. A higher Ni composition was measured in the matrix. The precipitate and matrix Ni composition is 57.4±3.0 and 21.0±1.6 wt% respectively.

The microstructure of the 300FNP30 alloy is basically the same as that of the 300FN30 alloy. A Ni composition profile of a precipitate in the 300FNP30 alloy is shown in Fig. 4.72. The precipitate and matrix composition is 54.1±1.0 and 23.0±0.8

wt% Ni respectively.

Once again, the 25 wt% Ni alloy is the most difficult alloy to analyze of all the alloys heat treated at the same temperature. Fig. 4.73 shows a TEM image of the 300FN25 alloy. The apparent width of the precipitates, about 10 nm, does not appreciably differ from that in the 300FN30 alloy. However, the measured precipitate Ni composition varies among individual precipitates from ~40 to 50 wt%, significantly lower than that measured in the 300FN30 alloy (~57 wt%). A typical Ni composition profile across a precipitate measured by the VG HB501 STEM is shown in Fig. 4.74. The precipitate composition of the 300FN25 alloy listed in the Table 4-2 is the highest Ni composition measured. The measured Ni composition of the matrix near different precipitates is consistent and is 20.5±1.0 wt% for the 300FN25 alloy.

The 300FN25 alloy was also analyzed using the atom probe. Fig. 4.75 is a field ion image of the 350FN25 alloy. The small areas composed of bright spots as indicated by the arrows are precipitates. The size of the precipitates can not be accurately estimated from a single field ion image because of the local magnification variation usually associated with the second phase. Layer-by-layer evaporation analysis was performed for this alloy. Fig. 4.76 shows some of the FIM images sequentially taken in the layer-by-layer analysis. The evaporation of one atomic layer is monitored by watching the pole (indicated by p in Fig. 4.76a). An FIM image is taken for every atomic layer. Whether a bright spot (or a group of bright spots) is a precipitate or intruding atom (or atoms) can be identified since the bright spot due to the intruding atom will not stay in the same position for more than one atomic layer while the bright spot due to the precipitate will appear at same position for more than one atomic layer. The spacing between each atomic layer is approximately 0.2 nm because the <110> poles are the most frequently and clearly observed poles for bcc crystals. By this method, the size of the precipitates observed in FIM image of the 300FN25 alloy is estimated to be 0.6 to 3 nm. The precipitates of this size are not the ones that are observed in the TEM image. The precipitate labeled A in the FIM image (Fig. 4.76a) is much larger than the other precipitates observed and presumably the same kind of precipitate as those observed in TEM.

The matrix composition of this alloy measured by the atom probe is 21±1.9 at% which is consistent with the x-ray measurement. The largest number of ions collected

from a precipitate is only about 100 due to the size of precipitates and the difficulty of aligning the precipitate toward the aperture. The precipitate composition measured is 57±11 at%. The error in the atom probe data is calculated by $2(N)^{1/2}/N$ where N is the total number of ions collected.

4.4.5 Summary of the Decomposed Martensitic Alloys

The measured precipitate and matrix Ni compositions of the decomposed martensite alloys of different composition and aging temperatures are listed in Table 4-2 and Table 4-3. The precipitate compositions listed are the average value of the data points in one or more precipitates measured in the alloy. The matrix compositions listed are the lowest value of the data points which is closest to the interface. For some composition profiles where a composition gradient exists, the extrapolation method was used to obtain the precipitate/matrix interface compositions. The extrapolated compositions are specified in the Table 4-2 or Table 4-3.

In some alloys, different precipitate and/or matrix compositions were obtained when measured using different analytical instruments. These composition differences are described in the results section and will be assessed in the discussion section.

4.5 Austenitic Alloys

4.5.1 Hardness Test

The microhardness of some austenite alloys before and after the heat treatment was measured. The test was conducted with a LECO M-400FT hardness tester. The results are shown in Table 4-4. The average Vickers hardness number of n measurements and the standard deviation are listed in Table 4-4 for measurements made in the three sessions for three groups of alloys.

4.5.2 AEM Analysis

Two alloys were analyzed using the AEM, 350FN44 (44 wt% Ni alloy heat treated at 350°C for 400 days) and 650FN35 (35 wt% Ni alloy heat treated at 650°C for 235 days). Fig. 4.77 shows the electron diffraction patterns of various zone axes of the 350FN44 alloy. The SAD patterns show that the alloy has a single crystal fcc

structure. Streaking is observed in the diffraction spots on all patterns. The streaking is along <110>, <112> and <331> directions. No streaking is observed along <111> and <100> direction and in the transmitted spot. The streaking is very weak. Fig. 4.78 is a CBED pattern of the $[114]_{fcc}$ zone. The HOLZ lines which are from the first order Laue zone diffractions are visible. Fig. 4.79 is a BF image of the 350FN44 alloy. The <1 nm fine structure shown in this image is probably not due to phase decomposition, but due to the surface contamination or oxidation introduced in the electropolishing. No composition variation was detected using the EM400T AEM.

Similar to the 350FN44 alloy, the TEM imaging did not show any structural features in the 650FN35 alloy except for the common diffraction contrast of single crystals. The 650FN35 alloy has an fcc structure and no streaking was observed in electron diffraction patterns as shown Fig. 4.80. The composition of the 650FN35 alloy was measured at random positions using the EM400T AEM. The average Ni composition is 35.3±0.8 wt%, the same as the average composition of the alloy before the heat treatment measured using the EPMA at ~1 μm scale (Table 4-1). The error reported here is the standard deviation of 30 measurements. This error is much smaller than the value calculated from $N^{1/2}/N$, where N is the x-ray counts collected for each data point.

4.5.3 Atom Probe Field Ion Microscope Analysis

Five austenitic alloys were analyzed using the APFIM: 400FN44, 350FN44, 300FN44, 350FNP44, and 650FN35. Typical field ion images of these alloys are shown in Fig. 4.81. The field ion images do not show any indication of phase separation. The composition of the alloys was analyzed with the atom probe using the random area analysis method (Miller, 1987). The diameter of the column from which the atoms were collected was approximately 1~2 nm. A statistically significant number of atoms was collected from all four 44 wt% Ni alloys. Fig. 4.82 is a Ni composition profile of the 400FN44 alloy. The composition profile was constructed by dividing the collected atom chain, which is a time series, into blocks with 25 ions in each block. The composition of each block is one data point in the profile. It is estimated that the size of the ion block (25 ions) corresponds approximately to 1 atomic layers according to the calibration made for Fe-Cr alloys on the ORNL atom

probe (Miller, 1990). The composition profile can not be interpreted directly due to the large statistical error of each data point. The number of the blocks is plotted against the composition. This is the so-called frequency distribution method (Miller and Smith, 1989). The frequency distribution of the composition profile shown in Fig. 4.82 along with a standard binomial distribution which corresponds to a uniform composition is shown in Fig 4.83. The χ^2 test was used to examine if the experimental distribution deviates from standard binomial distribution with statistical significance. If yes, the experimental distribution was fitted with a series of sinusoidal functions and a parameter P_a was calculated. The value of P_a is the amplitude of the composition fluctuation. For example, P_a=0 means a uniform composition and P_a=0.1 means there is a 20 at% composition fluctuation (Hetherington et al., 1991). The P_a value and its standard deviation of each alloy is listed in Table 4-5. Two other statistical methods, the Johnson-Klotz method and the mean separation method (Miller and Smith, 1989), were also used to analyze the collected atom chain in order to detect any departure of atomic arrangement from random distribution. The result for each alloy using these two methods is also shown in Table 4-5.

No statistically meaningful number of atoms was collected from the 650FN35 alloy due to the constantly premature failure of the tips. The failure of the tips is believed to be caused by the martensite transformation induced by the strong electric field at cryogenic temperatures (Miller and Russell, 1991).

5. DISCUSSION

5.1 Accuracy of the Measured Compositions by AEM

The statistical error of the measured compositions using the x-ray EDS technique is represented by the error bars in each composition profile. The systematic errors are minimized by following the procedures and precautions discussed in sections 2.4 and 3.4. However, there are a few problems which are related to the analytical accuracy and these are discussed in this section.

5.1.1 Difference between the Individual Instruments

The AEM instruments used in this study were equipped with different EDS/computer systems. In general, the three AEM instruments gave nearly the same analytical results within their individual spatial resolution limit for the same specimen. This consistency among these independently-calibrated instruments has shown that the systematic error for each instrument in the chemical analysis is very well minimized.

The EM430T AEM and the HB501 STEM have a specimen drift correction capability. The computer program for the drift correction works very effectively. This is demonstrated in Fig. 4.53a where an array of contamination spots can be seen across the lower precipitate. The contamination spots are accurately spaced and elongated regularly in one direction. This direction is the direction of specimen drift. The length of the elongated spots shows the specimen drift within 30 seconds, a time interval set between two drift corrections. It is such a regularity and accuracy in the specimen drift correction that allows the spatial resolution of experimentally measured compoeition profiles to approach the theoretically predicted values for the EM430T and the HB501. The lack of accurate specimen drift correction is the major reason why the spatial resolution obtained experimentally is much lower than the theoretical values for the EM400T. Another reason for the poorer spatial resolution of the EM400T is the use of a 70 μm C2 aperture which causes a tail in the focused electron probe. Improvement in these two aspects largely account for the improvement in the practically achievable spatial resolution of the EM430T over the EM400T (10 nm vs. 30~50 nm). Such an improvement is not predicted by an increase

in the accelerating voltage from 120 kV to 300 kV (see Equation 2-4-7 and 2-4-8).

5.1.2 The 25 wt% Ni Alloys

In the results section, we see that the 25 wt% Ni alloy is more difficult to analyze although the size of the precipitates in the 25 wt% Ni alloy is not much different from that in the 30 wt% Ni alloy heat treated at the same temperature. For example, in a typical Ni composition profile across a precipitate in the 300FN25 alloy measured by the VG HB501 STEM (Fig. 4.74), the measured precipitate composition is much lower than that measured for the 300FN30 alloy. The spatial resolution also seems to be worse. Since the typical width of the precipitate is about 10 to 20 nm, comparable to the typical specimen thickness chosen to perform the analysis in the VG STEM, it is suggested that the precipitates in the 25 wt% Ni alloys are of needle shape. The shape of the composition profile shown in Fig. 4.74 is a result of measuring a non-through-thickness precipitate. The precipitates in the 30 wt% Ni alloys are of plate shape so that they can be through-thickness even in the case when the width of precipitates is less than or comparable to the foil thickness. The same problem occurs for the 350FN25 alloy where the precipitate width is about 30 to 50 nm, the typical specimen thickness used to perform the analysis in the Philips AEMs. The EM430T can analyze the 350FN30 alloy accurately but not the 350FN25 alloy. For higher temperatures, the size of the precipitates is larger than the typical specimen thickness (~50 nm) used in the thermonic source TEM/STEM. Therefore, the precipitate shape is not a problem for accurate compositional analysis at >400°C.

Another problem in the 25 wt% Ni alloys is that the matrix composition is higher than that of the 15 wt% and the 30 wt% alloys when measured using the thermonic gun AEMs (see Table 4-2). From the field ion images shown in Fig. 4.75 and 4.76, it is seen that there are many very small precipitates (in nm scale) in addition to the larger precipitates (~10 nm for the 300FN25 alloy) observed in the TEM. Since these nanometer scale precipitates are not observed in the TEM, the matrix composition measured using the thermonic gun AEM which has a probe diameter of 10 nm is probably an average composition of the true matrix composition and some small precipitates which are included in the x-ray excitation volume. The FEG STEM has a probe diameter of about 1 nm, and therefore, the chance for the

electron beam to hit a precipitate is much smaller. This argument can explain why the measured matrix composition using the FEG STEM is lower than that measured using the EM400T (see Table 4-2, alloy 400FN25).

The x-ray EDS analyses for the 15 wt% Ni and the 30 wt% Ni do not suffer the above problem. This seems to suggest that the nanometer scale precipitates are not present in the 15 wt% and the 30 wt% Ni alloys. For the 15 wt% Ni alloys, the absence of such small precipitates is probably due to the insufficient driving force for the precipitates to nucleate (see section 5.4, Fig. 5.12). For the 30 wt% Ni alloys, the nucleation process is different from that in the 25 wt% Ni alloys. The precipitates in the 30 wt% Ni nucleated intragranularly and it is likely that all the precipitates have grown larger into those visible in the TEM. While in the 25 wt% Ni alloy, the precipitates observed in the TEM are all in the martensite lath boundaries and it is possible that those nanometer scale precipitates nucleated in the less favorable sites within the martensite lath.

5.1.3 Precipitate/matrix Interface Composition

According to the estimated diffusion coefficients of Ni in Fe-Ni martensite, the decomposition of the martensite will not reach full equilibrium within the heat treatment time of several hundred days at temperatures below 400°C. A composition gradient is expected to exist in the matrix of the decomposed martensite. The estimation of the precipitate/matrix interface composition is important because it is the true equilibrium composition of the matrix if the reaction is diffusion controlled. In an unequilibrated alloy the interface composition can be either measured directly if the spatial resolution of the analytical technique is smaller than the width of the solute depletion zone near the precipitate, or it can be calculated by extrapolating the measured composition gradient of the matrix to the interface position.

Only a few composition profiles measured in this study have a composition gradient in the matrix region which allows a relatively accurate extrapolation of the interface composition. The rest of the composition profiles either do not show any composition gradient or have a very small gradient. Therefore it is not possible to use an extrapolation method given the precision of each data point and the total number of data points (usually less than ten). More importantly, the measured (or

extrapolated where possible) interface compositions in the matrix regions of the alloys are all higher than those measured in iron meteorites and those predicted by the phase diagram. This high matrix composition is certainly beyond the statistical error range. The question that must be answered is whether there is a steep depletion zone near the precipitate/matrix interface which is too narrow to be detected.

To solve this question about the depletion zone, a numerical simulation of precipitate growth during martensite decomposition was developed. The simulation solves the diffusion equation using the Crank-Nicolson method and the Murray-Landis variable grid. (Murray and Landis, 1959) The boundary conditions are a constant composition at the precipitate/matrix interface and a zero flux at the middle of the matrix where the impingement occurs. The interface movement is calculated by the mass conservation method. The model involves the following assumptions: 1) the precipitate growth is controlled by volume diffusion in the matrix; 2) the growth is one dimensional planar growth; 3) the phase boundaries in the current Fe-Ni phase diagram can be used to fix the interfacial compositions; 4) there is no composition variation in the precipitate phase. The diffusion coefficient and impingement distance are then varied to obtain composition profiles for alloys of different composition and alloys heat treated at various temperatures.

The results of the simulation show that, for the temperatures and times used in this study once the value of the diffusion coefficient is large enough to allow the precipitates to grow to the experimentally observed size, the depletion zone is always much larger than the spatial resolution of the AEM instruments. Fig. 5.1 and 5.2 show two Ni composition profiles simulated using this model for two conditions corresponding to two alloys respectively, the 400FN25 and the 300FN30 alloy. Experimentally measured precipitate composition and a 5 wt% Ni interface composition were used in this simulation. The depletion zone shown in these simulated profiles is definitely large enough for the HB501 STEM, which has a 2 nm spatial resolution, to measure. For the 400FN25 alloy, the depletion zone should even be detectable using the EM400T which has a 30-50 nm spatial resolution. Clearly, the simulated profiles show quite different characteristics from the experimentally measured ones (see Fig. 4.45 and 4.71).

It is concluded that the measured composition profiles which are flat and show

very little depletion at the interface are not due to the insufficient spatial resolution of the AEM instrument. All the matrix composition data listed in Tables 4-2 and 4-3 are accurate within the statistical error reported.

5.2 Orientation Relationship between the Precipitate and Matrix Phase

There are only two basic crystal structures involved in both the meteorites and the alloys studied, bcc and fcc. However, the determination of the orientation relationship is not so simple. In general, the two most commonly observed orientation relationships between fcc and bcc crystal structures are the so-called N-W and K-S relationships. Both relationships have a pair of parallel planes in common, i.e. $\{111\}_{fcc} \parallel \{110\}_{bcc}$. The parallel directions for each relationship are:

N-W: $[101]_{fcc} \parallel [001]_{bcc}$

K-S: $[011]_{fcc} \parallel [111]_{bcc}$

It is worth noting that since both structures are cubic, the index of a crystal plane and a crystal direction can be used interchangeably.

The superimposed reciprocal lattice planes of some low indexed zone of fcc and bcc crystals which bear the N-W and K-S relationship are shown in Fig. 5.3. The ratio of lattice parameters is chosen to be those of γ-Fe and α-Fe. It is these reciprocal lattice planes that we see in the electron diffraction patterns.

The difficulty arises because, first of all, there are twelve <110> directions and eight <111> directions which are crystallographically equivalent in the cubic system. However, for the orientation relationships of an fcc and a bcc crystal across a particular interface, there will only be one set of $<110>_{bcc}$ and $<111>_{fcc}$ in parallel because the angle between <110>s is 60° and the angle between <111>s about 70°. When a particular $(111)_{fcc}$ plane is parallel to a particular $(110)_{bcc}$ plane, the rest of the $\{111\}_{fcc}$ planes will be at least ~10° away from the nearest $\{110\}_{bcc}$ plane. Therefore there will be many $<110>_{bcc}$ directions parallel to some high order index directions of fcc and many $<111>_{fcc}$ parallel to high order index directions of bcc. Secondly, as shown in Fig. 5.3, when $[10\bar{1}]_{fcc} \parallel [001]_{bcc}$ (N-W relationship), the angle between $[01\bar{1}]_{fcc}$ and $[1\bar{1}1]_{bcc}$ is only 4°. When $[01\bar{1}]_{fcc} \parallel [\bar{1}11]_{bcc}$ (K-S relationship), the angle between $[001]_{bcc}$ and $[10\bar{1}]_{fcc}$ is also 4°. Four degree tilt is not a large angle in electron diffraction since it only corresponds to about 4 cm on the TEM viewing screen for a

camera length of 60 cm. In bent samples local bending can easily tilt the zone axis by 4°.

The above discussion shows that the $<100>_{bcc}$ or the $<111>_{bcc}$ zone axis pattern obtained from one side of the interface must be exactly parallel to the $<110>_{fcc}$ zone axis pattern of the other side in order to determine the orientation relationship. If the parallel directions are off by a few degrees, as often observed, the orientation relationship can not be uniquely determined because the slight misorientation can arise for three different reasons as discussed in the previous paragraph. A better orientation to distinguish the N-W and the K-S relationship is by taking a diffraction pattern perpendicular to the interface i.e. along $<111>_{fcc}$ directions. However, this means that the interface has to lie parallel to the thin foil which is impractical from the specimen preparation point of view.

Now let us examine the experimentally observed orientation relationship in the iron meteorites and the alloys. Fig. 5.4 is an SAD pattern taken from the CZ of the Tazewell iron meteorite. The pattern is composed of a zone axis pattern of $L1_0$ ordered fcc<110> and of a bcc <111> zone axis with the $(111)_{fcc}$ parallel to the $(110)_{bcc}$. Both patterns are very close to the exact zone axis. Therefore, the orientation relationship of the CZ is the K-S type. However, electron diffraction patterns obtained in the plessite regions are more complicated and the N-W and K-S orientation relationship can not be distinguished so easily. In Fig. 4.8b,c for example, the CBED pattern of the matrix is close to the bcc <100> zone axis, but the CBED pattern of the precipitate is several degrees away from the fcc <110> zone axis. According to the previous discussion, the orientation relationship can be either N-W or K-S type.

Another orientation relationship is shown in Fig. 4.64. This pattern is composed of an fcc <110> and a bcc <100> zone axis pattern. Both patterns are not in the exact zone axis directions according to the intensity distribution of the diffraction spots around the transmitted spot. Moreover, the CDF imaging shows that the many strong diffraction spots are not from the same precipitates. The precipitates are too small to do CBED analysis. It can seen that one fcc <111> is almost parallel to one bcc <110> with another fcc <111> a few degrees away from another bcc <110> and the fcc <200> a few degrees away from bcc <200>.

The K-S and N-W relationships are crystallographically ideal cases. In a

practical system like the present one where the fcc precipitates are very fine plates and nucleated along all bcc <110> planes, only the $\{111\}_{fcc} \parallel \{110\}_{bcc}$ relationship is strictly followed and serves as the habit plane of the precipitates. The orientation relationship on the habit plane is most likely relaxed and fcc <110> can be parallel to either bcc <100> or bcc <111> or anywhere in between depending on the local strain situation. It is believed that this relaxed orientation relationship is responsible for the often observed split of major diffraction spots along the direction in which the lattice parameter is unchanged.

5.3 Rate-controlling factor of the Martensite Decomposition in Fe-Ni Alloys

Martensite decomposition in the Fe-Ni system is a nucleation and growth process. The γ (fcc) precipitates nucleate and grow in the metastable martensite matrix and eventually a stable α(bcc)+γ two phase structure is formed. The nucleation occurs very rapidly at the beginning of the transformation at the energetically favorable sites. A small amount of precipitation will change the mean concentration of solute in the matrix by an amount sufficient to decrease the heterogeneous nucleation rate by one or two orders of magnitude (Martin and Doherty, 1976a). So the subsequent nucleation can be neglected. The size of the precipitates and the phase equilibria of the structure are determined by the growth process.

The rate of precipitate growth is generally considered to be limited by two factors, the rate at which atoms are brought to or removed from the interface by diffusion and the rate at which they cross the interface. Whatever is slower controls the rate of growth. Since both atom diffusion within the solid phase and atom jumping across the interface are thermally activated migration, the diffusion which involves atomic movement through many lattice sites is likely to be slower than the jumping which normally involves movement through only one atomic distance. Therefore, most civilian (or diffusional) transformations in metallic systems are diffusion controlled. However, Aaronson (1962) has suggested that certain interphase interfaces may not allow rapid atomic transport across them, in other words, the interfaces are immobile. In this case, the growth of the precipitates will be controlled by whatever mechanism allows the interfacial movement, i.e interface reaction controlled.

Theoretical analysis shows that such immobile interfaces are those between two phases of different crystal structure but are coherent or semi-coherent due to the match of lattice spacing on certain atomic planes. A widely used example is the $(111)_{fcc}/(001)_{hcp}$ interface where the only difference between the two crystal structures is the stacking sequence of closely packed atomic planes. As shown in Fig. 5.5, the movement of such an interface will require the atoms move to a highly energetically unfavorable position (B atom on top of B atom). Five atomic layers have to be changed simultaneously to achieve a relatively stable situation in which only a partial dislocation loop is present. Although the interface can move forward by the glide of the partial dislocation loops, it will need repeated nucleation of such five atomic layers. Obviously the migration rate of such an interface is going to be greatly reduced due to the extra activation energy needed for nucleation on the interface. In the case of precipitation in a supersaturated solid solution, the driving force for nucleation on an interface can be provided thermally or chemically. At low temperatures, the thermal activation energy available is low. Therefore, Weatherly (1971) and Woodruff (1973) concluded that the nucleation would need significant supersaturation at the interface as a driving force. This means that the interfacial composition of both precipitate and matrix phase could be well off their equilibrium values during the growth. An effect of interface reaction controlled growth on the composition profile across precipitate and matrix is schematically shown in Fig. 5.6.

Another consequence of the interface reaction controlled growth is the shape of the precipitate. If the strain effect is neglected, the equilibrium shape of the precipitate will be determined by the ratio of the precipitate/matrix interfacial energy between the different atomic planes which encircle the precipitate. However, if one coherent or semi-coherent interface is highly immobile, the equilibrium shape of the precipitate may not be achieved due to different growth rates on coherent and incoherent interfaces. The precipitate will grow faster along the edge of a plate or the tip of a needle where the interface is usually incoherent. An example of such a thin plate precipitate morphology was given by Nicholson and Nutting (1961) in an Al-4 at% Ag alloy.

The only effective growth mechanism of the highly immobile coherent and semi-coherent interfaces is the ledge mechanism (Aaronson et al., 1970) By the ledge

mechanism, a coherent interface migrates via the lateral movement of incoherent ledges along the coherent interface. It is much easier for atoms to find a low energy configuration to accommodate themselves around ledges. Growth by the ledge mechanism has been observed experimentally in a number of metallic systems (Weatherly, 1971; Abbott and Haworth, 1973; Bäro and Gleiter, 1974). The only problem with the ledge mechanism, when applied to precipitate growth, is that a source of ledges must exist. The kinetics of the supply of ledges, of which little is known at present, is believed to be the real essence of interface reaction controlled growth (Martin and Doherty, 1976b). A structural origin of ledges has been proposed, such as the impinging point between precipitates (Weatherly, 1971).

Much experimental evidence in this study suggests that the precipitation in Fe-Ni martensite decomposition at low temperatures (<450°C) is mostly an interface reaction controlled process. First of all, the measured matrix compositions near the precipitate/matrix interface in the alloys are higher than those predicted in the current Fe-Ni phase diagram and those measured in iron meteorites. It should be mentioned that the current phase diagram below 400°C is determined primarily from the data of the α/γ interface and the high Ni rim of the taenite of iron meteorites. A previous study by Romig and Goldstein (1980) using decomposed martensite alloys also contributed to the phase diagram and their results were in agreement with the iron meteorite data. In this study, the plessite regions are investigated. The precipitate and the matrix composition measured in the low Ni plessite region agree with the current Fe-Ni phase diagram. The Ni composition in the middle of Widmanstätten plate (α) is about 7 wt%. This composition is considered to be the highest solubility of Ni in the α phase which occurs around 400°C to 500°C. However, the measured matrix composition of Fe-Ni martensitic alloys heat treated at 450°C to 400°C is about 8 wt%. The matrix Ni composition of the plessite is about 4–5 wt% for large γ precipitates (100 nm wide) and ~10 wt% for very small precipitates (~10 nm wide) of plate or needle shape. However, the measured matrix Ni composition is ~20 wt% for the alloy heat treated at 300°C.

Secondly, the measured Ni composition profiles are quite flat in the matrix regions. The flat composition profile and very shallow depletion zone near the interface do not agree with the simulated composition profiles based on a diffusion

controlled model (see Fig.5.1 and Fig 5.2). This disagreement, as discussed in section 5.1.3, is not due to analytical error but indicates that the assumptions used in the numerical simulation model may not be correct. Since the phase boundary data from the meteorites seem to be correct and using a three dimensional diffusion model does not alter the simulated composition profile very much, the only assumption which can be incorrect is that of diffusion control. The measured composition profiles do show characteristics predicted by theory of interface reaction controlled growth. The matrix composition at the interface is higher than the equilibrium value due to the necessity to provide a driving force for atoms to cross the interface. The composition profile in the matrix is flat because diffusion is relatively faster than the interface reaction.

Finally, the measured matrix Ni composition varies significantly among alloys of different composition but heat treated at the same temperatures (see Table 4-2). The measured matrix Ni composition around a precipitate also varies from precipitate to precipitate in some alloys. For example, a matrix composition in the 350FN30 alloy listed in Table 4-2 is 5.6 wt% Ni. However, the matrix composition of ~10 wt% Ni was also measured in the same alloy (Fig. 4.63b). This variation seems to be a logical consequence of the interface reaction controlled growth through a ledge mechanism. The alloys of different Ni composition have a different martensite structure to start with. So the mechanism of providing ledges can be quite different, resulting in a different growth rate and a different matrix Ni composition. In a particular alloy, there might be some favorable nucleation sites for ledges on some precipitate/matrix interfaces, so the Ni composition near these interfaces can be lowered to the equilibrium value relatively quickly.

The conditions for interface reaction controlled growth are met quite well in the alloys of this study. The temperatures at which the phase transformation occurs are very low, only about 0.4 to 0.3 T_m. The interface separating the precipitate and matrix is semi-coherent (fcc/bcc, N-W or K-S relationship). The presence of a semi-coherent interface is shown by 1) the presence of an orientation relationship and a habit plane as shown by electron diffraction and morphology of the precipitates; 2) the TEM image of the interface. Interfacial dislocations are observed in the precipitate/matrix interface, for example Fig. 4.53b. Morié fringes due to the overlapping of the precipitate and matrix are observed in alloys containing very fine precipitates (Fig.

4.62, Fig. 4.70). Although the $(111)_{fcc}/(110)_{bcc}$ interface is not an intrinsically good semi-coherent interface, (mismatch between fcc[110] and bcc[111] or bcc[100] is 3% and 11% respectively) the coherency of the precipitate/matrix interface in the Fe-Ni martensite alloys decomposed at low temperatures can still be high because the precipitates are very small. In fact, Morié fringes are much more strongly present in the 300°C alloys than in the 400°C alloys.

The above discussion of the interface controlled growth via a ledge mechanism can also be used to explain the discrepancy between the measured matrix Ni compositions in this study and those in the previous work by Romig and Goldstein (1980). The present study uses a similar experimental approach to that used by Romig and Goldstein (1980). However, the matrix composition of the alloy heat treated at 300°C measured by Romig and Goldstein is lower and closer to the matrix composition measured in the low Ni plessite regions and the α composition at the α/γ interface. The measured Ni composition profiles in the study of Romig and Goldstein (1980) show that their alloys are more equilibrated that those of this study. Since the AEM instruments used in this study have a much higher spatial resolution for chemical analysis than that used by Romig, the discrepancy in the measured matrix composition is not due to the analytical error. The only possible difference in the experimental procedures between the two studies is the quenching of alloys which is difficult to control. The possible difference in the quenching parameters may have resulted in some differences in the internal structure of the Fe-Ni martensite prepared in the two studies. The martensite structure formed in the alloys made in Romig's study was somehow able to provide a faster growth rate for the precipitates, most probably through a more effective supply of ledges. The faster growth rate of the precipitates resulted in the lower matrix composition measured by Romig and Goldstein (1980).

5.4 Measured Fe-Ni(P) Phase Equilibria at Low Temperatures

The measured precipitate and matrix Ni compositions of decomposed martensite alloys are plotted in Fig. 5.7 to Fig. 5.10. The precipitate compositions of binary alloys of different composition heat treated at same temperature are quite consistent. They represent the equilibrium conditions of $\alpha+\gamma$ formed by martensite

decomposition. Some of the data in Fig. 5.7 to 5.9 are plotted on the Fe-Ni phase diagram as shown in Fig. 5.11. The $\alpha+\gamma/\gamma$ phase boundary should be modified at 450°C according to the more accurate measurement in this study. The measured precipitate Ni composition at 400°C suggests that the eutectoid temperature is between 400°C and 450°C instead of the calculated 389°C (Chuang et al. 1986). No ordering was observed in the high Ni precipitate phase in the 300°C alloys. This indicates that the ordering transformation is a much slower process than the nucleation and growth process of the martensite decomposition. Another possibility is the ordering temperature is lower than 300°C instead of the previously reported 320°C.

It can be seen from Fig. 5.7 to Fig. 5.11 that the measured matrix compositions are generally higher than those measured in the meteorites and show large variations among the alloys heat treated at the same temperature. These two problems are explained by the mechanism which controls the precipitate growth as discussed in section 5.3. Most matrix compositions are not the equilibrium composition of the $\alpha+\gamma$ structure, but some intermediate compositions determined by a dynamic balance among diffusion, interface reaction and impingement of the diffusion fields. However, the experimental results show that the degree of the interface reaction control varies according to the heat treatment temperature and is the strongest at the lowest temperature (300°C). At 450°C, composition gradients toward grain boundaries are observed (Fig. 4.36b). The extrapolated matrix Ni composition (~7.6 wt%) is close to the equilibrium value at this temperature (~7 wt%), as determined by the maximum solubility limit of Ni in the kamacite plate in meteorite, indicating the chemical driving force needed for atoms to cross the interface is small at this temperature. Therefore, the precipitate growth at 450°C is probably in a medium ground between the completely interface reaction control and the completely diffusion control. In another extreme at 300°C, the matrix composition (~20 wt%) is much higher than the equilibrium value (4 to 5 wt%) at this temperature indicating the chemical driving force needed at this temperature is much higher. The large chemical driving force needed for the precipitate growth at 300°C is partially responsible for the experimental fact that no precipitates were found in the 300FN15 alloy. Similarly, very few precipitates were formed or grew to a sufficient size to be observed in the 15

wt% Ni alloys heat treated at 350°C and 370°C. Another reason for the smaller number of precipitates formed in the 15 wt% Ni alloys is that the driving force for nucleation is smaller for the alloy of lower Ni composition, and hence, lower saturation. As schematically shown in Fig. 5.12, the driving force for the transformation is ΔG_0 and the driving force for the nucleation is ΔG_n. The ΔG_n is larger for large X_0-X_e, the supersaturation. The precipitates can only form at high energy nucleation sites with the small driving force. Although the equilibrium volume fraction of the precipitates should be lower in the 15 wt% Ni alloys than in the higher Ni alloys, it is not the reason for fewer precipitates observed in the 15 wt% Ni alloys because the alloys are far from equilibrium and most of the matrix regions in the 15 wt% Ni alloys are still supersaturated with Ni.

A large variation in the matrix composition was measured in some alloys. In the 350FN30 alloy, the matrix compositions of ~5 wt% and ~10 wt% were measured (Fig. 4.63a,b). The lower Ni composition is more likely to be the equilibrium matrix composition at this temperature. The reason that the equilibrium composition can be reached at one precipitate area is probably a combined effect of effective growth by the ledge mechanism and impingement between the diffusion zones of the adjacent precipitates.

The composition data measured in the ternary alloys show the same characteristics as their binary counterparts. The precipitate composition at each temperature is slightly, but not significantly lower. The matrix Ni compositions measured in the ternary alloys are usually higher than those in the binary alloys (see Table 4-3). However, since matrix Ni composition variation of the same magnitude as that between the ternary and the binary alloys is also measured in the different places within the same binary alloy, it is not clear whether the higher matrix Ni composition in the ternary alloys is an equilibrium feature or due to the effect of P on the ability for the atoms to cross the interface.

5.5 Plessite Structure and Its Formation

It is shown in this study that the two phase structure of plessite in iron meteorites is composed of tetrataenite precipitates in an α (bcc) matrix. The size, shape and distribution of the precipitates vary over a wide range with the local

average Ni composition of the plessite. The Ni composition of the precipitate and matrix also varies with the local average Ni composition of the plessite. Two types of the precipitates are observed in the plessite region. The first type of precipitate is primarily found in plessite regions of low Ni content (9~10 wt%) i.e. the duplex plessite region. These precipitates are formed at the original martensite lath and block boundaries and have a relatively large size (>200 nm wide). The precipitates of the low Ni region have a ~50 wt% Ni composition (Fig.4.10) and are in equilibrium with a matrix phase of ~4 to 5 wt% Ni. The second type of precipitate usually forms in plessite regions of higher Ni concentration (>15 wt%) i.e. the black plessite region. The precipitates formed inside the original martensite plates along all crystallographically equivalent directions with the precipitate {111} plane parallel to the matrix {110} plane. These precipitates are very thin plates or fine needles, typically 10~20 nm wide. The precipitates of the high Ni region have ~57 to 60 wt% Ni and are in equilibrium with a matrix phase of ~10 wt% Ni (Fig. 4.13, Fig. 4.22). The two types of precipitates represent the extreme cases in the plessite. In many regions of Ni composition between 10 to 15 wt%, both type of precipitates exist (Fig. 4.11a and Fig. 4.17).

The formation of the duplex plessite can be understood according to the current Fe-Ni phase diagram (Fig. 5.13) and therefore is consistent with the phase equilibria observed in the other regions of iron meteorites. A retained taenite area containing ~10 wt% Ni will transform into martensite around 500°C during cooling. The γ phase will then nucleate at energetically favorable nucleation sites i.e. martensite lath boundaries and corners. In this temperature range (≤500°C), the diffusion rate is fast enough to allow the precipitates to grow and lower the supersaturation of Ni in the matrix. Further nucleation is suppressed. The Ni composition of the precipitates continuously increase following the equilibrium $\alpha+\gamma/\gamma$ boundary while the Ni composition of the matrix decreases following the $\alpha/\alpha+\gamma$ phase boundary. Below the eutectoid temperature (450-400°C), the precipitate composition reaches ~52 wt%, the stoichiometric composition of FeNi. The ordering transformation starts at ~320°C (Chamberod et al. 1980, Reuter et al. 1988) in the high Ni precipitates yielding the low temperature equilibrium two phase structure, tetrataenite precipitates in an α matrix of 4 to 5 wt% Ni. This phase equilibrium condition is the same as that

observed in the α/CT1 interface.

The phase transformation in the high Ni plessite region is more complicated than that in the low Ni plessite. A retained taenite region of ~20 wt% Ni is formed at about 600°C according to the simulation of Widmanstätten pattern growth (Fig. 2.7). The martensite transformation will not occur until the temperature reaches below 250°C. The nucleation of γ precipitates at martensite grain boundaries and corners probably still occurs but the growth of the precipitates at these low temperatures is not sufficient to bring down the Ni composition in most regions of the matrix since the diffusion is so slow. As cooling continues, the driving force for γ nucleation increases. The precipitation starts at less energetically favorable sites within the original martensite grain to form the intragranular precipitates. As shown in this study, the mobility of the semicoherent $(111)_{fcc}/(110)_{bcc}$ interface between the γ precipitate and the α matrix in Fe-Ni alloys is extremely low and the γ precipitate growth in the martensite decomposition is interface reaction controlled at low temperatures. Therefore, these intragranular precipitates can only effectively grow along the edges or tips to form thin plates or fine needles. The phase equilibrium between the fine intragranular precipitate and the matrix is determined by the equilibrium at the edges or tips of the precipitates. The composition of matrix in equilibrium with the sharp edge (tip) will be higher than it would be for the planar interface according to the Gibbs-Thomson effect (Hillert, 1957).

The equilibrium matrix composition at a fine tip of radius r, X_r, is:

$$X_r = X_\infty \exp\left(\frac{2\gamma V_m}{RTr}\right) \qquad (5\text{-}4\text{-}1)$$

For the present situation, the interfacial energy is that of an incoherent interface between bcc and fcc, assuming $\gamma \approx 0.3$ J/m^2, a typical value of semicoherent interface with substantial mismatches. The molar volume is $V_m \approx 7\times10^{-6}$ m^3. The temperature is 473K. The radius of the tip is estimated to be 3 nm since the maximum width of the precipitate is about 10 nm. Then Equation 5-4-1 gives:

$$X_r = 1.43 X_\infty$$

an increase of 43% from the equilibrium composition of a planar interface.

The free-energy vs concentration diagram used to derive Equation 5-4-1 is shown in Fig. 5.14. From Fig. 5.14a, the equilibrium solubility of B in the α phase, X_B^e, is derived as:

$$X_B^e = \exp(-\frac{\Delta G_B + \Omega}{RT}) \qquad (5\text{-}4\text{-}2)$$

where Ω is the enthalpy of mixing for a regular solution (Porter and Easterling, 1981). The free energy increase due to the Gibbs-Thomson effect goes in the term ΔG_B resulting in a smaller ΔG_B and a higher X_B^e. However, Equation 5-4-1 is derived by assuming the precipitate phase (β in the derivation) is pure B (Porter and Easterling, 1981). If we consider the composition of the precipitate is $X_B(\beta)$ and repeat the derivation, as shown in Fig. 5.14b, the change on ΔG_B will approximately be:

$$2\gamma V_m[1-X_B(\alpha)]/r[X_B(\beta)-X_B(\alpha)]$$

instead of $2\gamma V_m/r$, where term $X_B(\alpha)$ is the equilibrium solubility of B in the α phase without considering the Gibbs-Thomson effect ($X_B(\alpha)=X_\infty$). The revised Equation 5-4-1 is:

$$X_r = X_\infty \exp(\frac{2\gamma V_m}{RTr} \cdot \frac{1-X_B(\alpha)}{X_B(\beta)-X_B(\alpha)}) \qquad (5\text{-}4\text{-}3)$$

For the present system, $X_B(\beta)\approx 0.5$ and $X_B(\alpha)\approx 0.05$, then

$$X_r = 2.12X_\infty$$

X_∞, as determined by the matrix composition measured in the low Ni plessite region, is 4–5 wt%. Therefore, the measured ~10 wt% Ni matrix composition in the high Ni plessite region can be accounted for by using the Gibbs-Thomson effect.

It should be noted that the accuracy of estimated X_r is limited by the knowledge of interfacial energy and the accuracy in the measurement of r. The values of these two parameters used in the estimation are merely, although reasonably, estimated. However, the result of the estimation has shown qualitatively that for a fine precipitate (<10 nm) and at low temperatures (<250°C) an increase of >100% in the equilibrium matrix composition is possible.

The Ni composition of the fine intragranular precipitates is higher than the

stoichiometric FeNi composition which is measured in the larger intergranular precipitates in the low Ni plessite region. However, tetrataenite is still present in these intragranular precipitates. A possible explanation for the formation of the ordered FeNi of high Ni composition (~58 at% as opposed to the stoichiometric 50 at%) is the transformation sequence. According to the phase diagram, Fig. 5.13, the equilibrium structure for the Fe,5-50%Ni alloys should be $\alpha+\gamma'$ below ~400°C. The phase transformation path is $\gamma \rightarrow \alpha+\gamma'$. However, the real phase transformation sequence in the plessite formation is $\gamma \rightarrow \alpha_2 \rightarrow \alpha+\gamma \rightarrow \alpha+\gamma'$, the martensite decomposition (step 2) is a faster transformation than the ordering (step 3) and occurs first. The Ni composition of the γ phase formed by the martensite decomposition will be at the phase boundary value measured in this study shown in Fig. 5.7 to 5.10. For the low Ni plessite region, as discussed previously, the $\alpha_2 \rightarrow \alpha+\gamma$ transformation occurred at above 400°C so that the γ composition is less than 50 at%. When temperature decreased to the ordering temperature, the ordering transformation occurred in the γ phase and stabilized the Ni composition at ~50 at%. However, in the high Ni plessite region, the $\gamma \rightarrow \alpha_2 \rightarrow \alpha+\gamma$ transformations occurred at much lower temperature (<300°C for the regions of >17 wt% Ni according to the measured M_S). Therefore, the γ phase formed by $\alpha_2 \rightarrow \alpha+\gamma$ had a Ni composition >50 at% initially (Fig. 5.8-5.10). The FeNi ordering then occurred in the γ precipitates of >50 at% Ni. Therefore, the transformation sequence and the phase equilibria of the martensite decomposition at low temperatures are the major causes that the FeNi precipitates with a higher than stoichiometric Ni composition were formed.

Since meteorites cooled very slowly (1-10K/10^6 yrs), it is necessary to explain why coarsening of the precipitates does not occur in the plessite. According to the Ostwald ripening theory (Ostwald, 1900), the smaller precipitates that initially formed will dissolve and the larger precipitates will grow because of the difference of the matrix composition in equilibrium with the precipitates. As shown in Fig. 5.15, the matrix region near a smaller precipitate has a higher equilibrium solute concentration due to the Gibbs-Thomson effect, and therefore, solute atoms will diffuse toward the larger precipitate. The smaller precipitate must dissolve to keep the equilibrium until it diminishes. Apparently, this process did not finish in the plessite region as the small precipitates still remain. To understand this fact, it is useful to notice that the

coarsening only occurs after the diffusion zone of the precipitates of various sizes meet each other. The diffusion distance for the coarsening is likely to be longer than that for the growth which can be a relatively "local" event. For the present alloy system, the diffusion coefficient is probably different for growth and coarsening as well. The precipitates grow in the martensite matrix in which the diffusion coefficient is relatively larger due to the short-circuit diffusion along dislocations. The coarsening occurs in the equilibrium α matrix which has a lower defect density, and therefore, a smaller diffusion coefficient than the martensite. The diffusion coefficient of α(P) phase at 500K is ~10^{-28} cm^2/sec. The simplest estimation of diffusion distance using the square-root Dt expression for $t=10^{14}$ sec (~10 million years) shows that diffusion distance is about 1 nm. This distance is apparently not significant for the coarsening to penetrate the entire black plessite region.

5.6 Comparison of the Structure of Plessite and the Alloys

The basic phase transformation processes that occur are the same in both the plessite and the experimental alloys, that is, martensite transformation and successive decomposition. Therefore, there are many similarities in the microstructure of the plessite and the alloys such as the morphology and the composition of the precipitates. However, there are at least two significant differences which will be discussed in this section.

The first difference is the thermal treatment. The alloys have undergone an isothermal heat treatment for a relatively short time. The plessite has experienced a very slow cooling over an extremely long time period. As a result, the decomposition in the plessite has reached a stable state despite the very slow growth due to the interface reaction controlled mechanism at low temperatures. The ordering reaction has also occurred in the high Ni precipitate phase in the plessite. In most of the alloys particularly the low temperature ones, the γ precipitate growth is not complete and the matrix Ni composition is still higher than the equilibrium value. In many matrix regions, the Ni composition is still the average alloy composition.

The second difference is the presence of trace elements. The alloys are pure binary Fe-Ni or Fe-Ni with 0.2-0.3 wt% P. The plessite has many other trace elements such as C, Co, and S. What effect these trace elements have is not

understood at the present time. However, they might be responsible for the difference in microstructure between the meteoritic plessite and the alloy. In the 15 wt% Ni alloys, there are very few precipitates nucleated at low temperatures. In the 15 wt% Ni plessite region, not only are intergranular precipitates formed, but there are also the intragranular precipitates. This difference in microstructure might be explained by the very long annealing time that meteorites experienced. But it is quite possible that the trace elements are also providing additional nucleation sites.

The >28 wt% Ni region in most iron meteorites has not transformed to martensite although the meteorites are probably slowly cooled to below room temperature (below measured M_s at 28 wt% Ni). One explanation for this lack of martensite transformation is that the >28 wt% Ni region is cooled into the miscibility gap before the martensite transformation occurs (see Fe-Ni phase diagram in Fig. 5.13). There is enough time for the ordered FeNi to nucleate and form the CT2 structure (see section 2.2.3). The very fine ordered domains of FeNi which formed in the γ matrix can effectively suppress the martensite transformation.

However, this explanation cannot explain the structure of another iron meteorite, Tishomingo, which has a bulk Ni composition of 32.5 wt% and has a martensite structure (Buchwald, 1975d). The plate martensite structure of Tishomingo is exactly the same as that in the 30 wt% Ni alloy (Fig 4.63 for example). The formation of martensite in Tishomingo may suggest that Tishomingo was cooled to a much lower temperature than the other meteorites. However, another factor should not be ignored. It is that Tishomingo is a meteorite with exceptionally low trace element concentration and no carbides, graphides, phosphides, or silicates are found (Ives et al., 1978). If we assume that Tishomingo and other meteorites were cooled to a similar temperature, it seems that the presence of the trace elements have suppressed the M_s temperature. This argument is being further supported by another experimental observation.

In alloys, the 30 wt% Ni alloy forms plate martensite and a 25 wt% Ni alloy forms lath martensite. In the plessite, the plate martensite was formed in the 25 wt% Ni area according to the morphology of the decomposed martensite structure (Fig. 4.20). Because of this difference in the initial martensite structure, the microstructure of the 25 wt% Ni plessite region is similar to that of the 30 wt% alloy. A possible

scenario is proposed here to account for this difference in the martensite structure of the same Ni composition between the laboratory alloys and the meteorites.

One can use the same argument that the martensite start temperatures in the iron meteorites is decreased more than 100°C by the presence of the trace elements. According to the work of Brofman and Ansell (1982) on Fe-Ni martensite, the determining factor for the transition from lath morphology to plate morphology is the M_s. For the pure binary Fe-Ni alloy, the transition of morphology occurs at about 30 wt% Ni which corresponds to ~-40°C according to the measured M_s (Kaufman and Cohen, 1956). The transition observed in the plessite region of the iron meteorites is at about 25 wt% Ni which means that the martensite transformation occurred in the 25 wt% Ni region in the iron meteorites at about -40°C. The measured M_s for a pure Fe-Ni alloy at 25 wt% Ni is about 100°C. It is believed that this decrease in M_s is because the presence of the trace elements. Among the various trace elements present in the iron meteorites, C is known as an austenite stabilizer and will decrease the M_s. The effect of Co is not clear, but many other transition metal elements such as Pt and Mn are also austenite stabilizers (Krauss and Marder, 1971). The effect of P and S on the M_s is unknown.

If martensite forms in iron meteorites more than 100°C lower than we currently believe, the previous discussion about the plessite formation does not have to be changed significantly. The only problem which has to be considered is the decomposition of martensite of high Ni content. It has been shown that the martensite near the CT2 border which has >25 wt% Ni is also decomposed in the Carlton meteorite (Fig. 4.20 and 4.21) and that the size of the precipitates in this region is also on the order of 10 nm. A recent atom probe study by Russell et al. (1991) has shown that the martensite in Tishomingo is also decomposed with very fine precipitates of ~57 at% Ni in the matrix of ~20 at% Ni. The precipitates in the plessite region of >25 wt% Ni have to nucleate and grow in the 0 to -100°C temperature range. This low temperature growth is unreasonable since an estimation of the Ni diffusion coefficient in martensite, by extrapolating the high temperature data, shows that $D=10^{-26}$ to 10^{-28} cm^2/sec. It is suggested here that the Carlton and Tishomingo meteorite were reheated. The reheating did not exceed 320°C because the ordered FeNi phase is still present. Such a reheating hypothesis is supported by the

fact that undecomposed martensite is present in the high Ni plessite of some meteorites, for example Tazewell meteorite (Lin et al., 1979, Zhang, 1988).

5.7 Structure of High Ni Anomalous Meteorite

The most unusual feature of the microstructure of typical Santa Catharina samples, such as the BM#52283 sample used in this study, is the presence of dark and light regions from ~1 μm to >100 μm in dimension. This study shows that the dark and light regions are secondary structures formed by terrestrial corrosion and superimposed on the primary structure. The primary structure of Santa Catharina is a cloudy zone structure. The island phase, about 20 nm in size, is tetrataenite and the honeycomb phase is low Ni fcc taenite.

It is clear from electron optical observation of this study that the dark and the light regions are each multiphase having a cloudy zone structure. The morphology and the island phase of the dark and the light regions are the same. The only difference between the dark and the light regions is the honeycomb phase. The honeycomb phase in the dark region is an oxide, most probably Fe_2NiO_4, while the honeycomb phase in the light region is a low Ni fcc taenite phase. The presence of the oxide in the dark regions is confirmed by both structural and chemical analysis (electron diffraction and EELS). Therefore, the dark regions observed in the optical microscope and the SEM BSE imaging mode are formed by the oxidation of the low Ni honeycomb phase of the original cloudy zone structure. The original cloudy structure is preserved in the light regions.

The scale of the cloudy zone structure in Santa Catharina (20 nm) suggests that it was formed by the low temperature spinodal decomposition proposed by Chuang et al. (1986). The lack of larger scale microstructure features shows that no other phase transformations occurred in Santa Catharina (35 wt% Ni) before it was cooled into the low temperature miscibility gap. Although the cloudy zone in the octahedrites is also formed by the low temperature spinodal decomposition, the structures of the constituent phases of the CZ in Santa Catharina are not exactly the same as those observed in other meteorites, the Dayton, Carlton, Grant and Tazewell octahedrites or the Estherville stony iron meteorite (Reuter et al., 1988). In these meteorites, the honeycomb phase of the cloudy zone has a bcc structure. In

Estherville, a very slow cooled meteorite, the Ni content of the coarser honeycomb phase was 12 wt% as measured using the AEM. In this study, the Ni composition of a finer honeycomb phase (Carlton) was measured using a high spatial resolution STEM and is also about 12 wt%. As already noted, the cloudy zone structure is the product of the spinodal decomposition within the miscibility gap (Fig. 5.13). At about 200°C, the estimated final equilibrium temperature, the γ taenite boundary of the miscibility gap on the low Ni side is approximately 12 wt% Ni. If the meteorite cooled slowly enough so that decomposition proceeded to the quasi-equilibrium state in the miscibility gap, the low Ni phase would transform into bcc martensite as it is below the measured M_s (see Fig. 5.13). In Santa Catharina no bcc diffraction spots were observed in the TEM, and the honeycomb phase has the same fcc structure as the island phase. There are several possible reasons why the low Ni phase retained the fcc structure and did not transform to martensite. First of all, it might be a result of a much faster cooling rate of the Santa Catharina. A fast cooling rate would result in a honeycomb phase with a higher Ni composition. The atom probe study gave a honeycomb composition of 15 wt% Ni (Miller and Russell, 1990). This Ni composition is low enough for the martensite transformation to occur at 200°C. However, according to the discussion in the previous section, the M_s in meteorites might be decreased by as much as 100°C. Secondly, the martensite transformation in the CZ occurs in the honeycomb phase which is very thin layers between the island phase, ~50 nm in Estherville and ~10 nm in Carlton and Dayton. The much thinner honeycomb phase in Santa Catharina, <5 nm, will have an effect of suppressing the martensite transformation. Third, the stress-strain condition is likely to be quite different in the chemically homogeneous Santa Catharina meteorite from that in the steep Ni gradient where the CZ of the octahedrites is located. Therefore, the M_s could be affected. At present, there is no conclusive evidence in favor of any specific explanation. It is most likely that the difference in the structure of the honeycomb phase is a combined effect of all three factors discussed above.

5.8 Phase Decomposition in Austenitic Alloys

The experimental data from the austenitic alloys obtained in this study using different analytical techniques are not all self-consistent. The increase of the

hardness is an indication of possible phase separation. The data of the hardness test show that the hardness of the binary alloys is unchanged by the heat treatment and the hardness of the ternary alloys is increased by the heat treatment.

The results of the AEM analysis on the 650FN35 alloy is consistent with that suggested by the hardness test. No indication of phase decomposition is observed in the 650FN35 alloy. In the 350FN44 alloy, however, streaking of the diffraction spots is observed. The streaking is most likely due to the coherent strain effect since no streaking is present around the transmitted spot. The strain could be a result of solute segregation. The strain in this alloy, if it indeed exists, is very small since the HOLZ lines in CBED pattern are still distinguishable.

The atom probe data are mostly negative, i.e. no sign of phase separation is detected. Only in the 400FN44 alloy, the frequency distribution-P_a method has revealed a composition fluctuation of about 5 at%. Although this number is remarkably consistent with the phase separation below the tricritical point predicted by Chuang et al. (1986), it should be cautious to interpret the data as due to a true phase separation before the overwhelmingly negative results obtained in other alloys and by other methods are explained. The following arguments are made to support the idea that this composition fluctuation is true. First of all, the mean separation method has been shown not to be sensitive for the concentrated solutions (Miller and Smith, 1989). Secondly, the Johnson-Klotz method only considers the bond type of the nearest neighbors. Therefore, if the solute atoms form clusters and tend to order within the solute-rich cluster, the Johnson-Klotz method will most likely fail to detect the clustering. In the present system, this seems to be the case that there is an ordering tendency in the high Ni phase (FeNi). Finally, the previous studies show that the statistical methods used to detect phase separation or ordering tend to give the false negative result rather than the false positive result (Hetherington and Miller, 1988). In other words, the chance that these methods will pick up a clustering or ordering from a random solution is much less than that they will miss a truly existing clustering or ordering.

The phase transformation expected in the austenitic alloys is the spinodal decomposition. Since there is no energy barrier for the transformations by spinodal mechanism, the scale of the decomposition, or the wave-length of the composition

fluctuation, is determined by the diffusivity of the alloy system. Using the diffusion coefficients summarized by Saikumar and Goldstein (1988), the diffusion coefficient of Fe-44Ni alloy (γ phase) is 3.5×10^{-17} cm^2/sec, 4.9×10^{-23} cm^2/sec, and 5.8×10^{-27} cm^2/sec at 650°C, 400°C, and 300°C respectively. The diffusion distance within the heat treatment time can be estimated according to the $(Dt)^{1/2}$ rule using these diffusion coefficients. The estimated diffusion distance is 270 nm, 0.4 nm, 0.05 nm, and 0.004 nm for the alloys in this study heat treated at 650°C, 400°C, 350°C, and 300°C. For the ternary alloys with saturated P contents, the diffusion coefficients are ten times larger and the diffusion distances are more than three times longer.

The actual diffusion coefficients of the alloys might be larger than those just estimated because of the quench-in vacancies. The alloys were quenched from 1200°C to room temperature. The quenched alloys will have a vacancy concentration close to the equilibrium vacancy concentration at 1200°C which is much higher than those at the heat treatment temperatures. If the formation enthalpy of a vacancy, ΔH_v, is assumed to be 1 eV, the increase of the equilibrium vacancy concentration from the heat treatment temperatures to 1200°C can be calculated using the equation:

$$X_v = A \exp(-\frac{\Delta H_v}{kT})$$

where A is independent of temperature and k is the Boltzman constant. The equilibrium vacancy concentration at 1200°C is 10^2, 10^4, and 10^5 times higher than that at 650°C, 400°C and 300°C respectively. The diffusion coefficients will be increased by the same magnitude as the increase of vacancy concentration. The quenched alloys will not be able to maintain the vacancy concentration higher than the equilibrium value during the entire period of the heat treatment. But at least initially, the diffusion will be enhanced by the quench-in vacancies. Therefore, the diffusion distance in the alloys should be somewhat larger than the previously estimated values. The quantitative estimation is not possible due to the lack of accurate data of the vacancy diffusion coefficient and the quenching rate.

Based on above discussion, it can be concluded that if the spinodal decomposition is present, the scale of the structure formed should be large enough to

be analyzed using AEM for the 650°C alloy and analyzed using AP for the 400°C alloy. It is quite possible that the scale of the structures formed at 350 to 300°C is large enough for the AP to analyze.

The estimation of the diffusion distance only gives the maximum scale of the structure which can be formed by the spinodal decomposition. However, there is a lower limit on the scale of the two phase structure (or the wave-length of the composition fluctuation) which is determined by the strain energy caused by the decomposition and the interfacial energy between the two phases (see section 2.1.2, Equation 2-1-5). If the minimum wave length allowed for a certain alloy system at a specific temperature is larger than the maximum diffusion distance of the atoms at that temperature, the decomposition will not occur.

In summary, the data obtained in the austenitic alloys show that there is no phase decomposition in the 650FN35 alloy. There are various indications of the phase decomposition in the 44 wt% Ni alloys, however, the data obtained using different analytical techniques do not show a self-consistent picture about the phase decomposition. The reason for this inconsistency might be twofold. First the phase decomposition may have not occurred at the lowest temperature due to the slow diffusion. Second even if the decomposition does occur, it is in a very initial stage. This initial stage of the spinodally decomposed structure could pose various problems for the analytical techniques that have been used. More carefully designed analysis is apparently needed.

SUMMARY

(1) Two types of γ taenite precipitates are observed in the plessite of the octahedrites (Carlton and Grant). The first type of precipitate is formed at the original martensite lath/block boundaries and has a relatively large size (50~200 nm wide). The low Ni plessite regions (9~10 wt%) which have a coarse microstructure (duplex plessite) are composed of these intergranular precipitates. The precipitates in the low Ni plessite regions have a ~50 to 54 wt% Ni composition and have the $L1_0$ ordered fcc structure. Therefore, they are the tetrataenite. The matrix phase in the low Ni plessite regions has a bcc structure and a Ni composition of about 4~5 wt%. The second type of precipitate is formed inside the original martensite laths or plates along all crystallographically equivalent directions of the matrix ($\{110\}_{bcc}$). They are very thin plates or fine needles typically 10~20 nm wide. These intragranular precipitates are primarily formed in the plessite regions of high Ni content (>15 wt%), and therefore, the microstructure of the high Ni plessite regions is fine (black plessite). The precipitates in the high Ni plessite regions also have the $L1_0$ ordered fcc structure, however, they have a Ni composition of ~57 to 60 wt%. The matrix phase in the high Ni plessite regions has a bcc structure and a Ni composition of 10~12 wt%. Both types of precipitates are present in the plessite regions of 10 to 15 wt% Ni. The microstructure of the plessite varies continuously with the average Ni composition of the plessite region with the structures containing the two types of precipitates discussed above as two extreme cases.

(2) The complex structure of the plessite is a result of the martensite formation and decomposition which occurred at different temperatures for the plessite regions of different Ni composition during the continuous cooling process. The phase equilibrium of the low Ni plessite region is consistent with that measured at the Widmanstätten α/γ interface (4~5 wt% Ni bcc phase/~50 wt% Ni $L1_0$ ordered fcc phase). The higher matrix Ni composition in the high Ni plessite region is due to the growth of the very fine precipitates which, by the capillary effect, requires a matrix Ni composition higher than the equilibrium value for a planar interface. That the Ni composition of the tetrataenite precipitates in the high Ni plessite region is higher than the stoichiometric value of FeNi is because the ordering occurred after the high Ni fcc precipitates were formed by the martensite decomposition for which the

equilibrium precipitate composition is >50 at% below ~300°C.

(3) Intergranular precipitates are formed in the decomposed martensitic alloys of 15 wt% and 25 wt% Ni. The morphology of the precipitates in the 15 wt% Ni alloys decomposed at >400°C is similar to that of the low Ni plessite of the octahedrites. Intragranular precipitates are formed in the decomposed martensitic alloys of 30 wt% Ni. The morphology of the precipitates in the 30 wt% Ni alloys is similar to that of the high Ni plessite of the octahedrites. The typical width of the intragranular precipitates decreases from <100 nm at 400°C to <10 nm at 300°C. The precipitates formed in all alloys have an fcc structure and no ordering is observed. This indicates that the FeNi ordering is a very slow process or the ordering temperature is lower than the previously reported value of 320°C.

(4) The same orientation relationship is observed between the fcc precipitates and the bcc matrix in both the plessite and the decomposed martensitic alloys. The orientation relationship is a relaxed N-W or K-S relationship. The $\{111\}_{fcc}$ is exactly parallel to $\{110\}_{bcc}$. For the intragranular precipitates, $\{111\}_{fcc}$ is also the habit plane of the precipitates. The $\{110\}_{fcc}$ is not exactly parallel to either $\{100\}_{bcc}$ or $\{111\}_{bcc}$, but somewhere in between. The relaxation of this parallel relationship is to minimize the strain introduced by the formation of small semicoherent precipitates.

(5) The phase equilibria of the Fe-Ni and Fe-Ni(P) system below 450°C formed by isothermal martensite decomposition are established, as shown in Fig. 5.7 to 5.10. The Ni composition of the precipitates formed at high temperatures (>400°C) is consistent with that of the low Ni plessite regions. The Ni composition of the precipitates formed at low temperature (300°) is consistent with that of the high Ni plessite regions. The $\alpha+\gamma/\gamma$ phase boundary at 450°C is modified and a temperature range of the proposed eutectoid transformation (Chuang et al., 1986) is given according to the measured precipitate Ni composition. The matrix compositions of the alloys are generally higher than the matrix composition of the plessite and show large variation among the alloys of different Ni composition and among different places in the same alloy. The behavior of the matrix Ni composition of the alloys indicates that the precipitate growth in the Fe-Ni martensite decomposition is progressively interface reaction controlled as the temperature decreases. The measured phase equilibria below 400°C in these alloys are metastable representing an intermediate state in the

martensite decomposition.

(6) In the temperature range from 300°C to 450°C, no significant difference has been observed between the decomposed martensitic Fe-Ni and the Fe-Ni(P) alloys in terms of the morphology of the precipitates and the phase equilibria.

(7) It is suggested that the M_s may have been decreased in some iron meteorites by about 100°C from the M_s of pure Fe-Ni based on the experimentally observed difference in transition Ni composition from lath to plate martensite morphology between the meteorites and the alloys. In such iron meteorites, Carlton for example, the reheating is necessary to form the current plessite structure. The decrease of M_s in the meteorites may be attributed to the presence of trace elements after comparing the structures of these meteorites with that of the Tishomingo meteorite.

(8) The microstructure of the high Ni ataxite (Santa Catharina) is determined. It has a two phase honeycomb structure, the $L1_0$ ordered FeNi island phase and a low Ni fcc honeycomb phase. The morphology of this two phase structure is similar to that of the cloudy zone in the octahedrites, therefore, it is formed by the low temperature (<400°C) spinodal decomposition. However, the honeycomb phase of Santa Catharina has an fcc structure, different from the structure of the honeycomb phase in the cloudy zone which is bcc. The possible reasons for which the martensite transformation was suppressed in the honeycomb phase of Santa Catharina are discussed. No evidence of the high temperature spinodal decomposition is found in the Santa Catharina. The apparent "dark and light" large-scale (10~100 μm) structural features are a secondary structure superimposed on the primary CZ-type structure. The low Ni honeycomb phase in part of the meteorite is preferentially oxidized to form a Ni-rich oxide. The oxidized regions appear dark and the preserved metal regions appear light in the optical microscope. Therefore, the dark and light regions are formed by the terrestrial oxidation.

(9) Various experimental evidence is found indicating that the low temperature spinodal decomposition may have occurred in the long-term heat treated austenitic alloys. However, it is still premature to draw the conclusion due to the inconsistency of the experimental data obtained using different analytical techniques. No evidence of the high temperature spinodal decomposition is found in the long-term heat treated austenitic alloys.

Table 2-1. Estimated diffusion coefficients of Fe-Ni and Fe-Ni-P systems. (Dean and Goldstein, 1986, Saikumar and Goldstein, 1988, Romig and Goldstein, 1980)

	γ		γ(P)	α	α (P)	α_2	α_2
T (°C)	15% Ni	44% Ni	0.3 wt% P		0.3 wt% P		0.6 wt% P
1100	$3x10^{-12}$	$1x10^{-11}$	3.25 *	-	-	-	-
800	$2x10^{-15}$	$1x10^{-14}$	5.5*	-	-	-	-
650	$1x10^{-17}$	$6x10^{-17}$	10*	$6x10^{-16}$	23.7*	$(0.6\text{-}2.1)x10^{-14}$	$(1.2\text{-}4.2)x10^{-14}$
450	$3x10^{-22}$	$2x10^{-21}$	10*	$2x10^{-20}$	27.5*	$(0.2\text{-}1.2)x10^{-17}$	$(0.4\text{-}2.4)x10^{-17}$
400	$8x10^{-24}$	$5x10^{-23}$	10*	$5x10^{-22}$	27.5*	$(0.6\text{-}2.6)x10^{-18}$	$(0.8\text{-}3.6)x10^{-18}$
300	$1x10^{-27}$	$6x10^{-27}$	10*	$5x10^{-26}$	27.5*	$(1.0\text{-}3.0)x10^{-19}$	$(1.4\text{-}4.2)x10^{-19}$

The unit of D is cm^2/sec.
* : to obtain diffusion coefficient of γ(P) or α(P), multiply the binary coefficient by this value. γ(P) and α(P) are saturated with P.

Table 3-1 Nominal Ni compositions and heat treatment temperatures of the martensitic alloys.

	Nominal Ni composition in wt%		
Temperature	15	25	30
450°C	x	x	x
400°C	x	x	x
370°C	x	x	x
350°C	x	x	x
300°C	x	x	x

x: A binary Fe-Ni alloy and a P saturated ternary alloy were prepared.

Table 3-2 Nominal Ni compositions and heat treatment temperatures of the austenite alloys.

T	Nominal Ni composition in wt%	
	44	35
650°C		y
400°C	x	
350°C	x	
300°C	x	

x: A binary Fe-Ni alloy and a P saturated ternary alloy were prepared.
y: Binary Fe-Ni alloy only.

Table 3-3 Information about iron meteorites studied. (Buchwald, 1975)

	Grant	Carlton	Santa Catharina
Chemical group	IIIB	IIIC	Anomalous
Structural group	Octahedrite	Octahedrite	Anomalous
Structural subgroup	Om	Of	-
Bulk Ni content (wt%)	9.34	13.3	35.3
P content (wt%)	0.8	0.6	0.2

Table 3-4 Results of chemical analysis of raw materials.

Iron rod		Nickel rod		Phosphorus polycrystalline lump	
Al	5	Cr	3	As	5
Ca, Cr, Co, Mg, Mn, Ni, Si	each <1	Co	3	Si	2
		Si	3	Fe	1
		Ag	3	Cu,Mg	<1
		Ca, Mg	<1		

Unit: ppm.
Major analytical techniques: optical emission arc spectrography.
Detection limit: 1 ppm.
Data provided by: Johnson Matthey Chemical Limited.

Table 3-5 Composition of master Fe-P alloy.

element	Fe	P	Si	Cr
wt%	97.37	2.60	0.02	0.01

Wet chemistry analysis performed by J. Dirats and Co., Inc.

Table 3-6 Heat treatment time and temperature of each alloy.

Martensite, binary			Martensite, ternary			Austenite		
Alloy	T°C	t days	Alloy	T°C	t days	Alloy	T°C	t days
450FN15	450	60	450FNP15	450	60	400FN44	400	362
450FN25	450	60	450FNP25	450	60	400FNP44	400	362
400FN15	400	362	400FNP15	400	362	350FN44	350	400
400FN25	400	362	400FNP25	400	362	350FNP44	350	208
400FN30	400	362	400FNP30	400	362	300FN44	300	370
370FN15	370	275	370FNP15	370	275	300FNP44	300	370
370FN25	370	275	370FNP25	370	275	650FN35	650	235
370FN30	370	275	370FNP30	370	275			
350FN15	350	400	350FNP15	350	208			
350FN25	350	400	350FNP25	350	208			
350FN30	350	400	350FNP30	350	208			
300FN15	300	370	300FNP15	300	370			
300FN25	300	370	300FNP25	300	370			
300FN30	300	370	300FNP30	300	370			

Table 3-7 Measured electron beam current of EM400T at 120 kV and EM430T at 300 kV.

Spot Size Setting	Beam current in nA	
	EM400T 70 μm C2	EM430T 50 μm C2
STEM3	0.3 - 1.1	0.57 - 1.4
STEM4	0.06 - 0.3	0.16 - 0.35
STEM5	0.03 - 0.11	0.02 - 0.06

Table 3-8 Measured electron probe diameters of EM400T at 120 kV and EM430T at 300 kV.

		Probe Diameter in nm		
	C2 aperture	EM430T 50 μm	100 μm	EM400T 70 μm
Spot Size Setting				
STEM3	FWHM	11.9	18.0	-
	FWTM	19.2	65.0	-
STEM4	FWHM	7.0	8.1	8.5
	FWTM	11.8	19.3	23.8
STEM5	FWHM	4.0	4.1	3.9
	FWTM	6.8	10.6	11.6

Table 4-1. Homogeneity range of the as-quenched laboratory alloys.

Alloy	Ni (wt%)	P (wt%)	Homogeneity Range at 99% confidence level Ni (wt%)	P (wt%)
FN15	14.8		0.14	
FN25	25.0		0.08	
FN30	29.6		0.15	
FN35	34.7		0.20	
FN44	44.1		0.15	
FNP15	14.9	0.24	0.06	0.008
FNP25	25.0	0.28	0.07	0.009
FNP30	30.6	0.27	0.23	0.008
FNP44	44.5	0.24	0.17	0.006

Table 4-2. Ni composition of precipitate and matrix phases in binary alloys. (wt%)

Alloy	Precipitate(γ)	Matrix(α)	Comments
450FN15	39.7± 0.8	7.6 ±0.9*	EM400T
450FN25	39.6± 1.3	9.4 ±0.5	EM430T
400FN15	48.2 ±1.3	8.5± 0.8	EM400T
400FN25	49.8 ±1.7 50.6 ±1.5	13.2± 1.8 9.1± 0.5	EM400T HB501
400FN30	50.9 ±2.1	9.3 ±0.5	EM430T
370FN15	50.9± 1.7	9.1 ± 0.5*	EM430T
370FN25	49.8± 3.9	15.0± 2.0	EM430T
370FN30	52.7± 2.2	12.4± 0.7	EM430T
350FN15	52.0± 1.7	10.0± 0.7*	EM430T
350FN25	~42	~18	not accurate, precipitates are too small for EM430T
350FN30	52.0± 2.8	5.6 ±0.7	EM430T
300FN25	50.8 ±2.3 57 ± 11	20.5± 1.0 21 ± 1.9	HB501 Atom probe
300FN30	57.4 ±3.0	21.0± 1.6	HB501

* extrapolated precipitate/matrix interface composition. see the results section for explanation of the data.

Table 4-3. Compositions of precipitate and matrix phases in ternary alloys.

Alloy	Precipitate(γ) Ni (wt%)	Matrix(α) Ni (wt%)	Comments
450FNP15	39.2 ± 0.5	12.2 ± 0.7	EM400T
400FNP15	48.7 ± 2.7	12.7 ± 0.6	EM400T
400FNP25	46.9 ± 1.1	13.9 ± 0.7	EM400T
370FNP25	49.1 ± 1.5	12.2± 0.6	EM430T
350FNP30	50.2 ± 2.6	17.1± 1.2	EM400T
300FNP30	54.1 ± 1.0	23.0 ± 0.8	HB501

	Phosphide Ni (wt%)	Phosphide P (wt%)	Matrix (α) Ni (wt%)	
400FNP15	45.1 ± 2.3	16.1 ± 1.1	10.3 ±0.8	EM400T

Table 4-4. Vickers hardness of the austenite alloys

Alloy	HV	σ_{n-1}	n
Group I			
FN30	232	6.5	18
FN35	121	1.4	21
650FN35	123	0.8	23
FN44	123	1.1	15
FNP44	140	3.0	14
FN52	115	1.6	19
Group II			
FN44	120	1.0	21
350FN44	116	2.6	17
400FN44	118	0.5	19
FNP44	139	3.9	18
350FNP44	169	4.1	15
Group III			
FN44	118	1.1	8
300FN44	121	1.4	9
FNP44	144	2.0	8
300FNP44	161	12.9	9

Load: 300g

Table 4-5. Statistical analysis of the atom chains collected from the austenite alloys using the atom probe.

Alloy	Johnson and Klotz Markov chain method	Mean separation method	Pa	σ
300FN44	random	random	0	
350FN44	random	random	0	
400FN44	random	random	0	
350FNP44	random	random	0.027	0.025

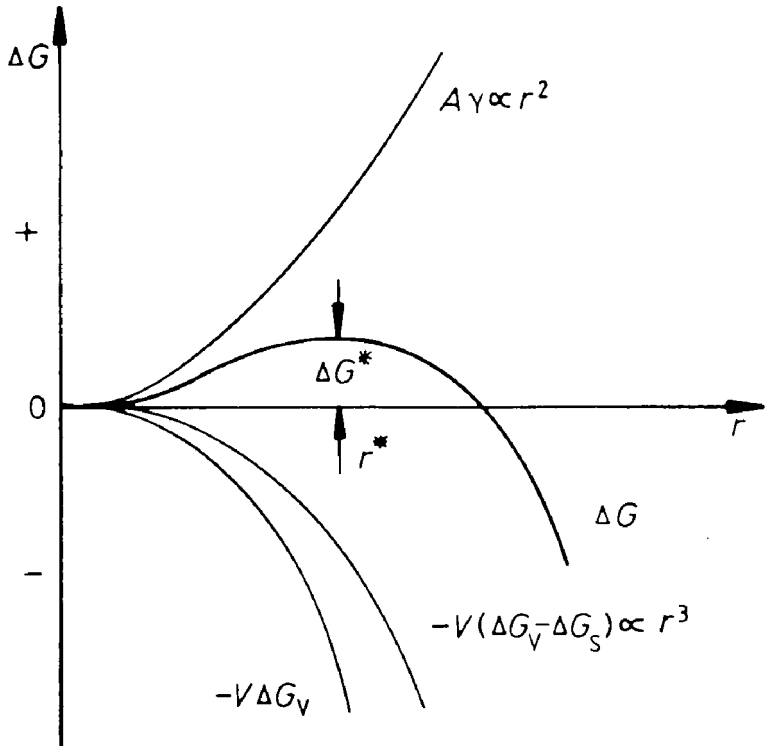

Fig .2.1 The variation of ΔG with radius r for a nucleus. ΔG is the free energy change due to the formation of a homogeneous nucleus. There is an activation energy barrier ΔG* (Porter and Easterling, 1981).

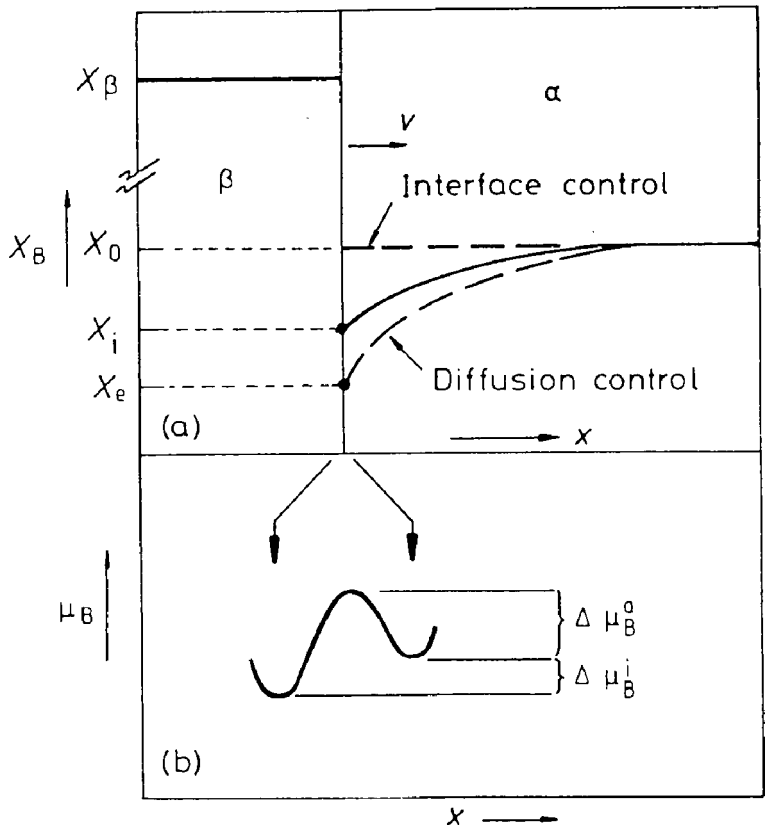

Fig. 2.2 Interface migration with long-range diffusion. a) Schematic composition profiles of solute across the interface. b) The origin of the driving force for interface migration into α phase (Porter and Easterling, 1981).

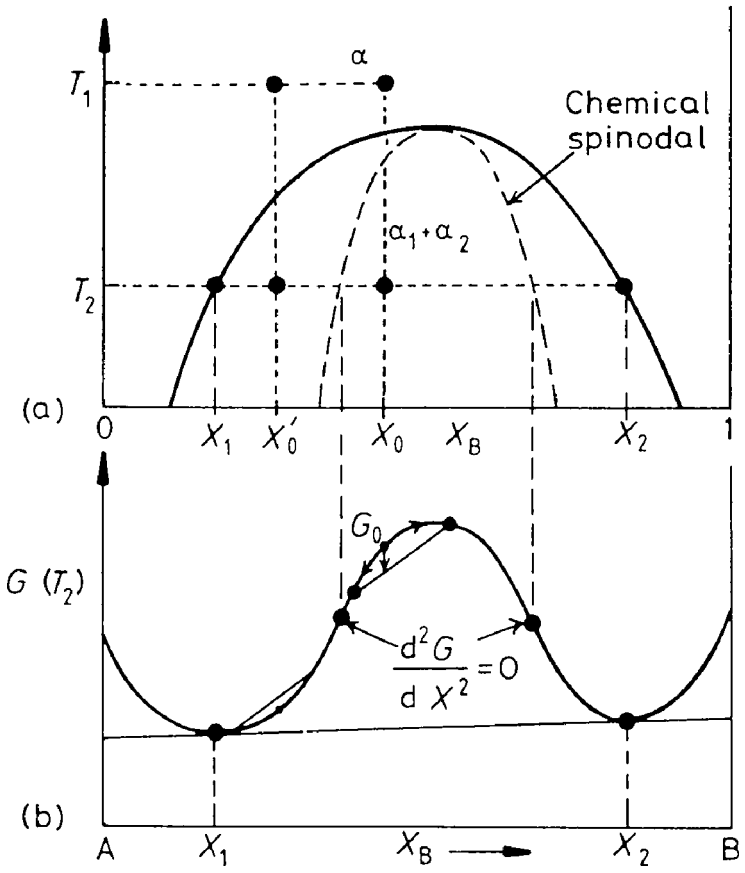

Fig. 2.3 Alloys between the spinodal points are unstable and can decompose into two coherent phases without overcoming an energy barrier. a) Binary phase diagram. b) Free energy curve at T_2 (Porter and Easterling, 1981).

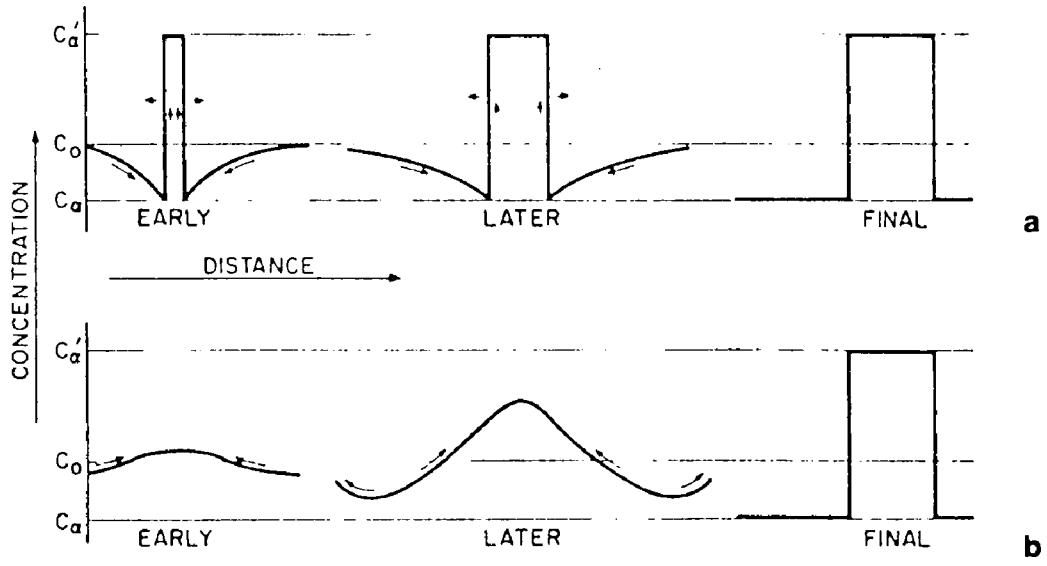

Fig. 2.4 Schematic evolution of concentration profiles to illustrate the difference between the nucleation and growth (a) and the spinodal mechanism (b) (Cahn, 1968).

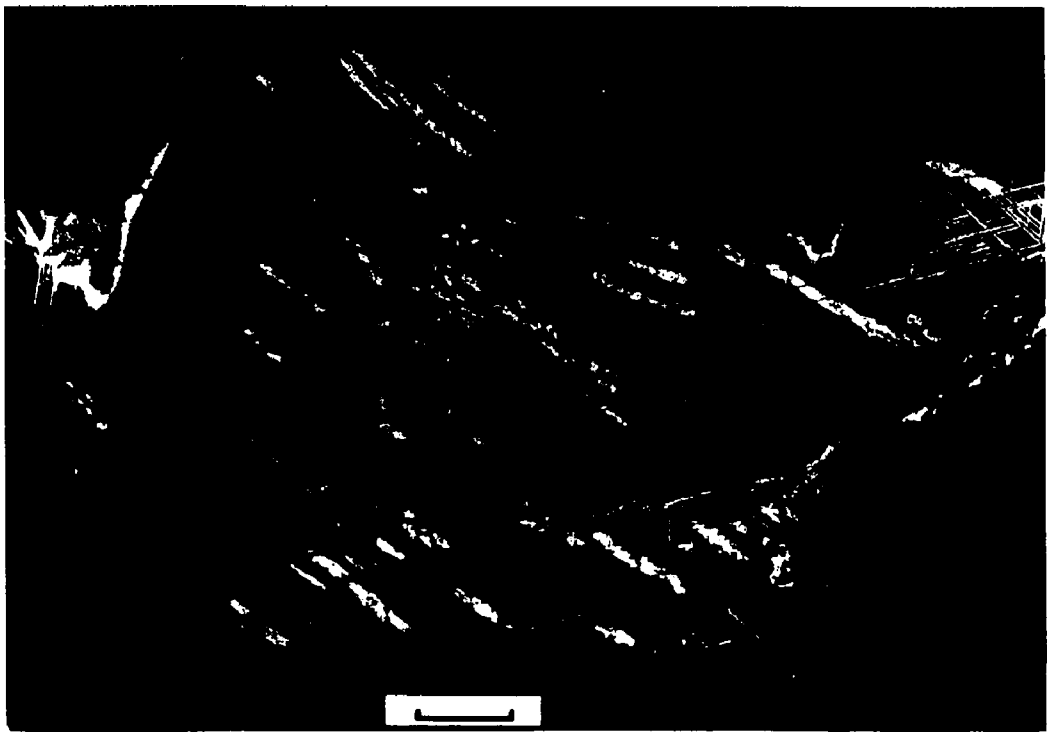

Fig. 2.5 Optical photograph of a deep-etched section of iron meteorite Edmonton (Kentucky, USA. sample USNM#1413) showing a typical Widmanstätten pattern in a fine octahedrite. Scale bar=20 mm. (Buchwald, 1975)

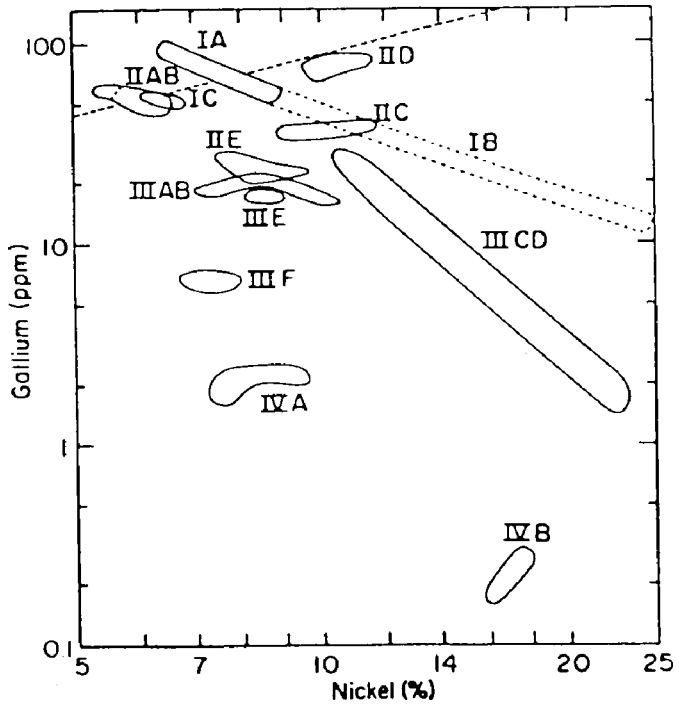

Fig. 2.6 Logarithmic plot of Ga content vs. Ni content of iron meteorites. The outlined areas show the iron meteorite groups of the chemical classification (Scott and Wasson, 1975).

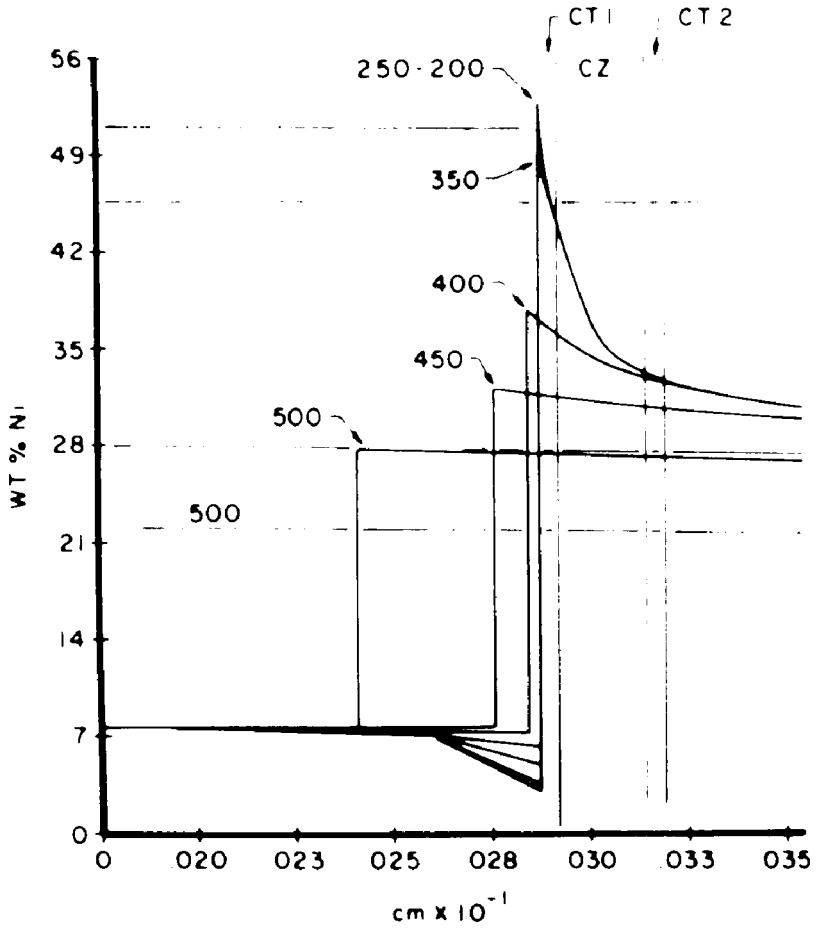

Fig. 2.7 Computer simulated Ni composition profiles across the α/γ interface at various temperatures during the cooling process of the iron meteorite. Simulation parameters are: cooling rate: 50°C/10^6 yrs; bulk Ni content: 17 wt%; P content: 0.4 wt% (Saikumar and Goldstein, 1988; Reuter et al., 1988).

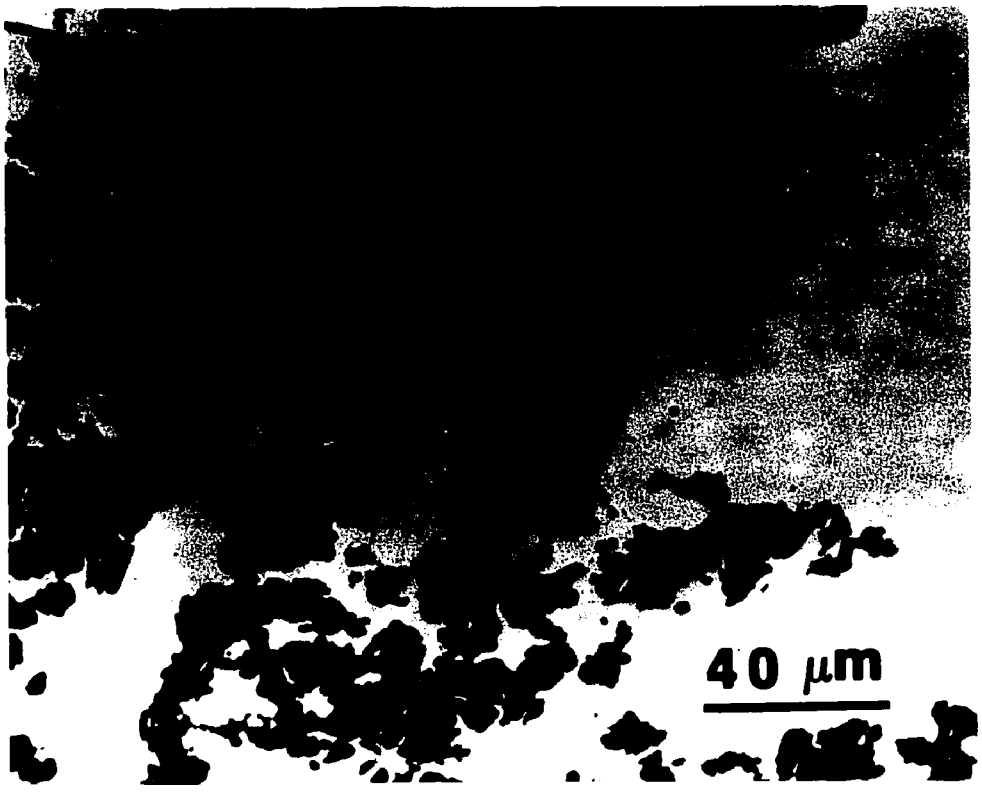

Fig. 2.8 Optical micrograph of a polished, unetched section of Santa Catharina iron meteorite (USNM#3043) showing the typical "dark" and "light" regions.

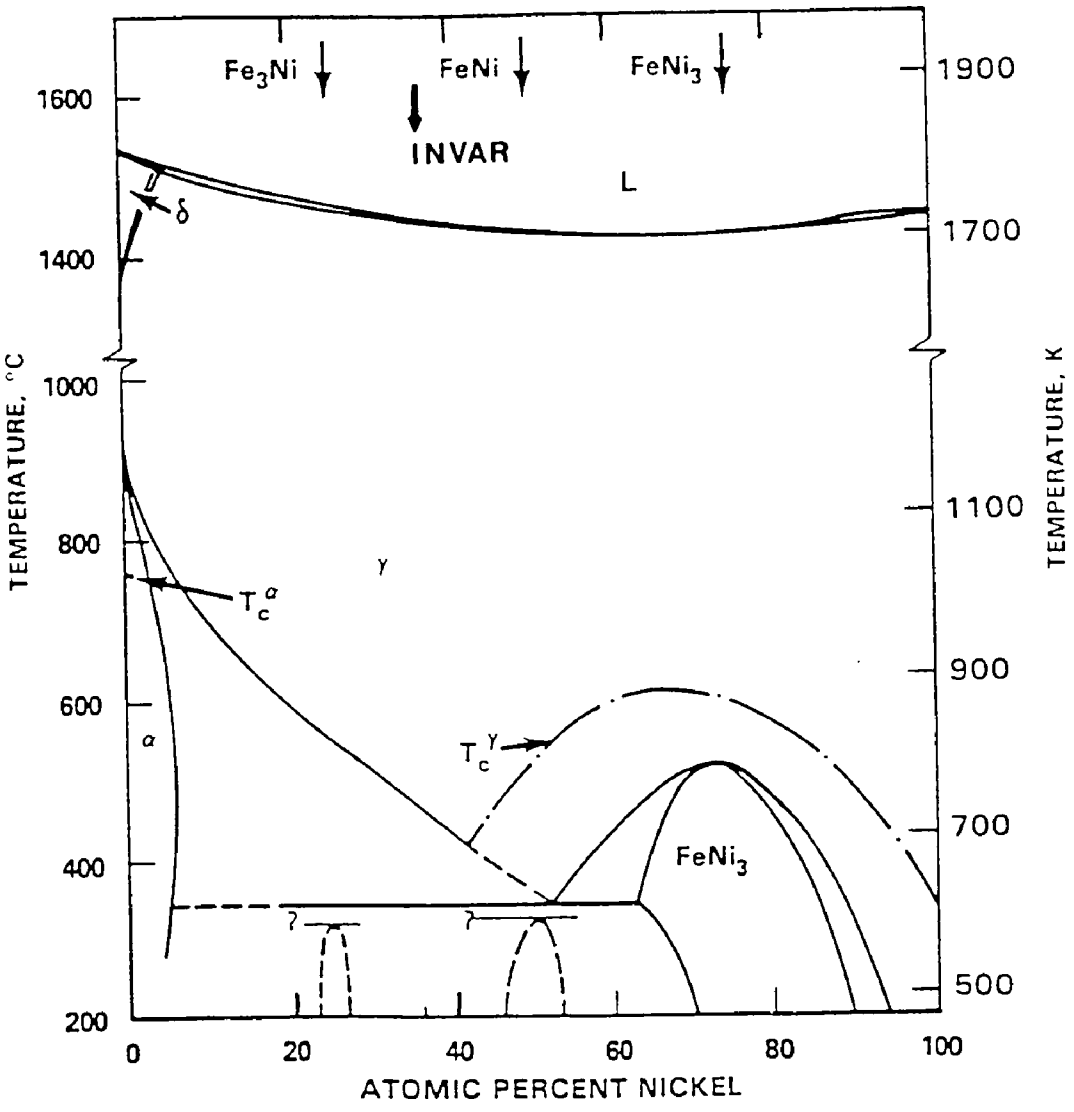

Fig. 2.9 Complete Fe-Ni phase diagram assessed by Kubaschewski (1982).

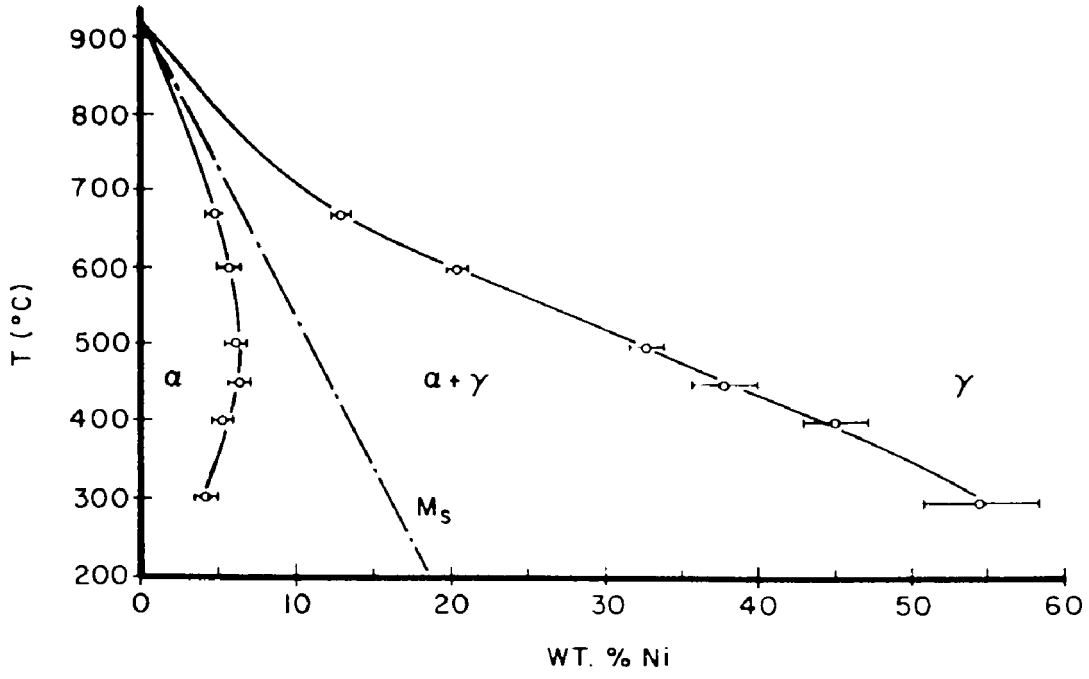

Fig. 2.10 Fe-rich portion of low temperature Fe-Ni phase diagram (Romig and Goldstein, 1980). The M_S was measured by Kaufman and Cohen (1956).

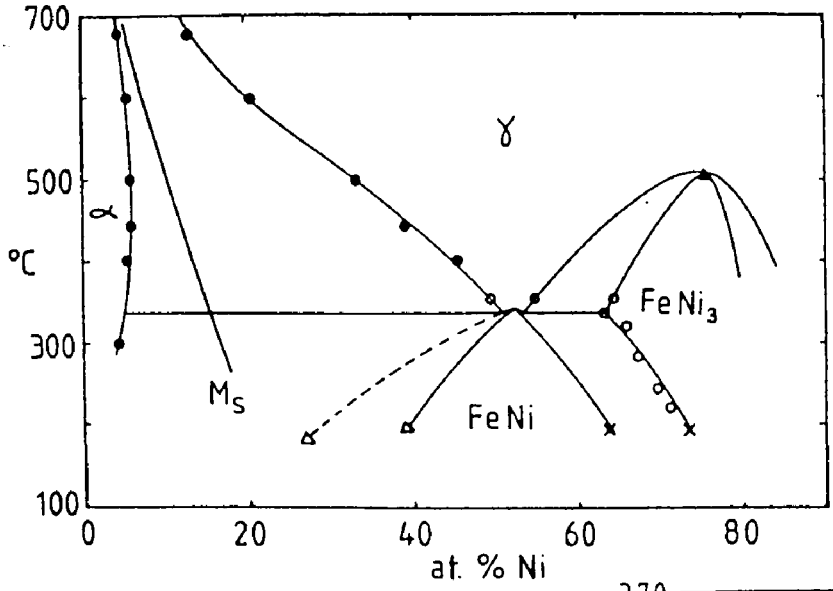

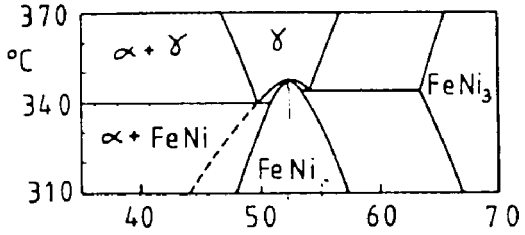

Fig. 2.11 (top and right) Fe-Ni phase diagram proposed by Rossiter and Jago (1984) based on the investigation of iron meteorite structures.

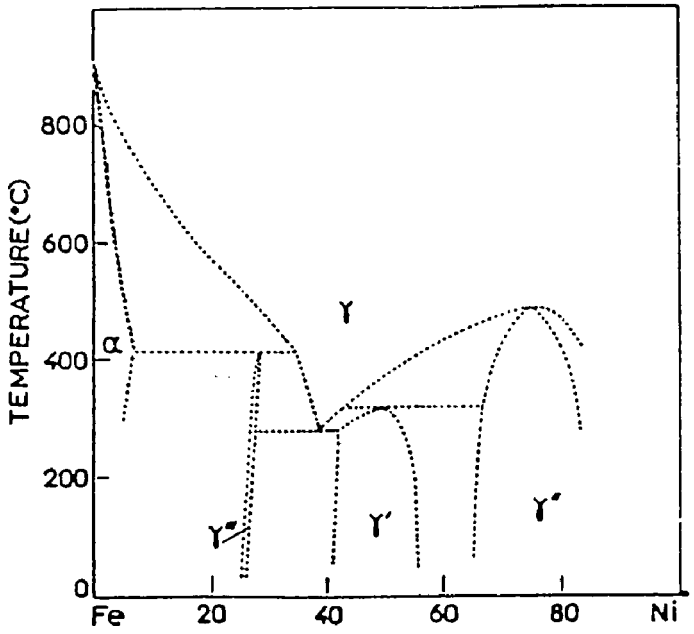

Fig. 2.12 Fe-Ni phase diagram proposed by Chamberod et al. (1979) based on the investigation of electron irradiated alloys.

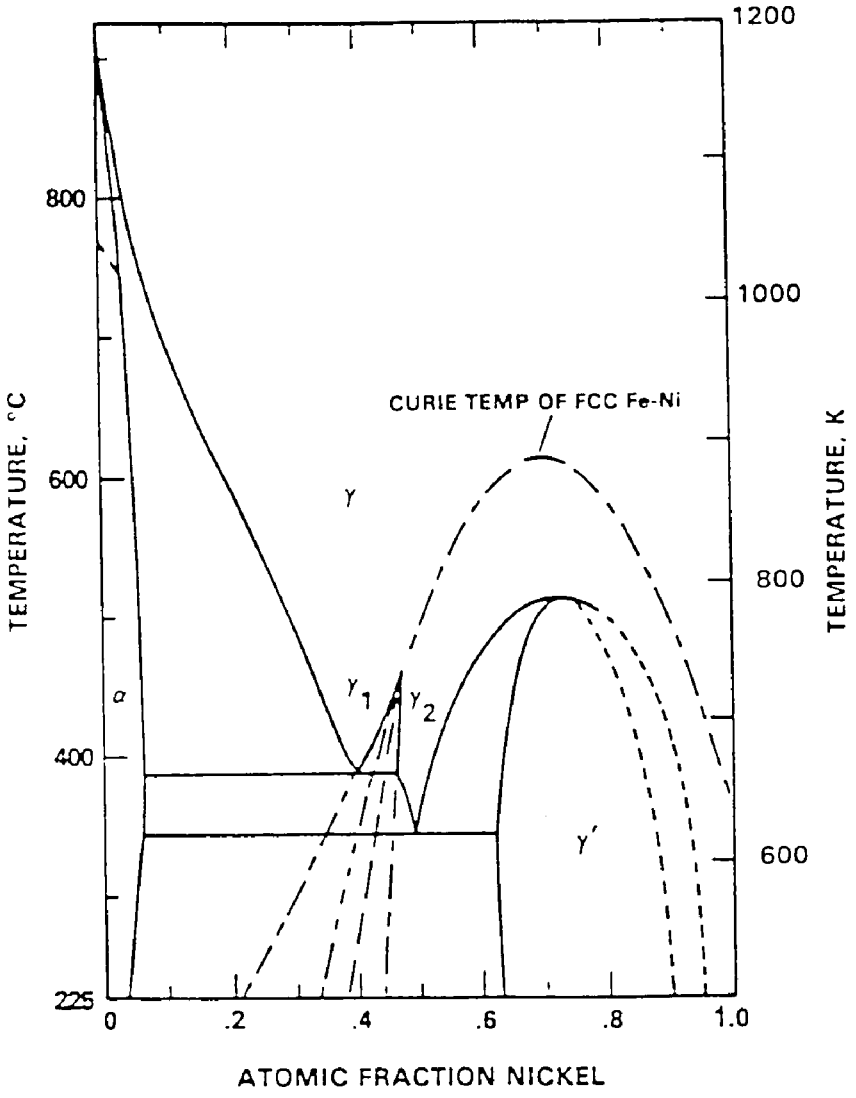

Fig. 2.13 Fe-Ni phase diagram calculated by Chuang et al. (1986). A miscibility gap induced by magnetic transition is proposed.

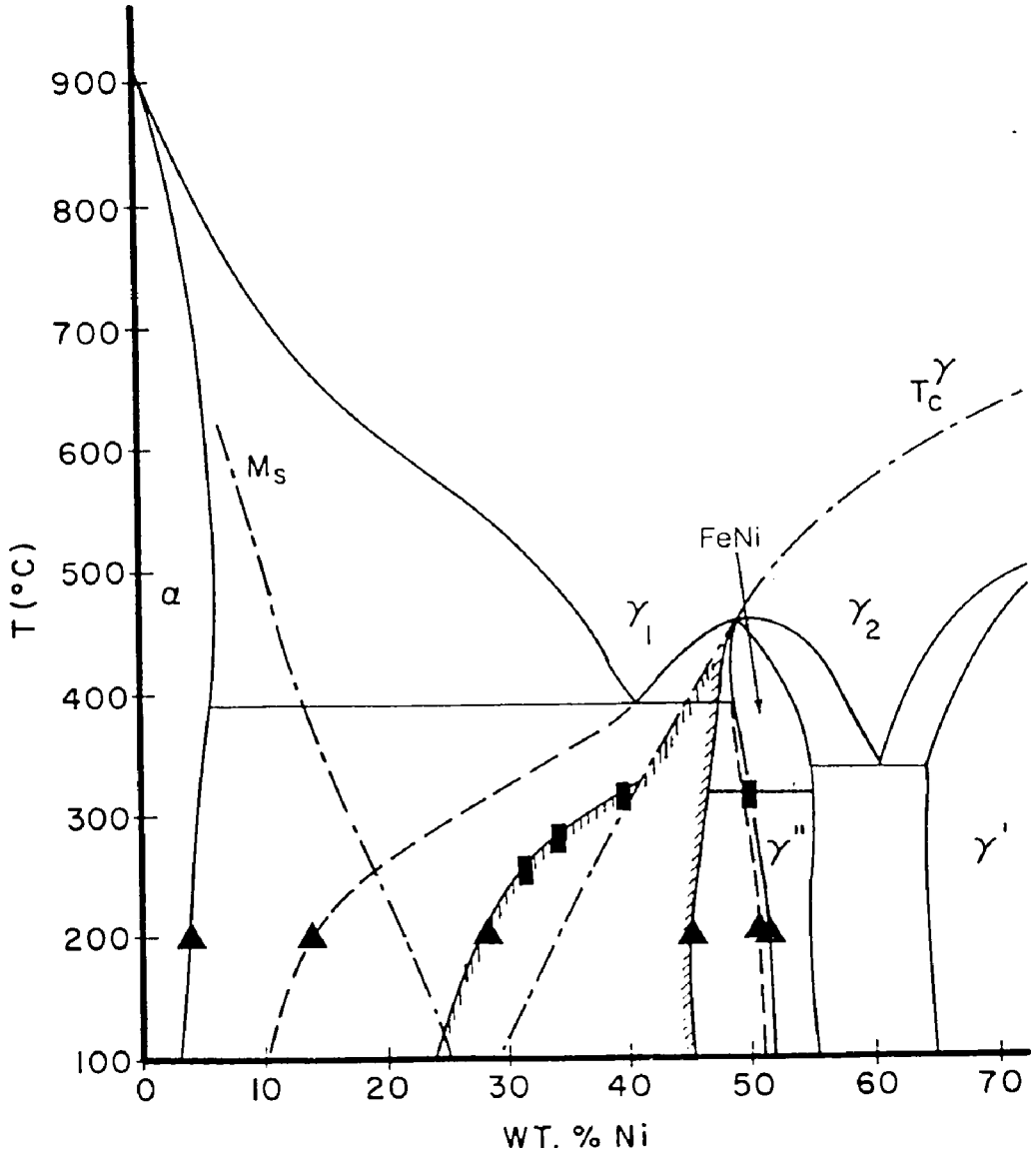

Fig. 2.14 Fe-Ni phase diagram proposed by Reuter et al. (1989) based on the investigation of iron meteorite structures and electron irradiated alloys, and the calculated diagram by Chuang et al. (1986). ▲ : data measured from iron meteorites. ■ : data measured from electron irradiated alloys.

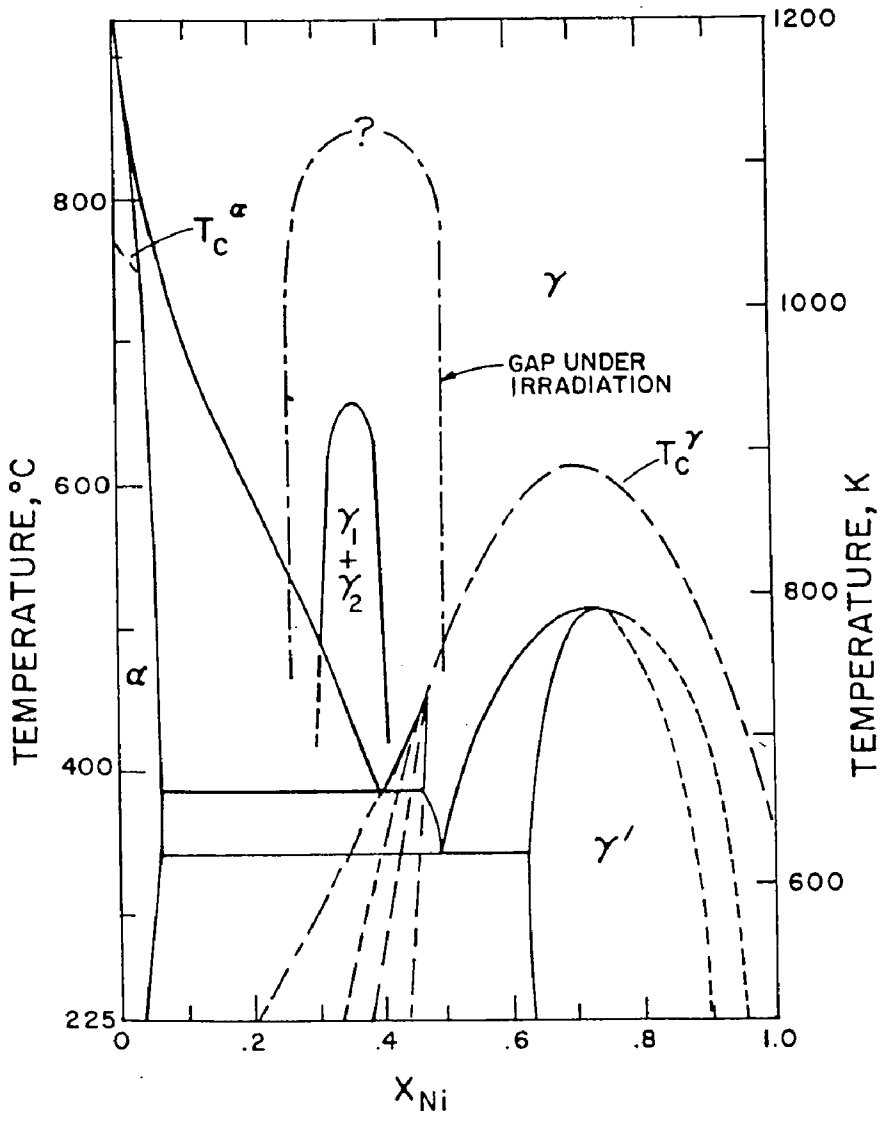

Fig. 2.15 Fe-Ni phase diagram proposed by Russell and Garner (1991) based on the investigation of neutron irradiated alloys. High temperature coherent miscibility gaps for thermally annealed and for irradiated alloys are incorporated.

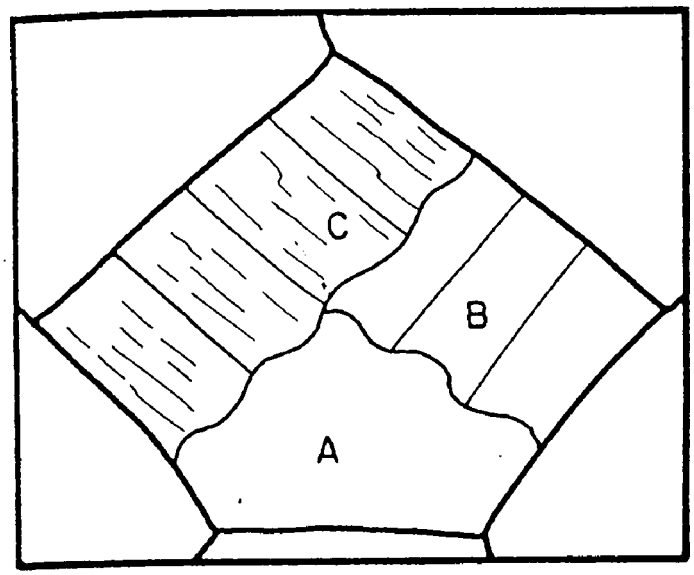

Fig. 2.16 Schematic drawing of three packets of lath martensite within a prior austenite grain. Section A represents a packet, section B shows blocks within a packet and section C shows laths within blocks.

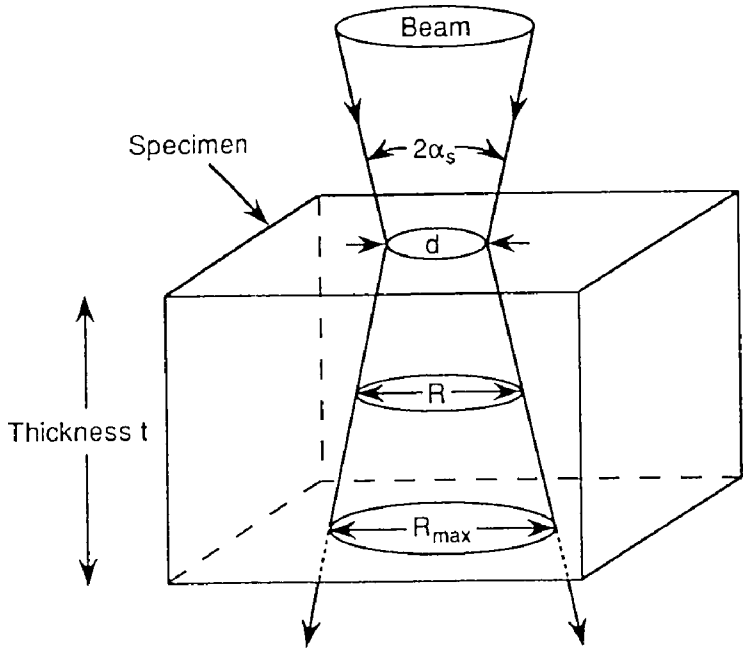

Fig. 2.17 Schematic diagram showing the definition of spatial resolution of thin film x-ray microanalysis in AEM.

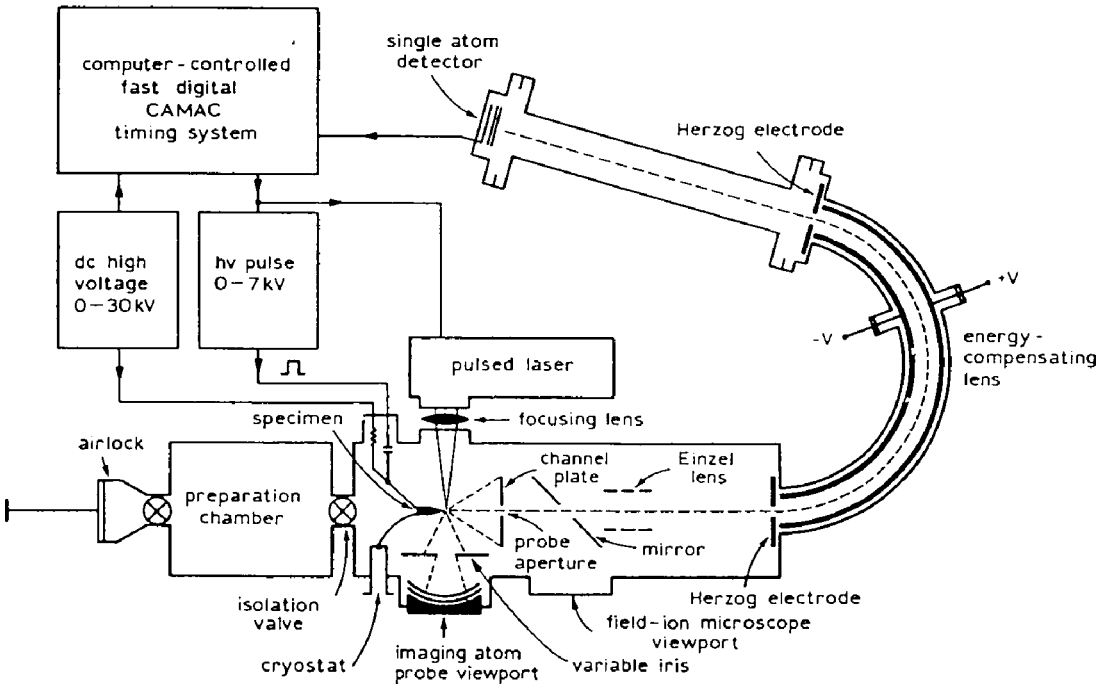

Fig. 2.18 Schematic diagram of main components of modern atom probe, including field-ion microscope energy compensated time-of-flight mass spectrometer, imaging atom probe, and pulsed-laser atom probe as indicated in the diagram. (Miller, 1987).

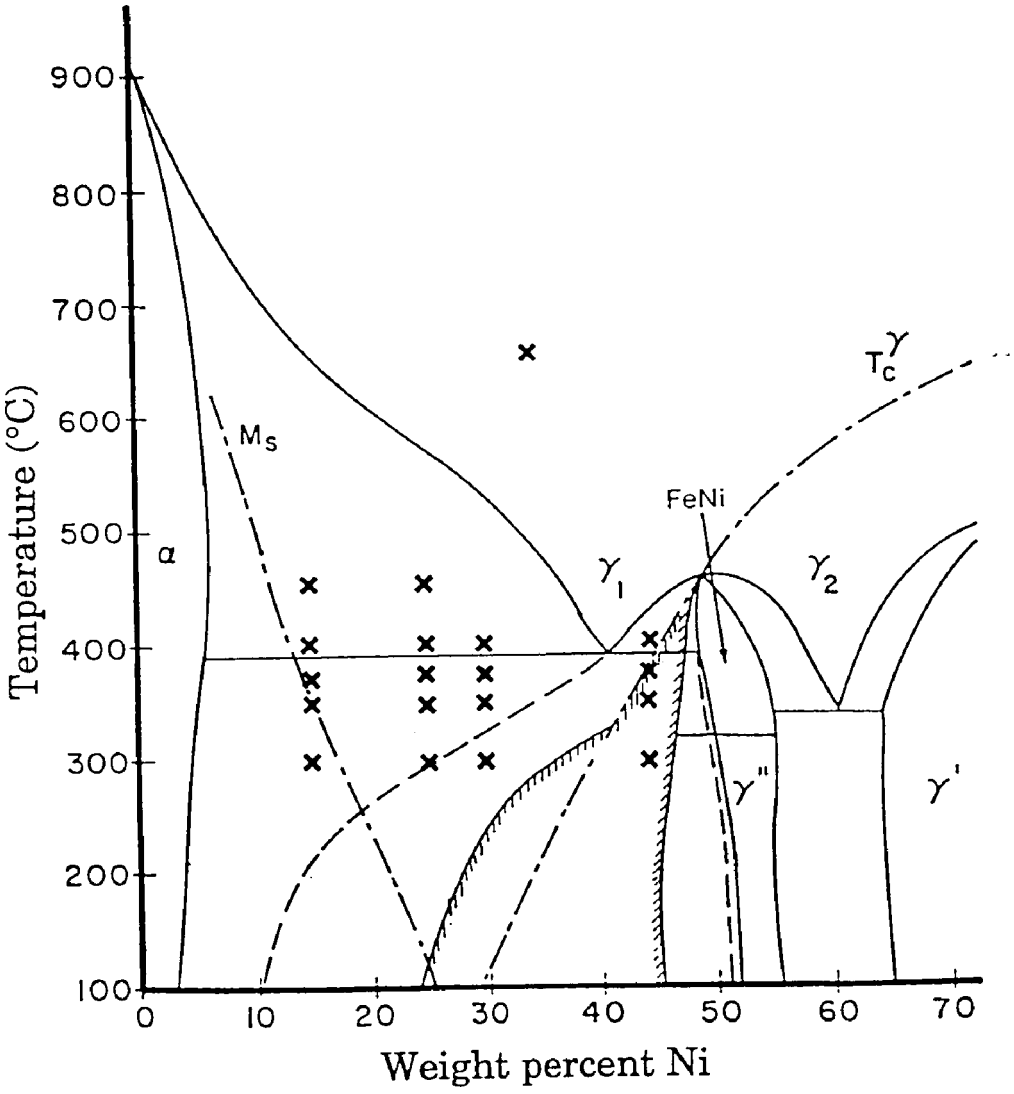

Fig. 3.1 Composition and heat treatment temperature of the alloys in this study, which are represented by an **x**, are shown in the Reuter's phase diagram. For each binary alloy shown in this diagram, there is Fe-Ni-P alloy with 0.2-0.3 wt% P, except for the 650°C alloy.

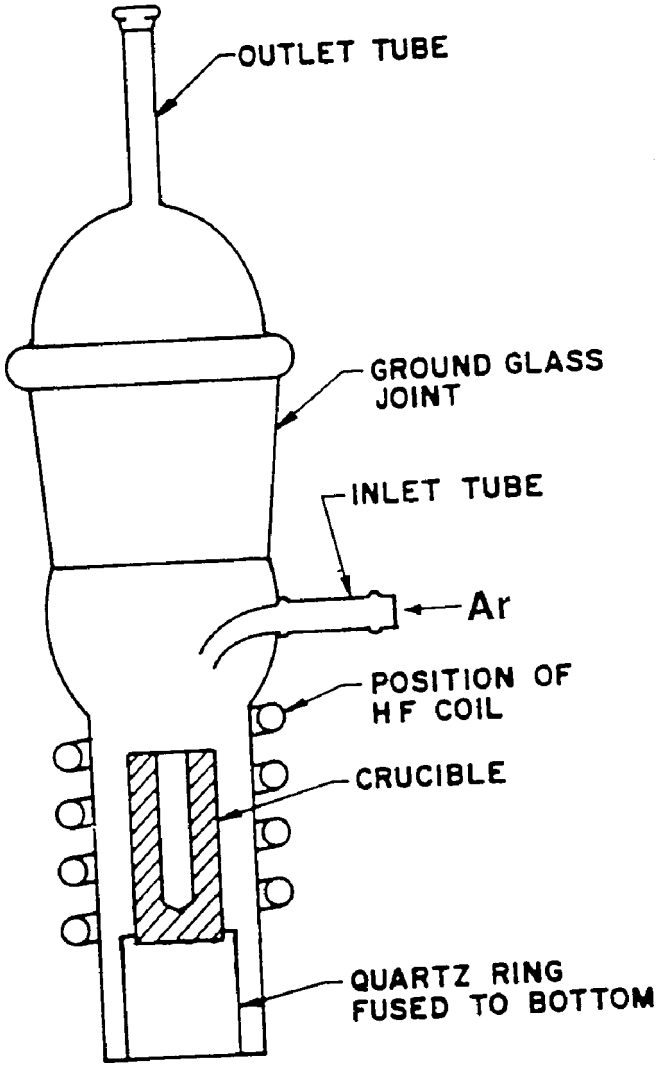

Fig. 3.2 Schematic diagram of the melting equipment set-up used for the ternary alloys in this study.

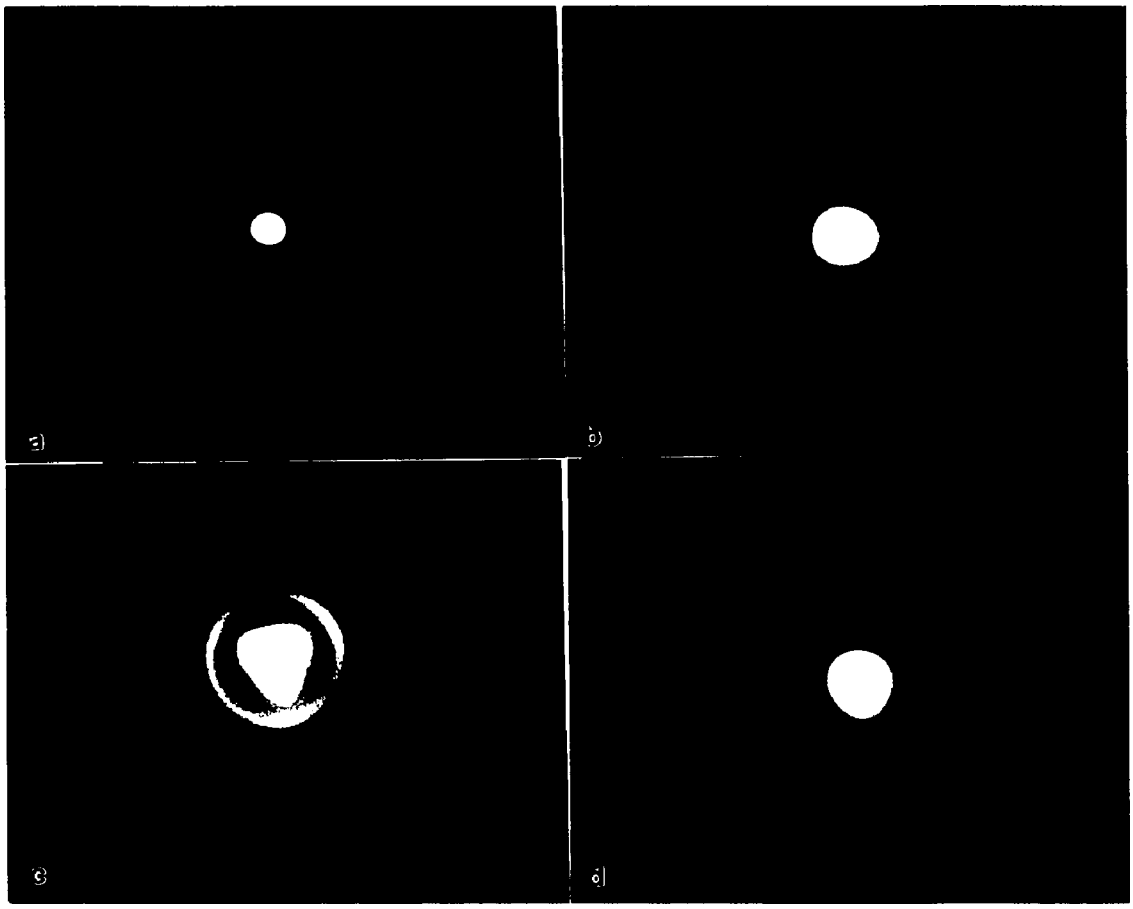

Fig. 3.3 Typical electron probe images of STEM mode of the Philips EM430T AEM at spot size setting STEM4. a) and b) 50 μm C2 aperture, slightly different objective lens focusing conditions. c) and d) 100 μm C2 aperture, slightly different objective lens focusing conditions.

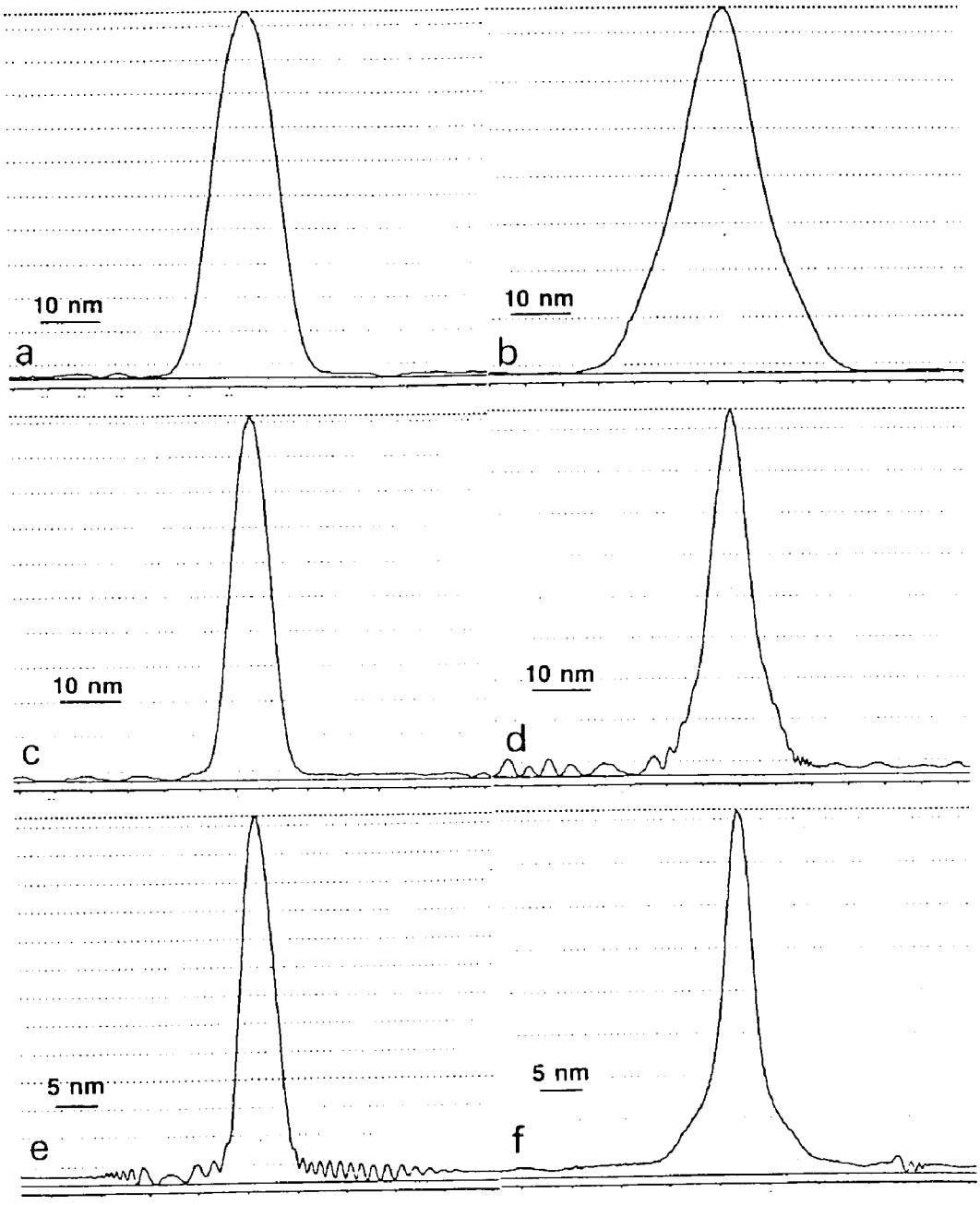

Fig. 3.4 Intensity profiles of the electron probes of the EM430T AEM with a 50 μm C2 aperture measured by the densitometer. a)&b) spot size setting STEM3, slightly different objective lens focusing conditions. c)&d) spot size setting STEM4, slightly different objective lens focusing condition. e)&f) spot size setting STEM5, objective focusing condition is at "disc of minimum confusion" for e) and at "Gaussian image plane" for f).

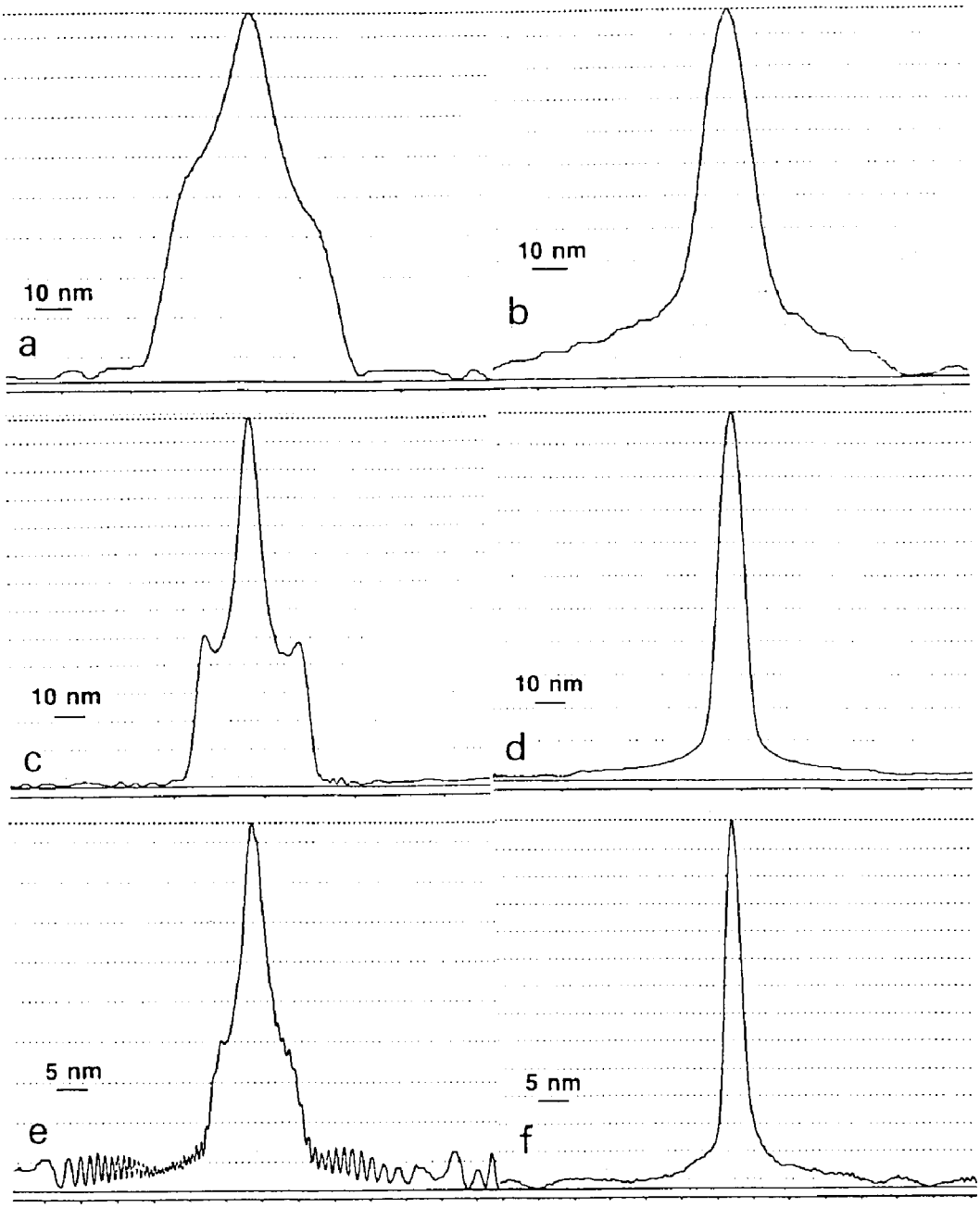

Fig. 3.5 Intensity profiles of the electron probes of the EM430T AEM with a 100 μm C2 aperture measured by the densitometer. a)&b) spot size setting STEM3. c)&d) spot size setting STEM4. e)&f) spot size setting STEM5. For all spot sizes, a tail around the probe is unavoidable no matter which objective lens focusing condition is used.

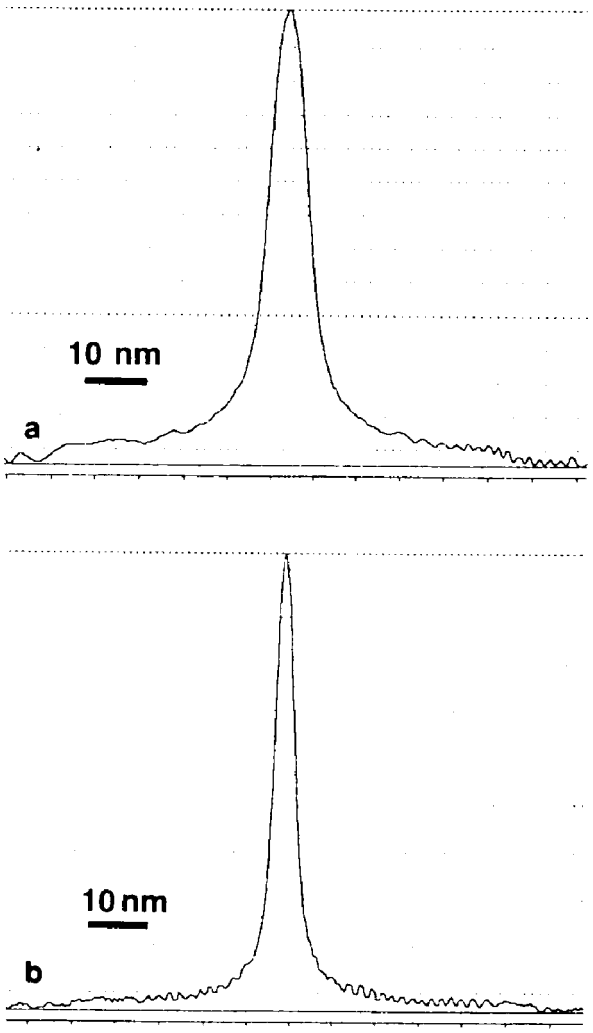

Fig. 3.6 Intensity profiles of the electron probes of the EM400T AEM with a 70 μm C2 aperture measured by the densitometer. a) spot size setting STEM4. b) spot size setting STEM5.

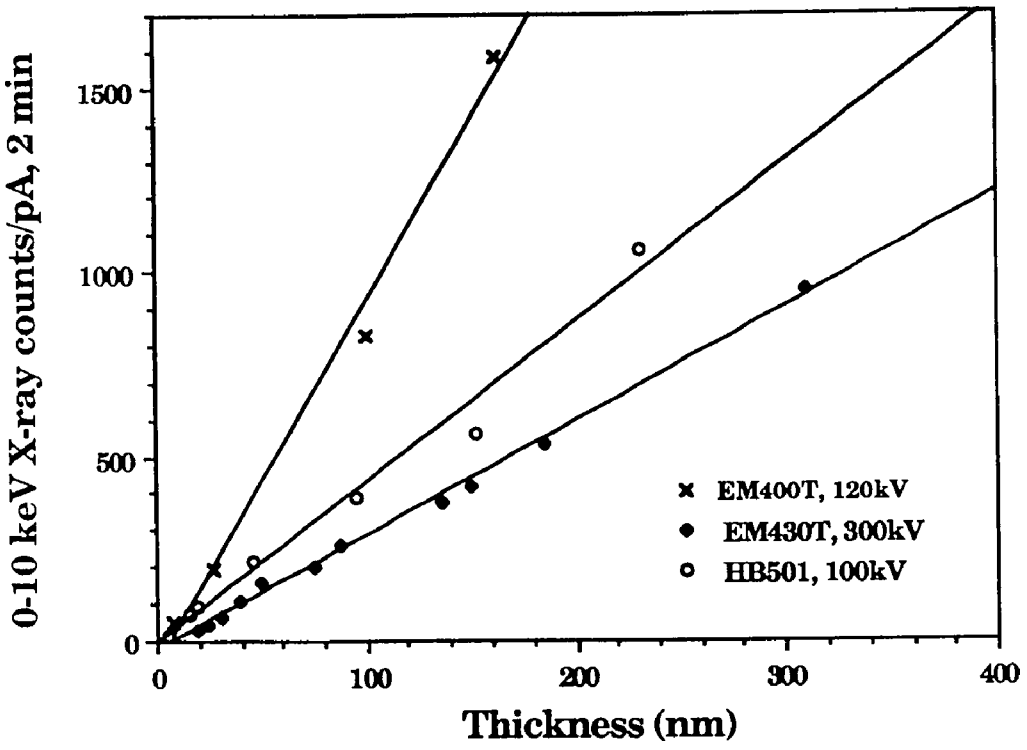

Fig. 3.7 Calibration curve of 0-10keV x-ray count/pA vs specimen thickness for three different AEMs. The specimen is Fe-25wt%Ni alloy and the counting time is 2 min. The specimen thickness is measured using the EELS log-ratio method.

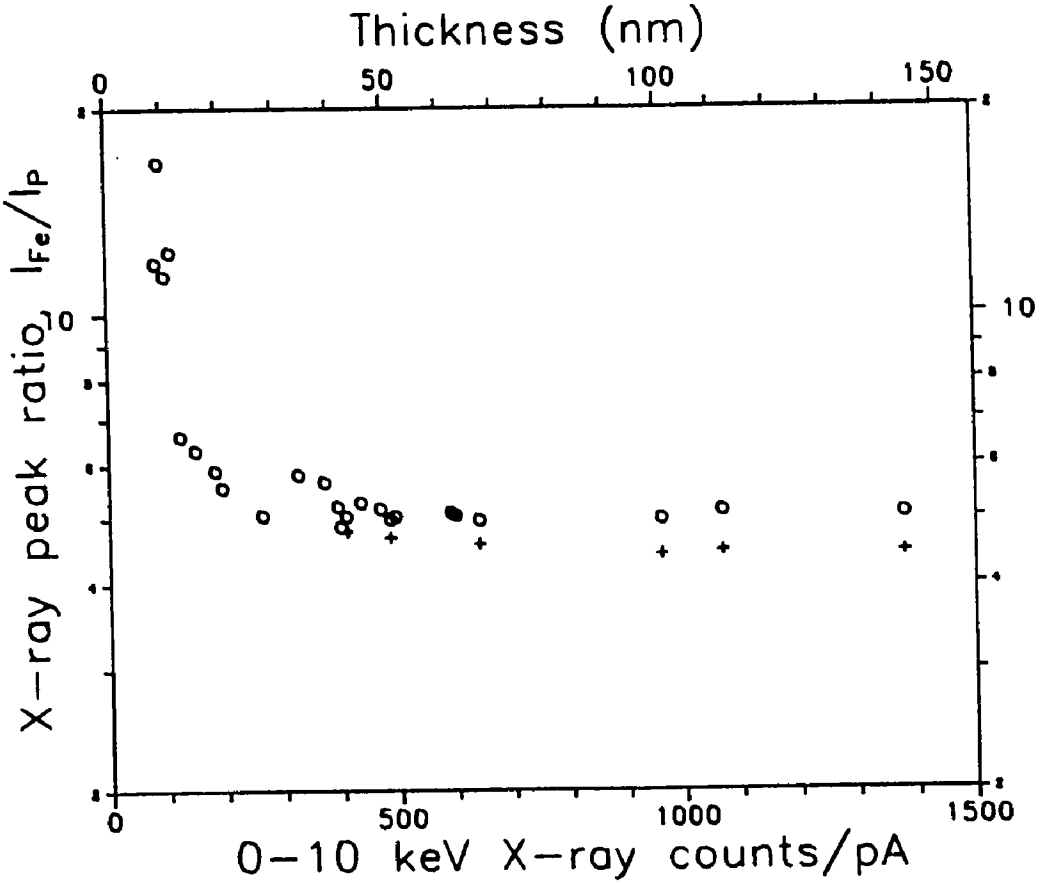

Fig. 3.8 Measured peak x-ray intensity ratio of Fe-K_α and P-K_α as a function of specimen thickness. EM400T and Fe_3P specimen. The specimen is dimpled to ~10 to 5 μm before ion-beam thinning at 4.5kV. o : data which were not absorption corrected, + : absorption corrected.

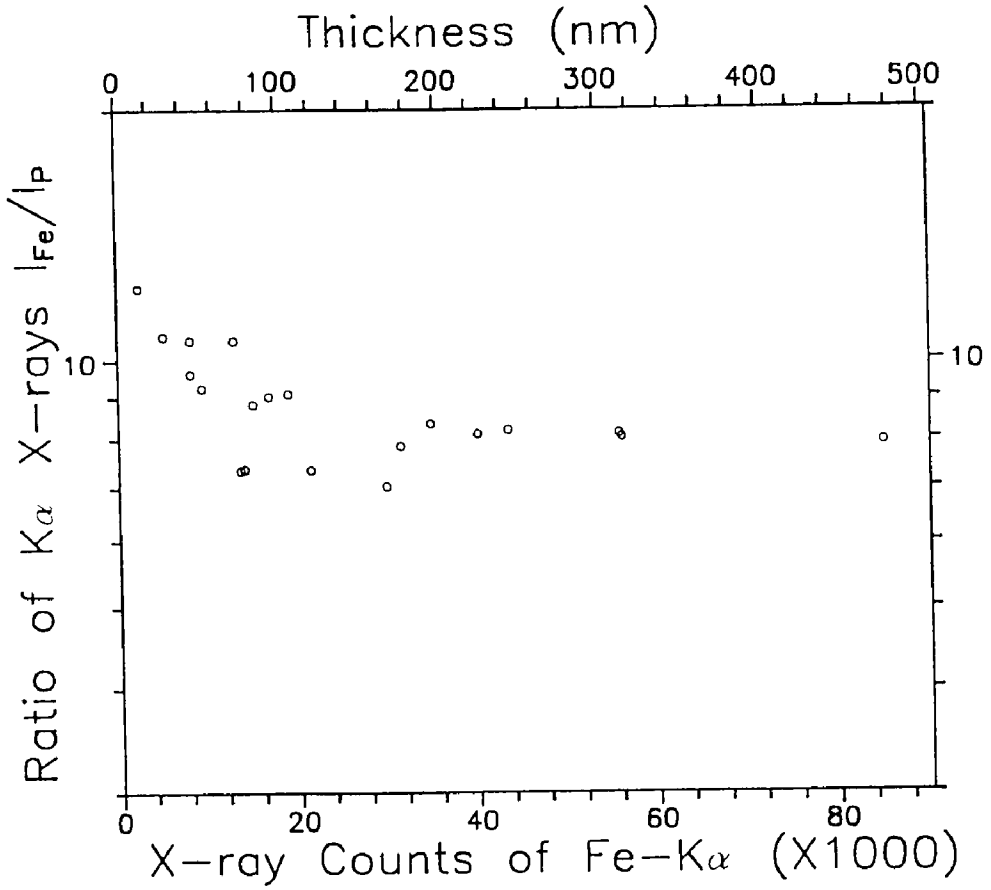

Fig. 3.9 Measured peak x-ray intensity ratio of Fe-K_α and P-K_α as a function of specimen thickness. EM400T and Fe_3P specimen. The specimen is ion-beam thinned from about 40 μm at 4.5kV.

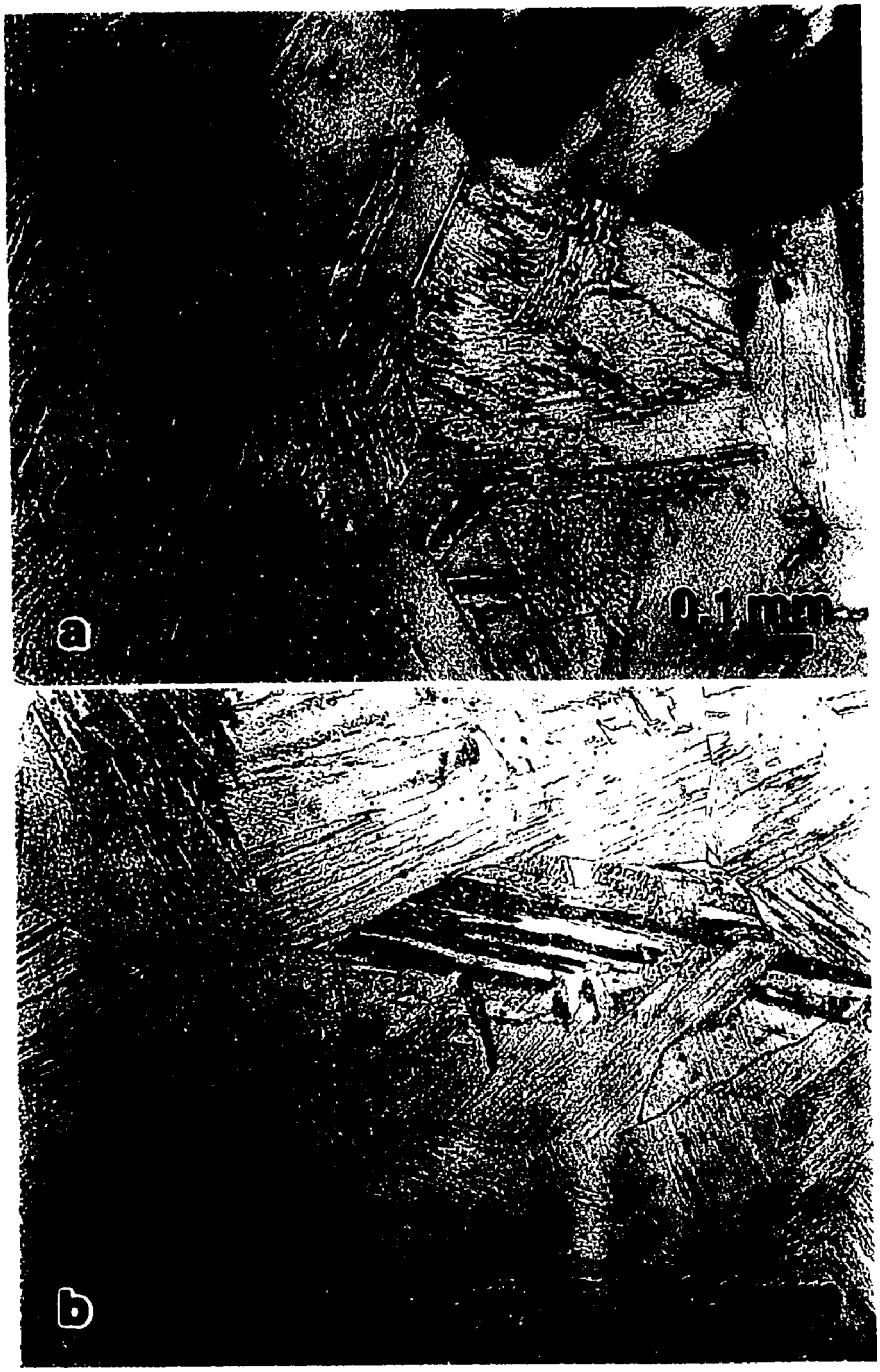

Fig. 4.1 As-quenched microstructure of FN15 and FNP15 alloy, 2% Nital etched. The microstructure is lath martensite. a) Light optical micrograph of FN15 alloy; b) light optical micrograph of FNP15 alloy; c) SEM SE image of FNP15.

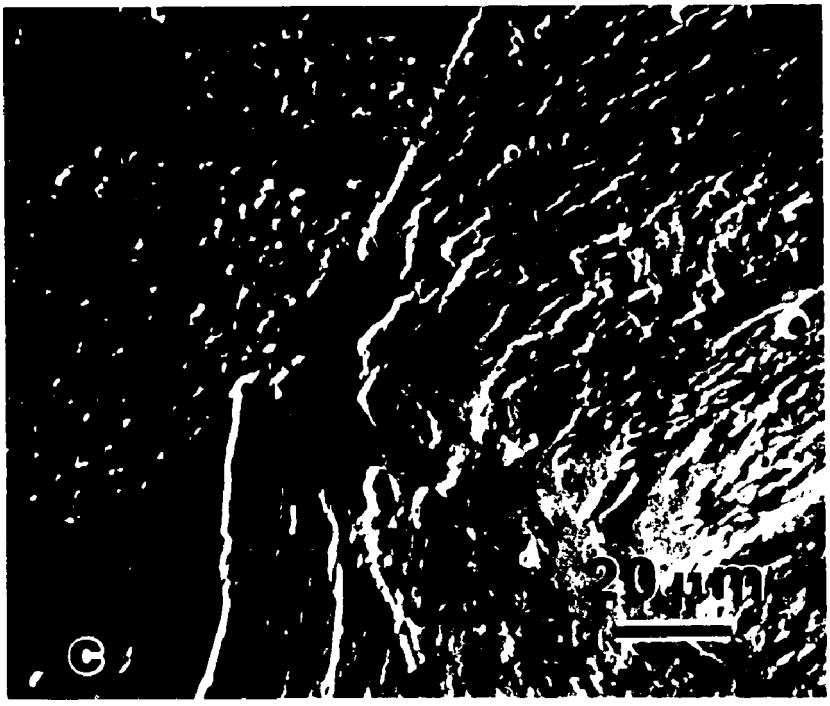
C
20 μm

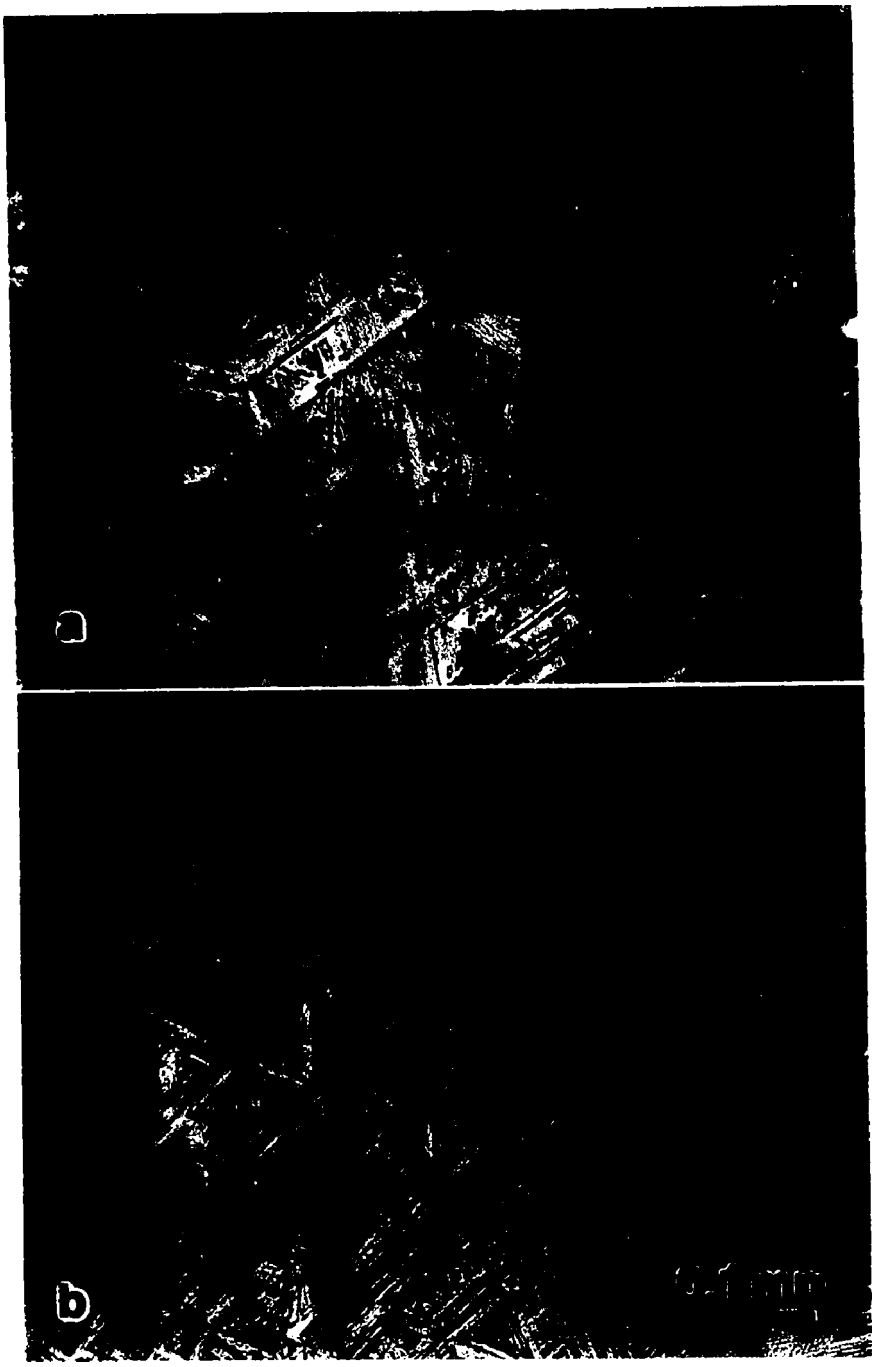

Fig. 4.2 As-quenched microstructure of FN25 and FNP25 alloy, 2% Nital etched. The microstructure is lath martensite. a) Light optical micrograph of FN25 alloy; b) light optical micrograph of FNP25 alloy; c) SEM SE image of FN25.

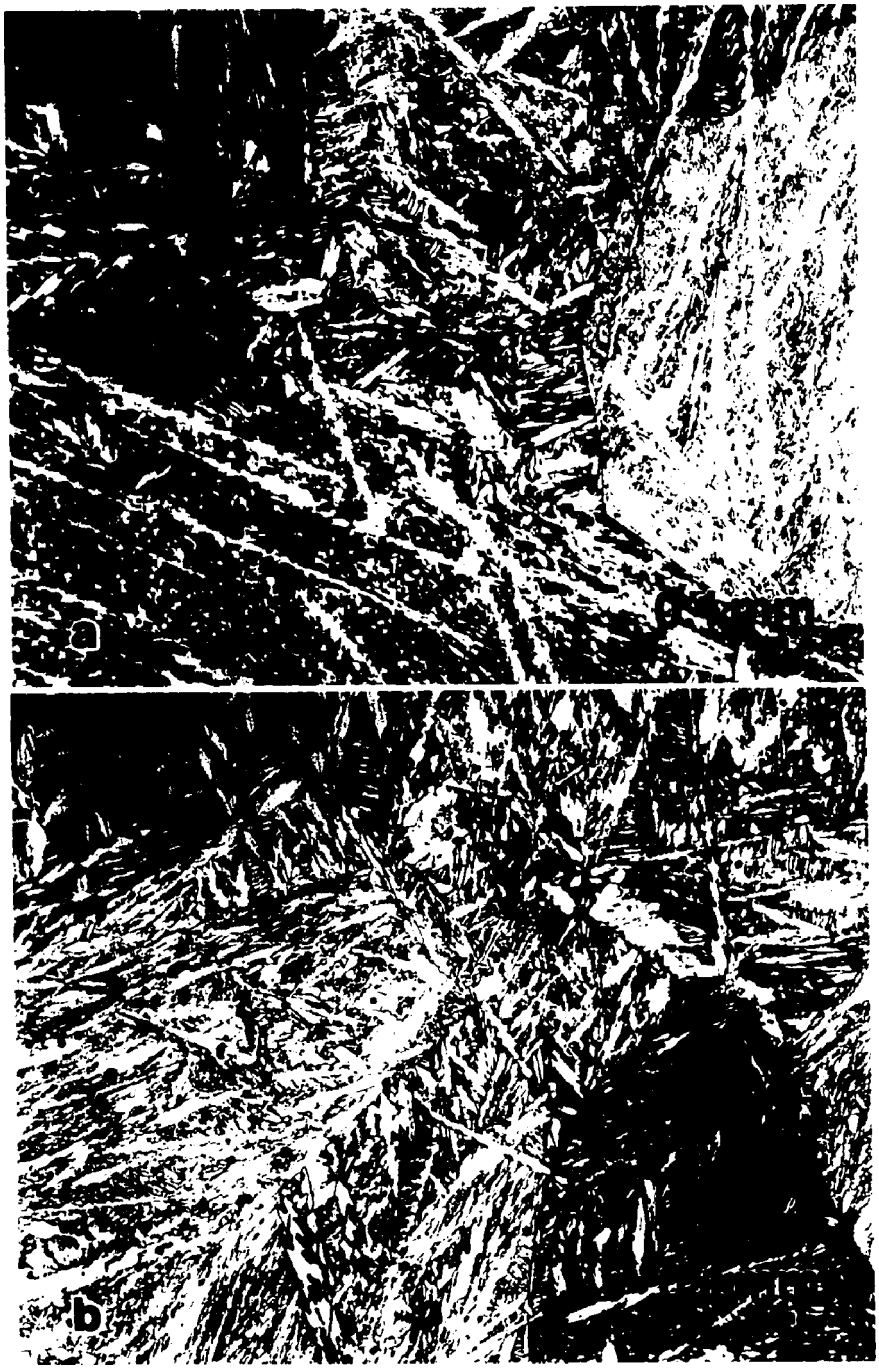

Fig. 4.3 As-quenched microstructure of FN30 and FNP30 alloy, 2% Nital etched. The microstructure is plate martensite. a) Light optical micrograph of FN30 alloy; b) light optical micrograph of FNP30 alloy; c) SEM SE image of FNP30.

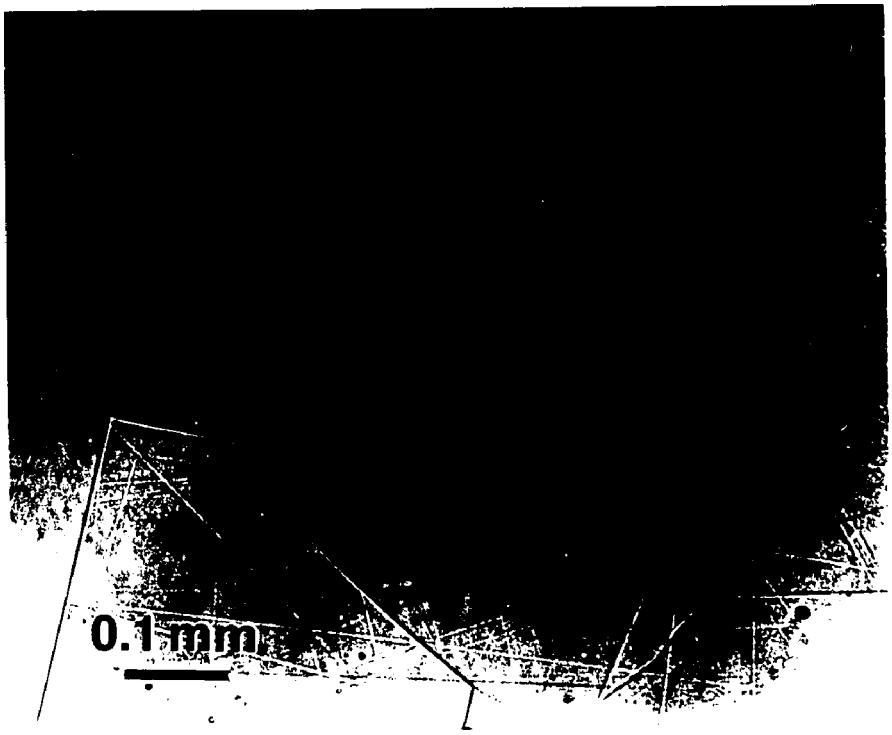

Fig. 4.4 LOM of as-quenched microstructure of FN44 alloy. The structure is austenite. The FNP44 and FN35 alloy have the same microstructure.

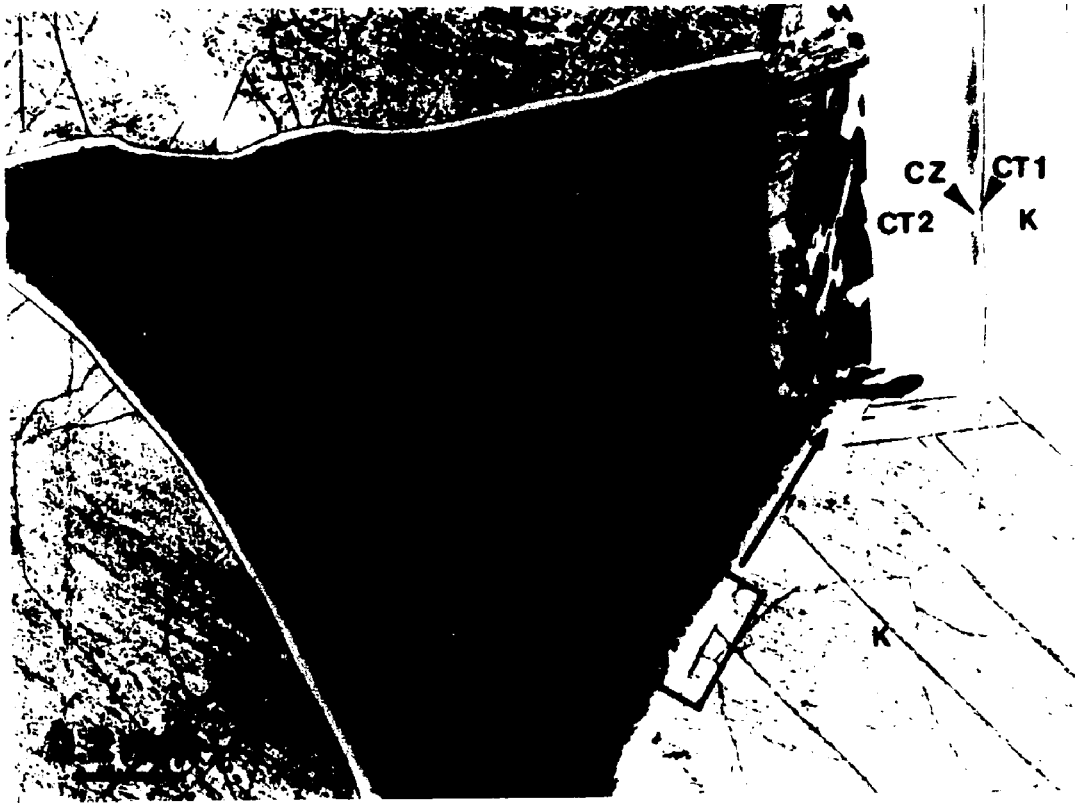

Fig. 4.5 An optical micrograph of a typical plessite region surrounded by three kamacite plates (k) in octahedrite Grant. The inset shows an enlarged portion of the high Ni border. CT1: clear taenite 1, CZ: cloudy zone, CT2: clear taenite 2, DP: duplex plessite, BP: black plessite.

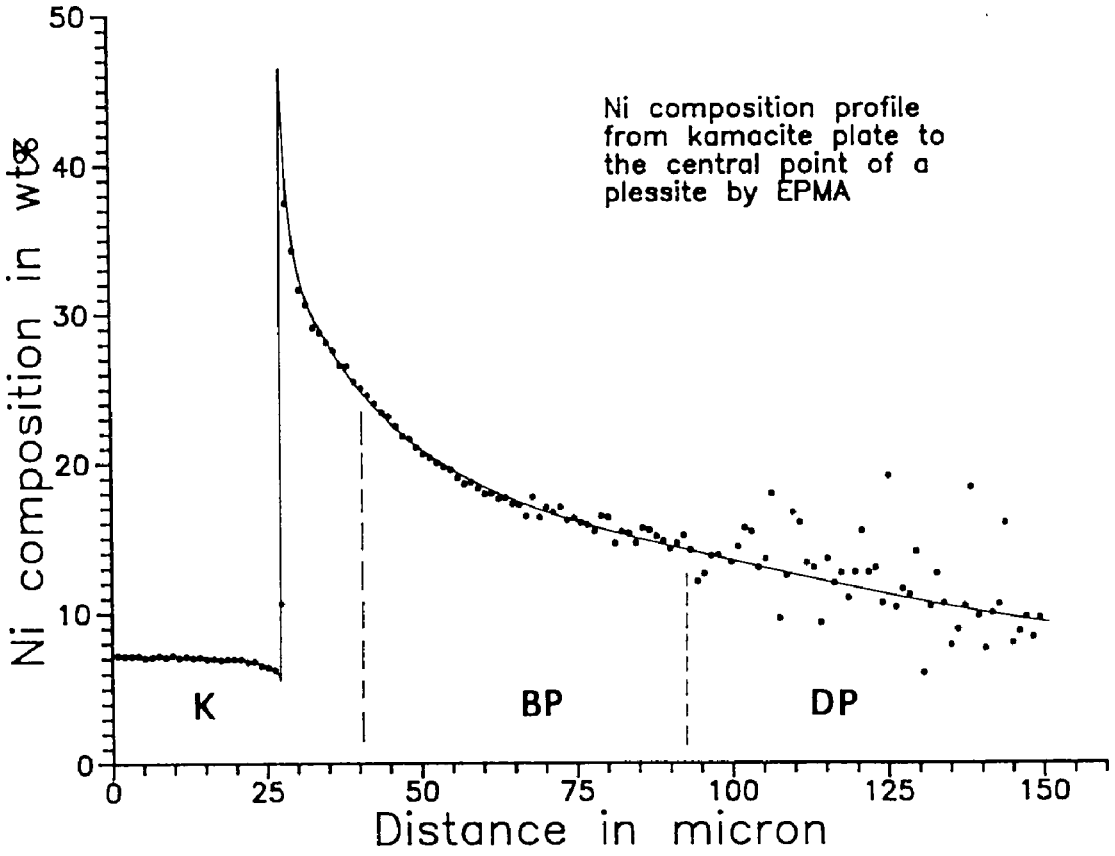

Fig. 4.6 Ni composition profile across half of a plessite region in Grant measured using the EPMA.

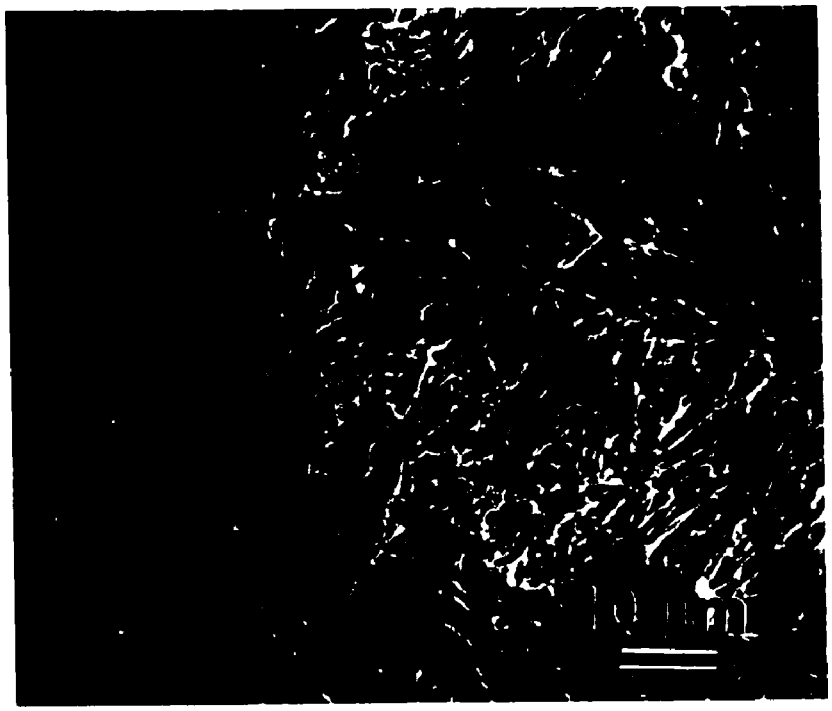

Fig. 4.7 SEM SE image of duplex plessite region of Grant. ETEC, 20 kV.

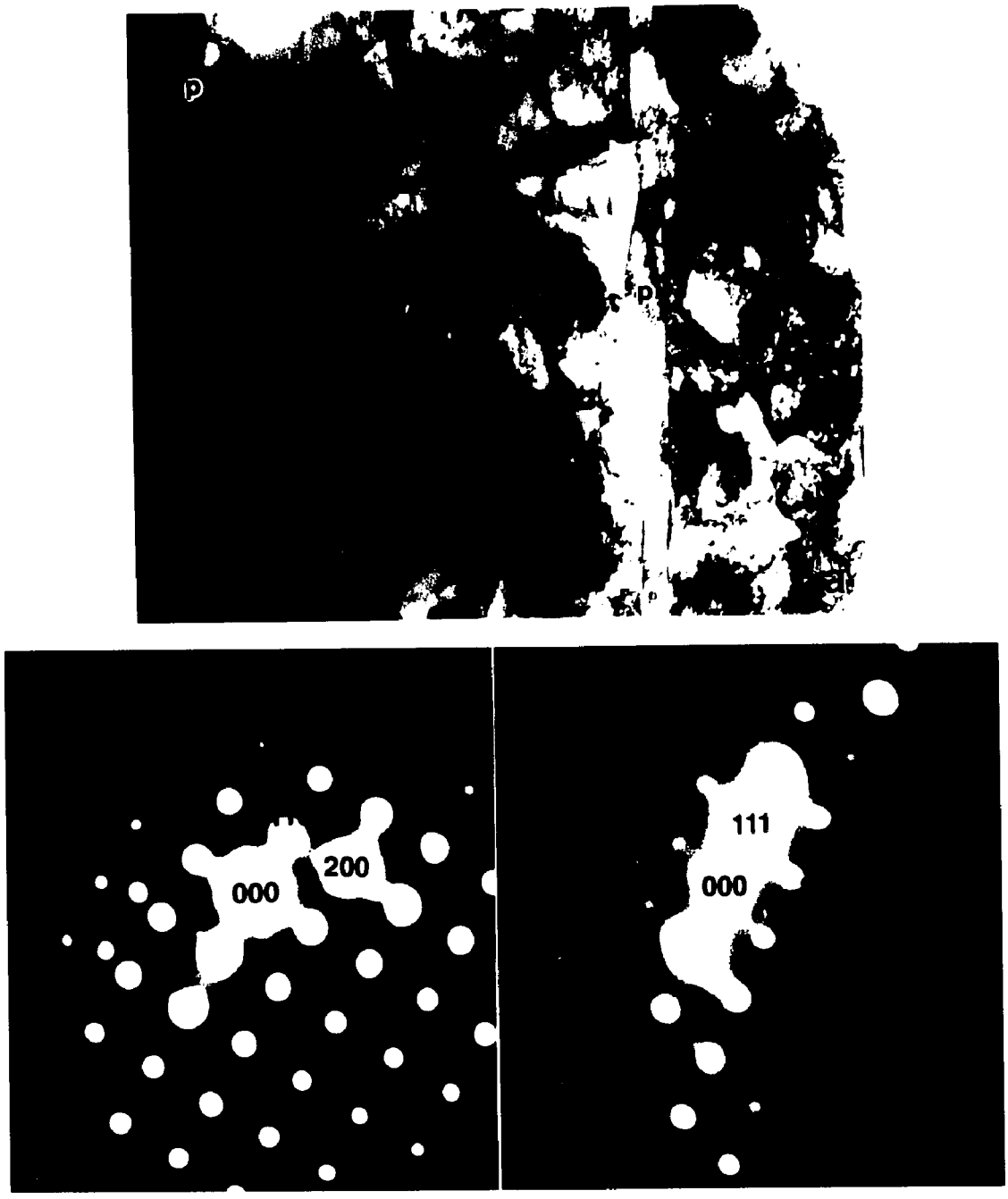

Fig. 4.8 a) TEM BF image of grain boundary precipitates (p) in DP region of Grant. b) SAD pattern of the matrix phase. c) SAD pattern of the precipitate. No ordering is observed in the precipitate phase.

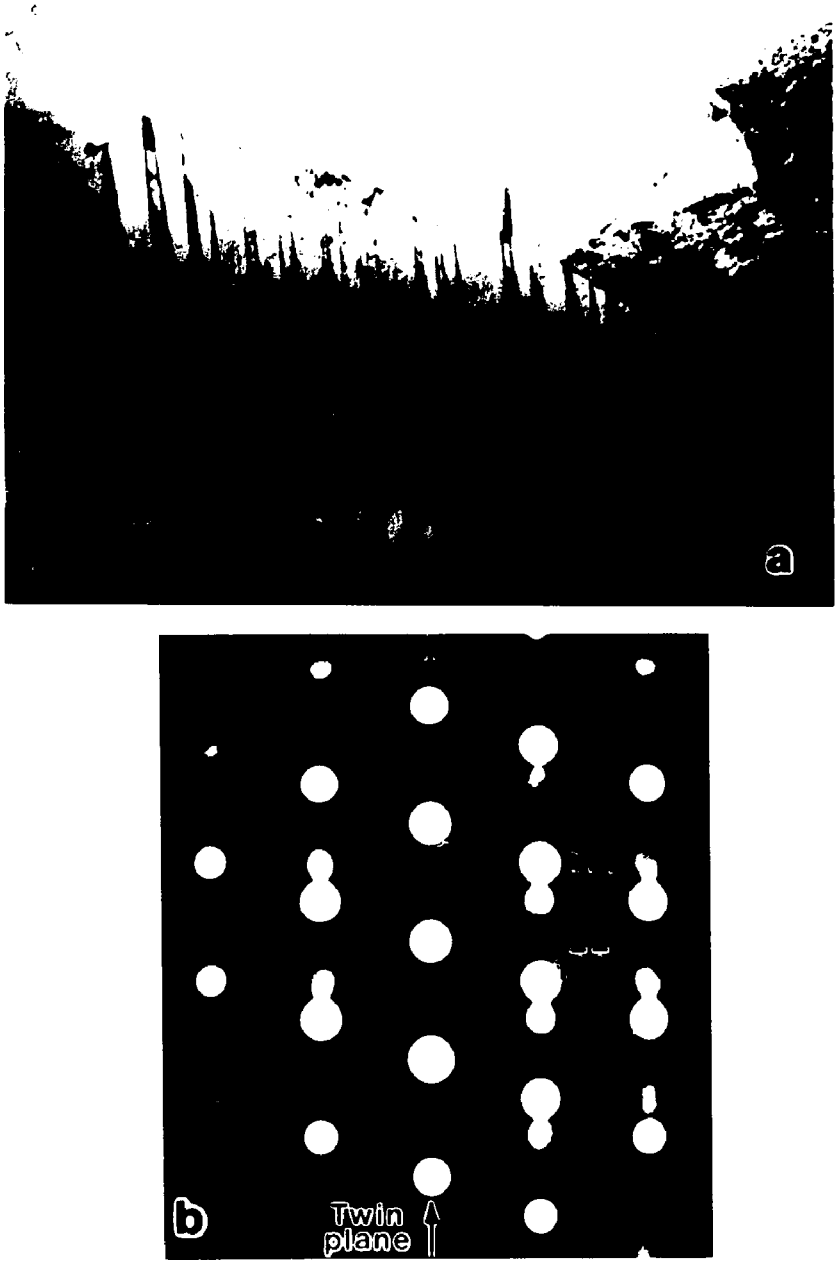

Fig. 4.9 TEM images of a twinned precipitate in duplex plessite region of Grant. a) BF image; b) SAD pattern; c) CDF image of the twin $(111)_{fcc}$ diffraction spot; and d) CDF image of the main $(111)_{fcc}$ diffraction spot.

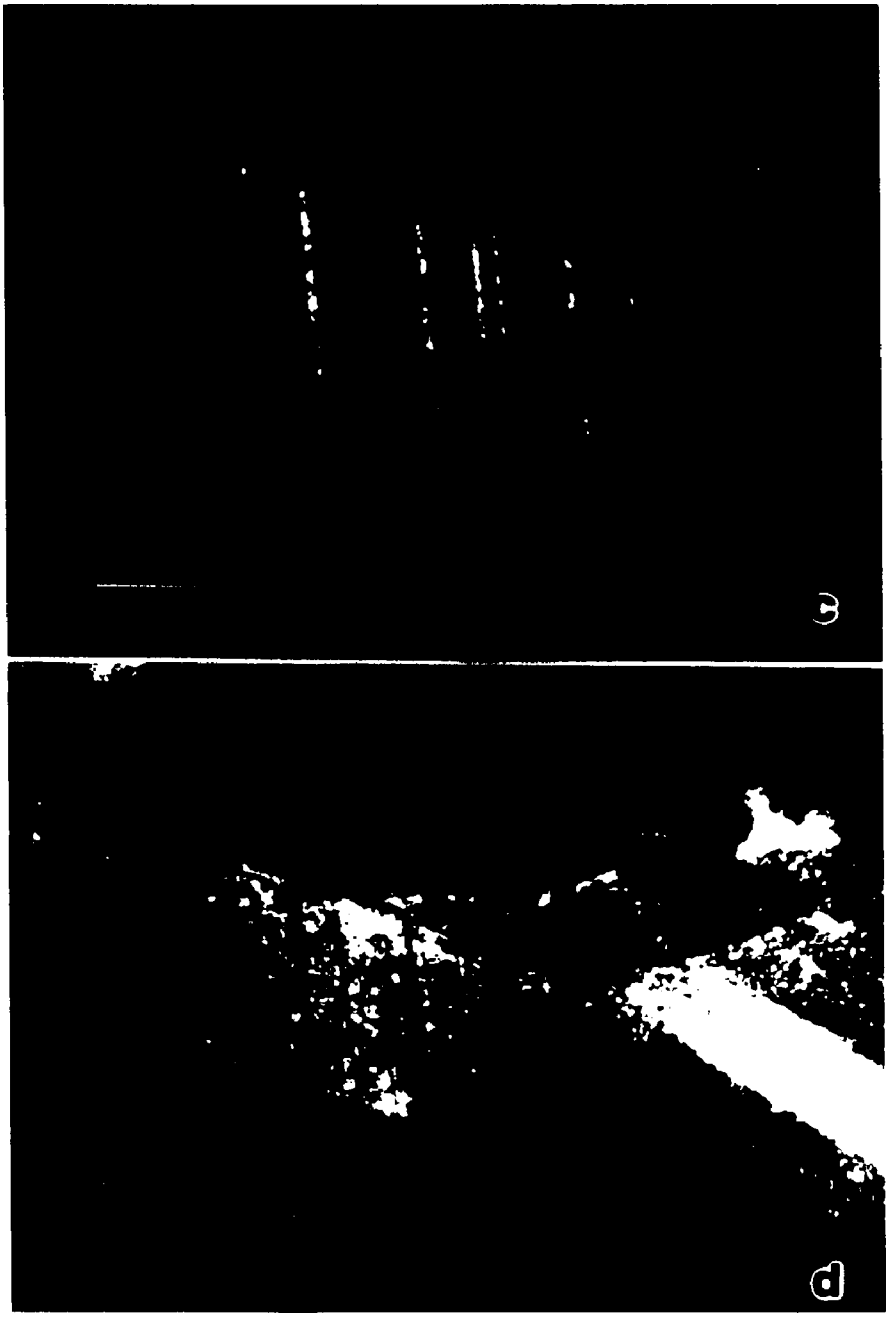
c
d

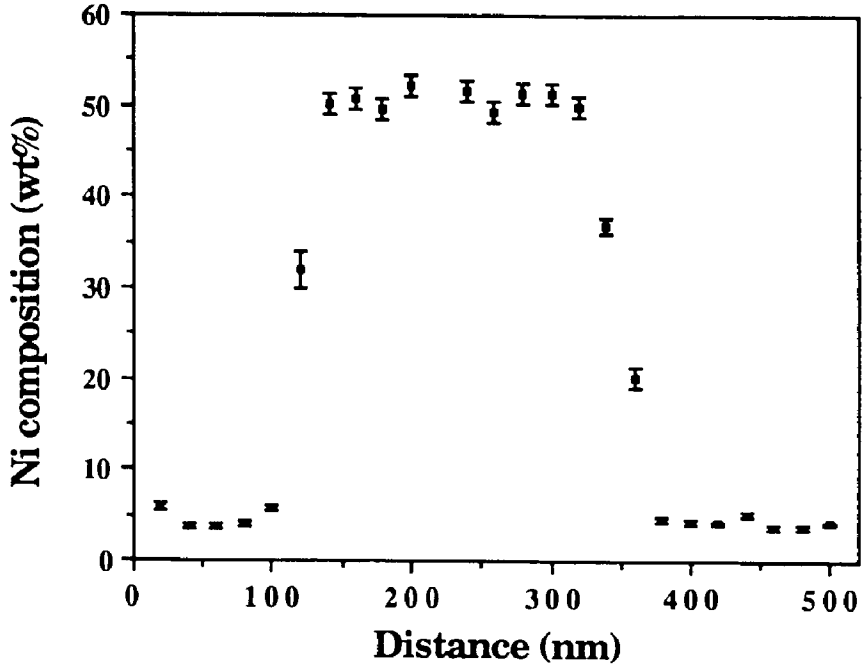

Fig. 4.10 EDS Ni composition profile of a precipitate in DP region (~9 wt% Ni) of Grant. The precipitate phase is the high Ni phase. EM400T.

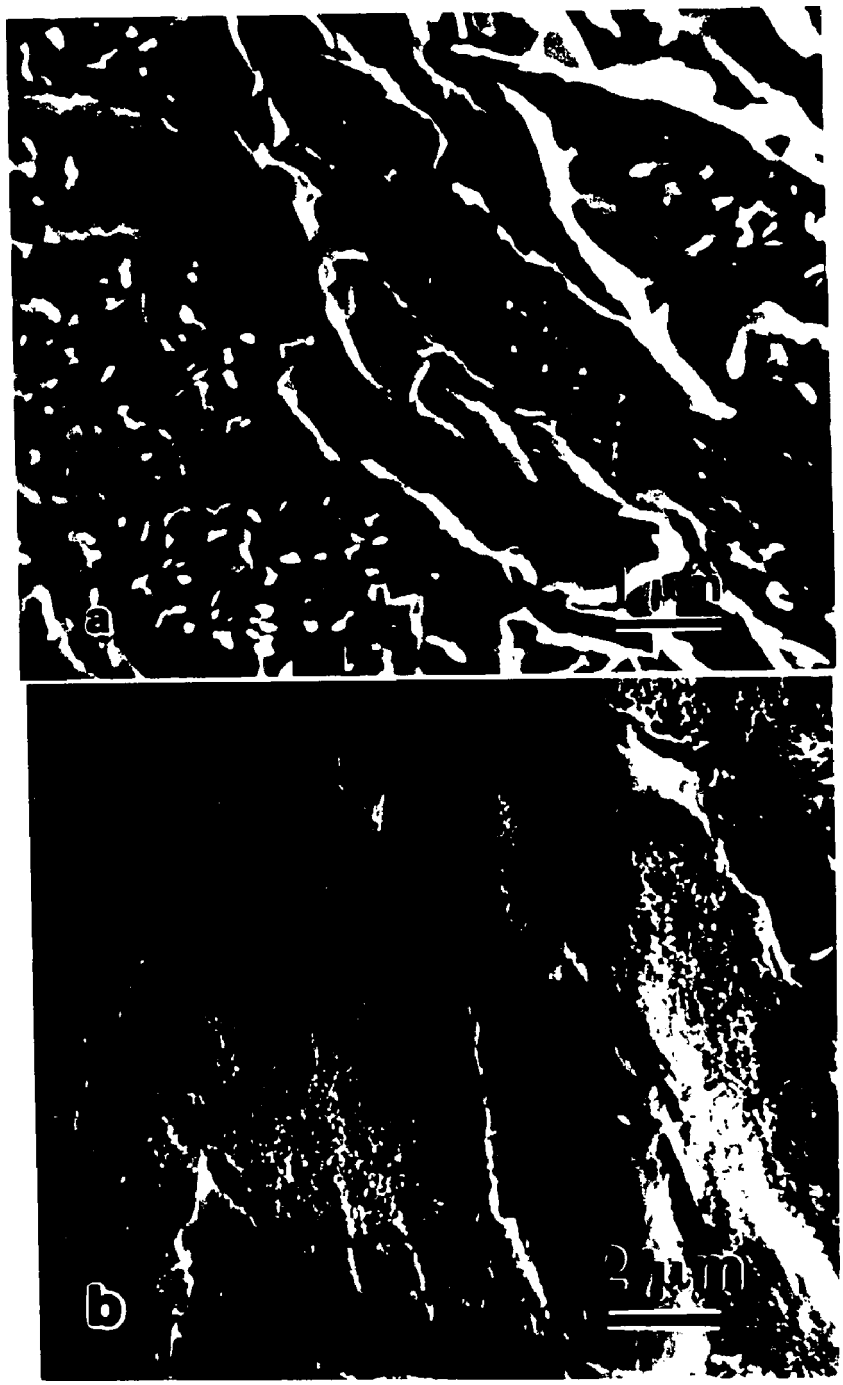

Fig. 4.11 SEM SE images of BP regions of Grant showing the intragranular precipitates (a) and the very finely decomposed martensite near the CT2 region (b).

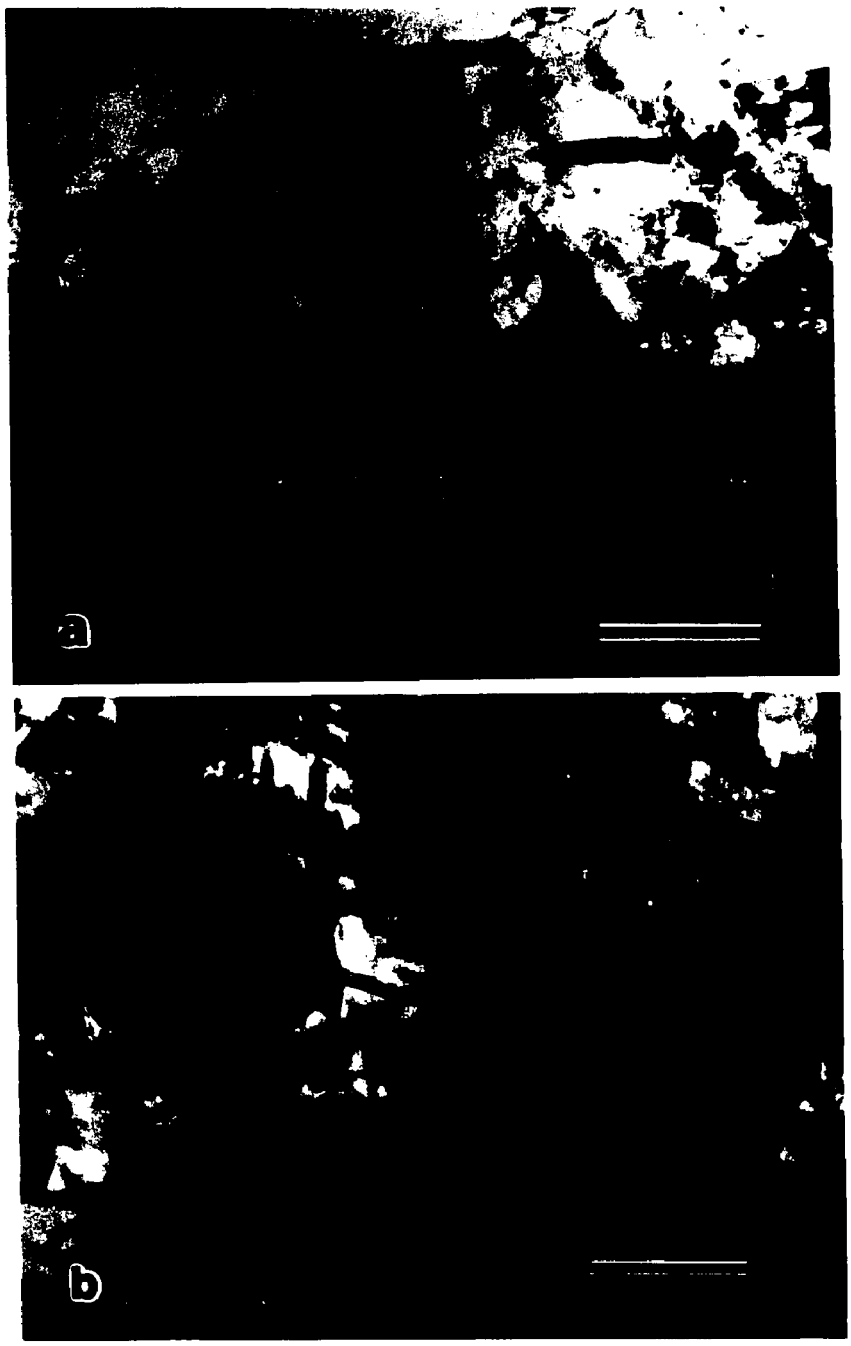

Fig. 4.12 TEM BF images of precipitates in BP region of Grant. The area shown in a) has a lower average Ni composition (~14 wt%) than that of the area shown in b) (~20 wt% Ni), and therefore has a larger average precipitate size.

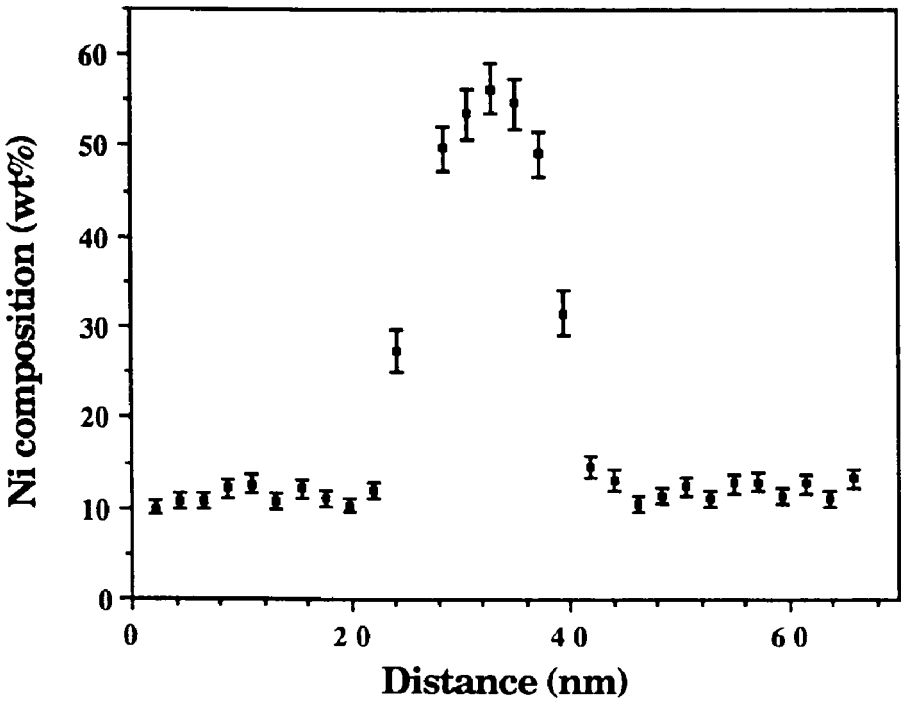

Fig. 4.13 EDS Ni composition profile across a precipitate in BP region (~17 wt% Ni) of Grant. The precipitate phase is the high Ni phase. HB501.

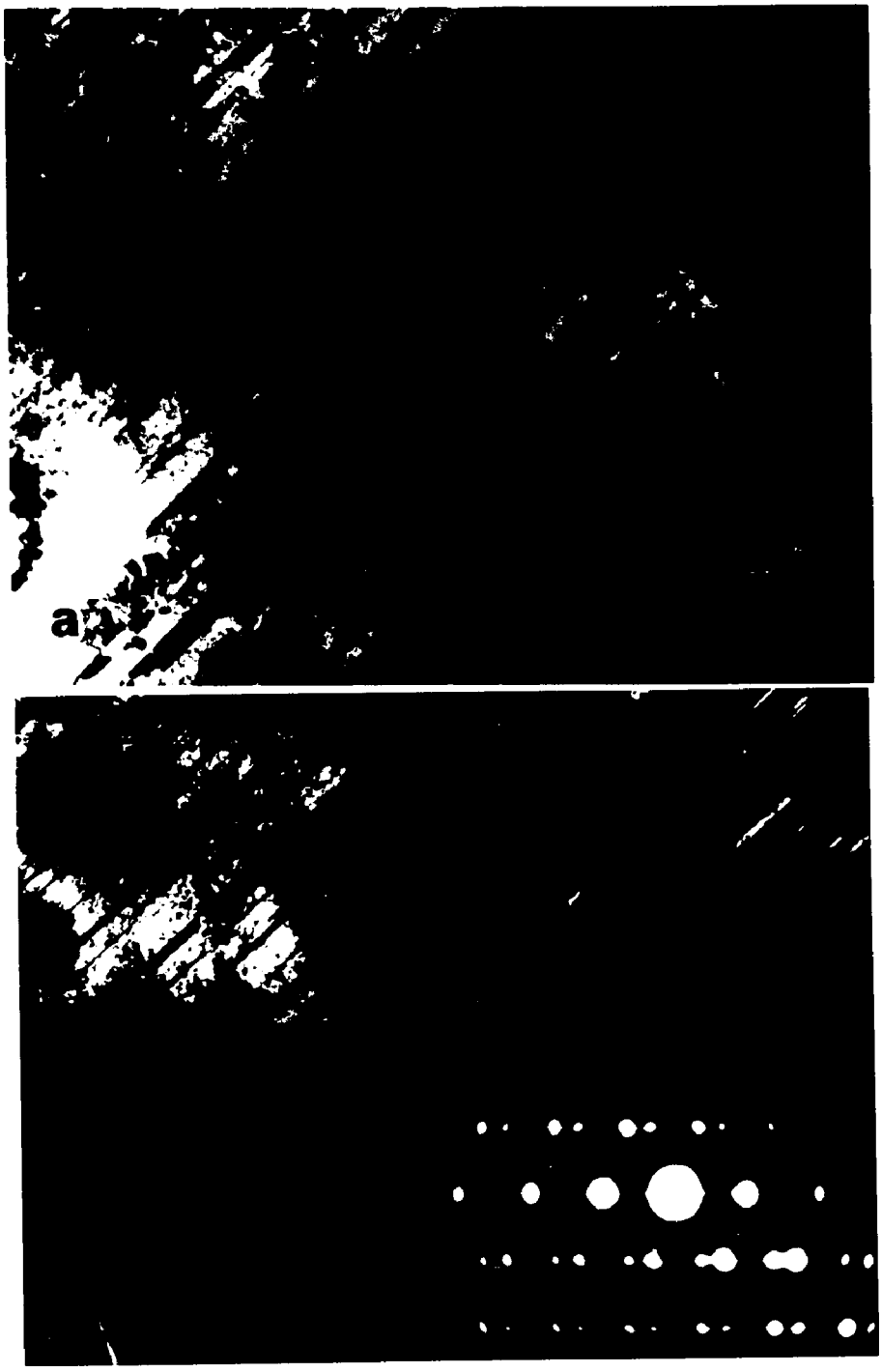

Fig. 4.14 TEM images of fcc twinning in CT2 region of Grant. a) BF image; b),c) and d) CDF images which was taken using the diffraction spot labeled by the same character in SAD pattern e); f) the indexing of the SAD pattern.

f

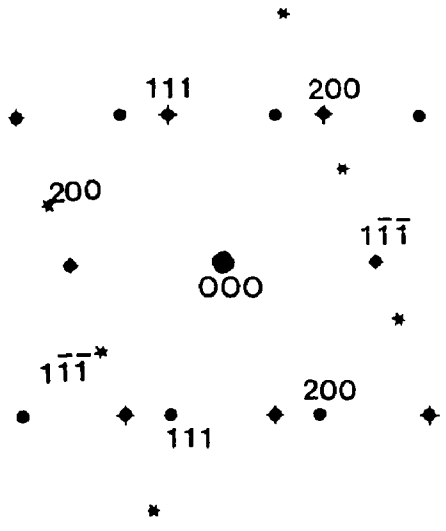

fcc <1 1 0> zone

◆ matrix ● $\bar{1}$11 twin * 111 twin

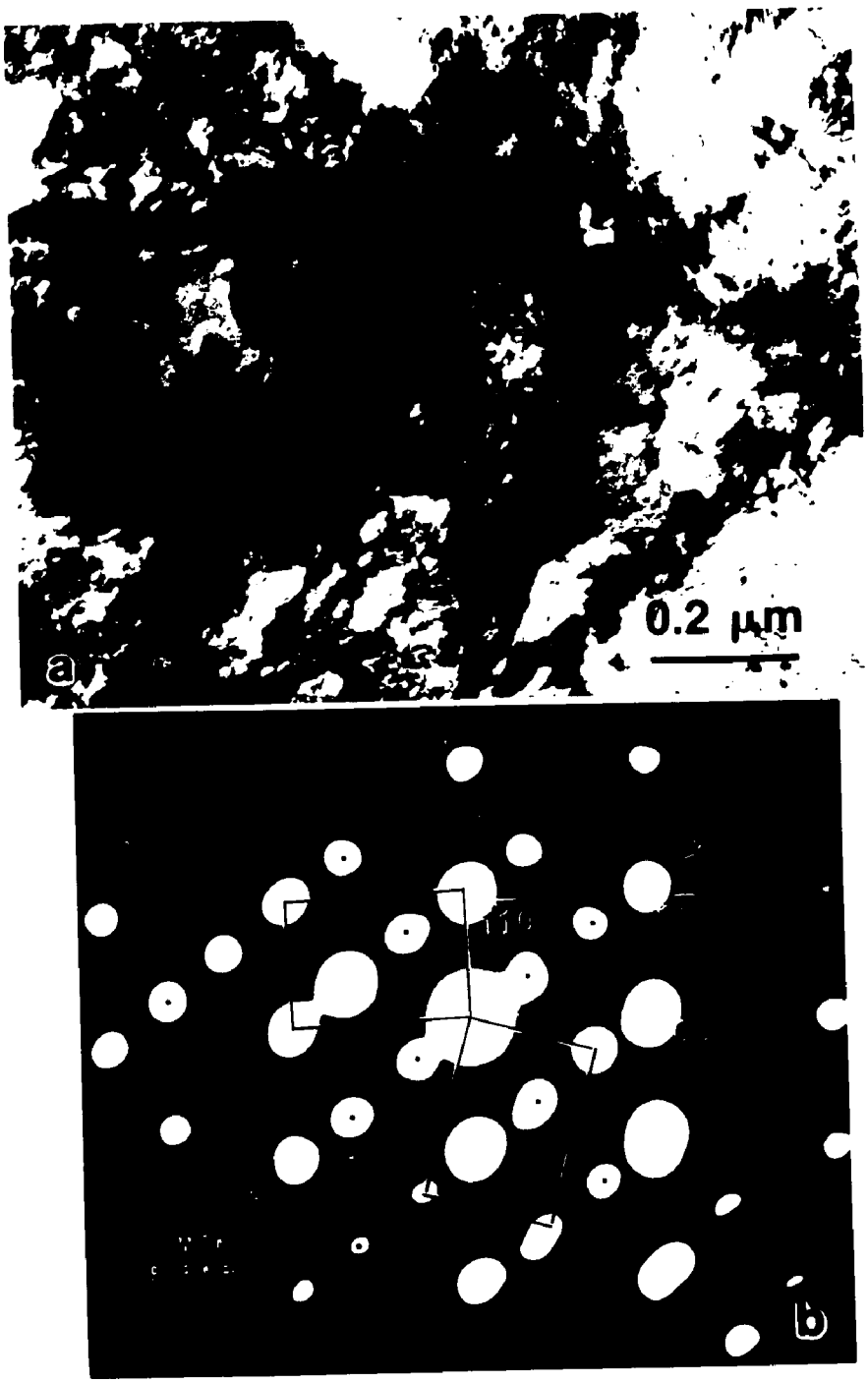

Fig. 4.15 TEM images of a kamacite region of Grant. a) BF image; b) CBED pattern showing a bcc structure and bcc(112) twin. The diffraction discs with a dot are due to double diffraction; c)&d) CDF images of the twinning grains.

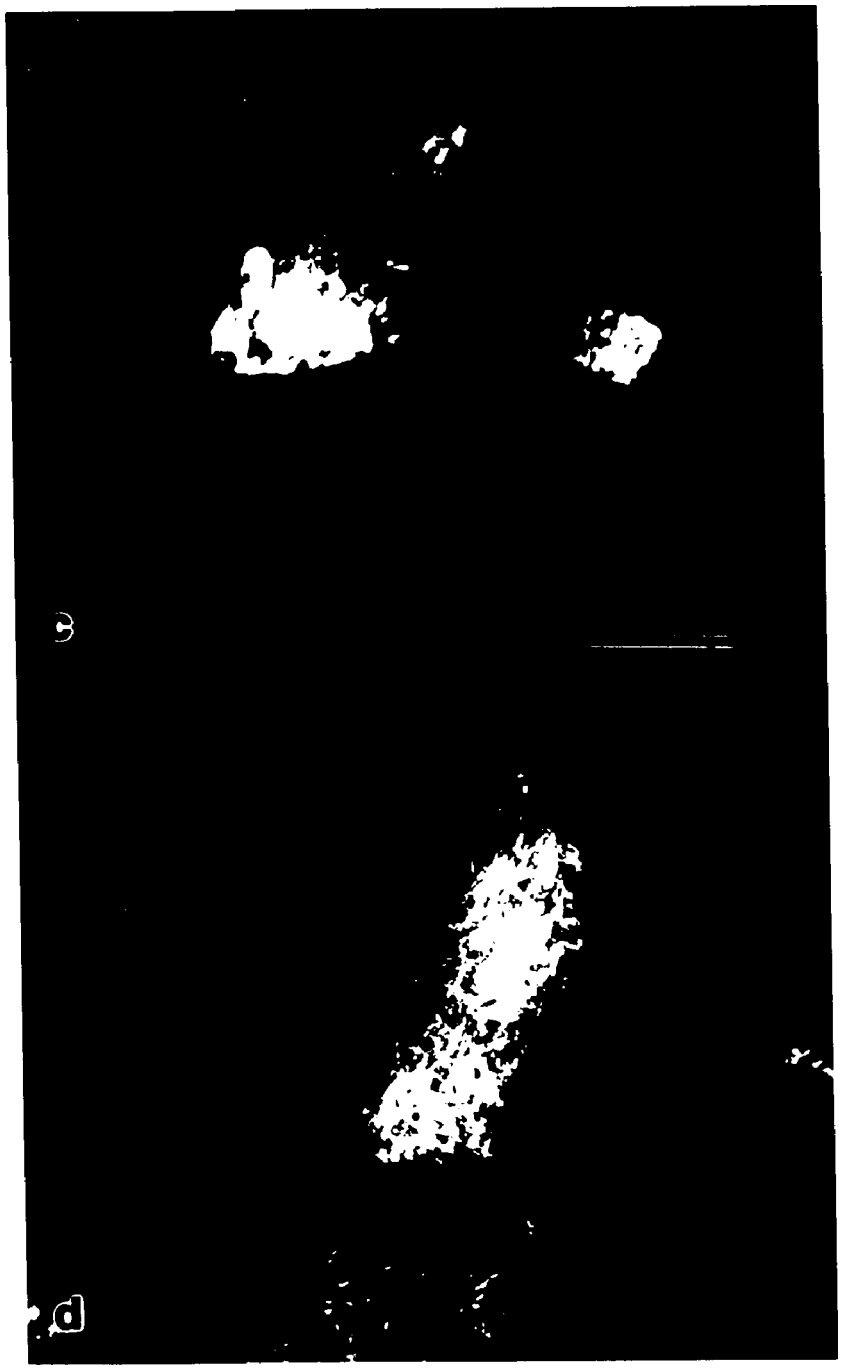
c
d

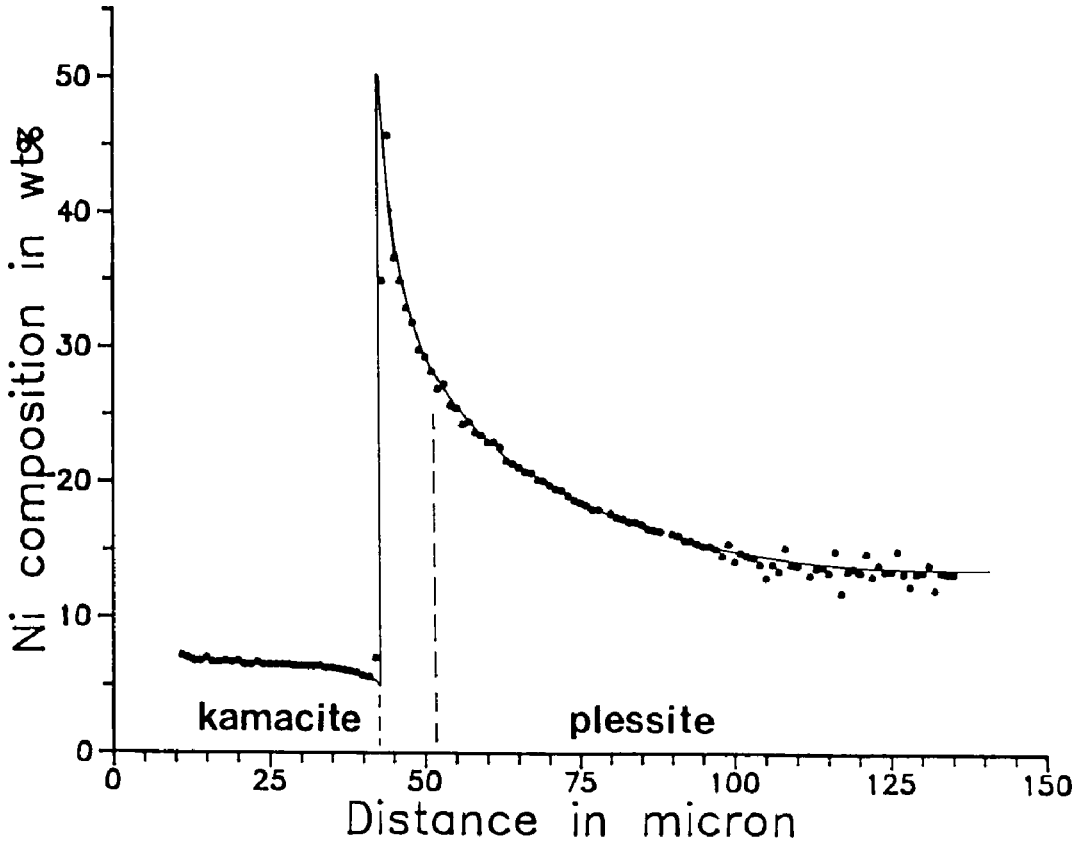

Fig. 4.16 Ni composition profile across half of a plessite region in the octahedrite Carlton measured using the EPMA.

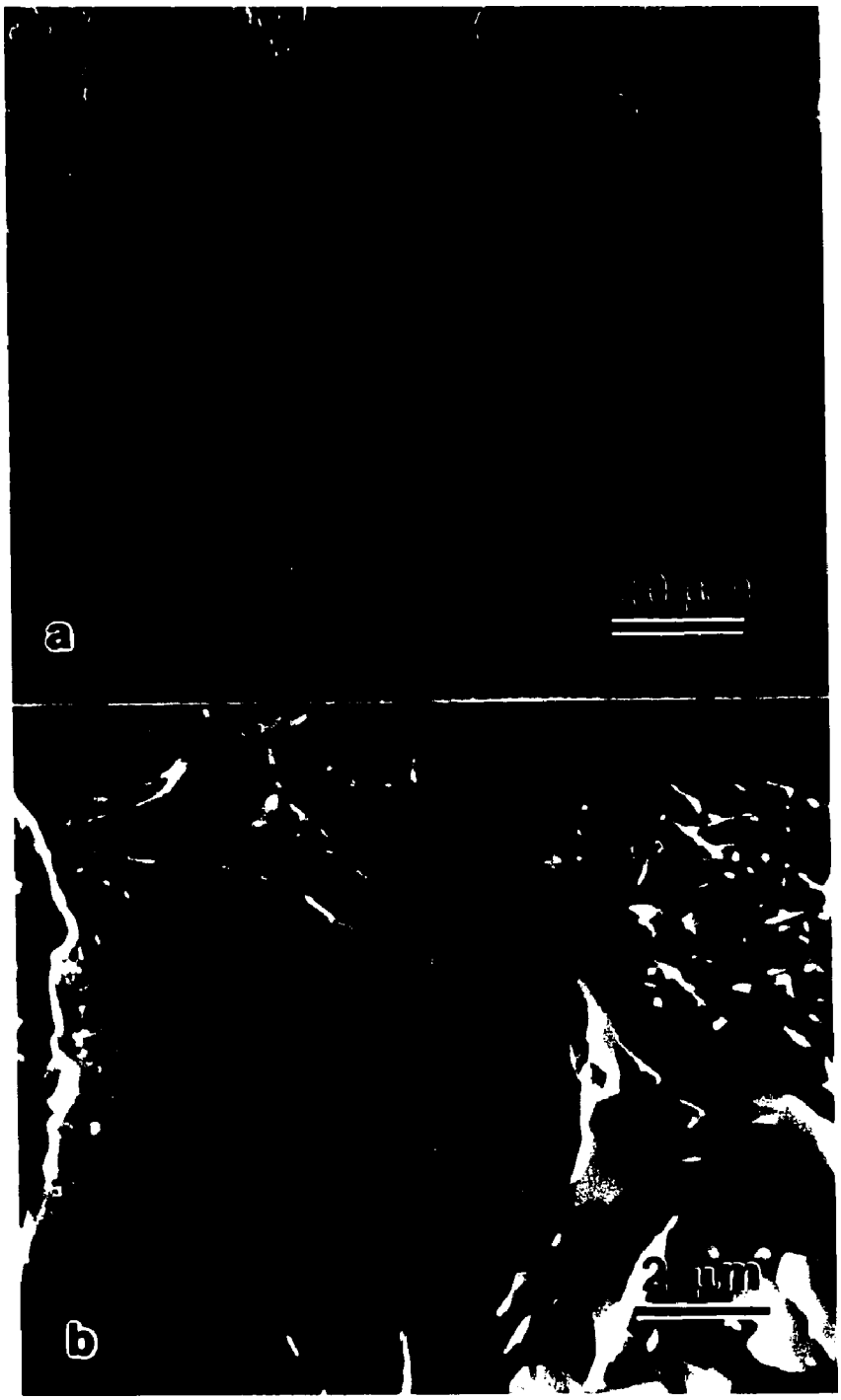

Fig. 4.17 SEM SE images of the center region of the plessite (~13 to 14 wt% Ni) of Carlton. The low magnification (a) and the high magnification (b) images show that both intergranular and intragranular precipitates are present. ETEC 20kV.

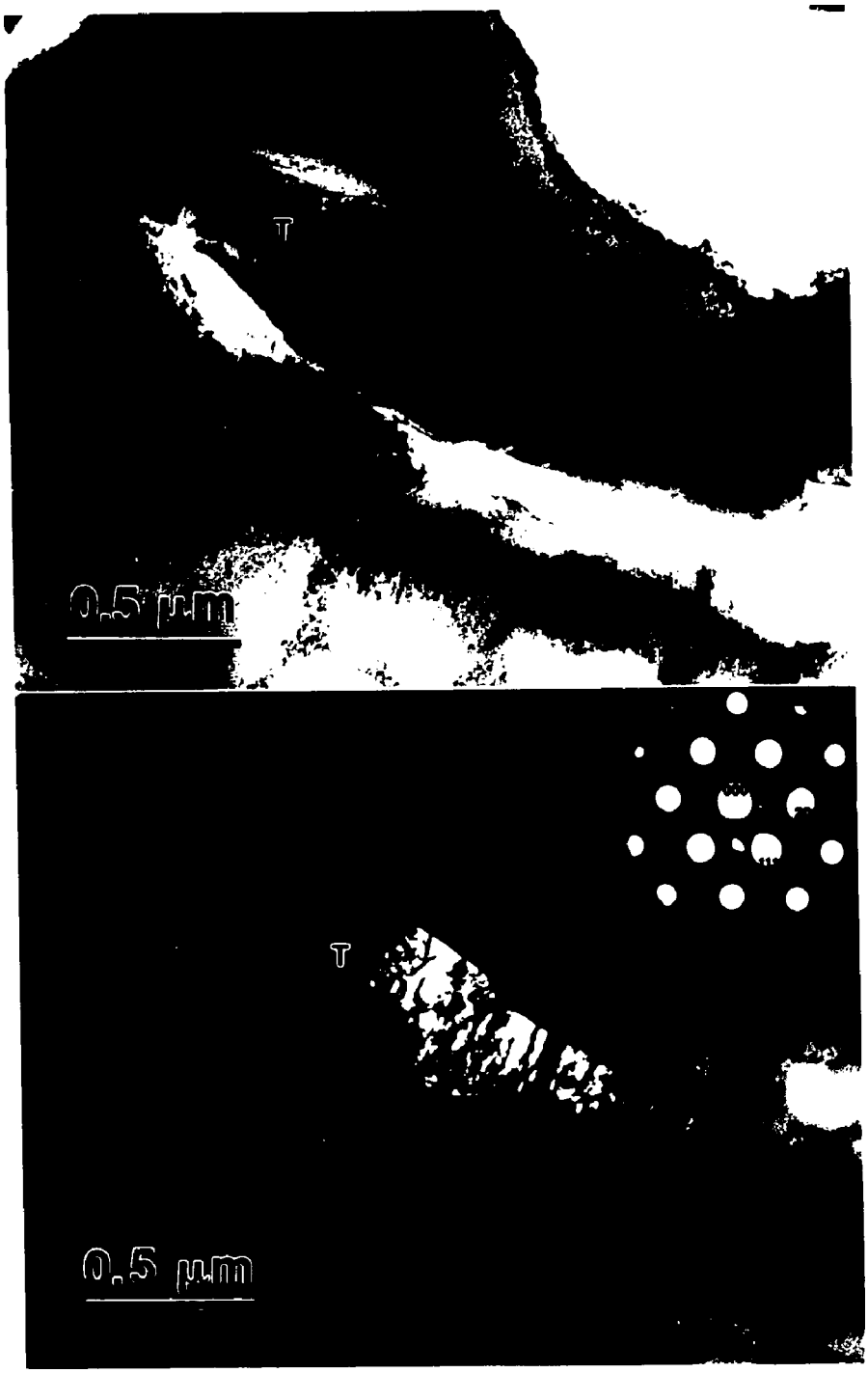

Fig. 4.18 TEM BF and CDF image of an $L1_0$ ordered grain boundary precipitate in the duplex plessite region of Carlton. The inset is a CBED pattern of the precipitate.

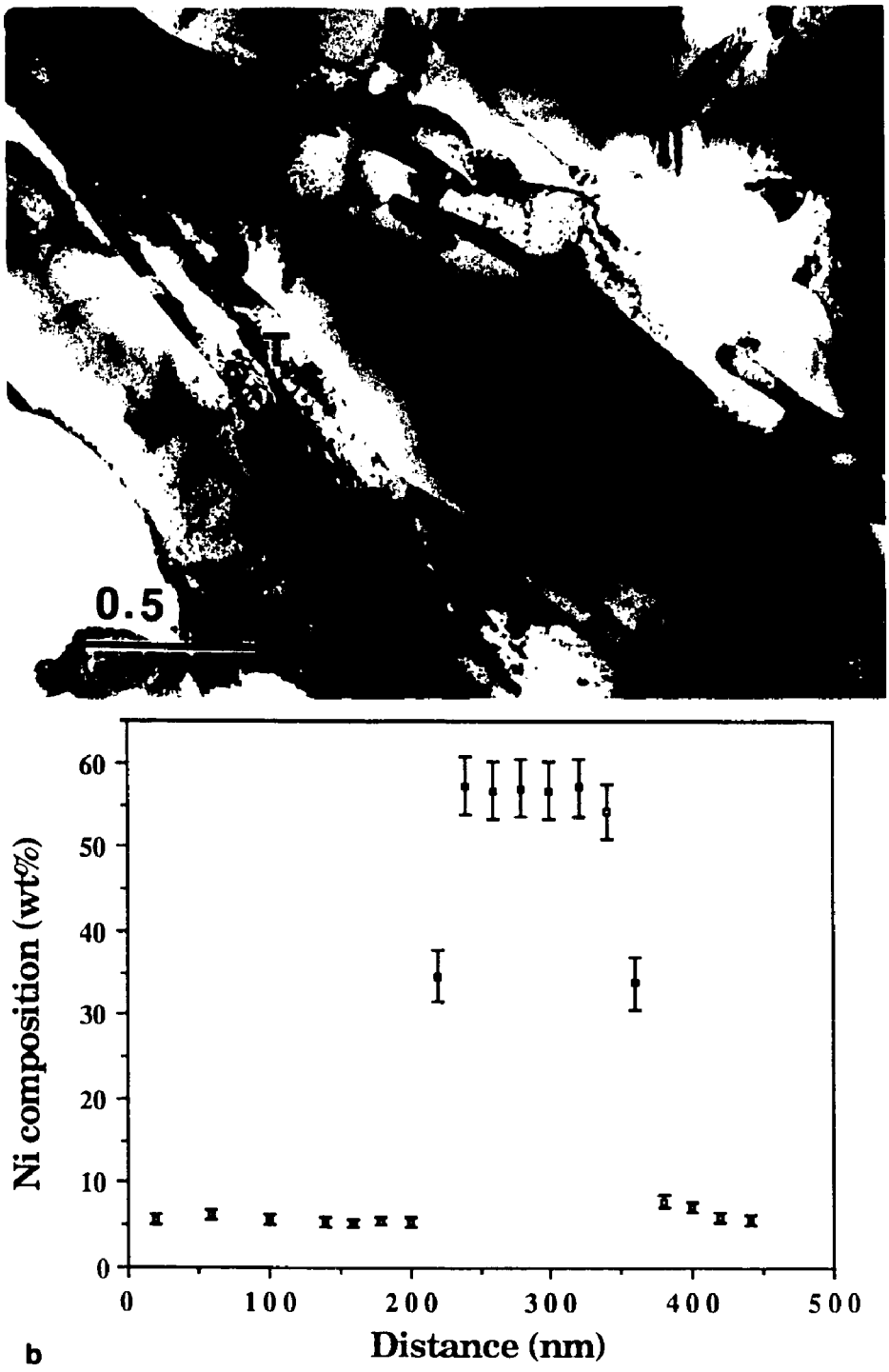

Fig. 4.19 a) TEM BF image of the intergranular precipitates in a 13 wt% Ni region of Carlton. T: tetrataenite. b) EDS Ni composition profile across one precipitate in this region. The precipitate phase is the high Ni phase. EM400T.

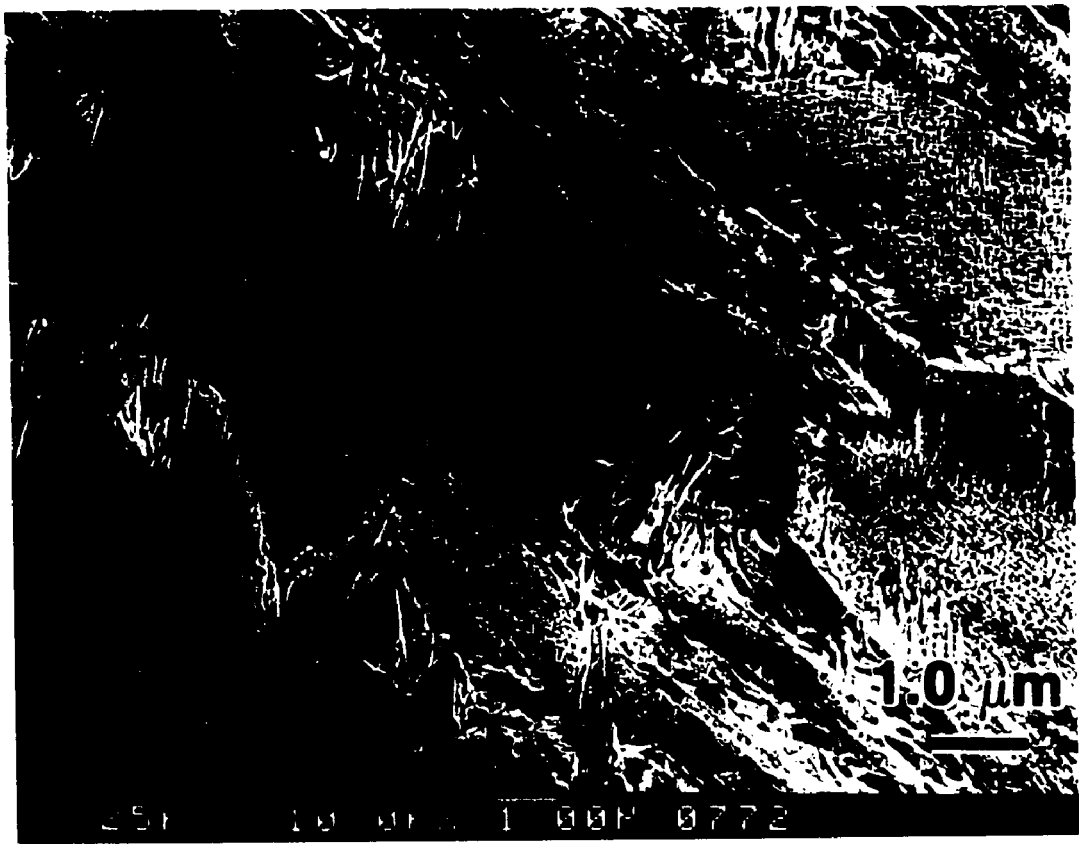

Fig. 4.20 SEM SE image of a decomposed martensite region near CT2/BP boundary of Carlton. JEOL840F 10kV.

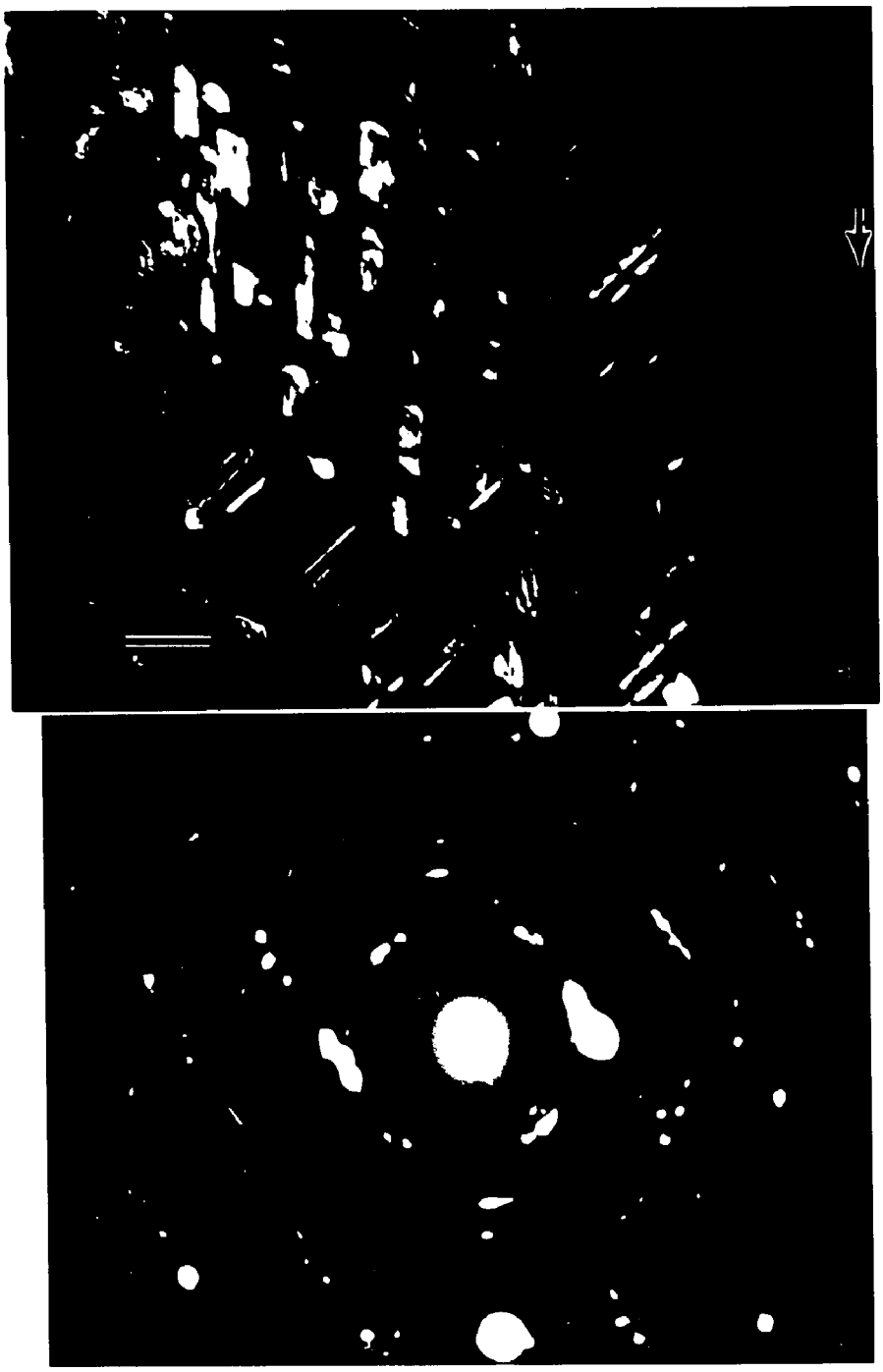

Fig. 4.21 a) TEM CDF image of $(111)_{fcc}$ diffraction spot of the precipitate phase showing the intragranular precipitates in CT2/BP boundary region. b) SAD pattern from the same area, very weak ordering spots can be seen as indicated by the arrow.

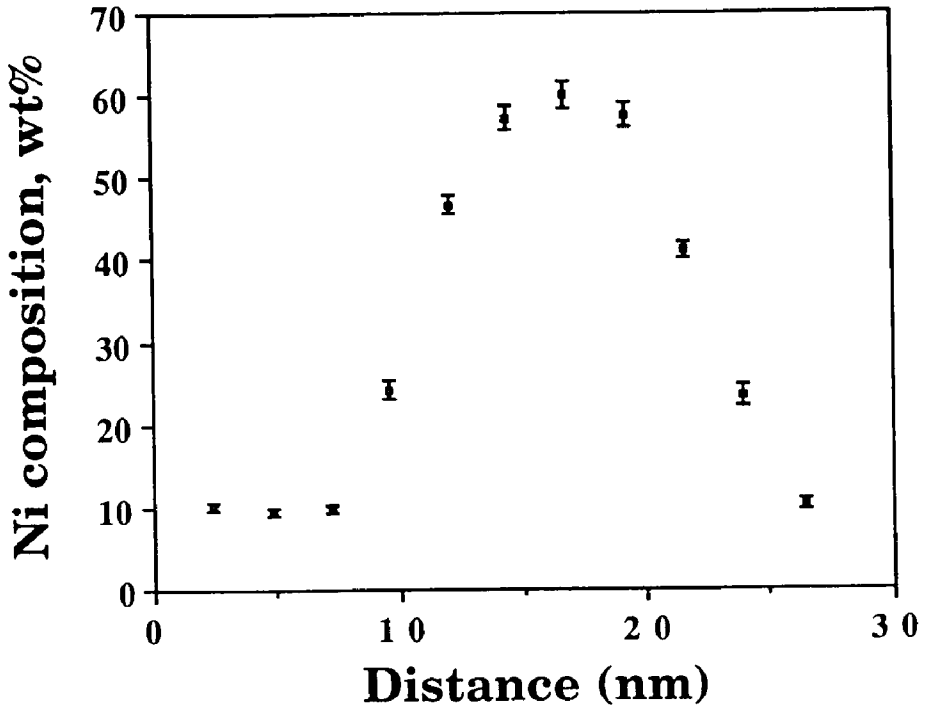

Fig. 4.22 EDS Ni composition profile across an intragranular precipitate in an 18 wt% Ni area of Carlton. The precipitate phase is the high Ni phase. HB501.

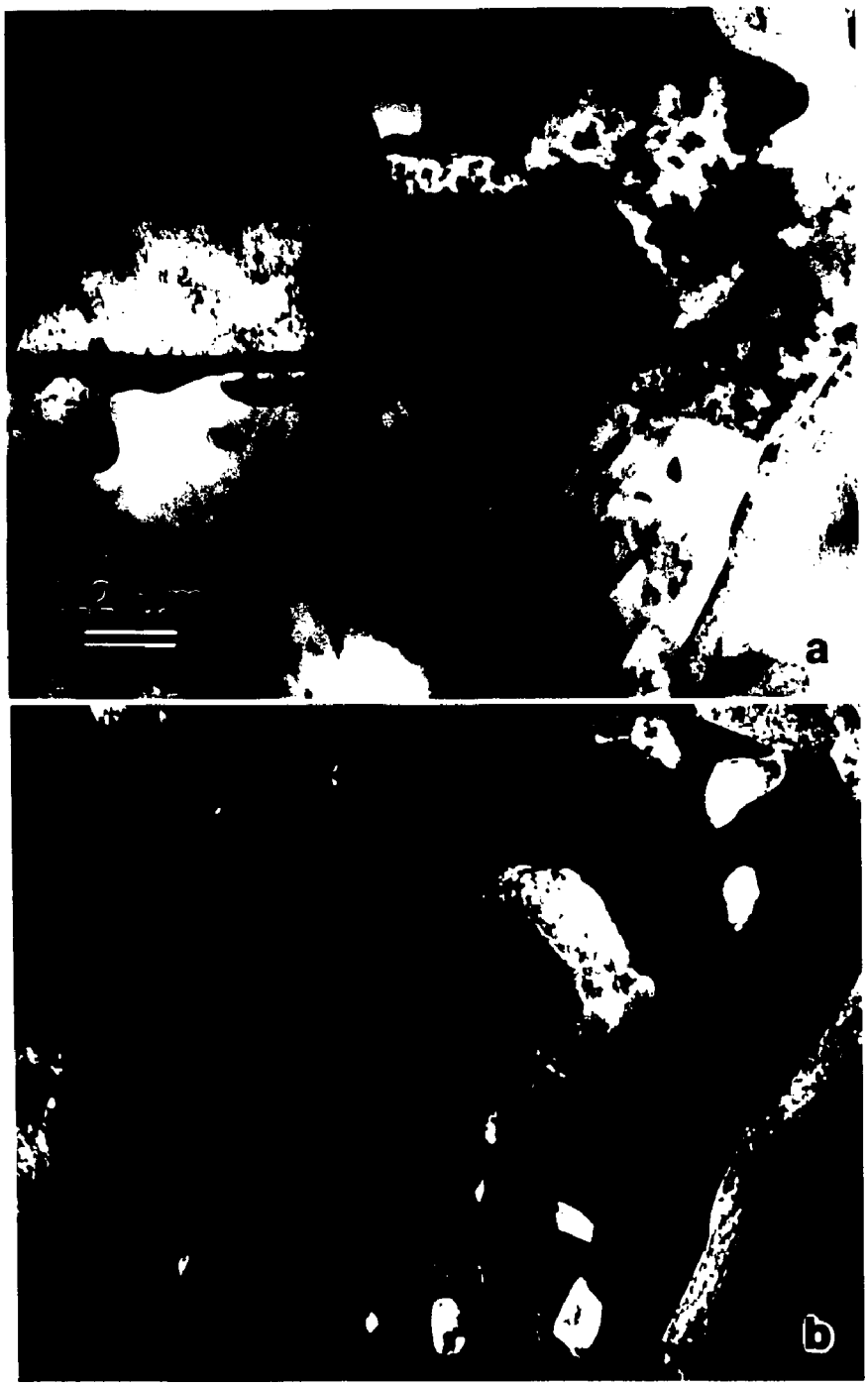

Fig. 4.23 TEM BF (a) and CDF (b) image of an α precipitate in a low Ni plessite region of Carlton. The bright regions in (b) are the fcc γ phase.

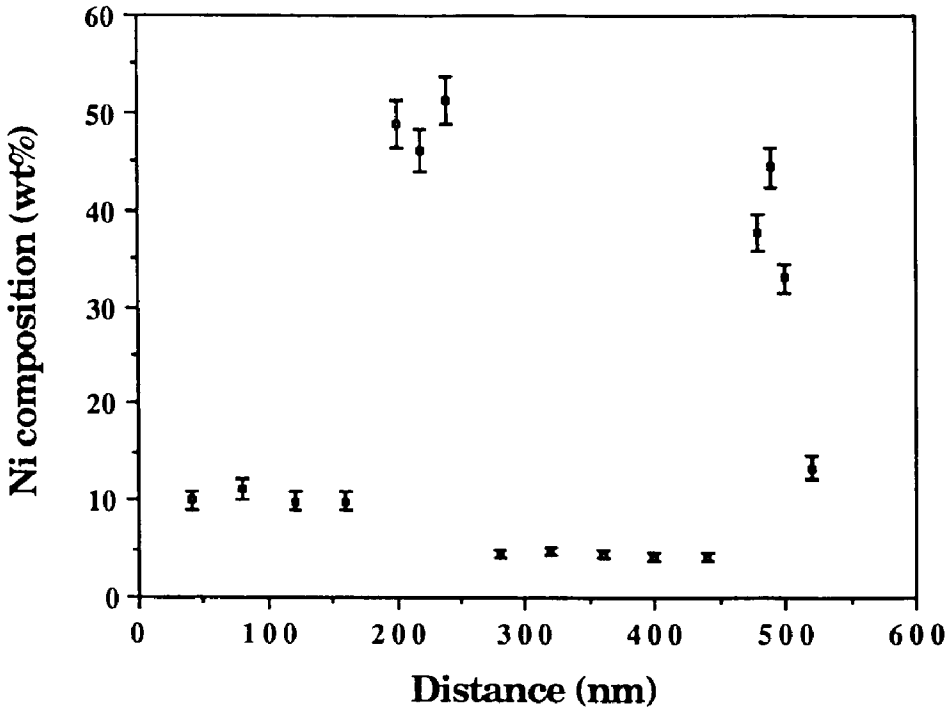

Fig. 4.24 EDS Ni composition profile across the α precipitate in Fig. 4.23. The precipitate phase is the high Ni phase. EM400T.

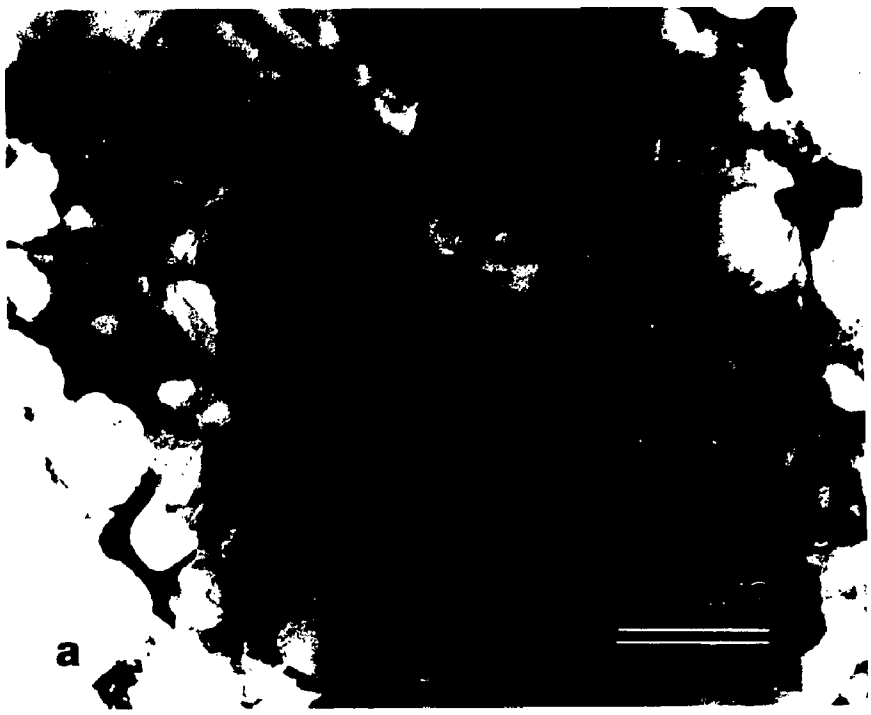

Fig. 4.25 a) TEM BF image of a CZ region of Carlton. b) SAD pattern of the CZ region showing the ordering and the orientation relationship. c) the indexing of the SAD pattern. ⊙ (hkl): fcc [110] zone axis pattern; • hkl: bcc[111] zone axis pattern; * : another bcc[111] zone axis pattern which is in a twinning orientation with respect to the first bcc[111] pattern, the twinning plane is $(002)_{fcc}$; ★ superlattice diffraction spots due to the ordering of the fcc phase, tetrataenite.

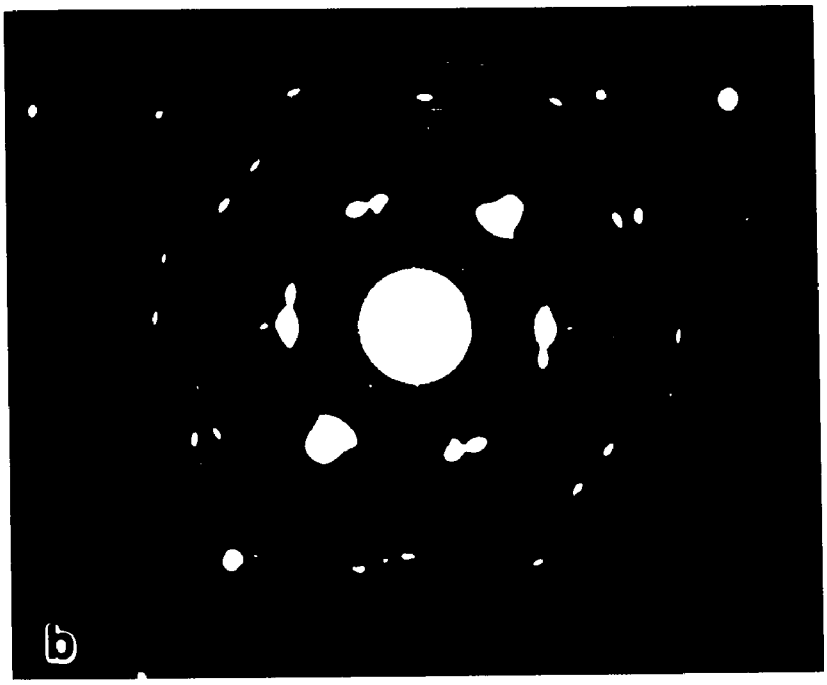

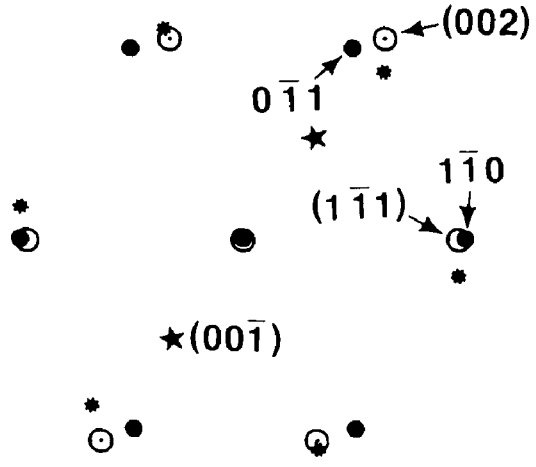

c

Fig. 4.26 BSE image of a polished and unetched section of the BM#52283 sample of Santa Catharina meteorite.

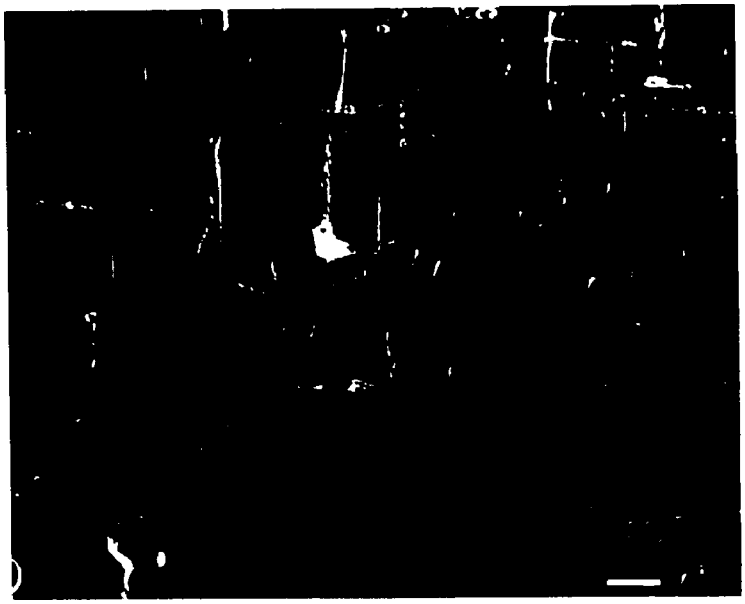

Fig. 4.27 SEM SE image of the polished and etched section of the BM#52283 sample of Santa Catharina. P-rich precipitates which are often associated with small holes are observed.

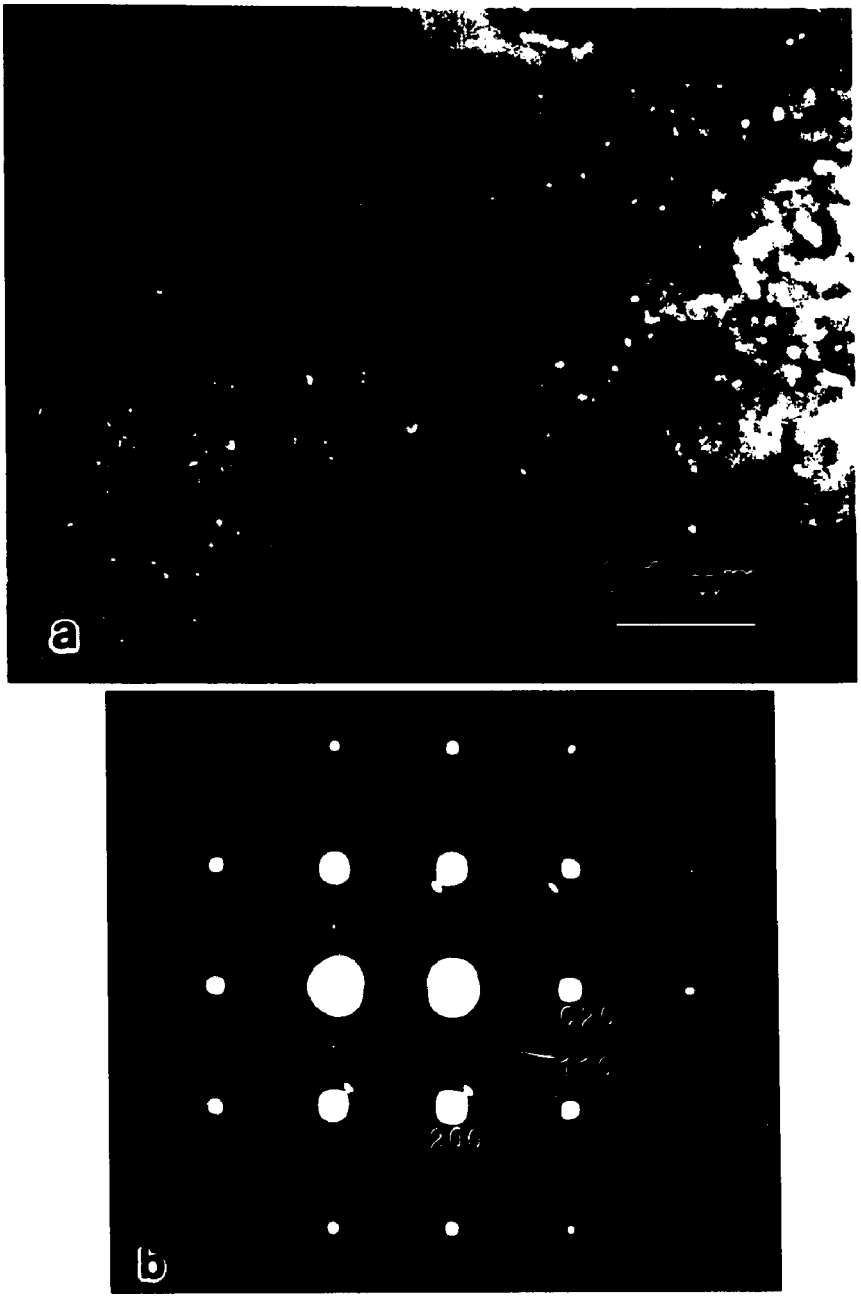

Fig. 4.28 TEM image and diffraction pattern of the BM#52283 sample of Santa Catharina. a) CDF image from a {100} superlattice diffraction spot showing the very small size of the ordered FeNi domains, which appear as bright dots. b) SAD pattern of $<100>_{fcc}$ zone axis showing the superlattice spots due to the ordering.

Fig. 4.29 Optical micrograph of a polished and unetched section of the USNM#3043 sample of Santa Catharina meteorite. p: phosphide.

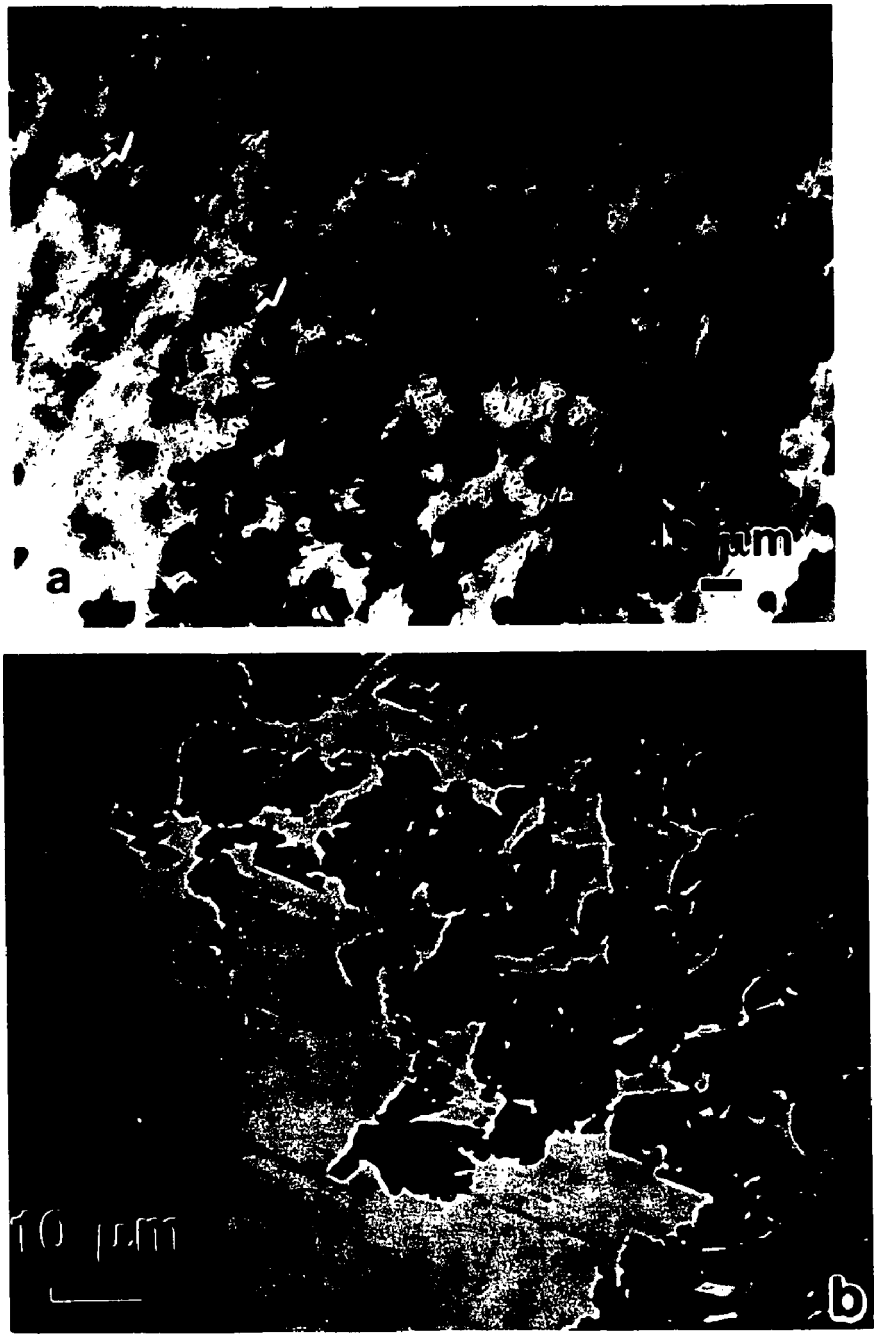

Fig. 4.30 a) Optical micrograph of an etched section of the USNM#3043 sample. The grey areas (indicated by the arrow) in the light regions are similar to the cloudy zone of the octahedrites. b) BSE image of a polished and unetched section of the USNM#3043 sample showing the characteristic dark and light regions.

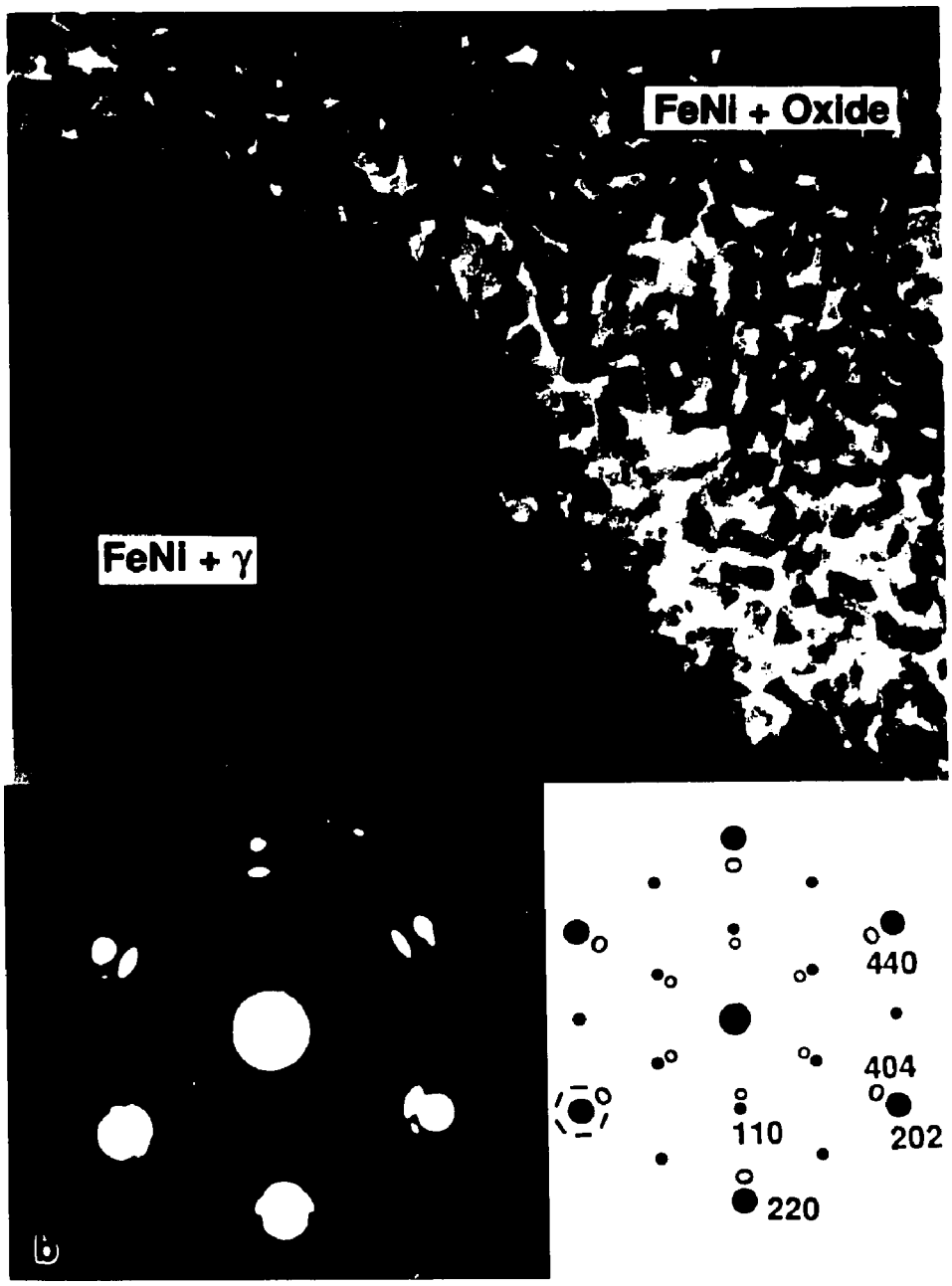

Fig. 4.31 a) TEM bright field image of the USNM#3043 sample showing two different regions, upper right and lower left corresponding to the dark and the light regions in the optical micrograph (Fig. 4.29) and the BSE image (Fig. 4.30b) respectively. b) SAD pattern from the upper right region in (a) and an indexing of major diffraction spots. ● $[-1,1,1]_{fcc}$ zone, ordered FeNi, • superlattice diffraction of FeNi. ○ o $[-1,1,1]_{fcc}$, Fe_2NiO_4 or Fe_3O_4. / double diffraction (only shown around one major diffraction spot). c) and d) CDF images of $(220)_{FeNi}$ (tetrataenite island phase) and $(440)_{oxide}$ (oxide honeycomb) diffraction spots.

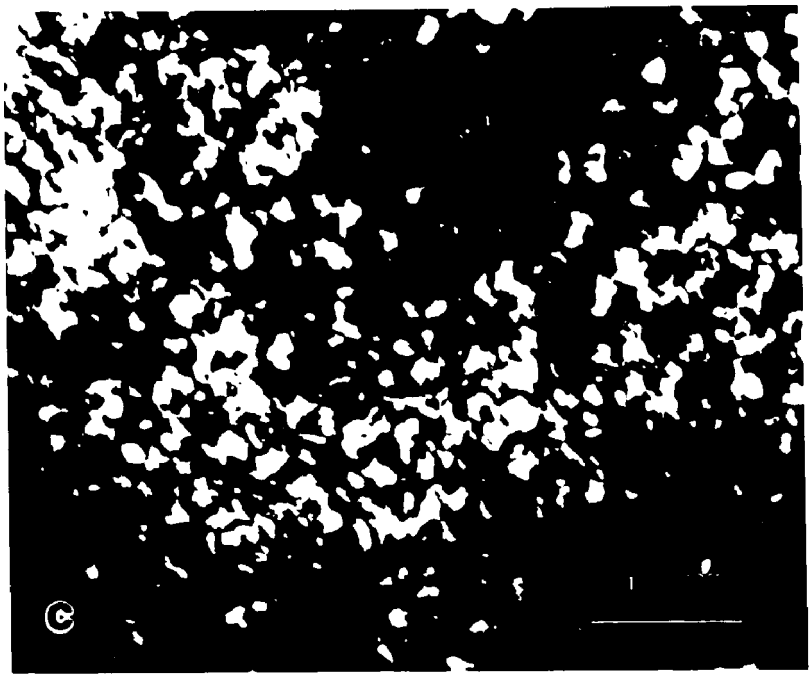
c

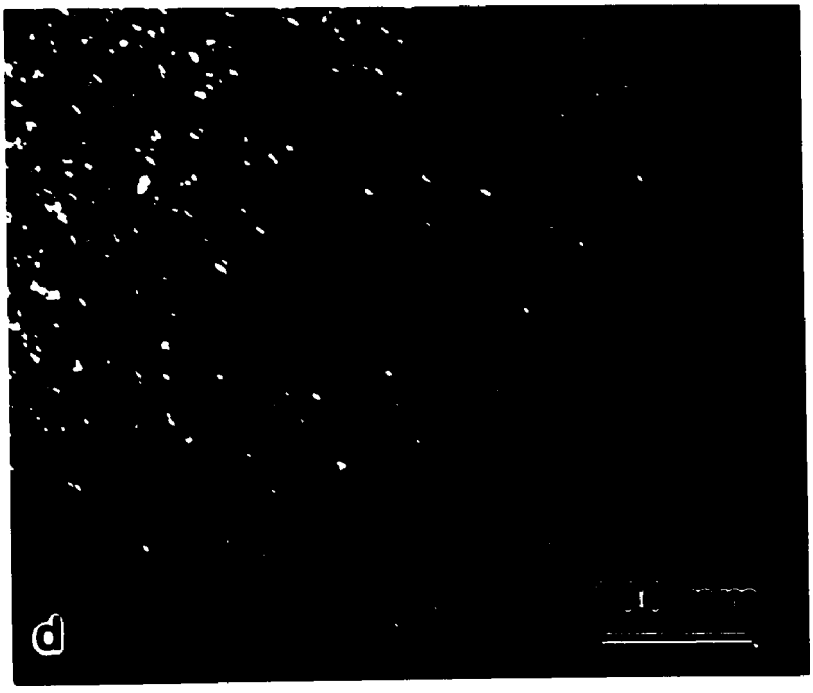
d

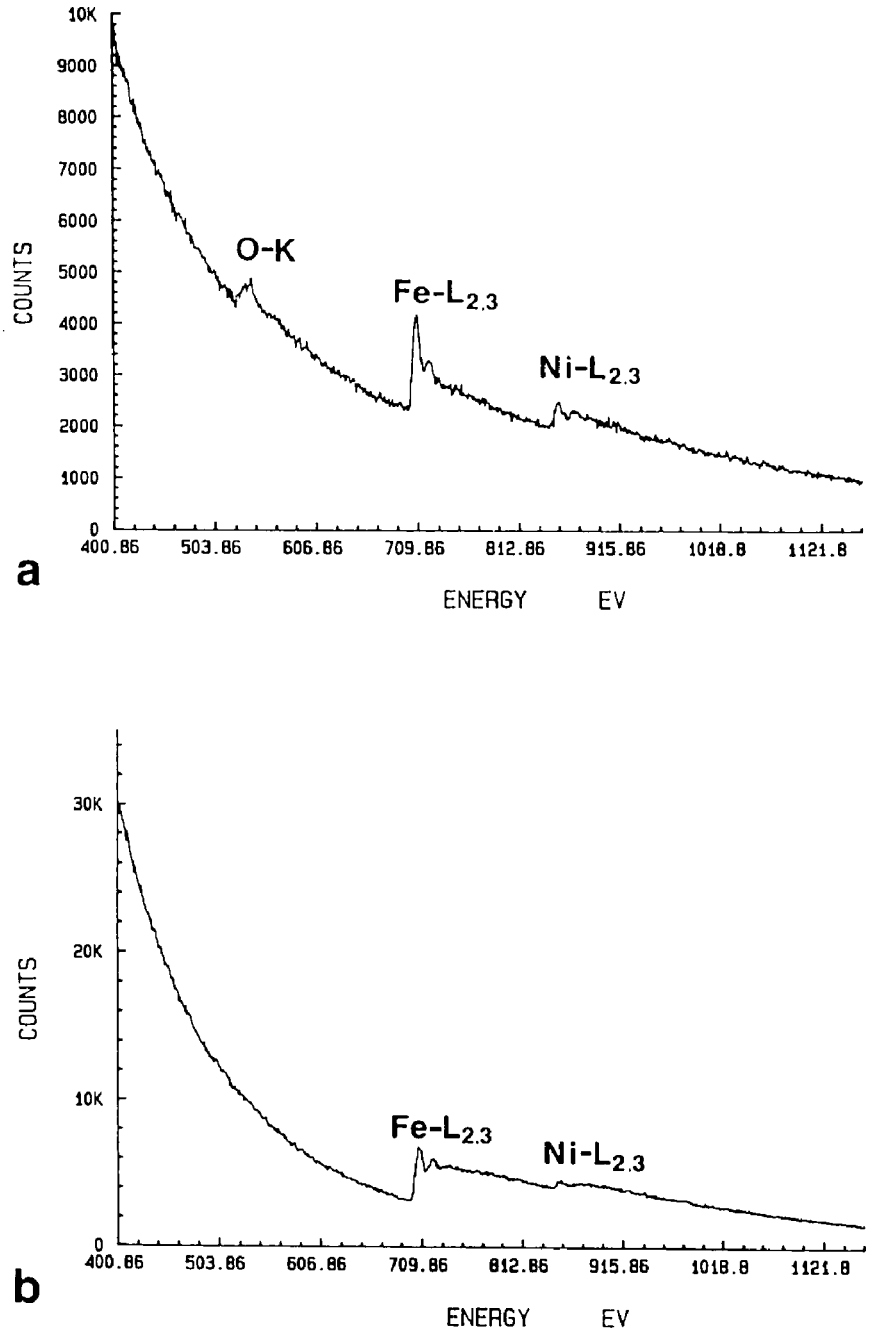

Fig. 4.32 EELS spectra of the USNM#3043 sample taken from a) FeNi+Oxide region and b) Fe+γ region in Fig. 4.31a.

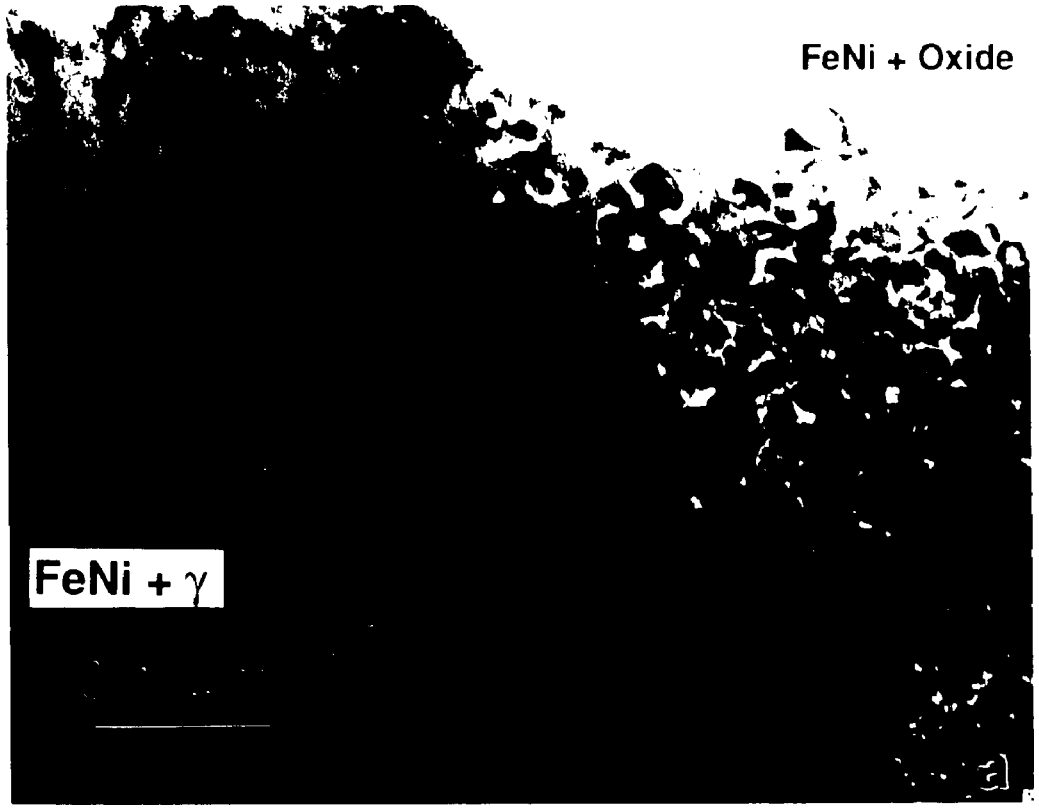

Fig. 4.33 a) TEM BF image of the USNM#3043 sample. A cloudy zone-like structure in the non-oxidized region labelled FeNi+γ is observed. b) and c) $<110>_{fcc}$ zone axis electron diffraction patterns taken from non-oxidized (light regions in the BSE image) and oxidized (dark in the BSE image) regions showing the presence of ordered FeNi in both type of regions.

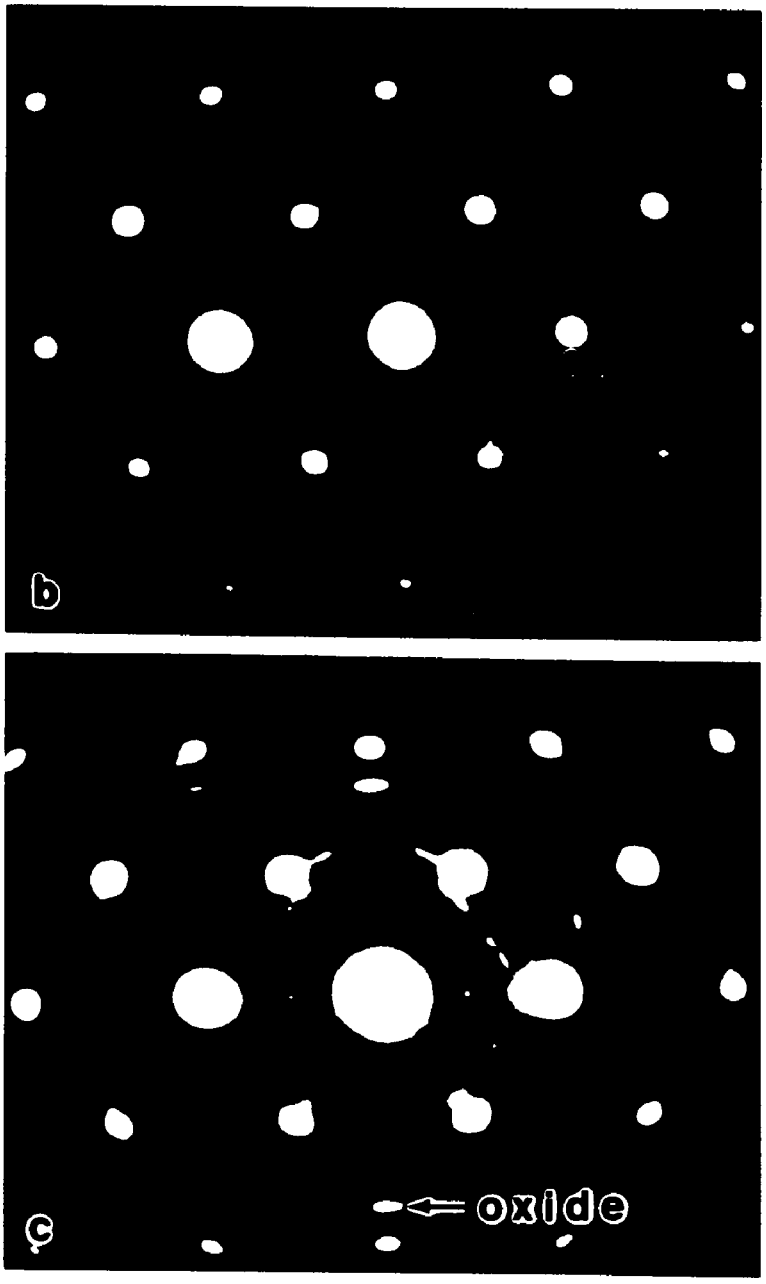
b
c
oxide

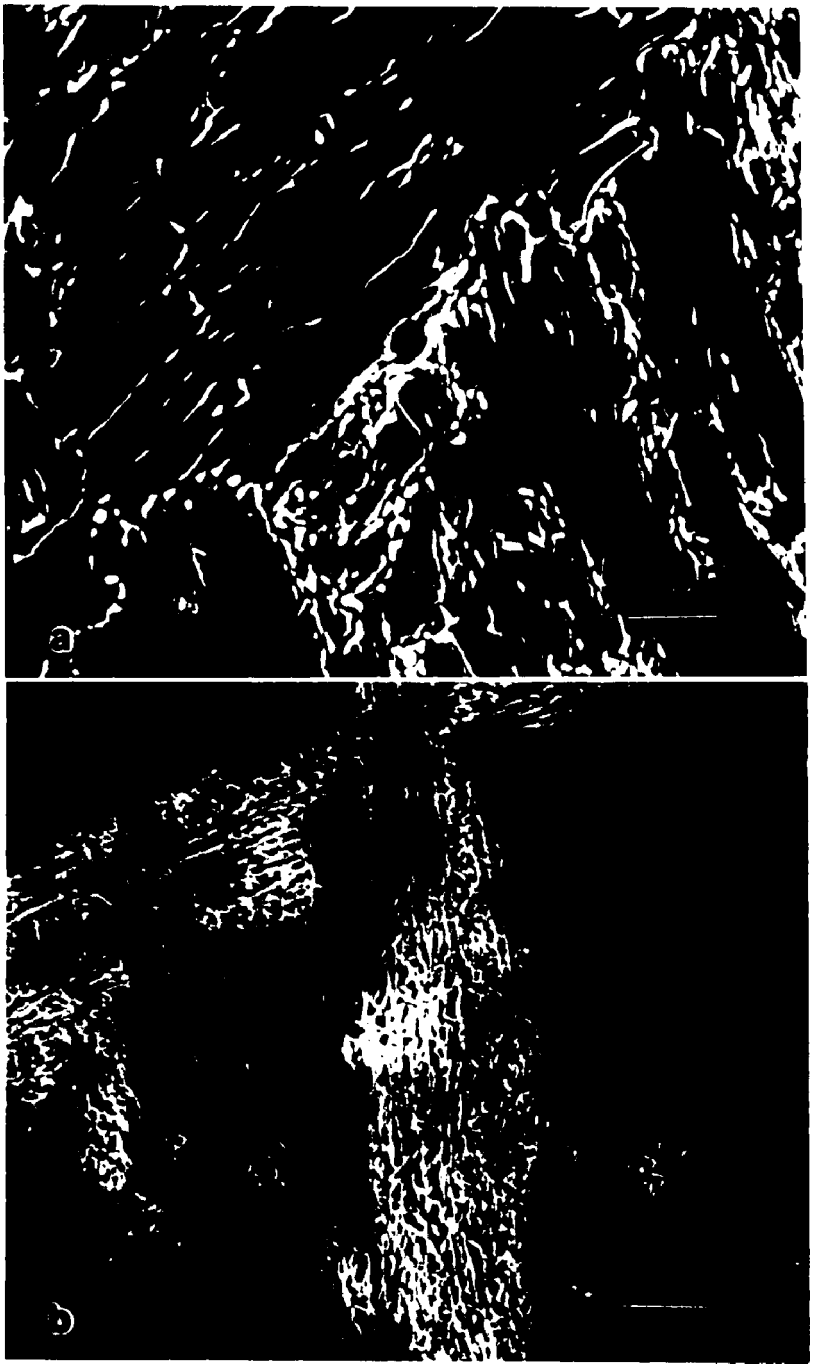

Fig. 4.34 SEM SE images of decomposed martensite alloys. a) 450FN15 alloy, arrow points out the typical contrast of precipitate phase. b) 450FN25, the precipitate phase is the one which is less etched. ETEC 20kV.

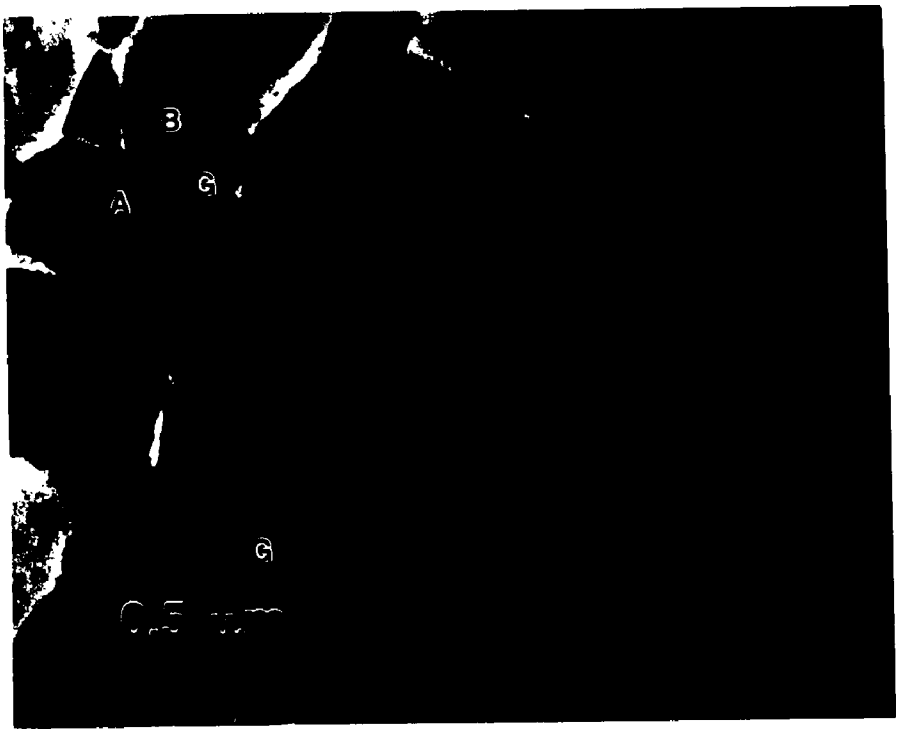

Fig. 4.35 TEM BF image of 450FN15 alloy, G: γ precipitate.

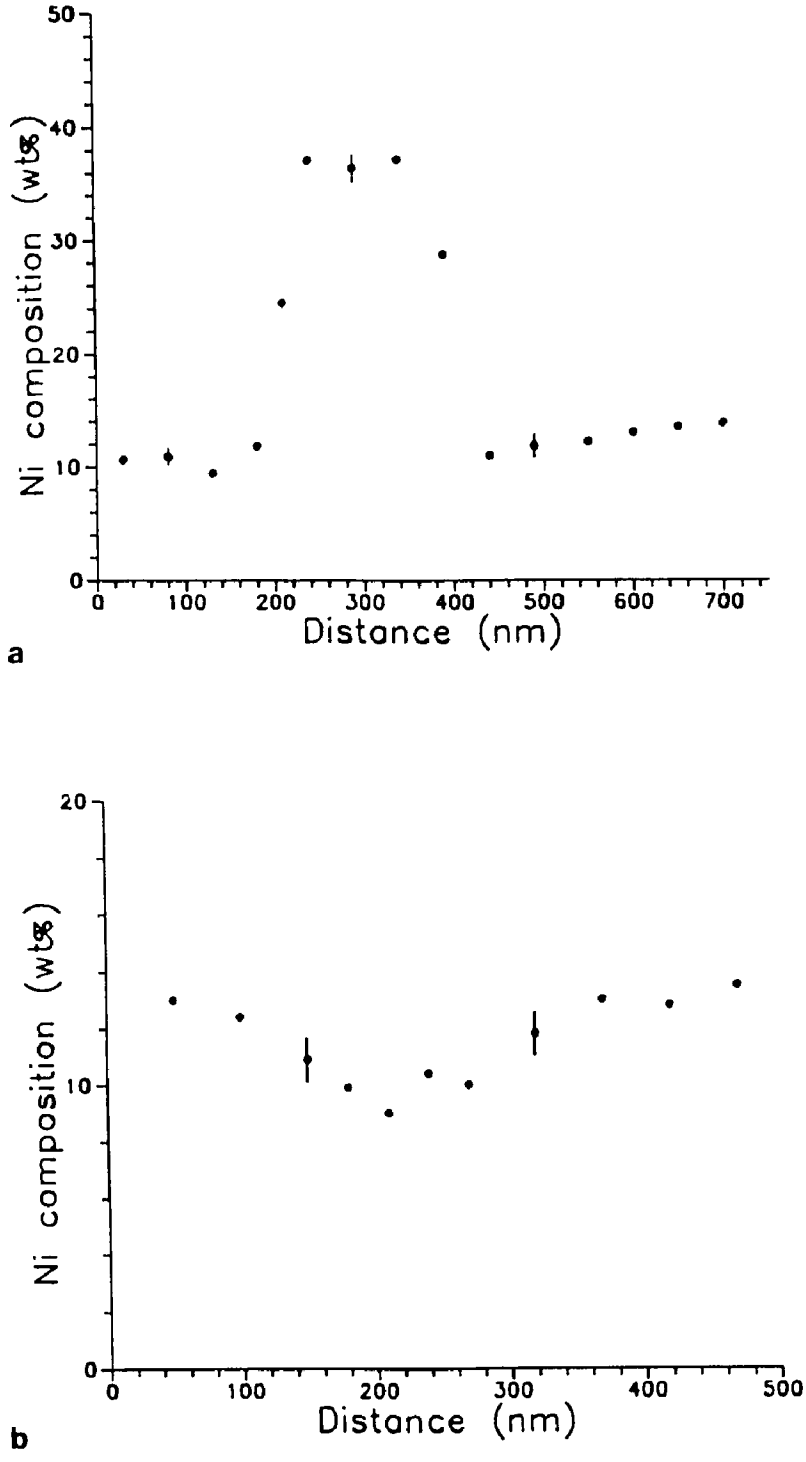

Fig. 4.36 EDS Ni composition profiles. a) Across a precipitate, the precipitate phase is the high Ni phase. b) Across a grain boundary along A-B shown in Fig. 4.35. EM400T.

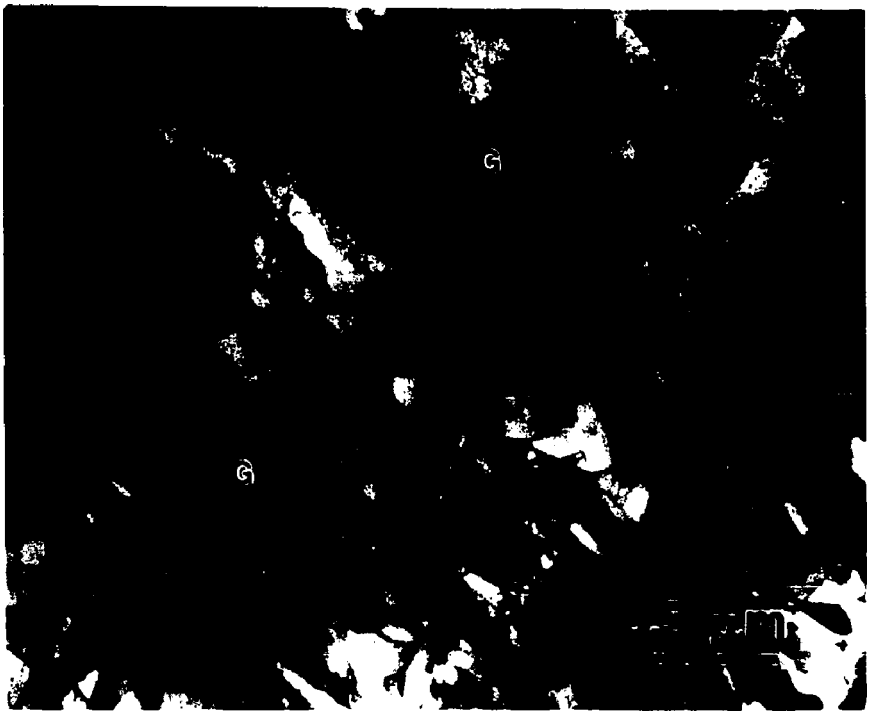

Fig. 4.37 TEM BF image of 450FN25 alloy, G: γ precipitate.

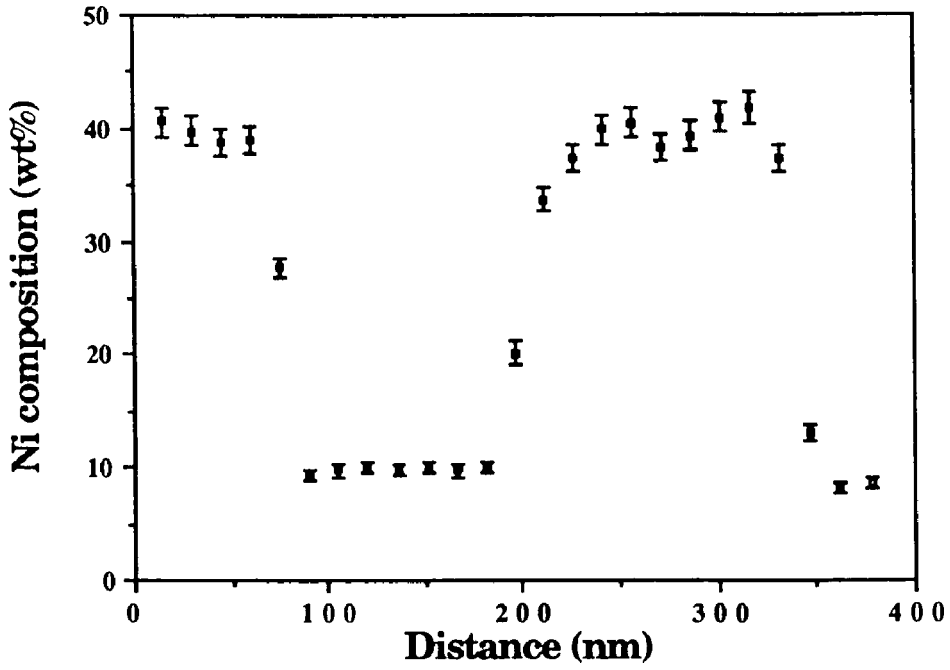

Fig. 4.38 EDS Ni composition profile of 450FN25 alloy. The precipitate phase is the high Ni phase. EM430T.

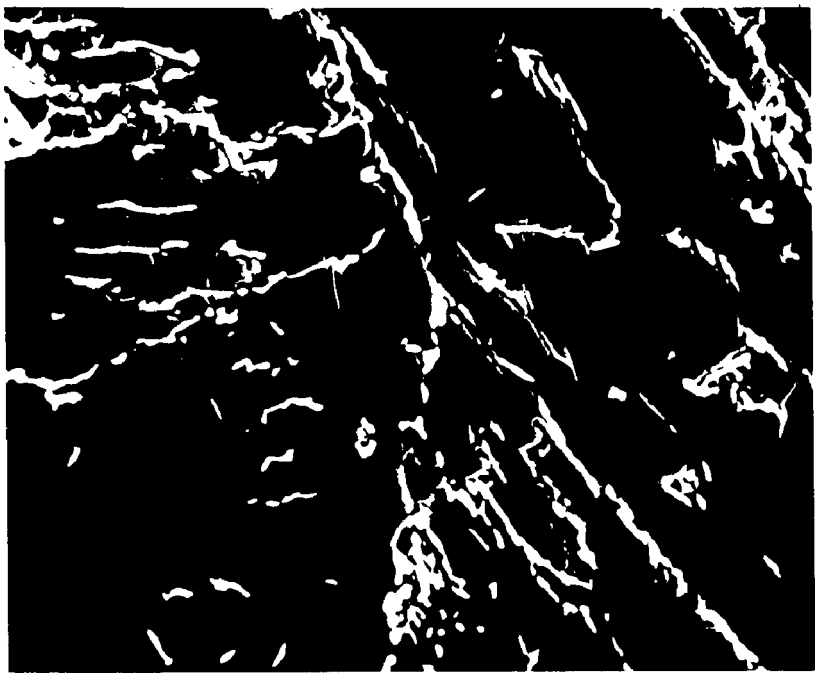

Fig. 4.39 SEM SE image of 450FNP15. ETEC 20kV.

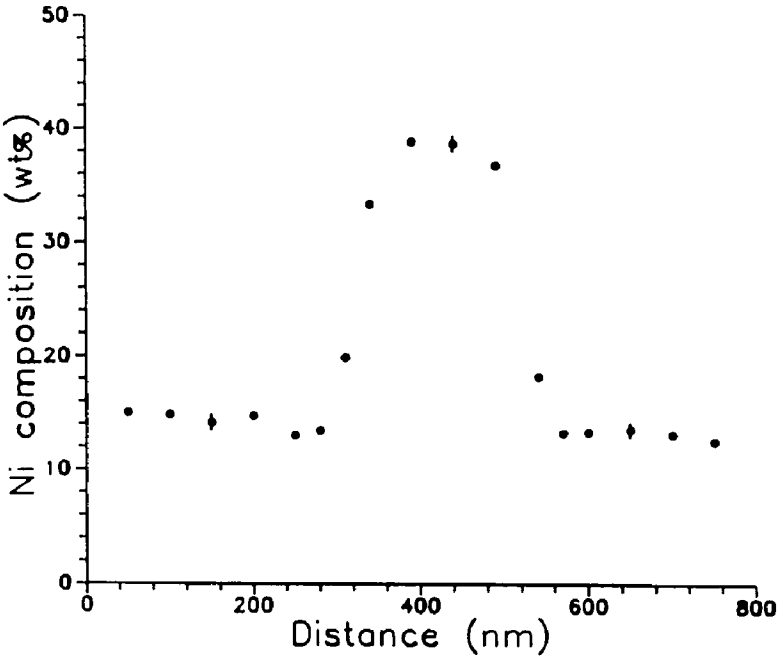

Fig. 4.40 EDS Ni composition profile of a γ precipitate in 450FNP15. EM400T.

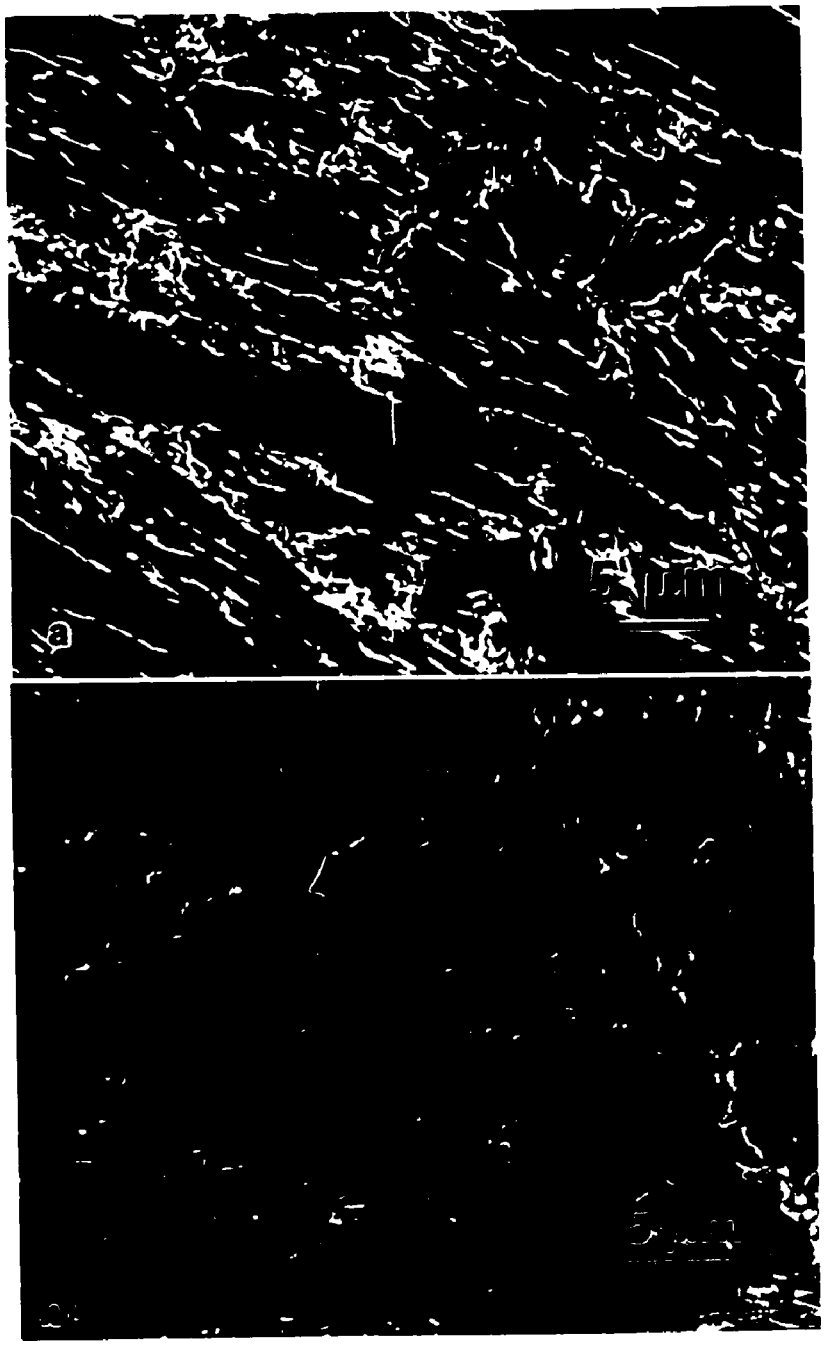

Fig. 4.41 SEM SE images of alloys heat treated at 400°C. a) 400FN15; b) 400FNP15; c) 400FN25; d) 400FNP25; e) 400FN30; f) 400FNP30. A typical precipitate is indicated by an arrow in the two 15 wt% Ni alloys. The precipitate phase is the less etched phase in the 25 wt% and the 30 wt% Ni alloys. A: retained austenite. a) to d), ETEC 20kV. e) and f), JEOL840F.

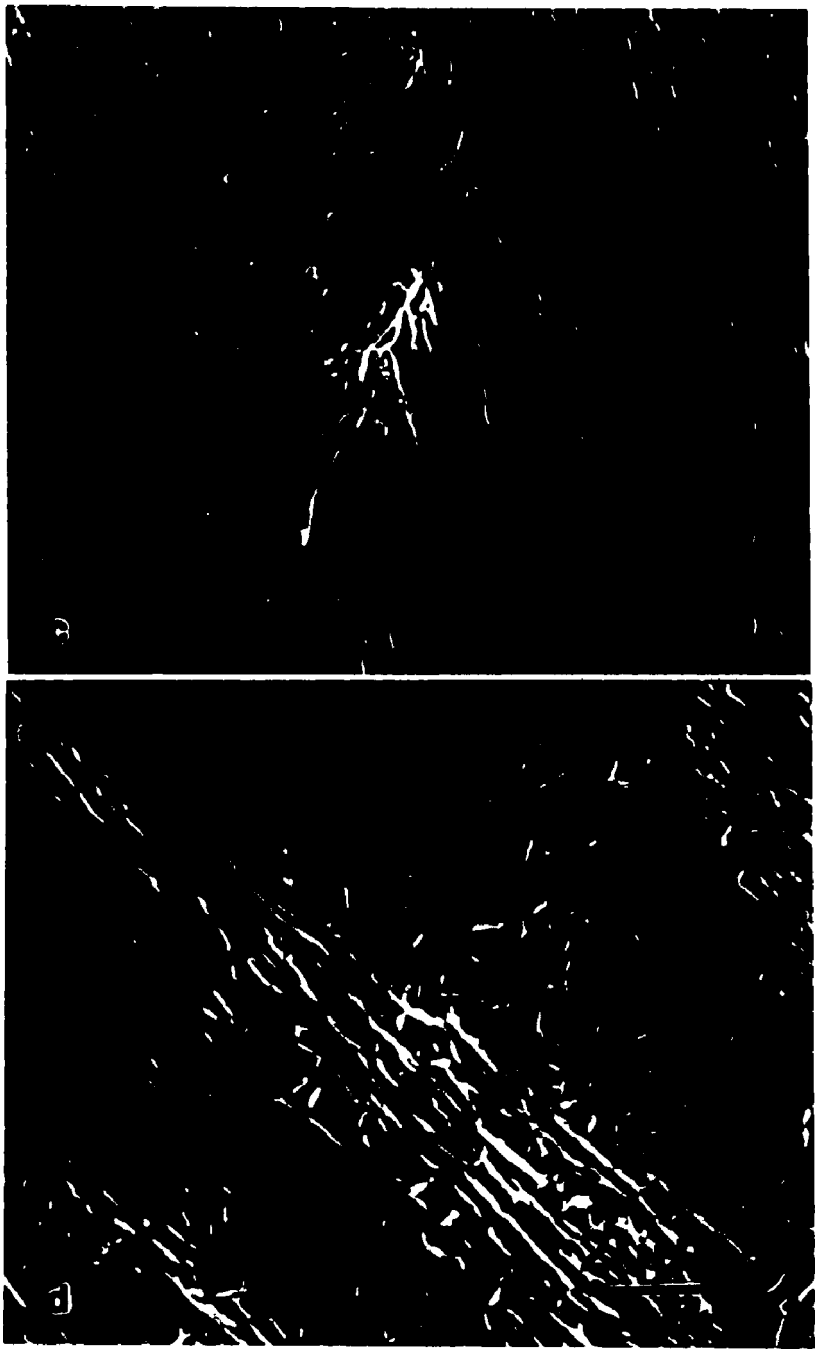

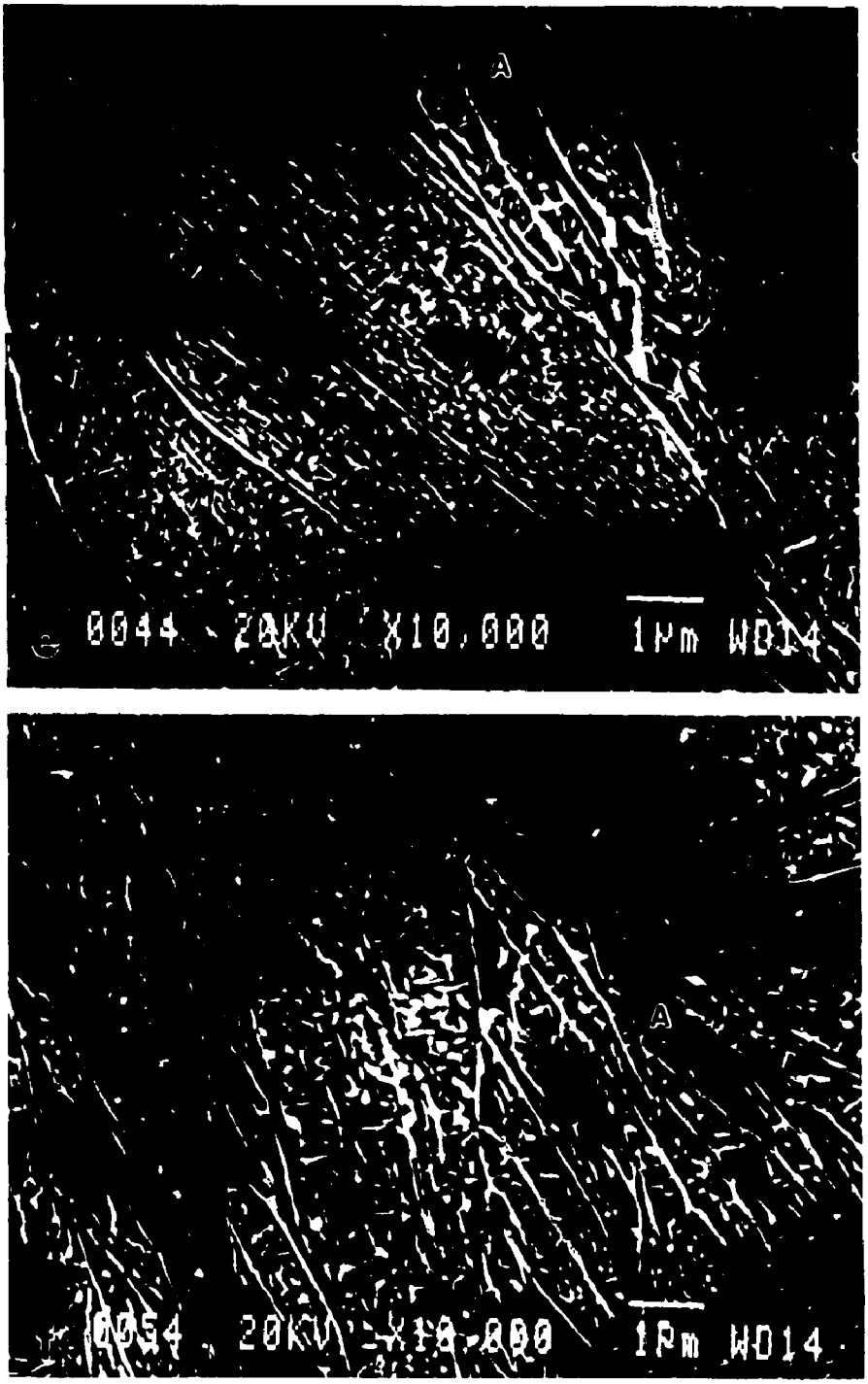
A
0044 20KV X10,000 1μm WD14
A
0054 20KV X10,000 1μm WD14

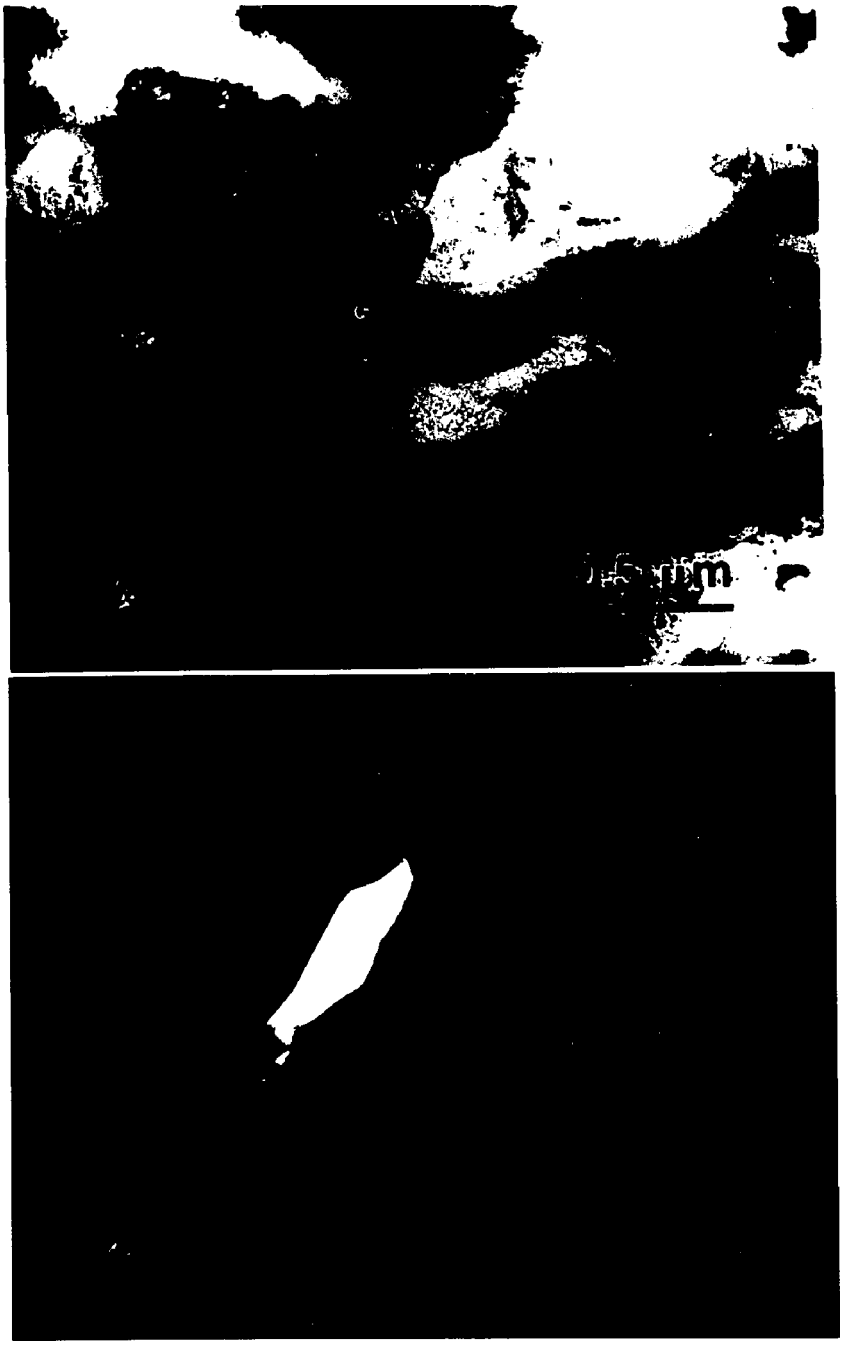

Fig. 4.42 TEM images of the 400FN15 alloy. a) BF image; b) CDF image from an fcc (200) diffraction spot.

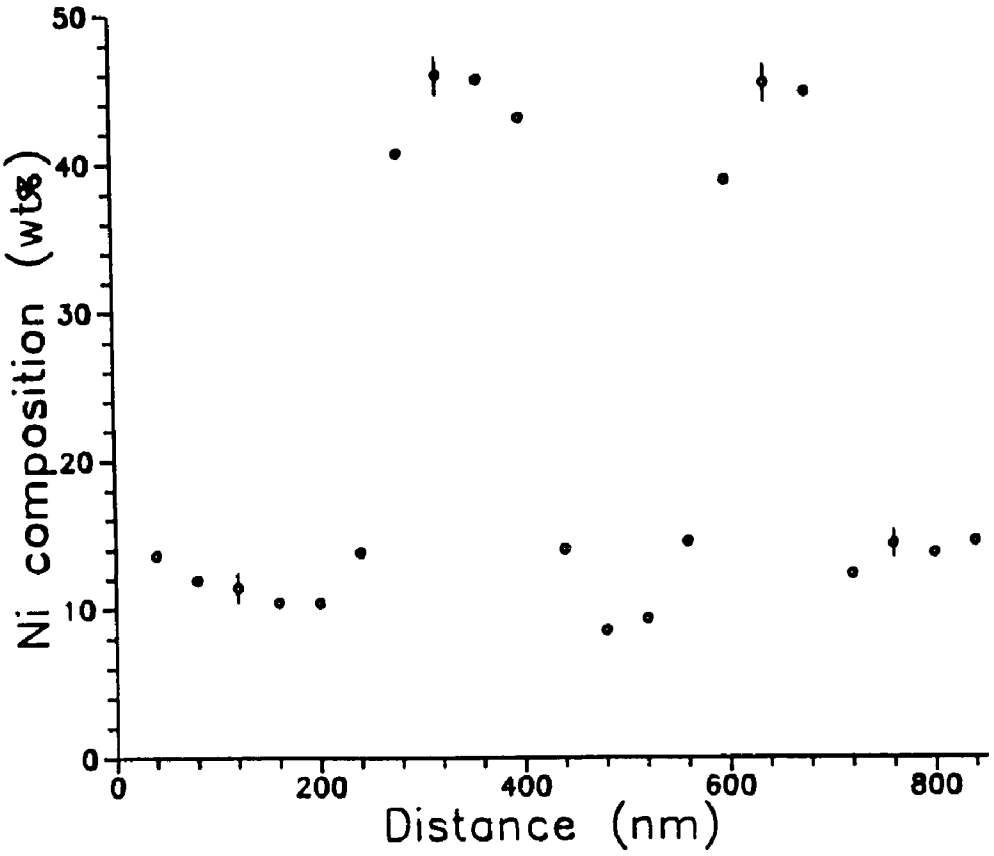

Fig. 4.43 EDS Ni composition profile across a precipitate (high Ni) in the 400FN15. EM400T.

Fig. 4.44 TEM BF image of the 400FN25 alloy. G:γ precipitate.

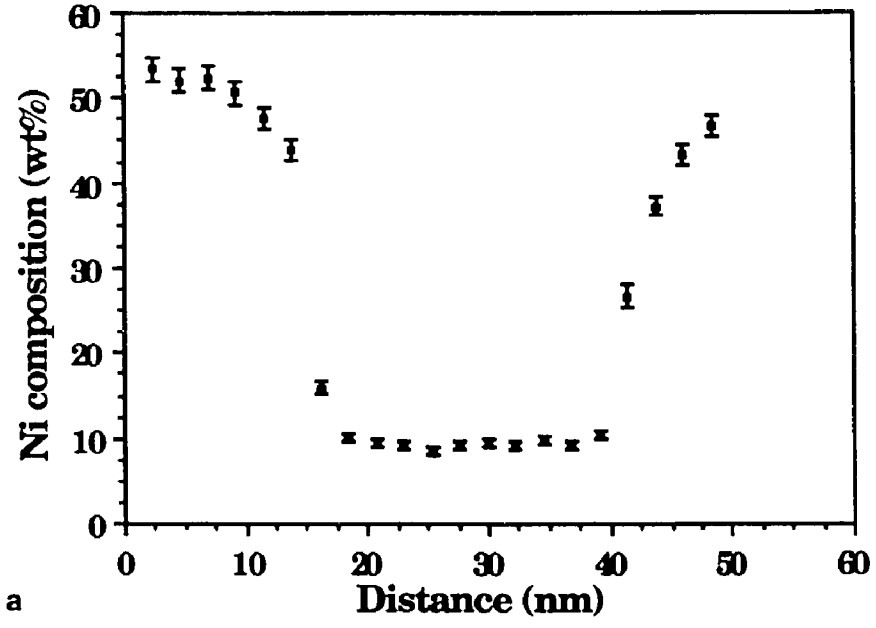

Fig. 4.45 EDS Ni composition profiles of the 400FN25 alloy. The precipitate phase is the high Ni phase. a) and b) measured using the HB501; c) measured using the EM400T.

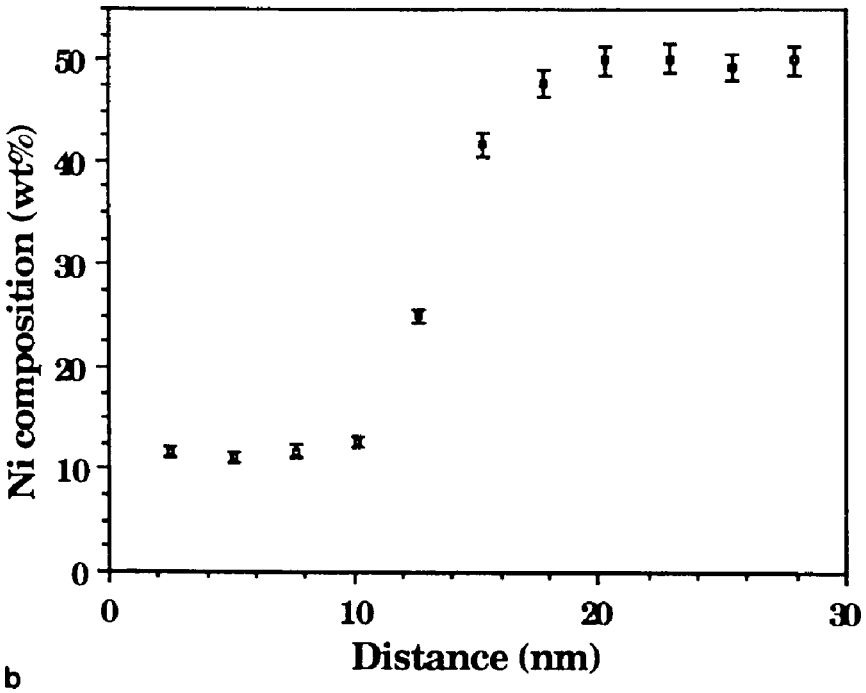
Ni composition (wt%)
0
10
20
30
40
50
0
10
20
30
Distance (nm)

b

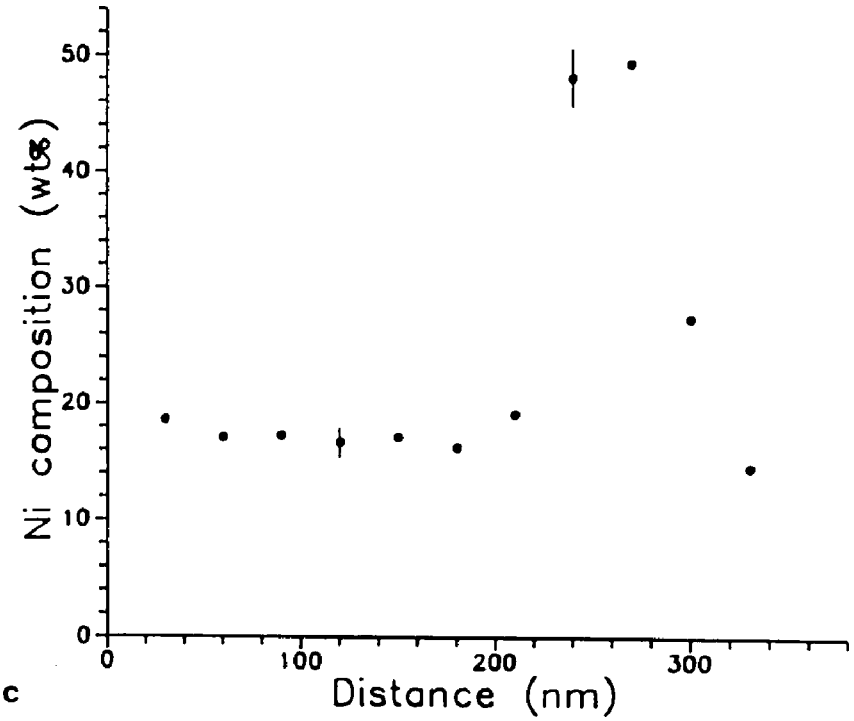
Ni composition (wt%)
0
10
20
30
40
50
0
100
200
300
Distance (nm)

c

Fig. 4.46 TEM BF image of the 400FN30 alloy. G: γ precipitate.

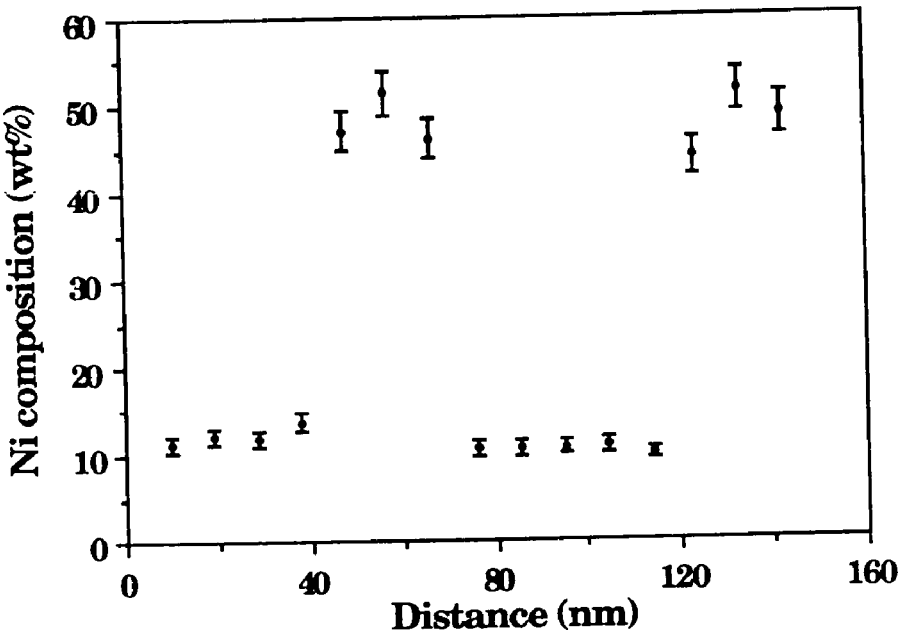

Fig. 4.47 EDS Ni composition profile of the 400FN30 alloy. The precipitate phase is the high Ni phase. EM430T.

Fig. 4.48 TEM BF image and diffraction pattern of a phosphide in the 400FNP15 alloy. a) BF image; b) SAD pattern of $(Fe,Ni)_3P$ tetragonal [1,-1,-1] zone, zero order Laue zone. c) CBED FOLZ ring.

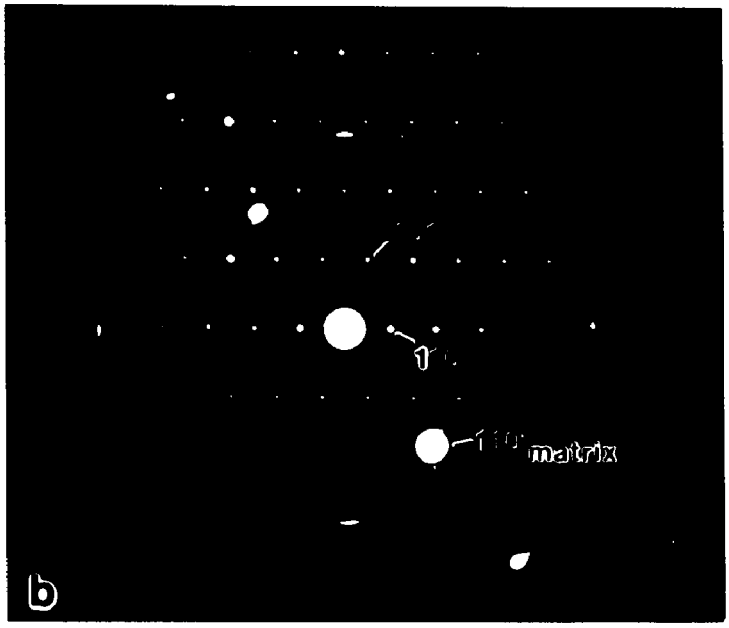
matrix
b


a

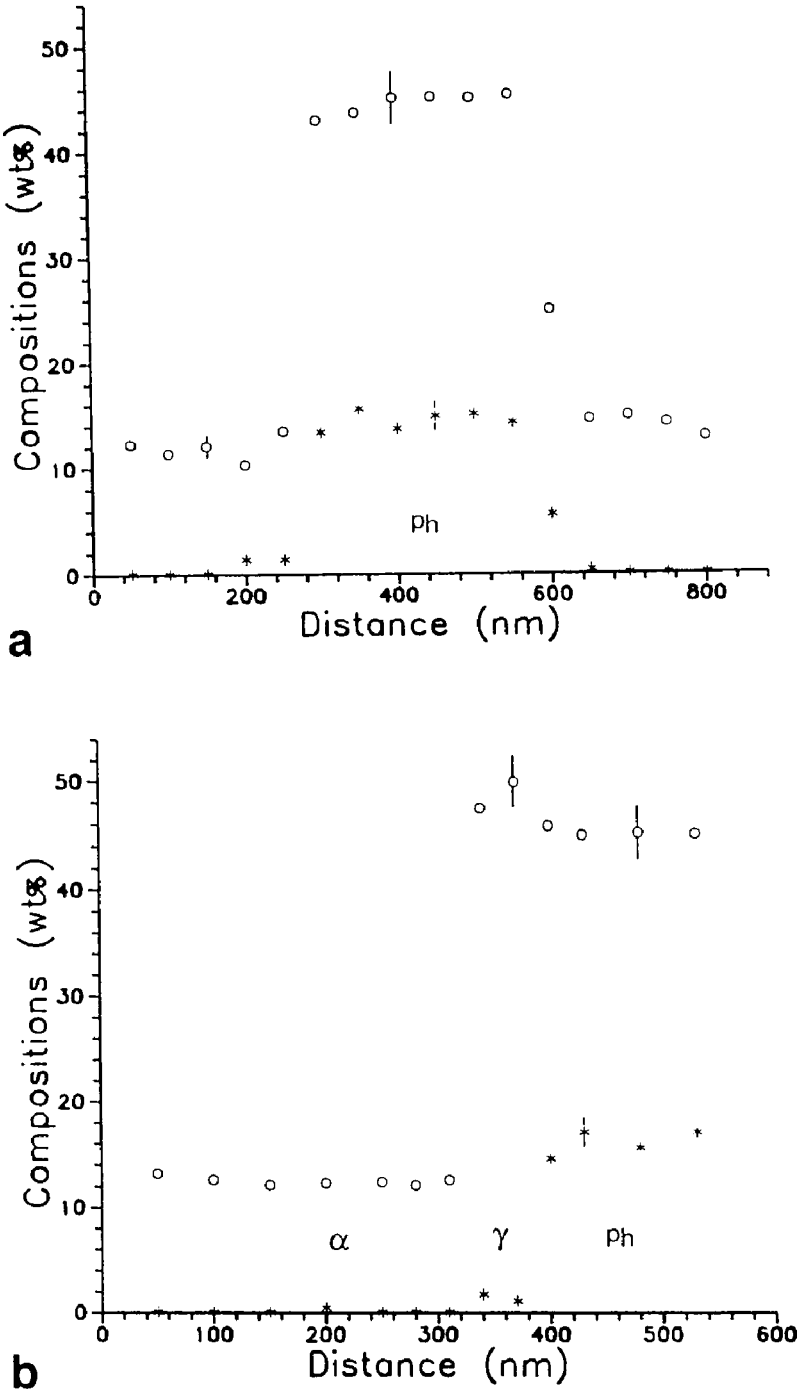

Fig. 4.49 a) EDS composition profiles of the phosphide in the 400FNP15 alloy. * : P; o : Ni. b) EDS composition profiles of α/γ/Ph. EM400T.

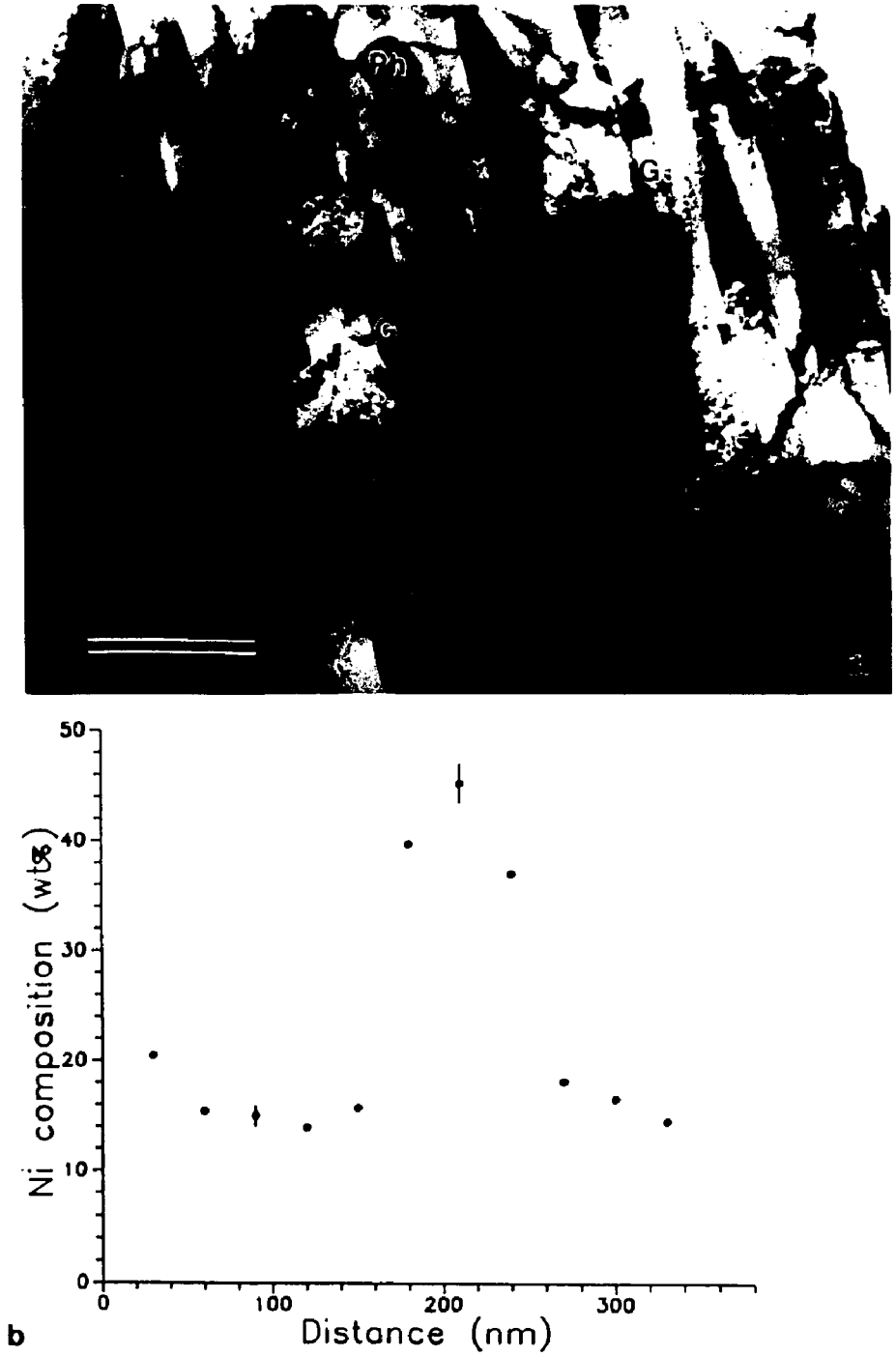

Fig. 4.50 a) TEM BF image of the 400FNP25 alloy. G: γ precipitate. Ph: phosphide. b) Ni composition profile of across a γ precipitate in this alloy.

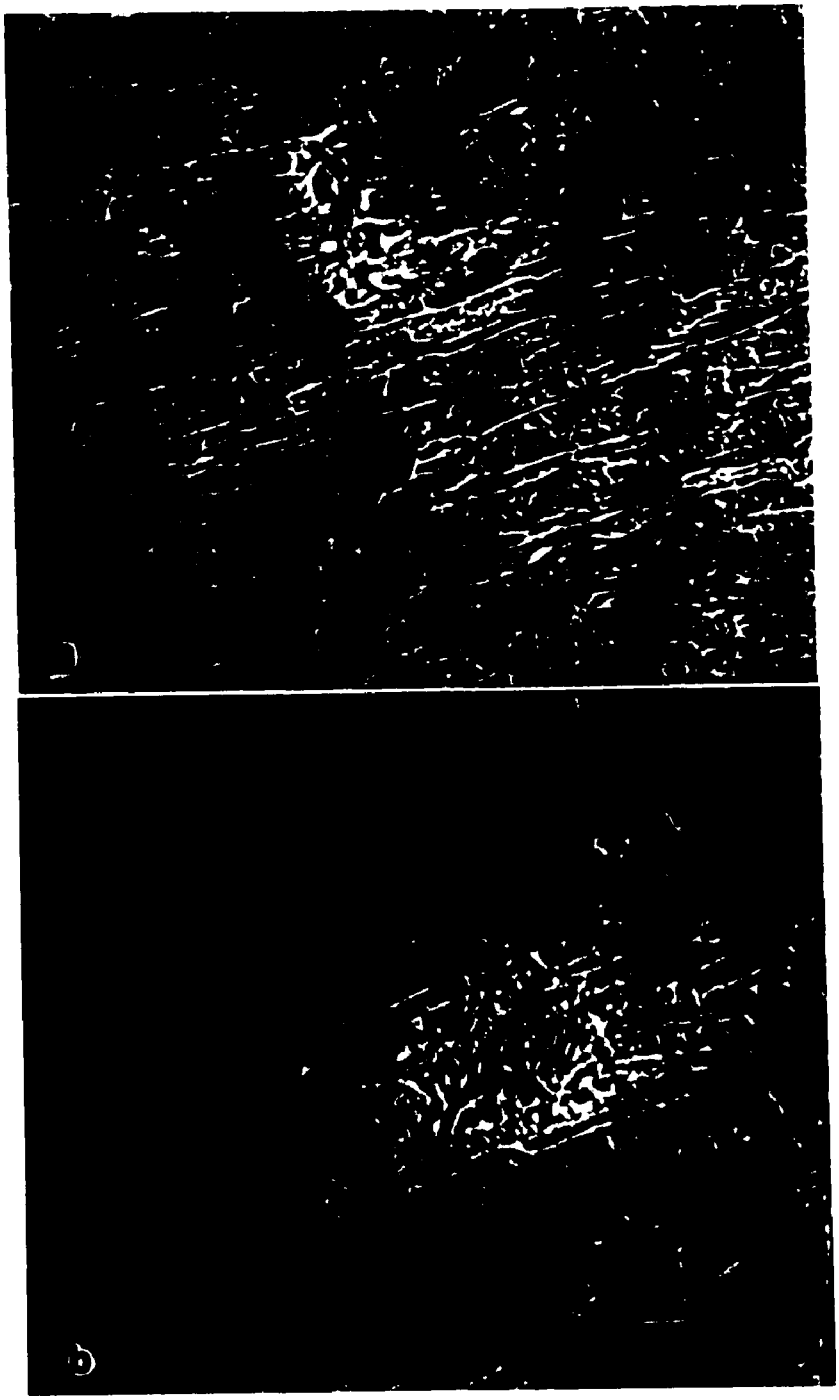

Fig. 4.51 SEM SE images of alloys heat treated at 370°C. a) 370FN25; b) 370FNP25. ETEC 20kV.

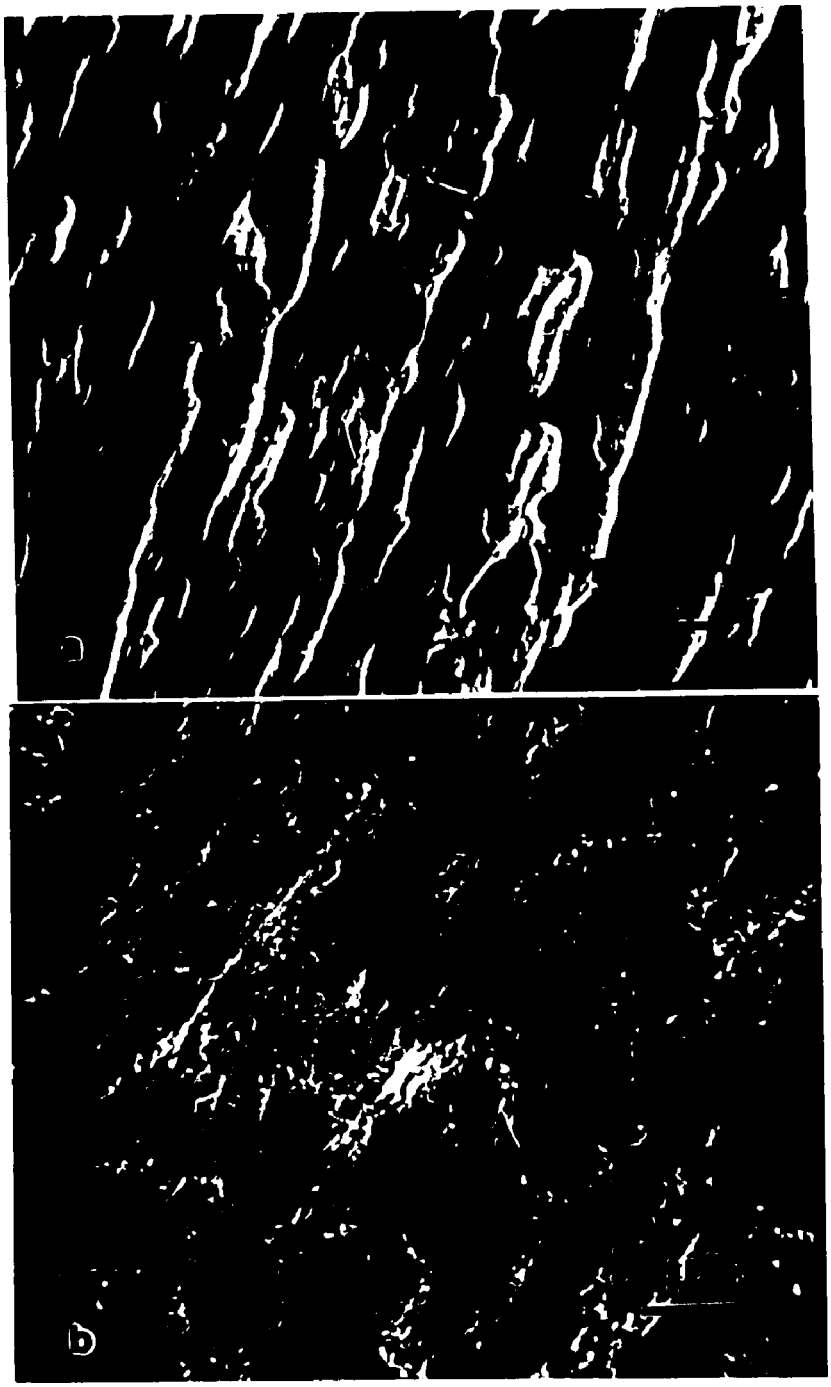

Fig. 4.52 SEM SE images of alloys heat treated at 350°C. a) 350FN15; b) 350FNP15; c) 350FN30; d) 350FNP30. A: austenite. ETEC 20kV.

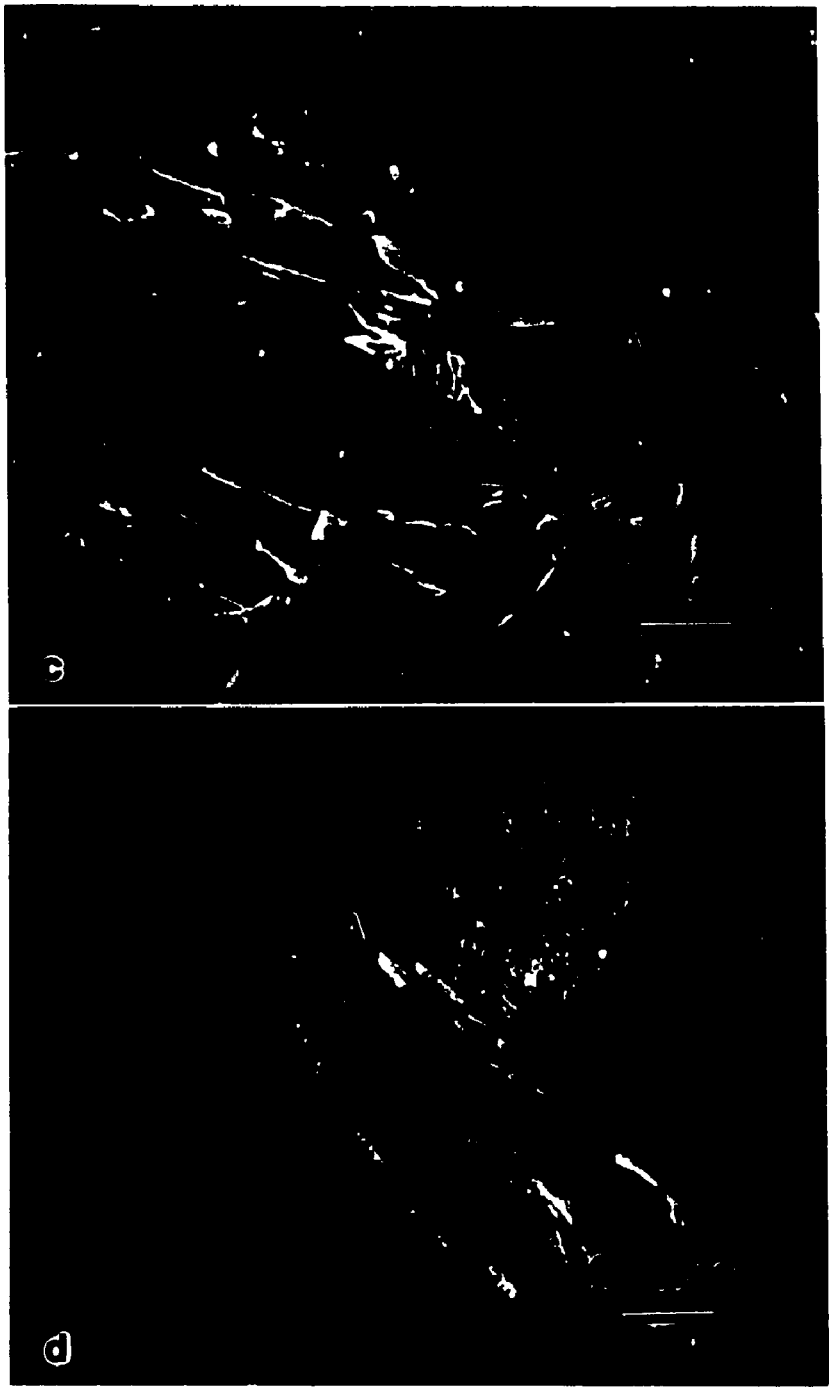
c
d

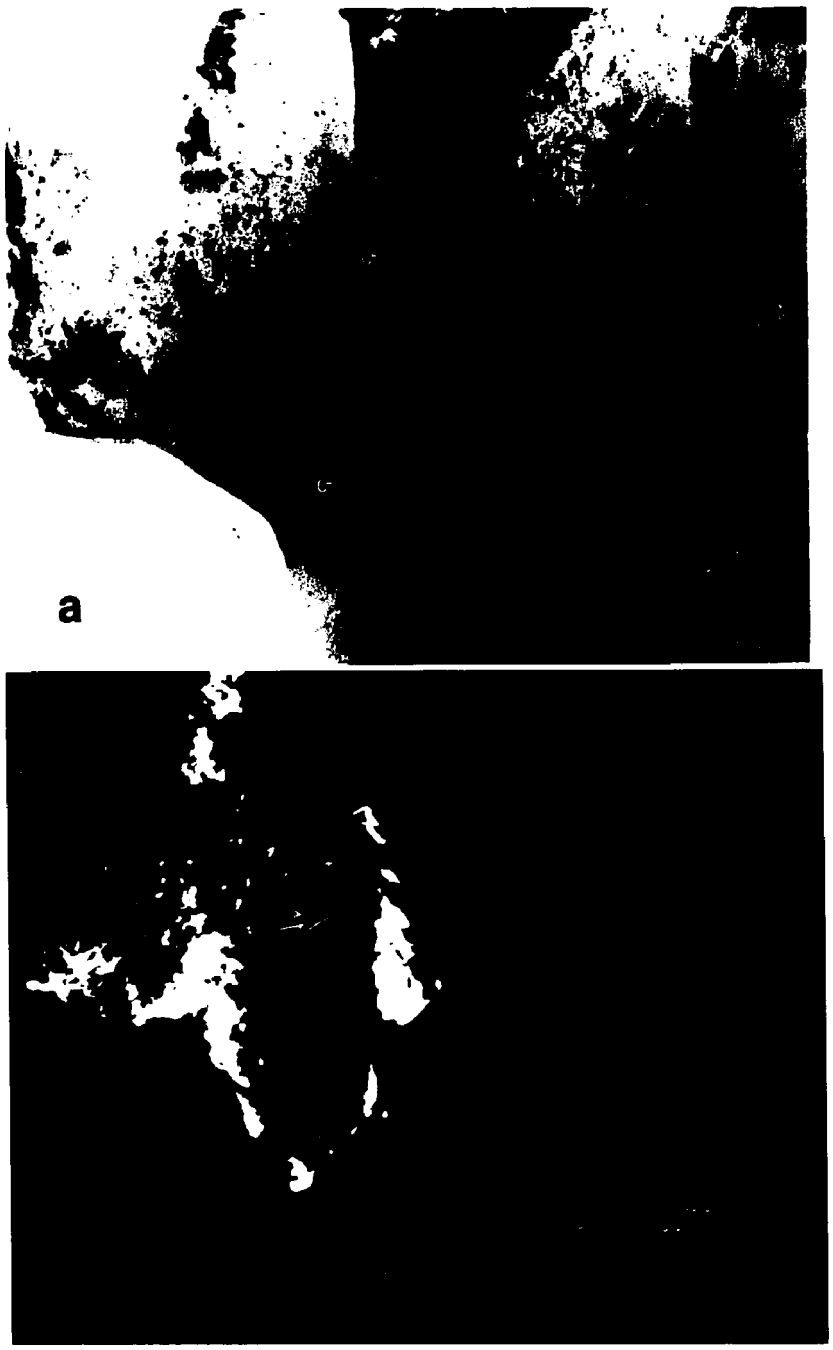

Fig. 4.53 a) TEM BF image of the 370FN15 alloy. b) CDF image of a $(111)_{fcc}$ diffraction spot and a $(110)_{bcc}$ diffraction spot which are too close to each other to be separated by the aperture. Interfacial dislocations are observed as indicated by an arrow.

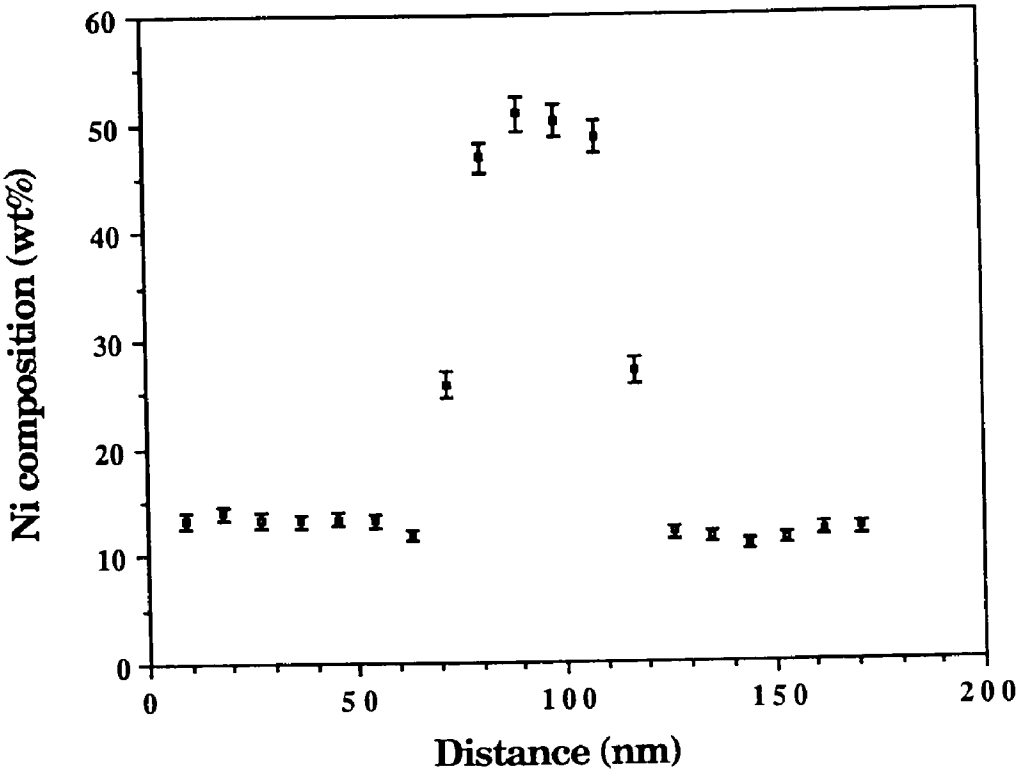

Fig. 4.54 EDS Ni composition profile of the 370FN15 alloy. The precipitate phase is the high Ni phase. EM430T.

Fig. 4.55 TEM BF image of the 370FN25 alloy. G: γ precipitate.

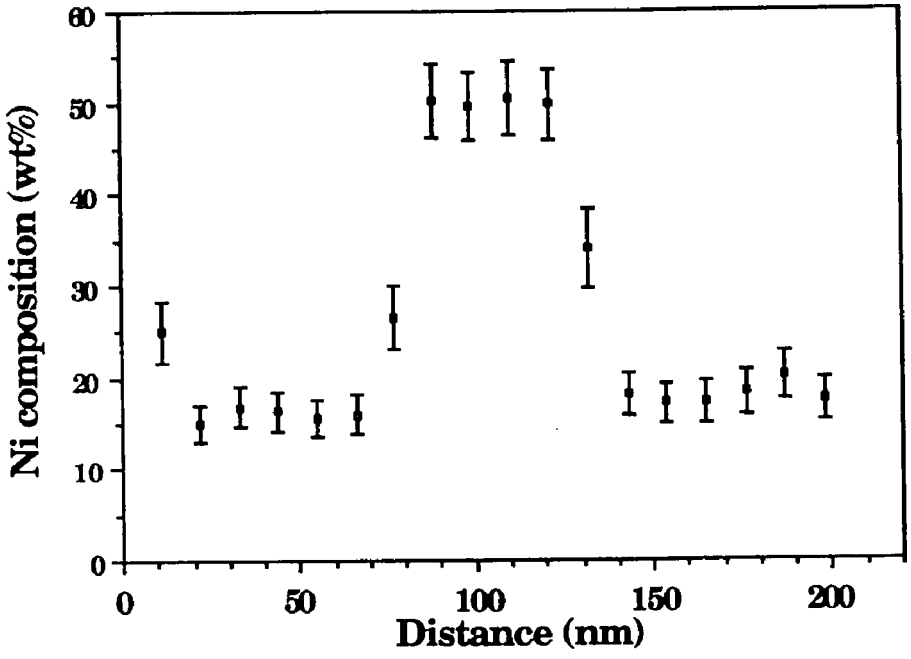

Fig. 4.56 EDS Ni composition profile of the 370FN25 alloy. The precipitate phase is the high Ni phase. EM430T.

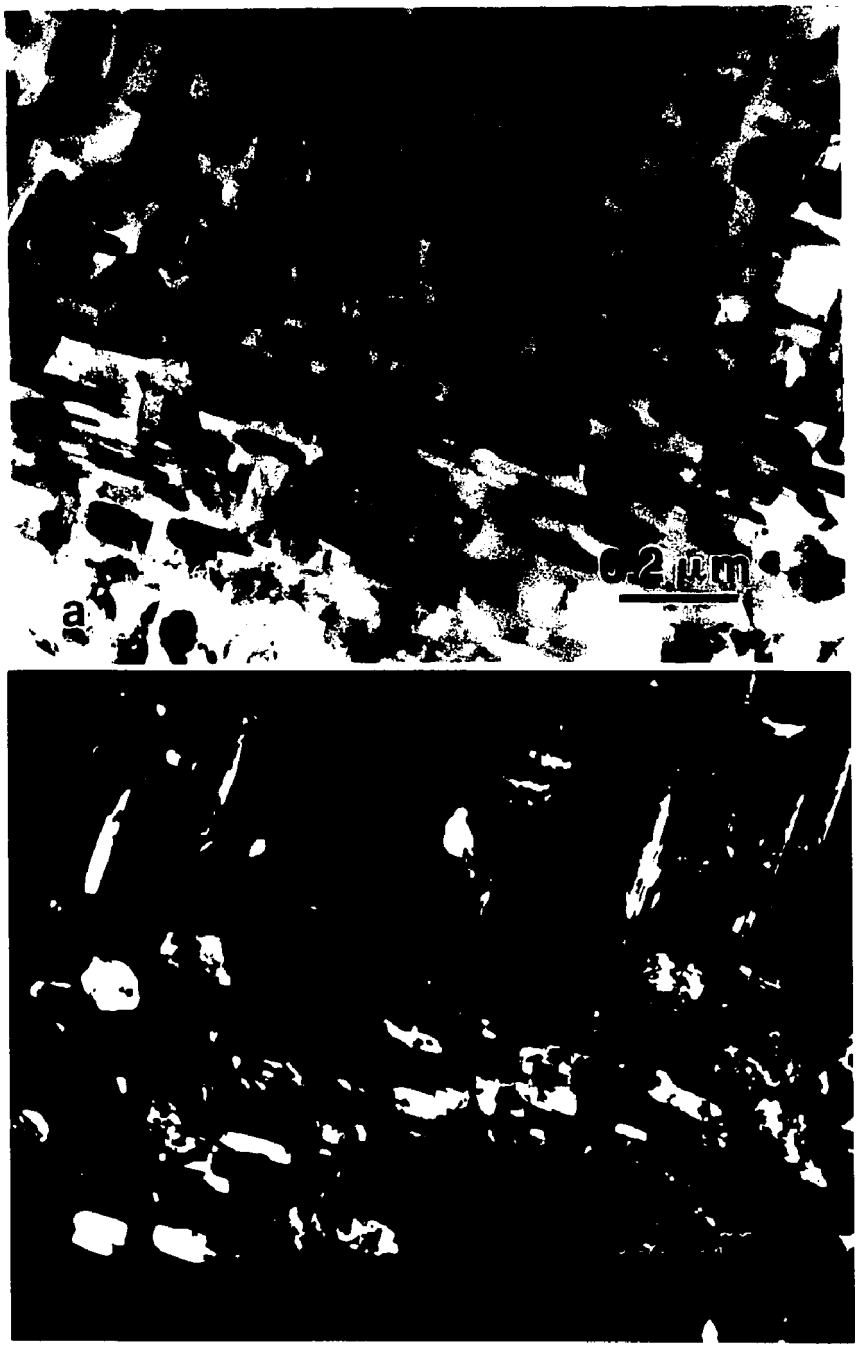

Fig. 4.57 a) TEM BF image of the precipitates of the 370FN30 alloy. b) CDF image of a $(111)_{fcc}$ diffraction spot. c) and d) SAD pattern and its indexing.

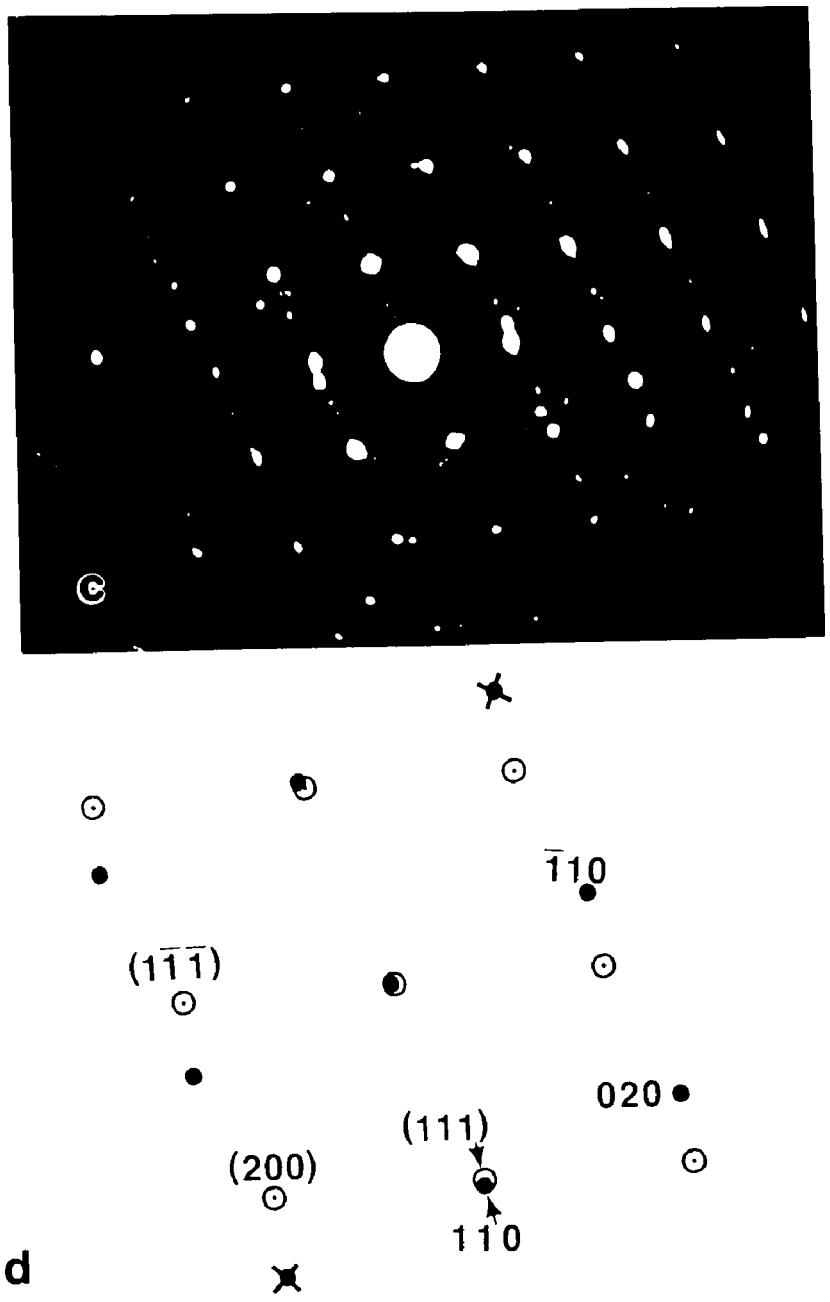

⊙ (hkl): fcc[011] zone axis pattern; • hkl: bcc[001] zone axis pattern. The diffraction spots labelled "X" do not appear in Fig. 4.57c, therefore, the matrix region that gives the SAD pattern shown in Fig. 4.57c is not in the exact bcc[001] zone axis orientation.

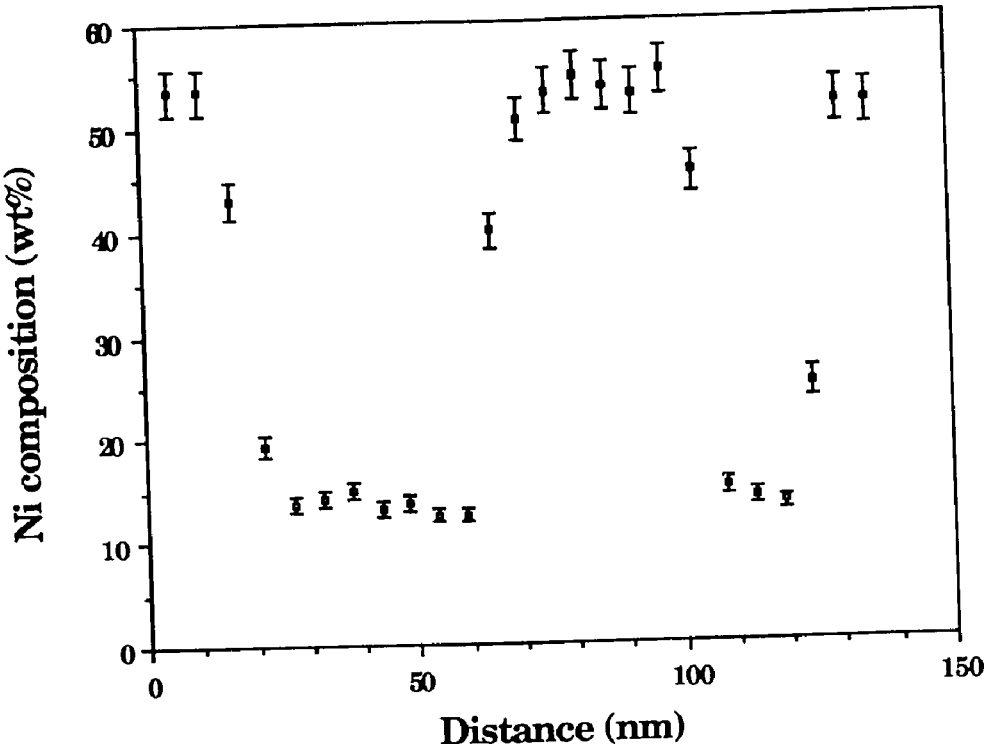

Fig. 4.58 EDS Ni composition profile of the 370FN30 alloy. The precipitate phase is the high Ni phase. EM430T.

Fig. 4.59 TEM BF image of the 350FN15 alloy. G: γ precipitate.

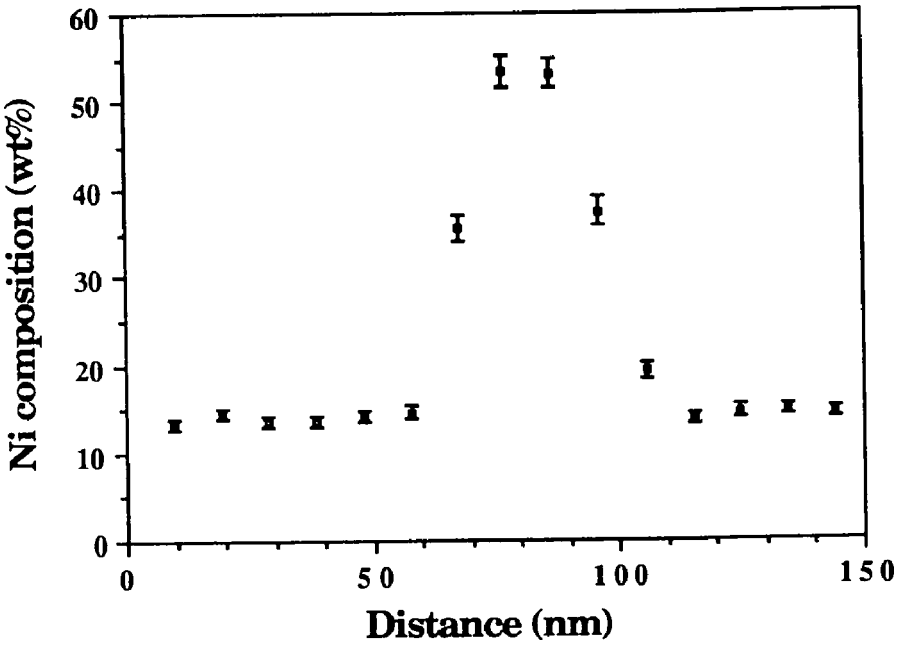

Fig. 4.60 EDS Ni composition profile of across the precipitate in the 350FN15 alloy. EM430T.

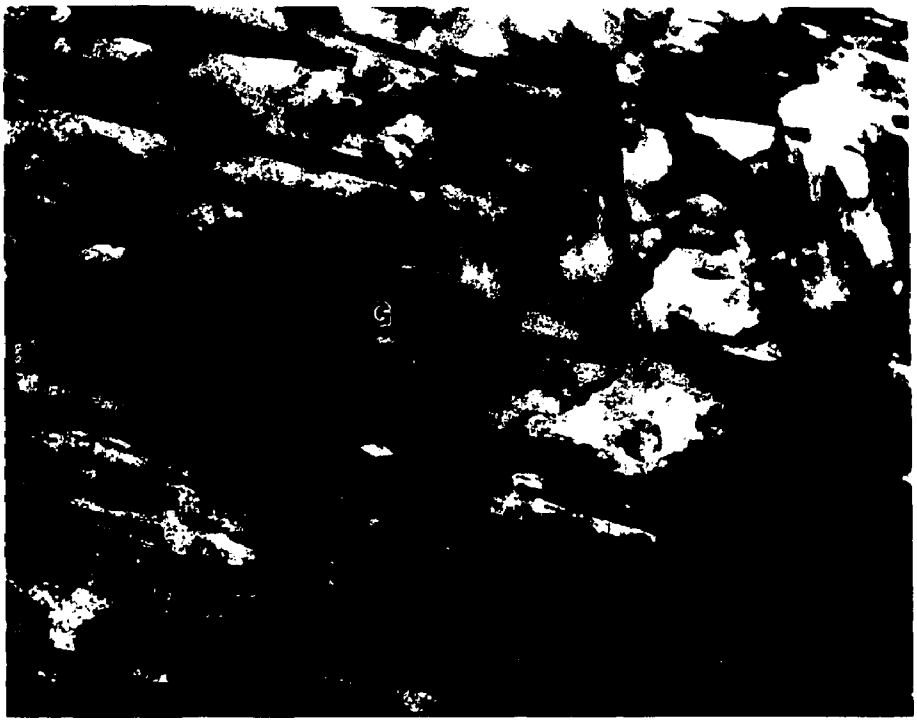

Fig. 4.61 TEM BF image of the 350FN25 alloy. G: γ precipitate.

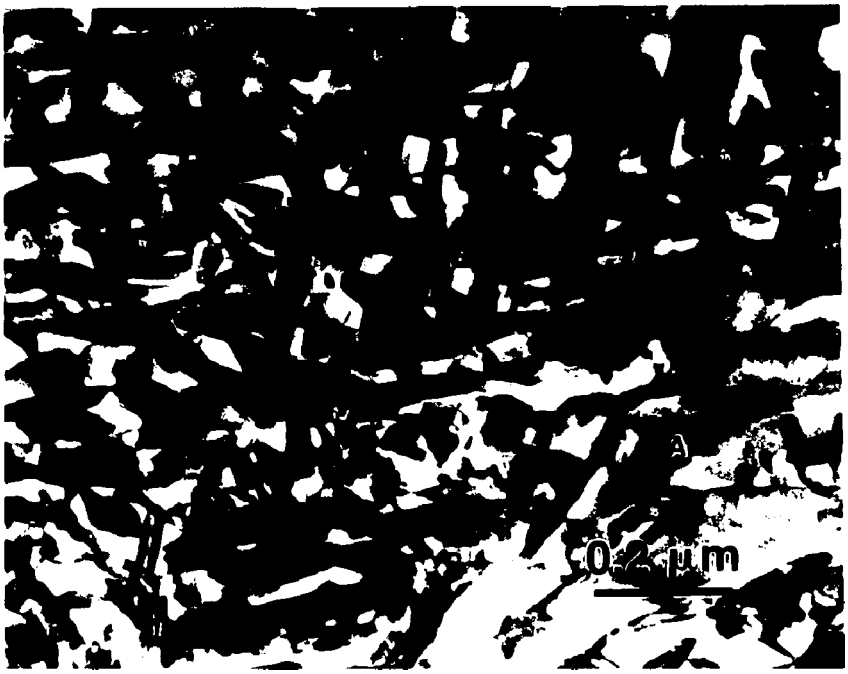

Fig. 4.62 a) TEM BF image of the 350FN30 alloy. b) CDF image of a $(111)_{fcc}$ diffraction spot. Morié fringes are observed showing that the precipitates and the matrix have a well-defined orientation relationship. c) SAD pattern of this area. The SAD pattern is composed of a bcc{111} axis pattern and many fcc{111} diffraction spots. For detailed indexing, see Fig. 4.25c or 5.3c.

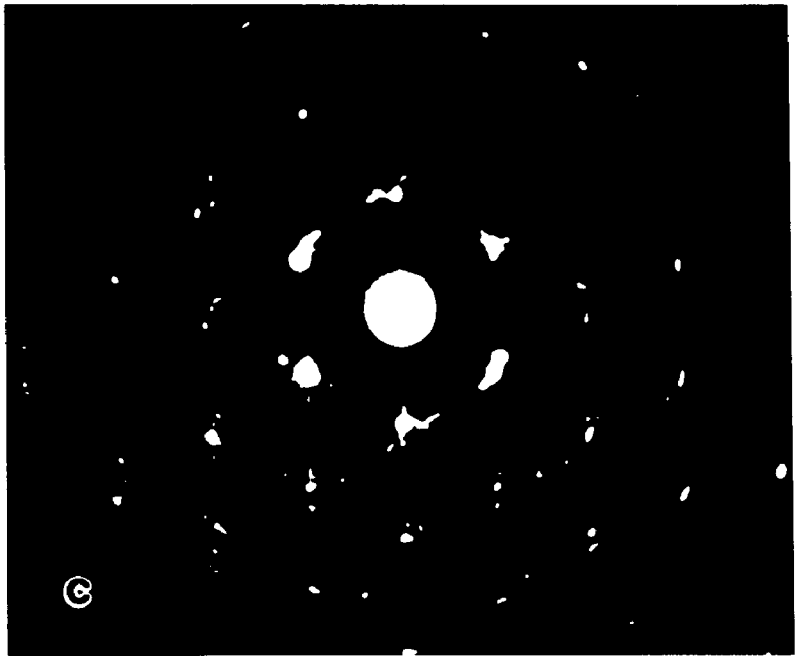

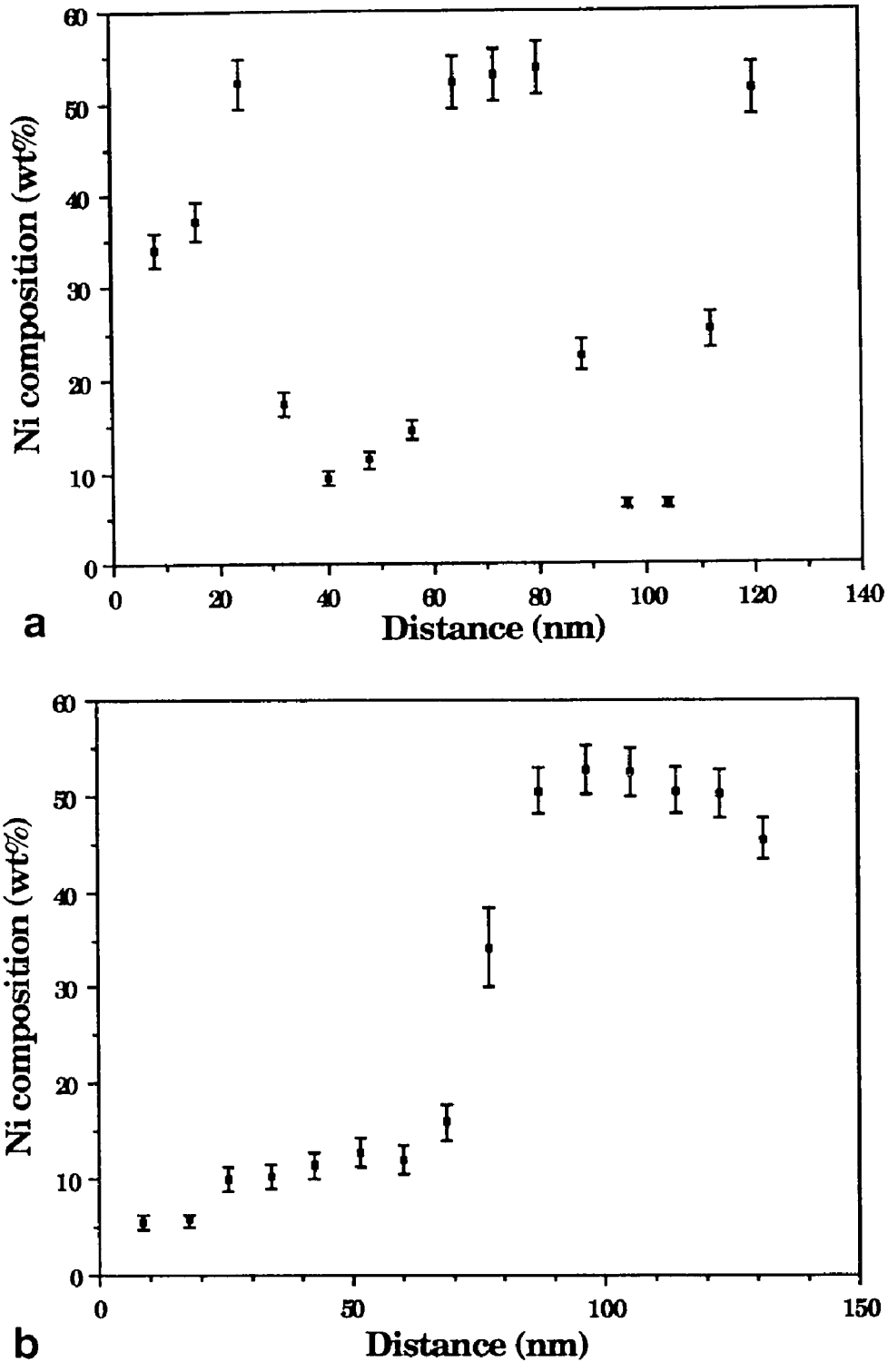

Fig. 4.63 EDS Ni composition profiles of the 350FN30 alloy showing the different matrix Ni composition for a) and b). EM430T.

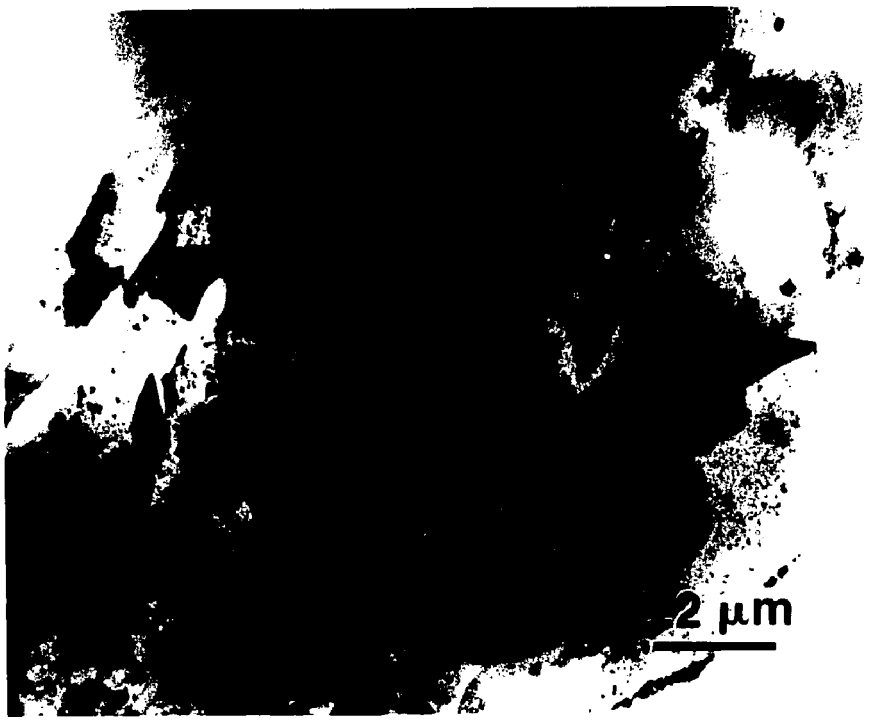

Fig. 4.64 TEM BF image of the 370FNP25 alloy.

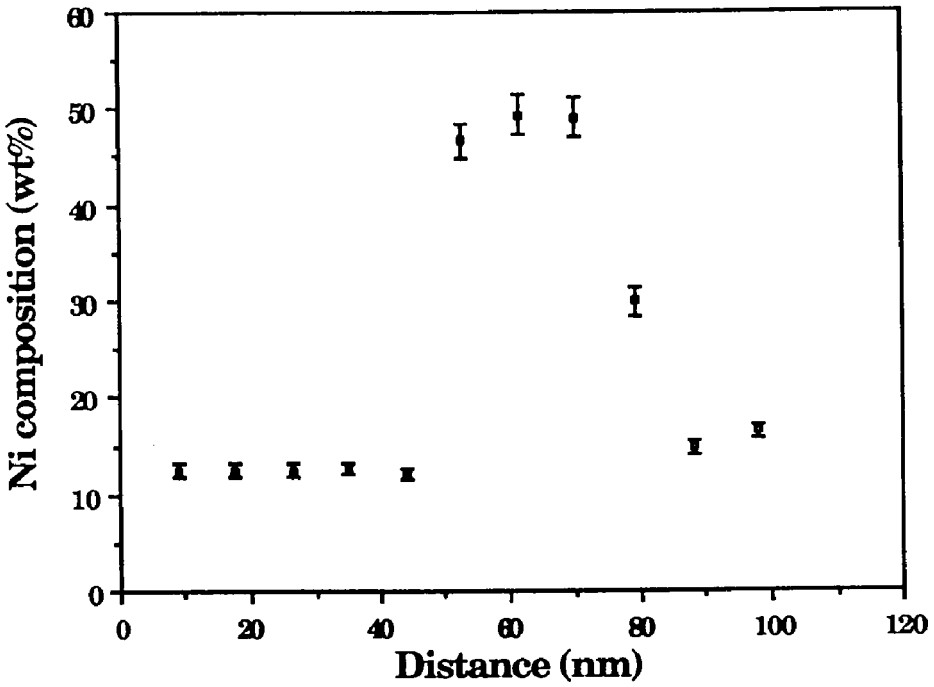

Fig. 4.65 EDS Ni composition profile across a γ precipitate in the 370FNP25 alloy. EM430T.

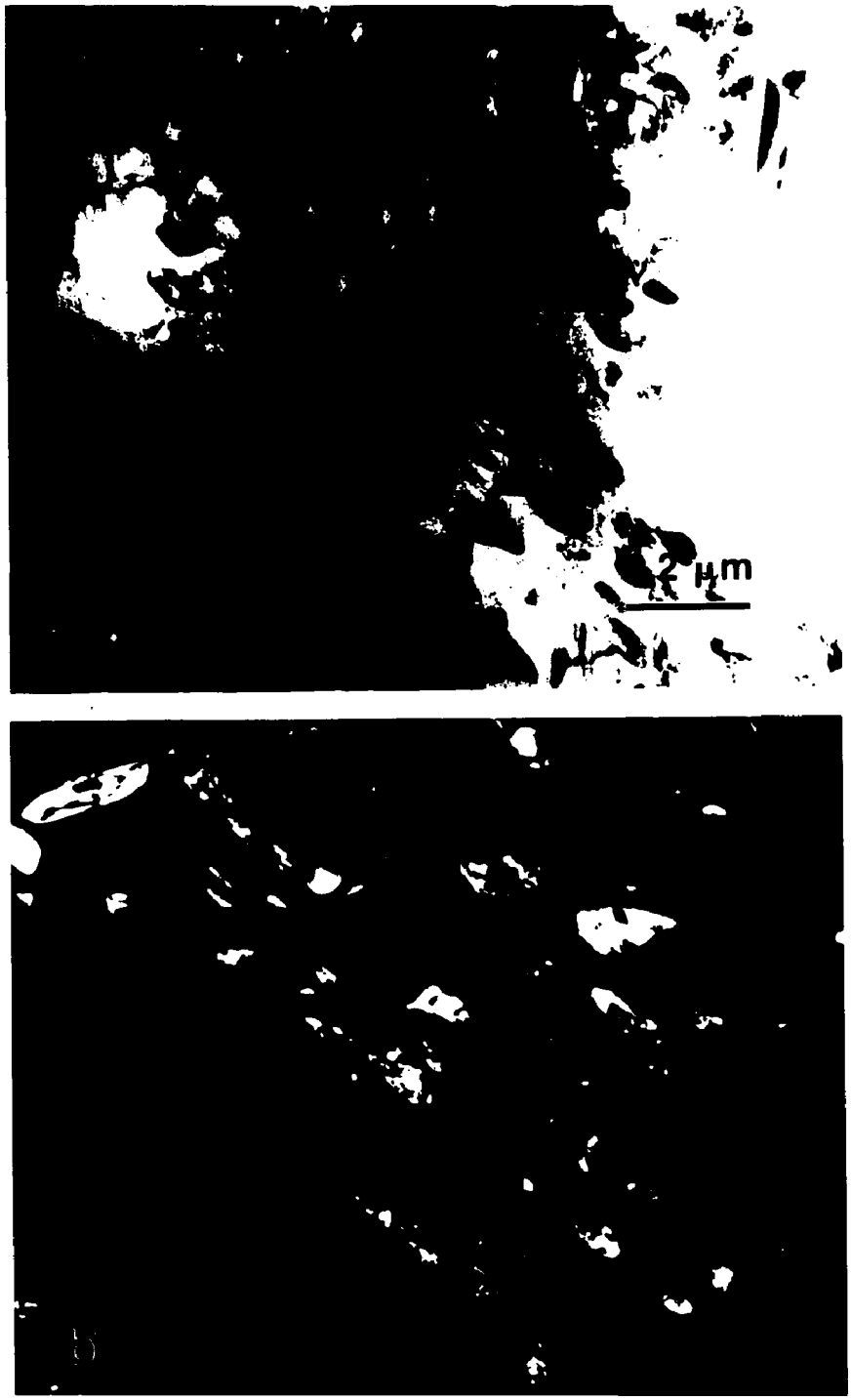

Fig. 4.66 a) TEM BF image of the 350FNP30 alloy. b) CDF image from a $(111)_{fcc}$ diffraction spot.

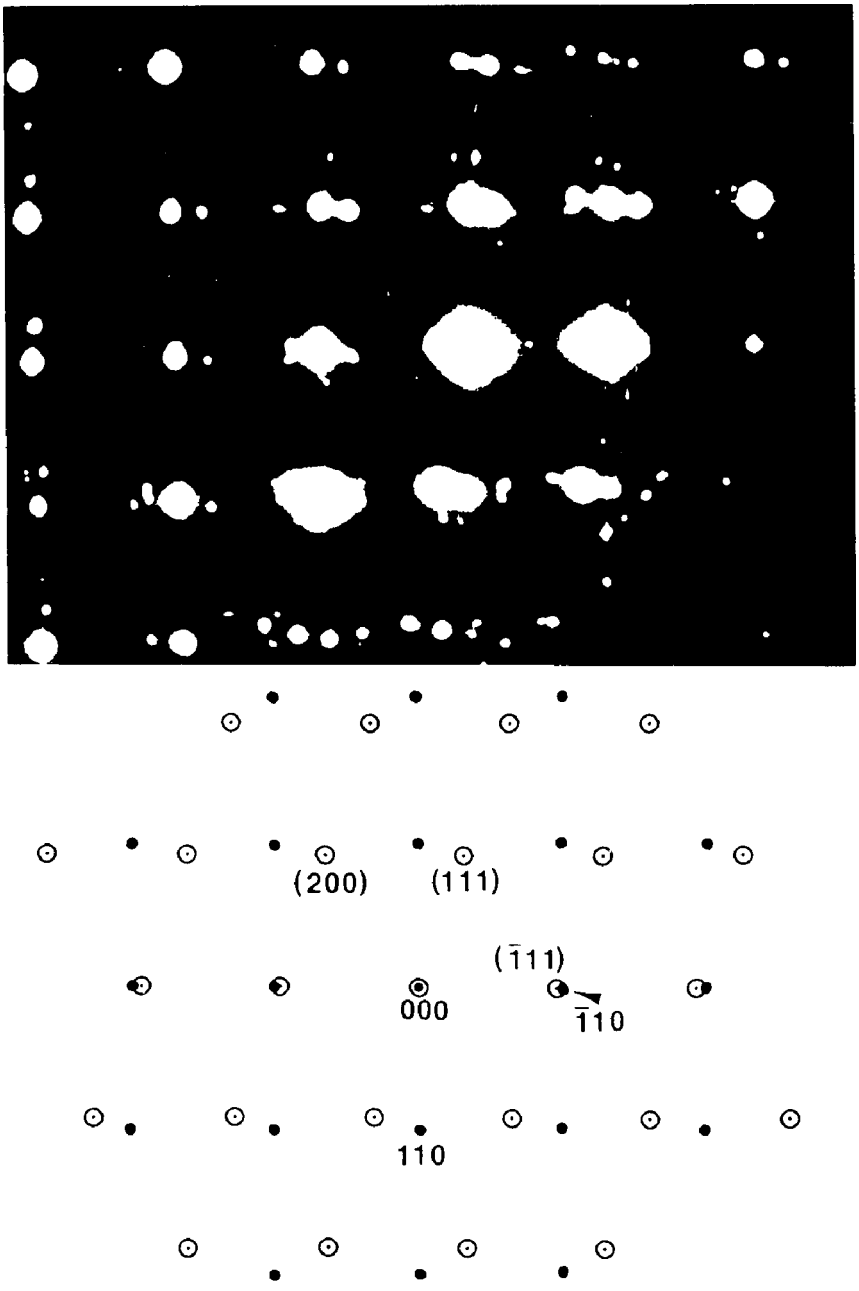

Fig. 4.67 An SAD pattern and its indexing of the 350FNP30 alloy. ⊙ (hkl): fcc[0,1,-1] zone axis pattern; • hkl: bcc[001] zone axis pattern. The rest satellite diffraction spots around the bcc<110> diffraction spots are due to double diffraction effect.

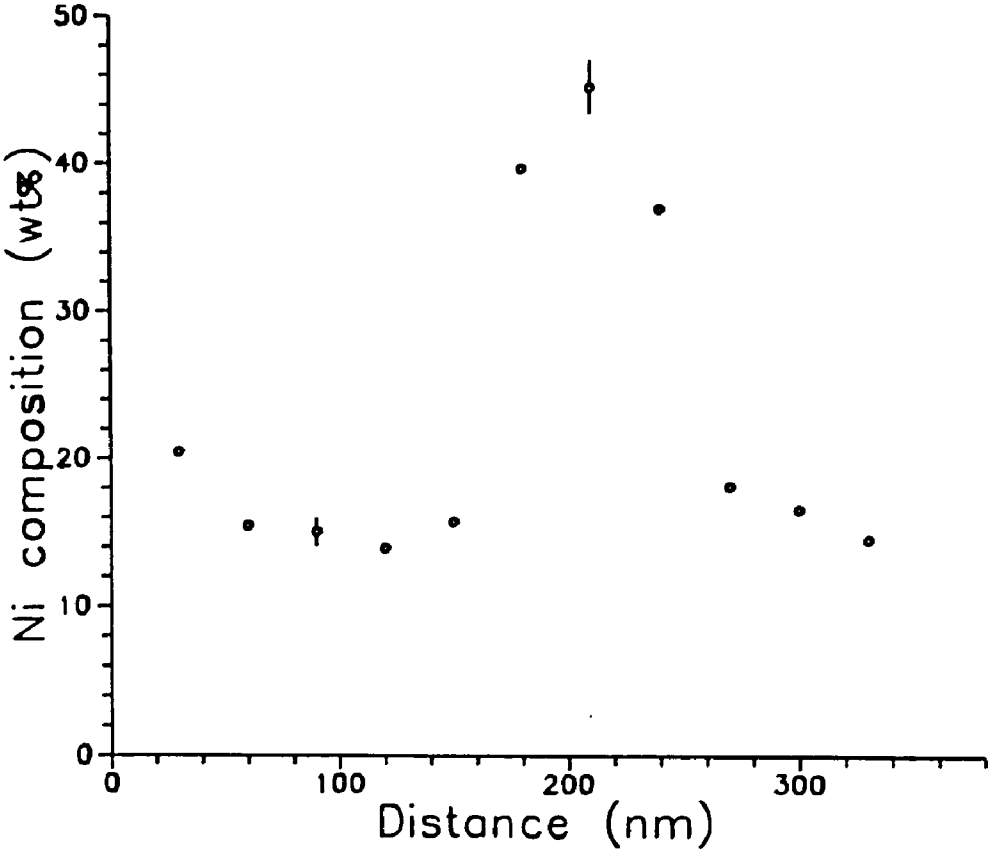

Fig. 4.68 EDS Ni composition profile across a γ precipitate in the 350FNP30 alloy. EM400T.

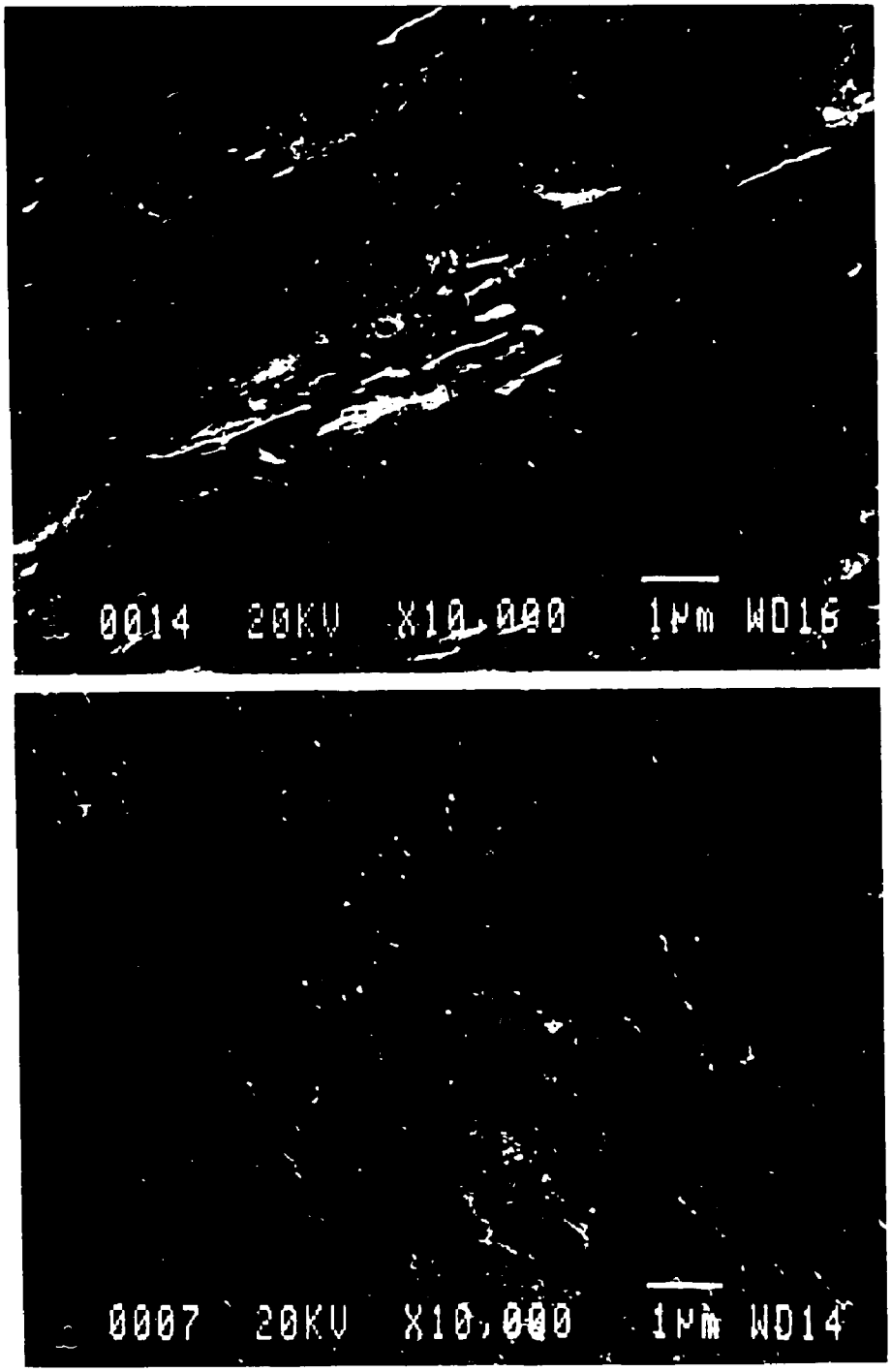

Fig. 4.69 SEM SE images of alloys heat treated at 300°C. a) 300FN25; b) 300FNP25; c) 300FN30; and d) 300FNP30 alloy. A typical precipitate is indicated by an arrow in the 25 wt% Ni alloys. The precipitate phase is the less etched phase in the 30 wt% Ni alloys. A: retained austenite. JEOL840F.

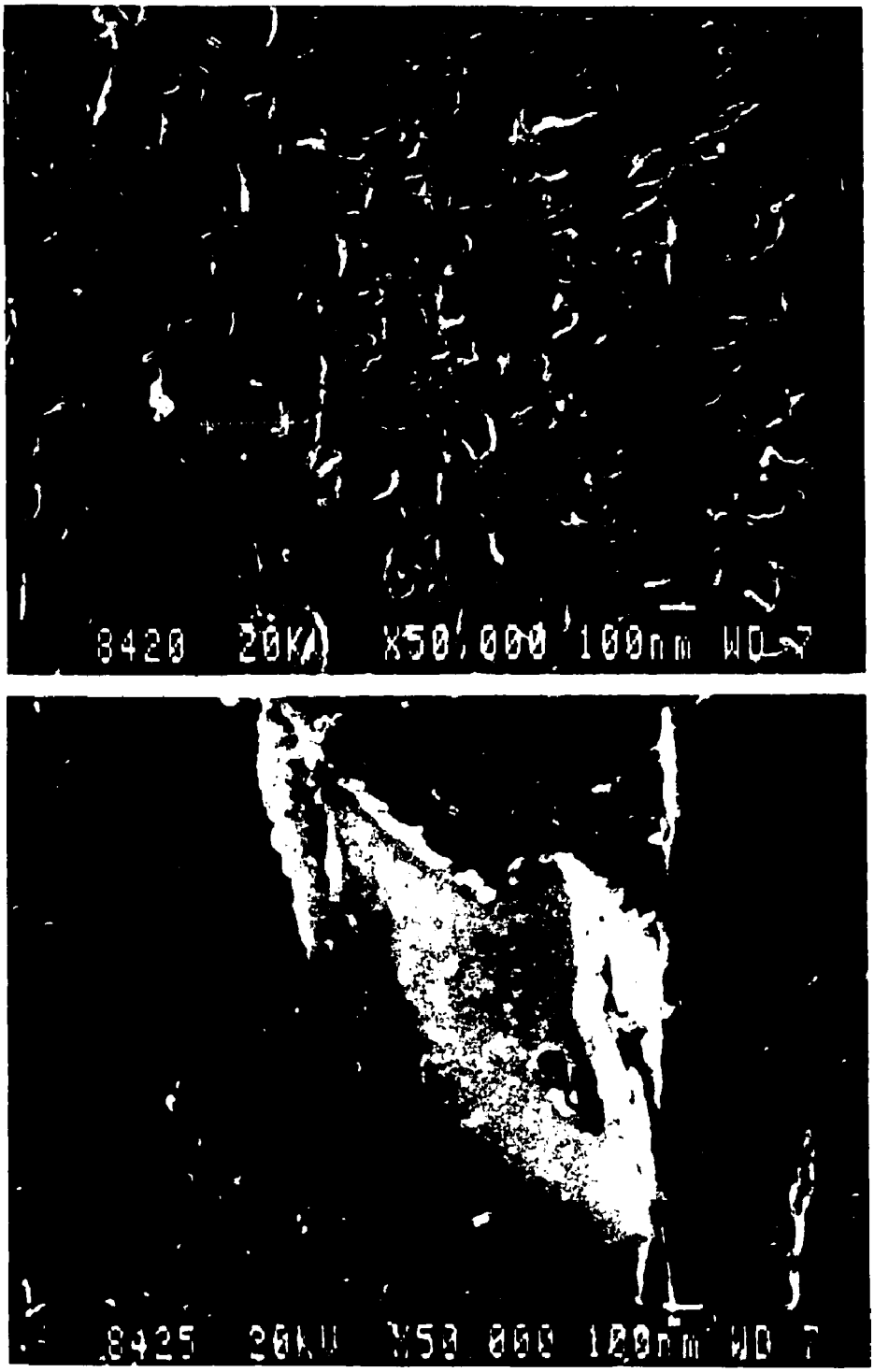
8420 20kV X50,000 100nm WD 7
8425 20kV X50,000 100nm WD 7

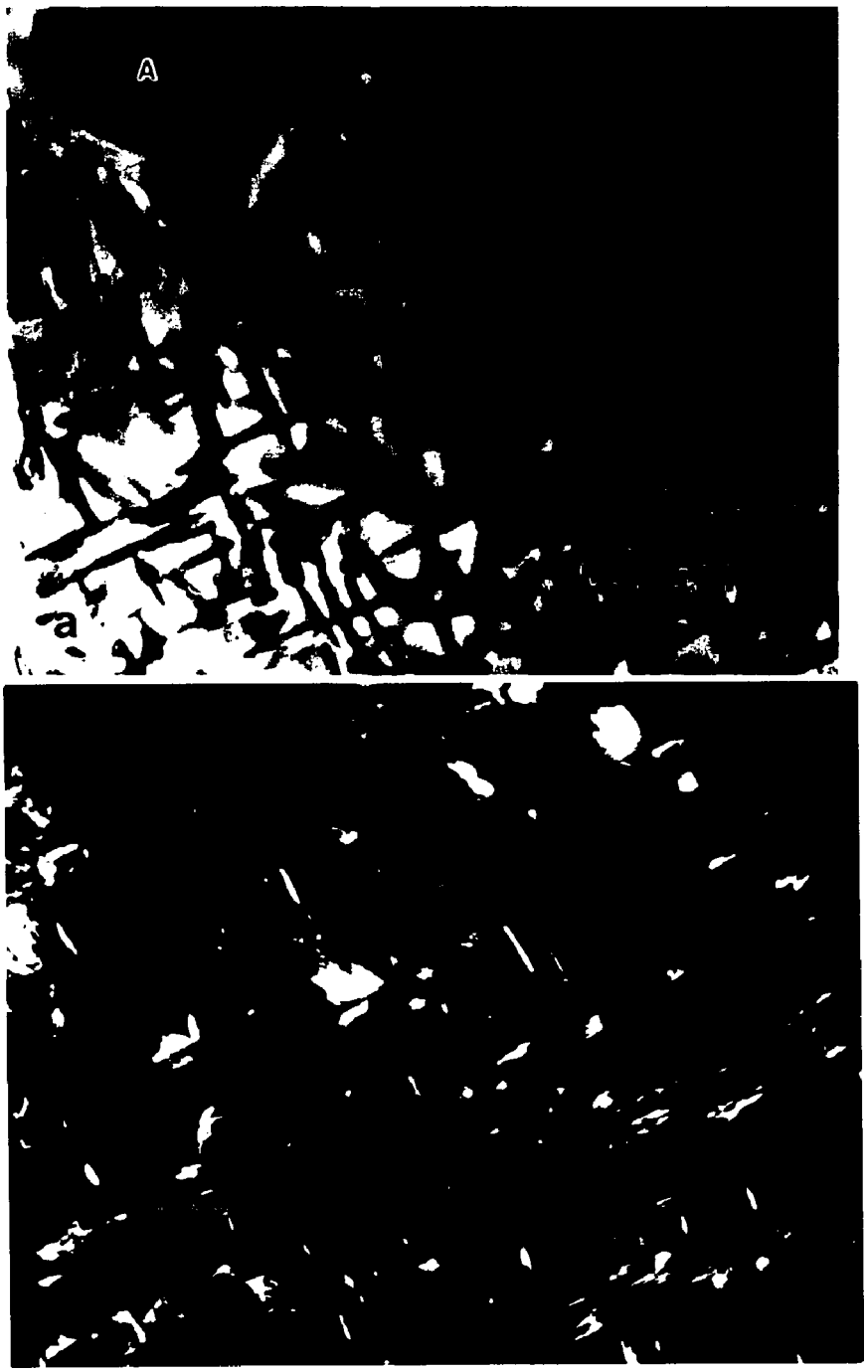

Fig. 4.70 a) TEM BF image of the 300FN30 alloy. b) CDF image of a weak fcc spot. Morié fringes are observed. c) SAD pattern showing streaking. For the indexing of this pattern, see Fig. 4.67.

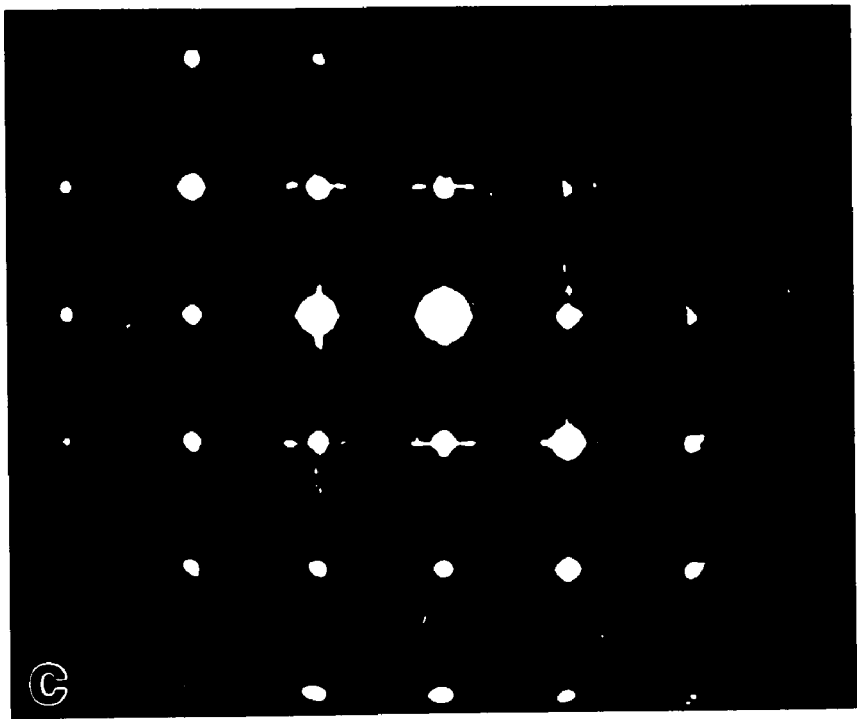
C

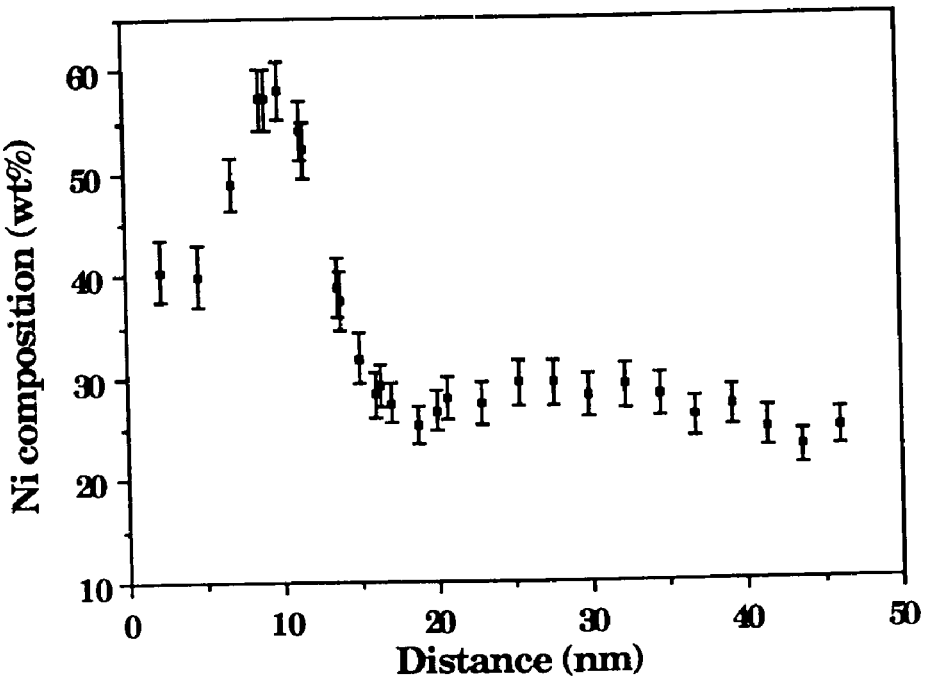

Fig. 4.71 EDS Ni composition profile of the 300FN30 alloy. The precipitate phase is the high Ni phase. HB501.

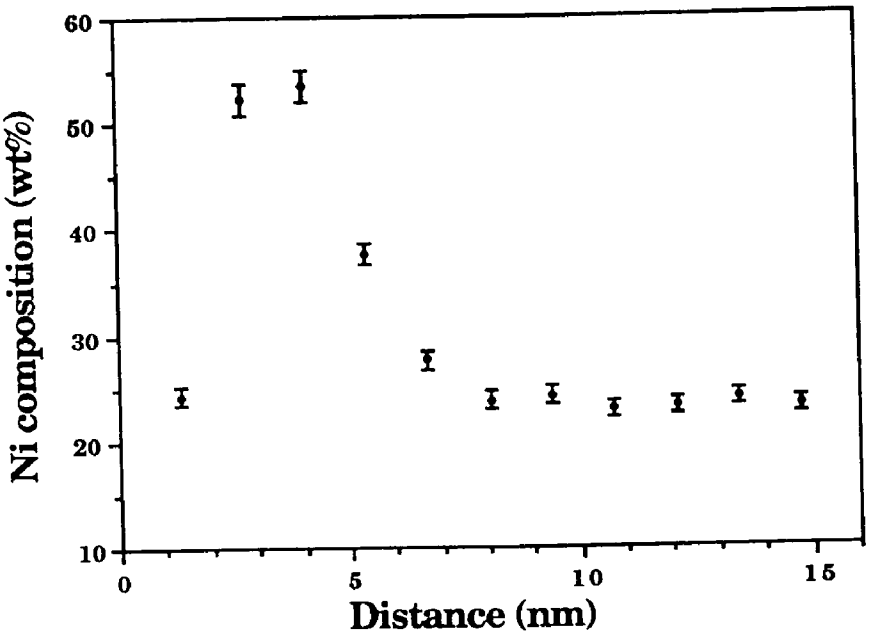

Fig. 4.72 EDS Ni composition profile of a γ precipitate in the 300FNP30 alloy. HB501.

Fig. 4.73 TEM BF image of the 300FN25 alloy.

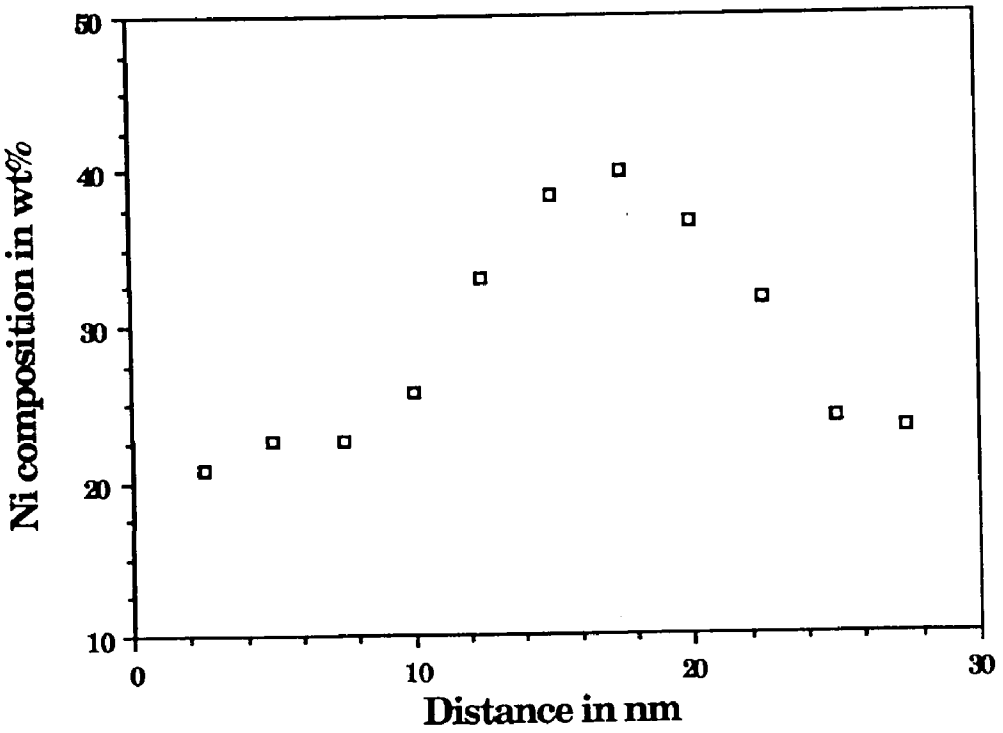

Fig. 4.74 EDS Ni composition profile of a γ precipitate in the 300FN25 alloy.
HB501

Fig. 4.75 FIM image of the 300FN25 alloy. The area shown in the image corresponds to an area of approximately 200 nm in diameter on the specimen tip. The arrows point at the small precipitates.

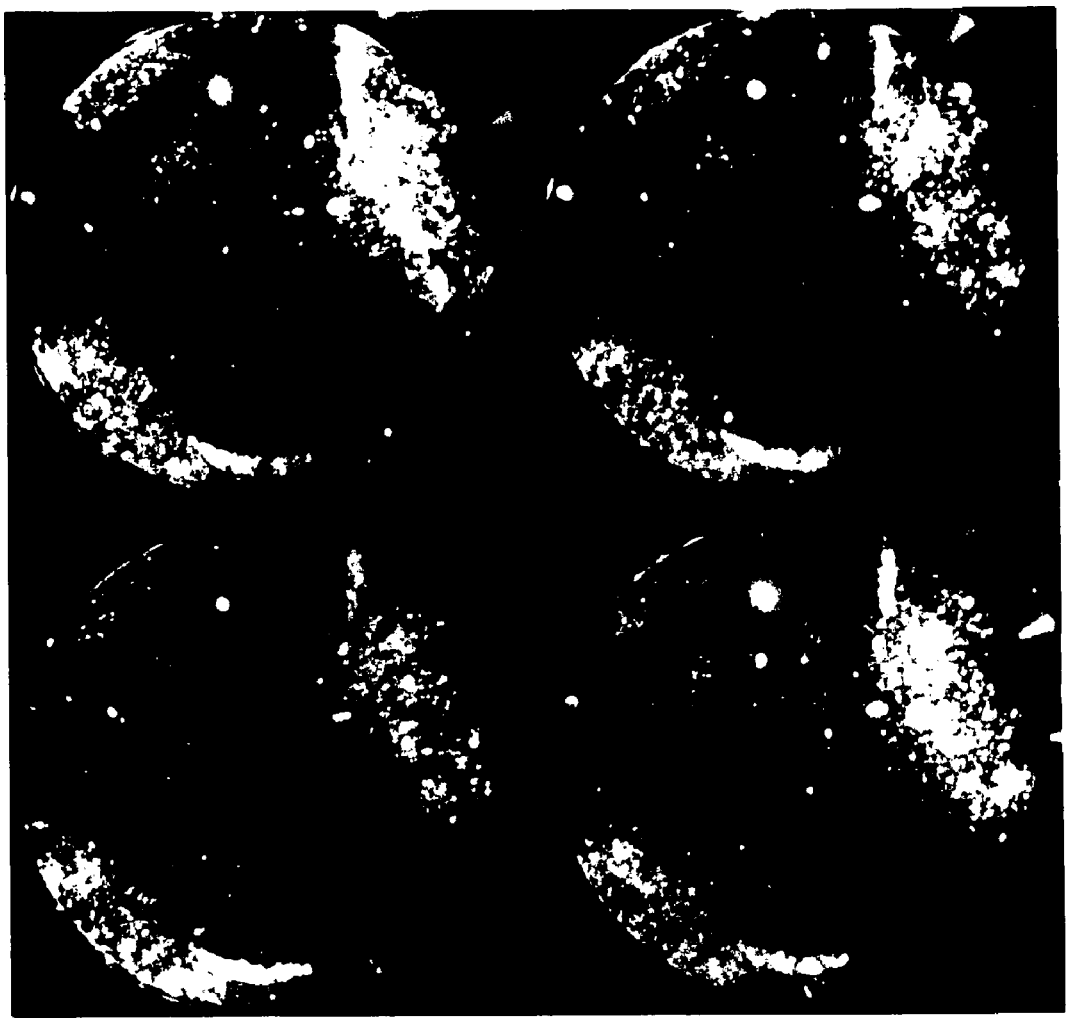

Fig. 4.76 A series FIM images of the 300FN25 alloy showing the layer-by-layer analysis. From a) to d), an image was taken after one atomic layer on the tip is field-evaporated. p: pole.

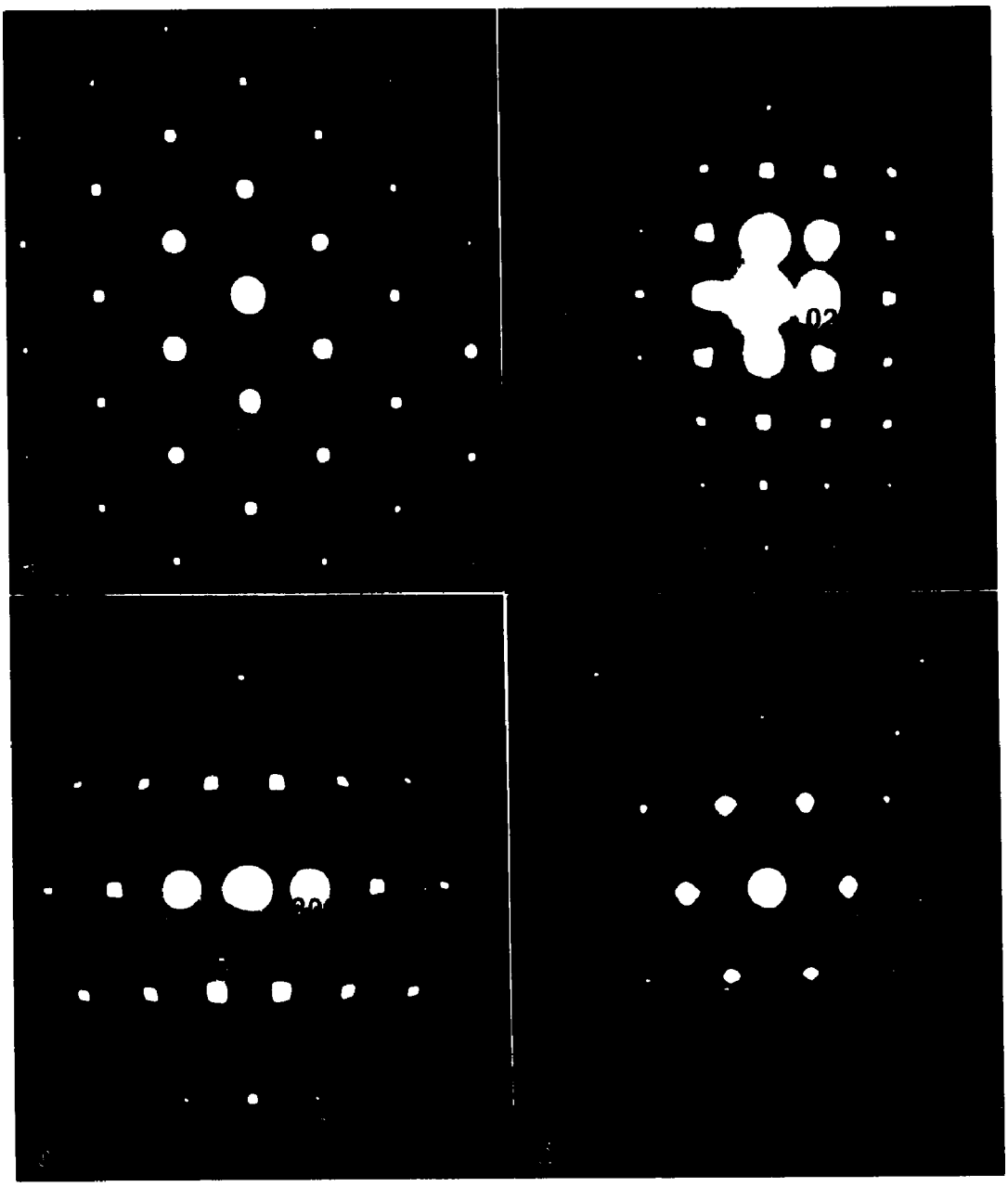

Fig. 4.77 SAD patterns of the 350FN44 alloy showing the streaking. Zone axis: a) [011]; b) [001]; c) [013]; d) [-114].

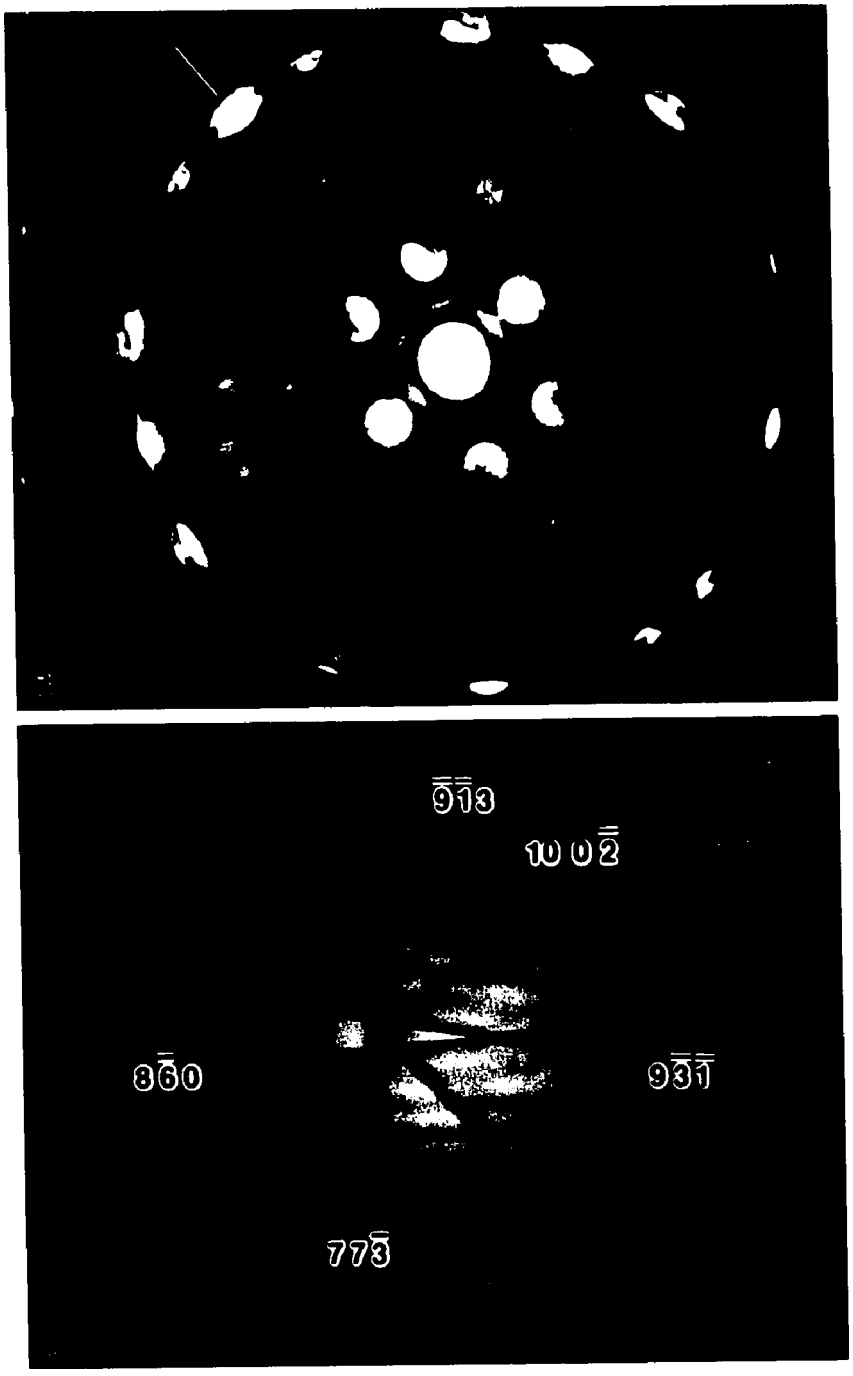

Fig. 4.78 CBED patterns of [114] zone axis of the 350FN44 alloy. a) whole pattern; b) bright field disc.

Fig. 4.79 TEM BF image of the 350FN44 alloy.

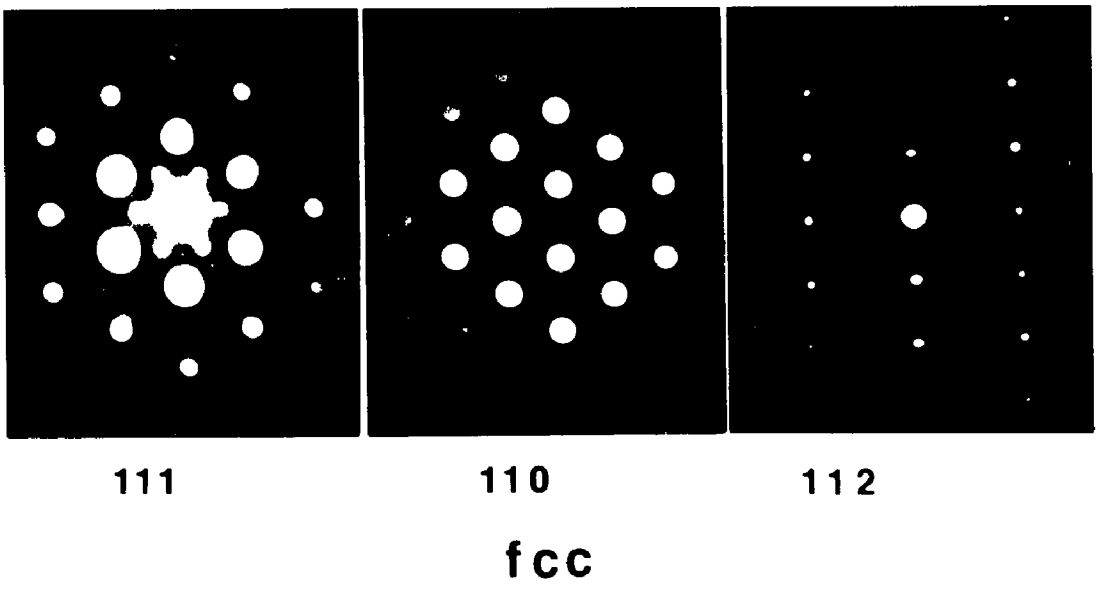

Fig. 4.80 SAD patterns of the 650FN35 alloy.

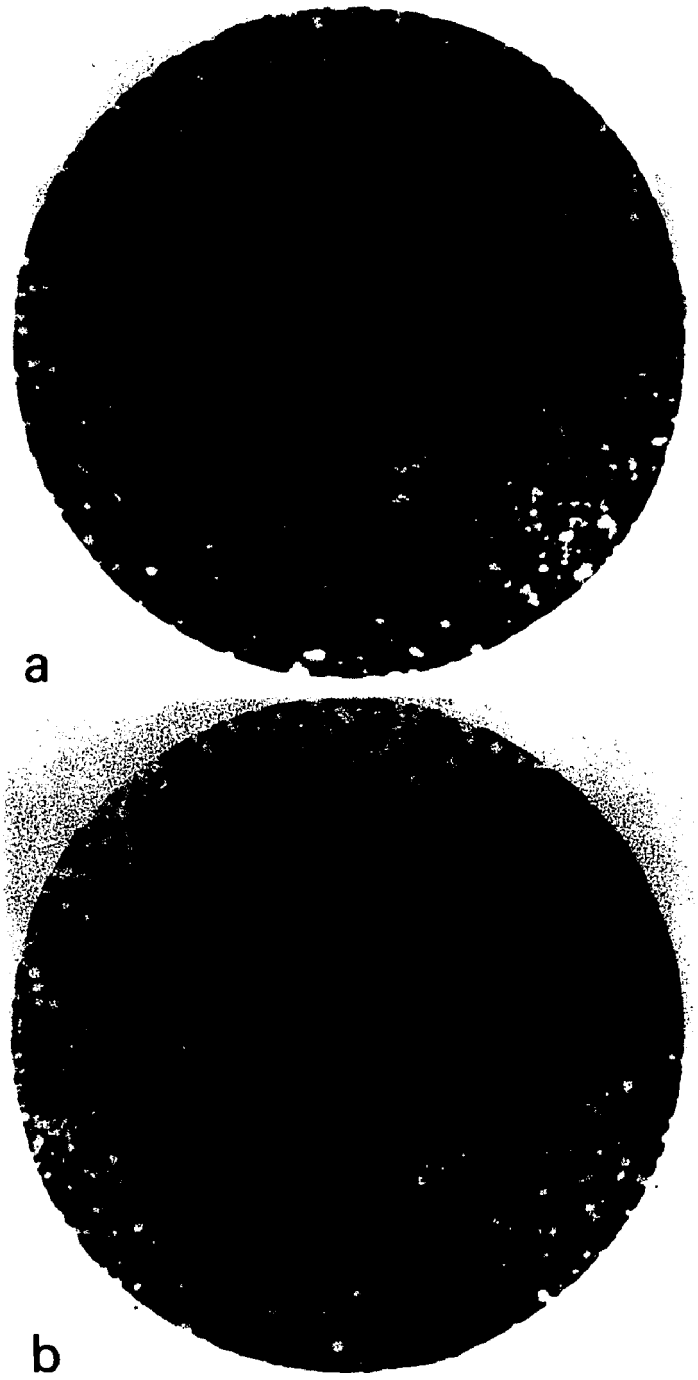

Fig. 4.81 FIM images of a) the 400FN44 alloy and b) 350FN44 alloy. The area shown in these images corresponds to an area of approximately 100 nm in diameter on the specimen tip.

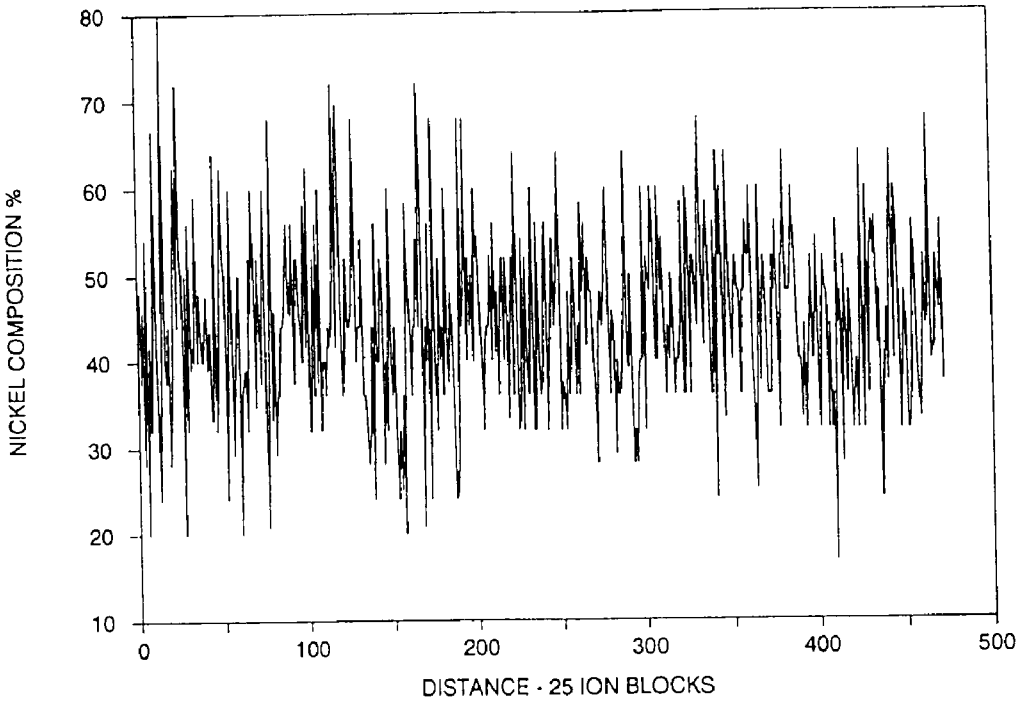

Fig. 4.82 Ni composition profile of the 400FN44 alloy measured using the atom probe. Composition of each point is calculated from a 25 ion block in the total data chain.

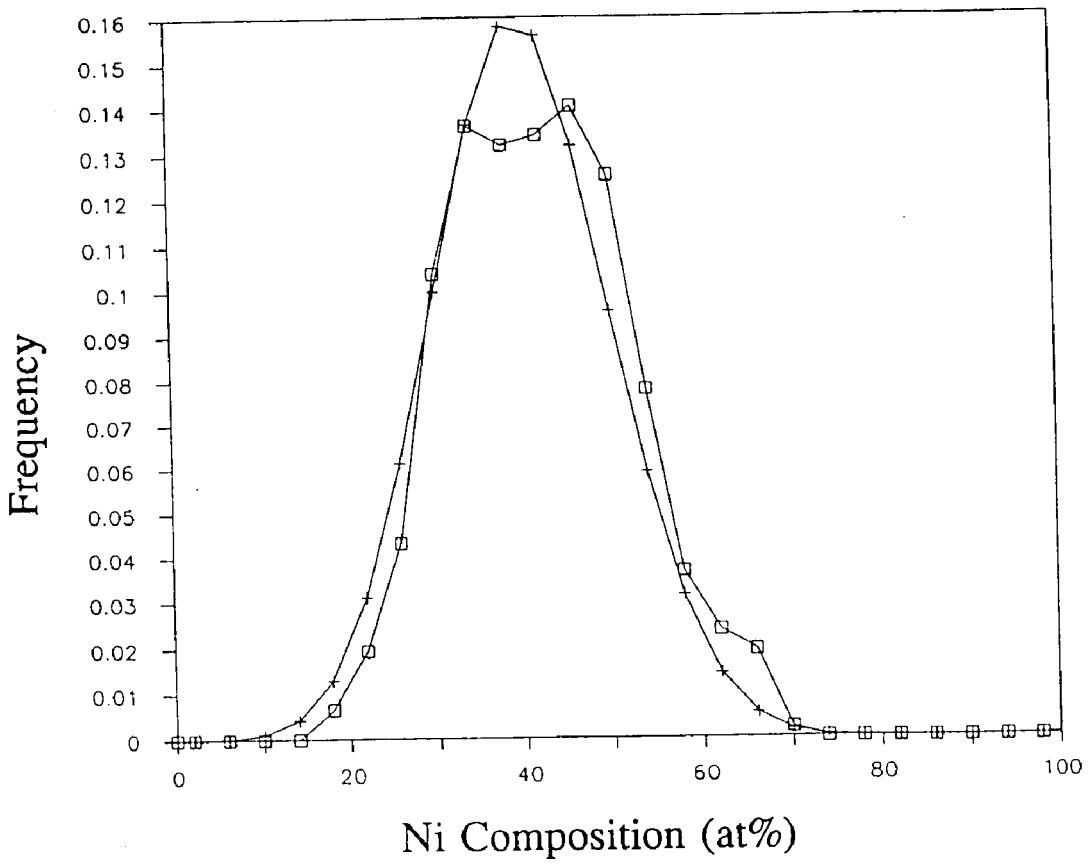

Fig. 4.83 Frequency distribution of the 25 ion block in the data chain of the 400FN44 alloy. □ : experimental data. + : theoretical binomial distribution.

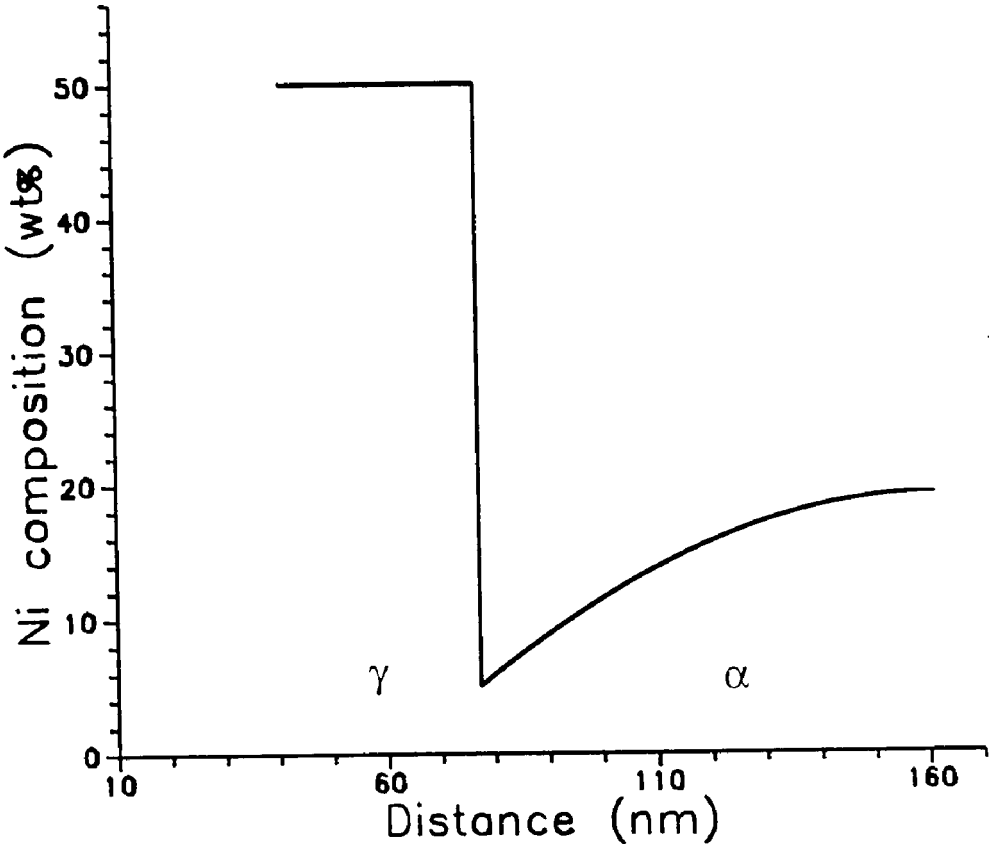

Fig. 5.1 Numerically simulated Ni composition profile of the 400FN25 alloy. The simulation parameters are: bulk Ni composition, 25 wt%; precipitate and interface Ni composition, 50 wt% and 5 wt%; total diffusion time, 360 days; diffusion coefficient, 8×10^{-19} cm^2/sec; impingement distance, 120 nm. The final precipitate half width is 35.9 nm.

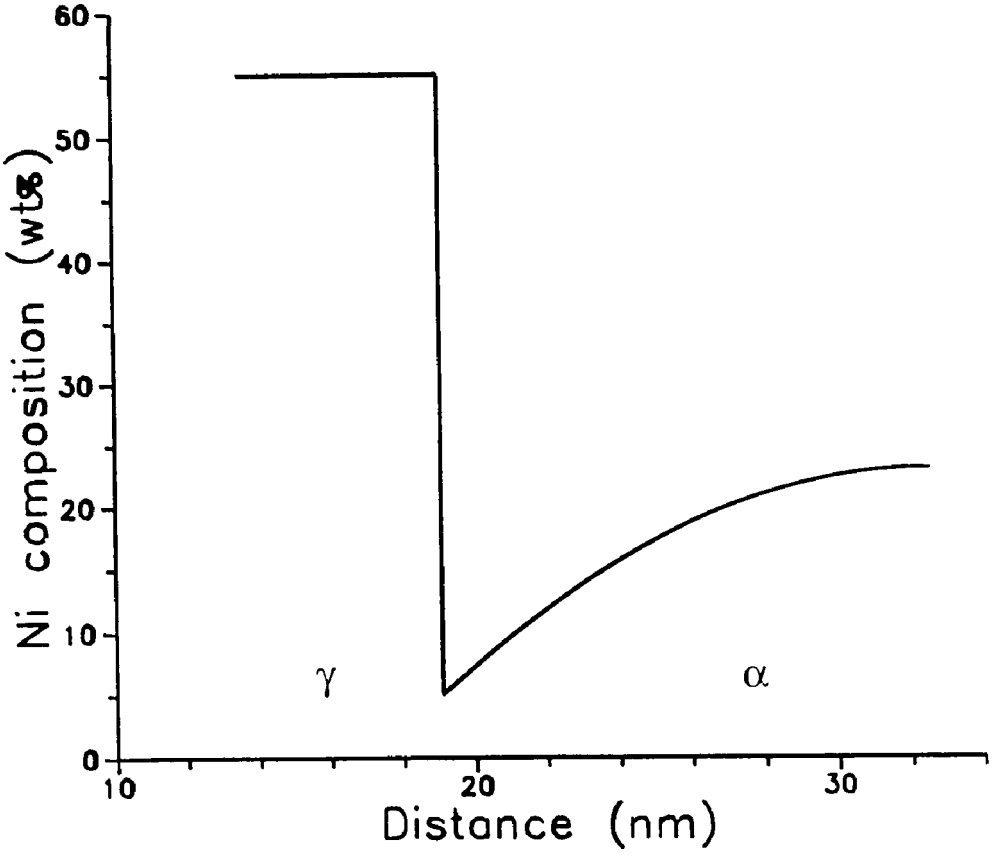

Fig. 5.2 Numerically simulated Ni composition profile of the 300FN30 alloy. The simulation parameters are: bulk Ni composition, 30 wt%; precipitate and interface Ni composition, 55 wt% and 5 wt%; total diffusion time, 370 days; diffusion coefficient, 2×10^{-20} cm^2/sec; impingement distance, 20 nm. The final precipitate half width is 5.6 nm.

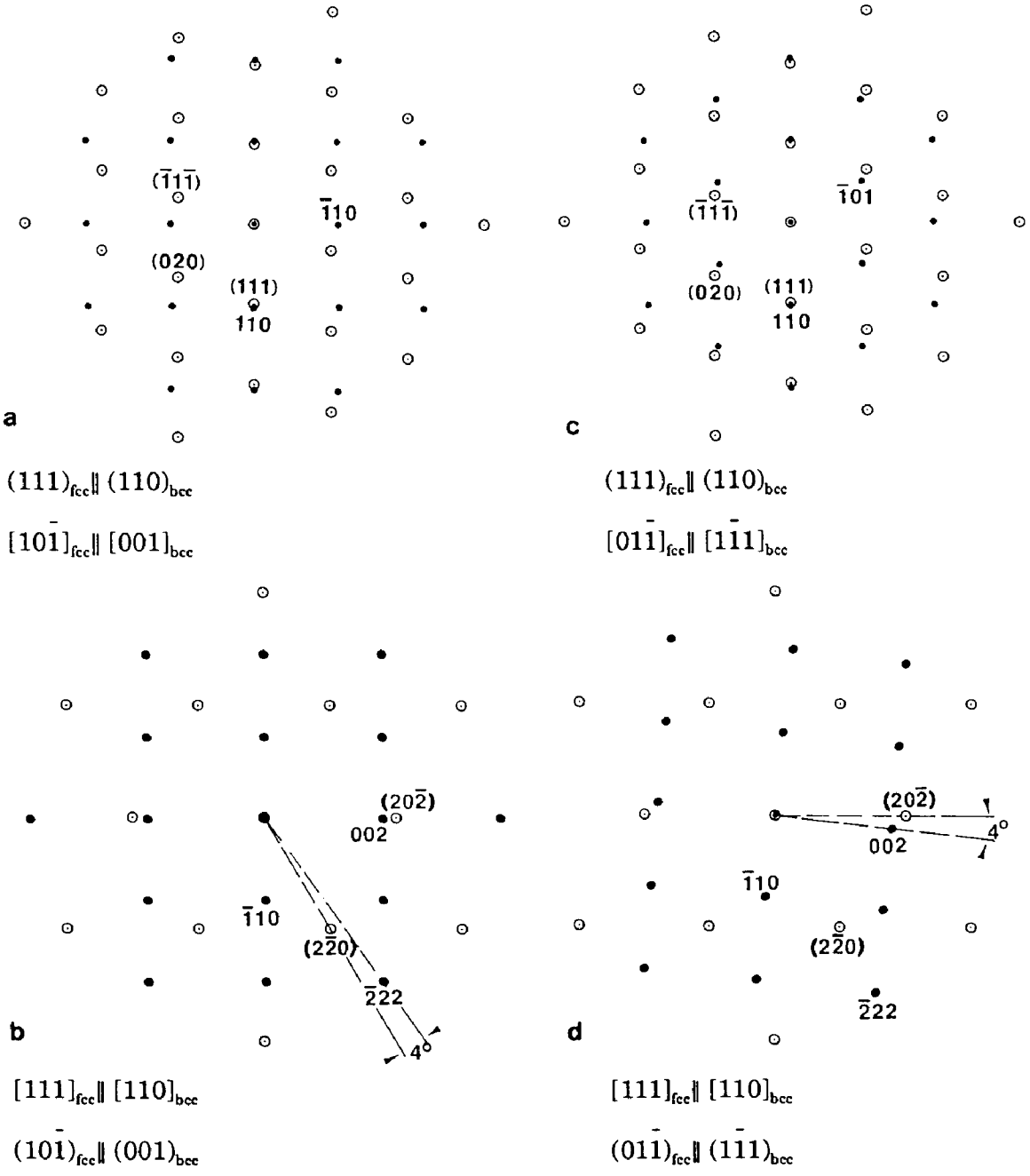

Fig. 5.3 Superimposed reciprocal lattice planes (electron diffraction patterns) of a bcc and an fcc crystal with, a) and b), a N-W orientation relationship, c) and d), a K-S orientation relationship. ⊙ (hkl): fcc diffraction spots, ● hkl: bcc diffraction spots.

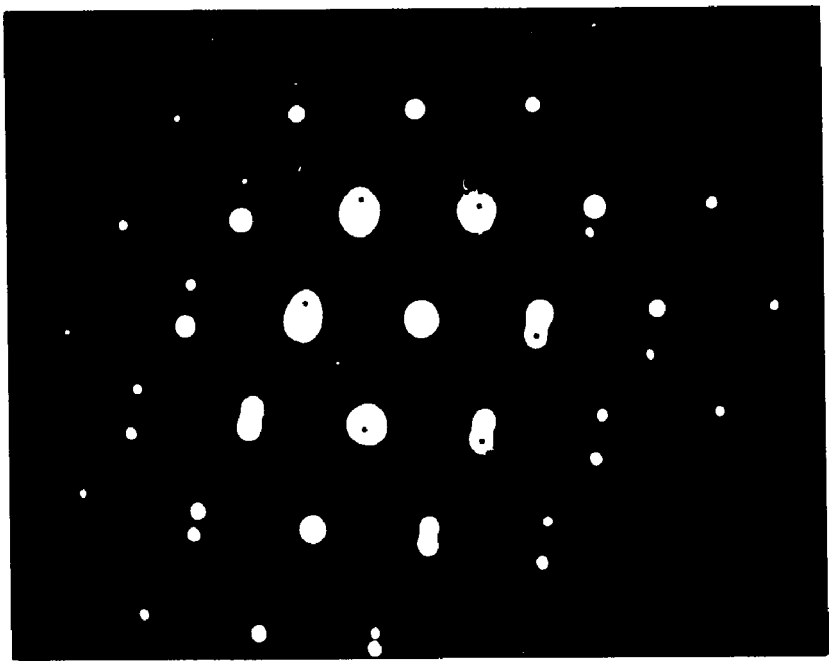

Fig. 5.4 SAD pattern taken from the CZ region of Tazewell meteorite showing a K-S orientation relationship. For the indexing of this pattern, see Fig. 5.3c. The small extra spots in this pattern which are in the Fig. 5.3c are due to the ordering of the fcc phase i.e. tetrataenite.

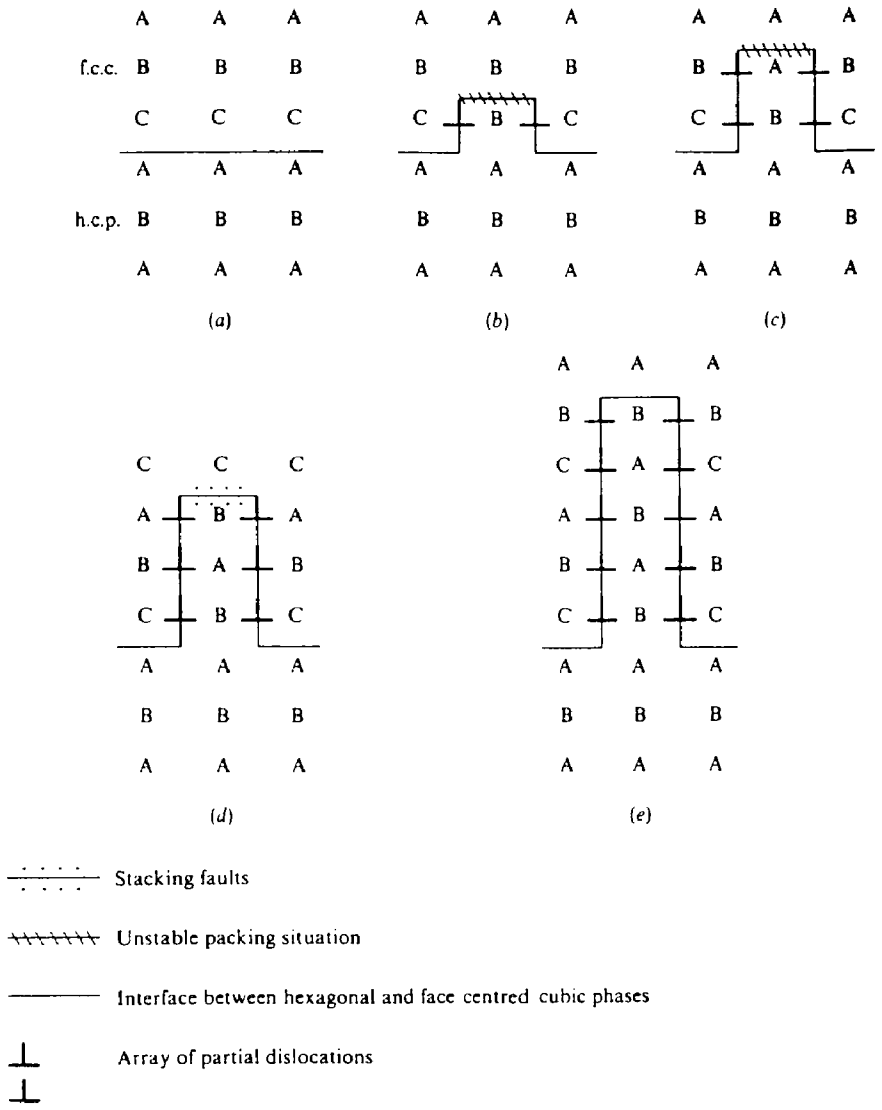

Fig. 5.5 Schematic diagram showing the problems in the growth on the coherent interface between fcc(111) and hcp(001) by single atom jump mechanism. The letters indicate the stacking sites of the atoms in the fcc or the hcp lattice (Matin and Doherty, 1976).

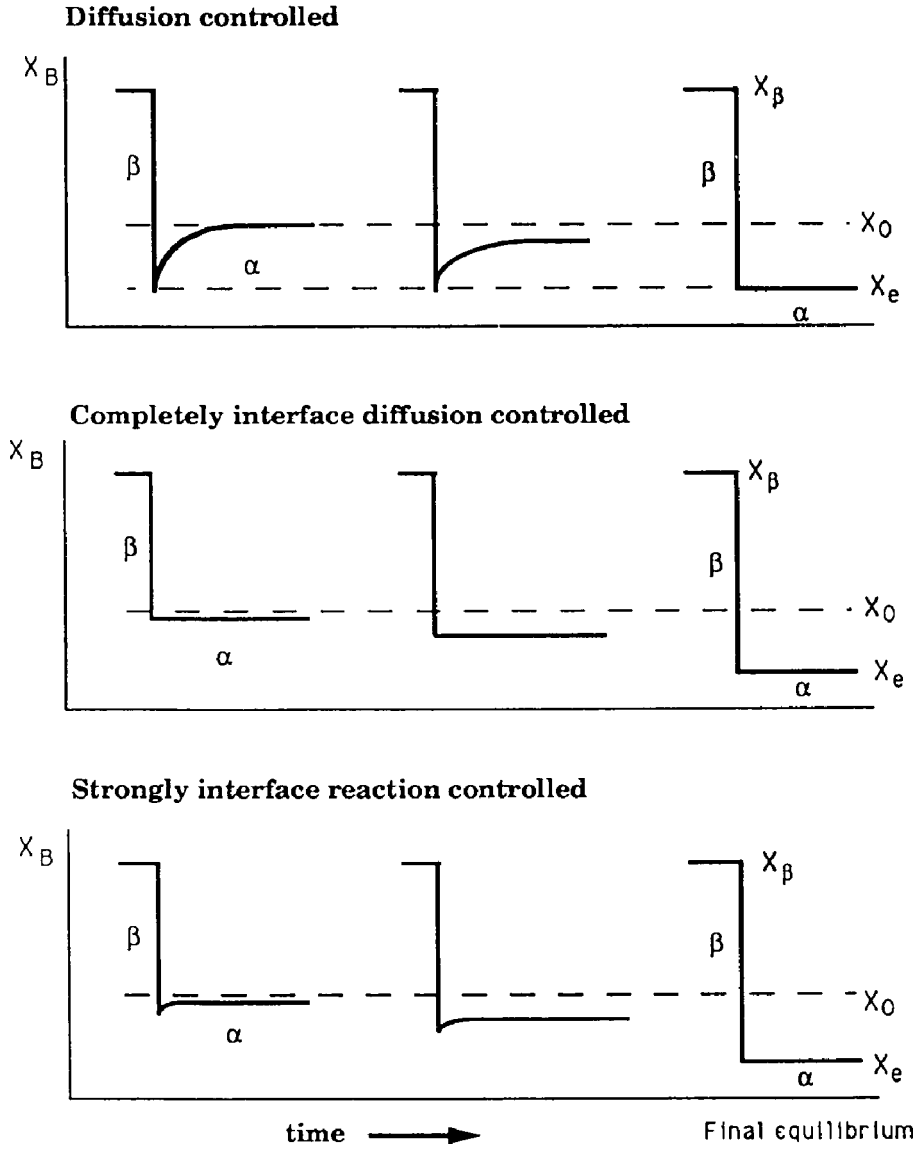

Fig. 5.6 Schematic composition profiles of various stages of a precipitation process. X_0: the composition of the supersaturated α phase. X_β and X_e: equilibrium composition of the precipitate and the matrix.

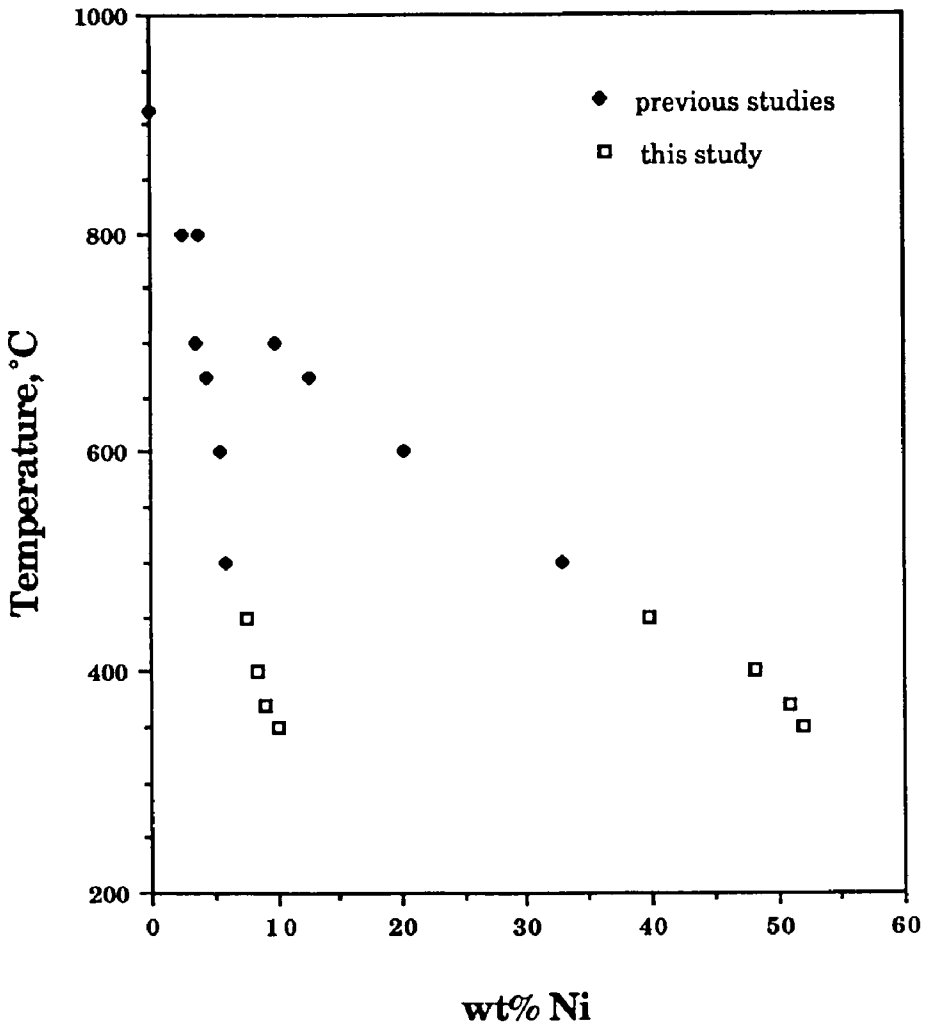

Fig. 5.7 Ni composition data of the precipitate and the matrix in the binary alloys measured in this study at ≤450°C and measured in the previous studies (Goldstein and Ogilvie, 1964; Romig and Goldstein, 1980) at >450°C. The data of this study are those measured in the alloys of 15 wt% Ni.

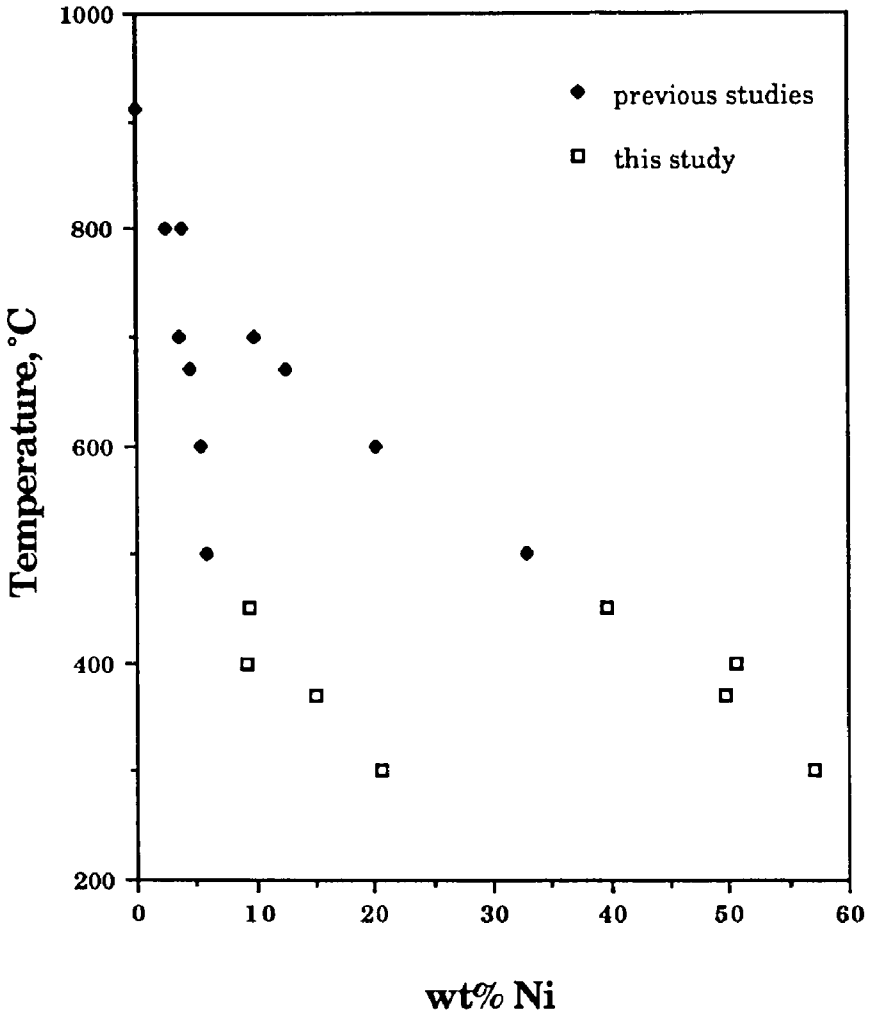

Fig. 5.8 Ni composition data of the precipitate and the matrix in the binary alloys measured in this study at ≤450°C and measured in the previous studies (Goldstein and Ogilvie, 1964; Romig and Goldstein, 1980) at >450°C. The data of this study are those measured in the alloys of 25 wt% Ni.

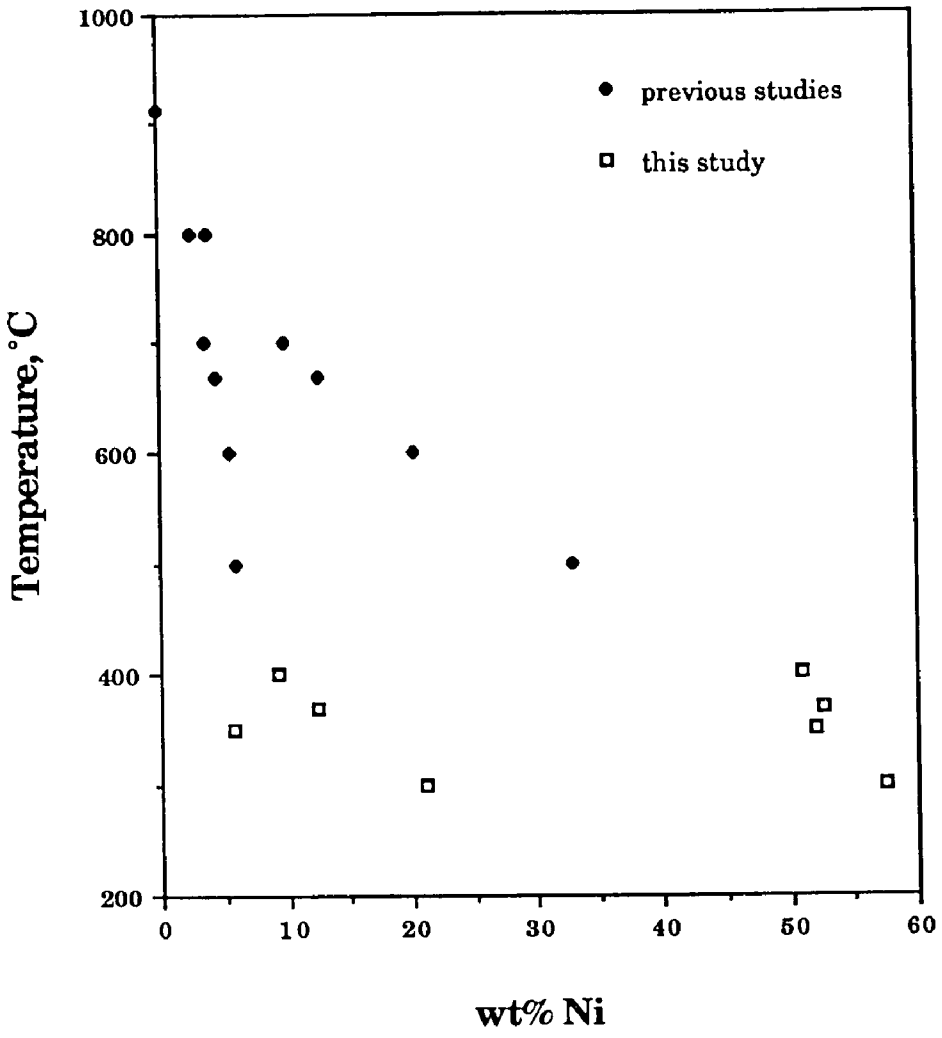

Fig. 5.9 Ni composition data of the precipitate and the matrix in the binary alloys measured in this study at ≤450°C and measured in the previous studies (Goldstein and Ogilvie, 1964; Romig and Goldstein, 1980) at >450°C. The data of this study are those measured in the alloys of 30 wt% Ni.

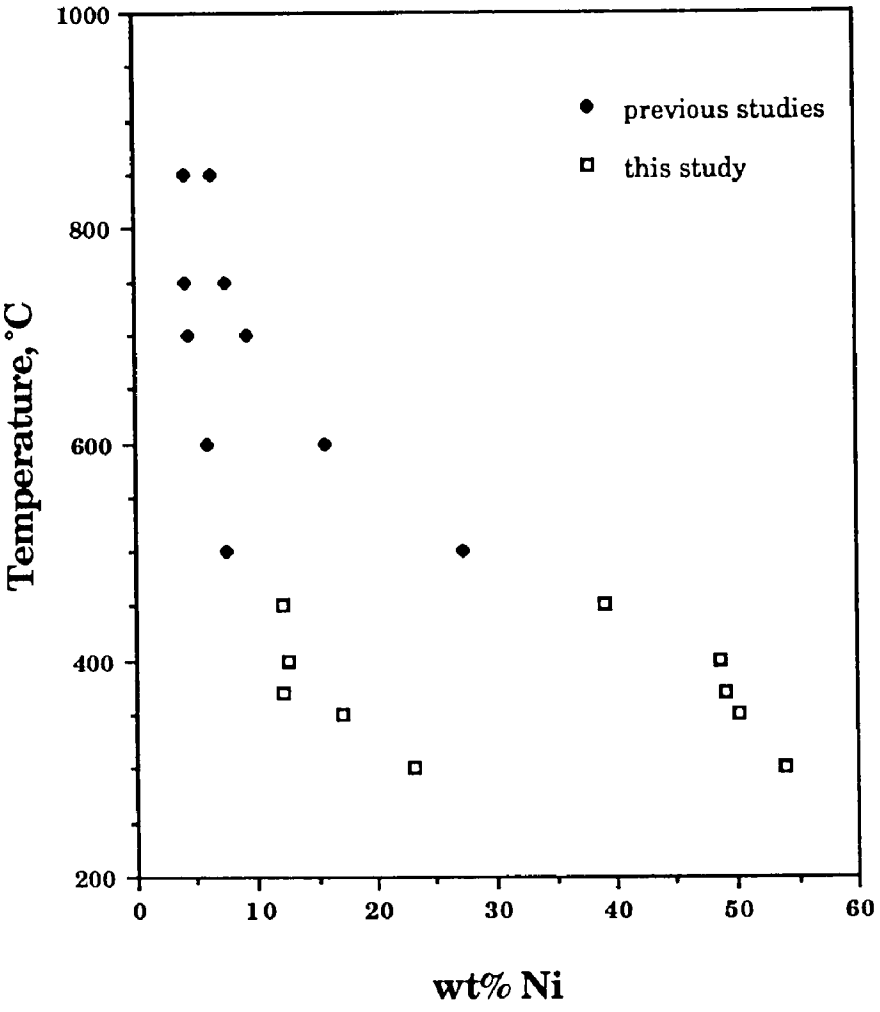

Fig. 5.10 Ni composition data of the γ precipitate and the matrix in the ternary alloys measured in this study at ≤450°C and measured in the previous studies (Doan and Goldstein, 1970; Romig and Goldstein, 1980) at >450°C.

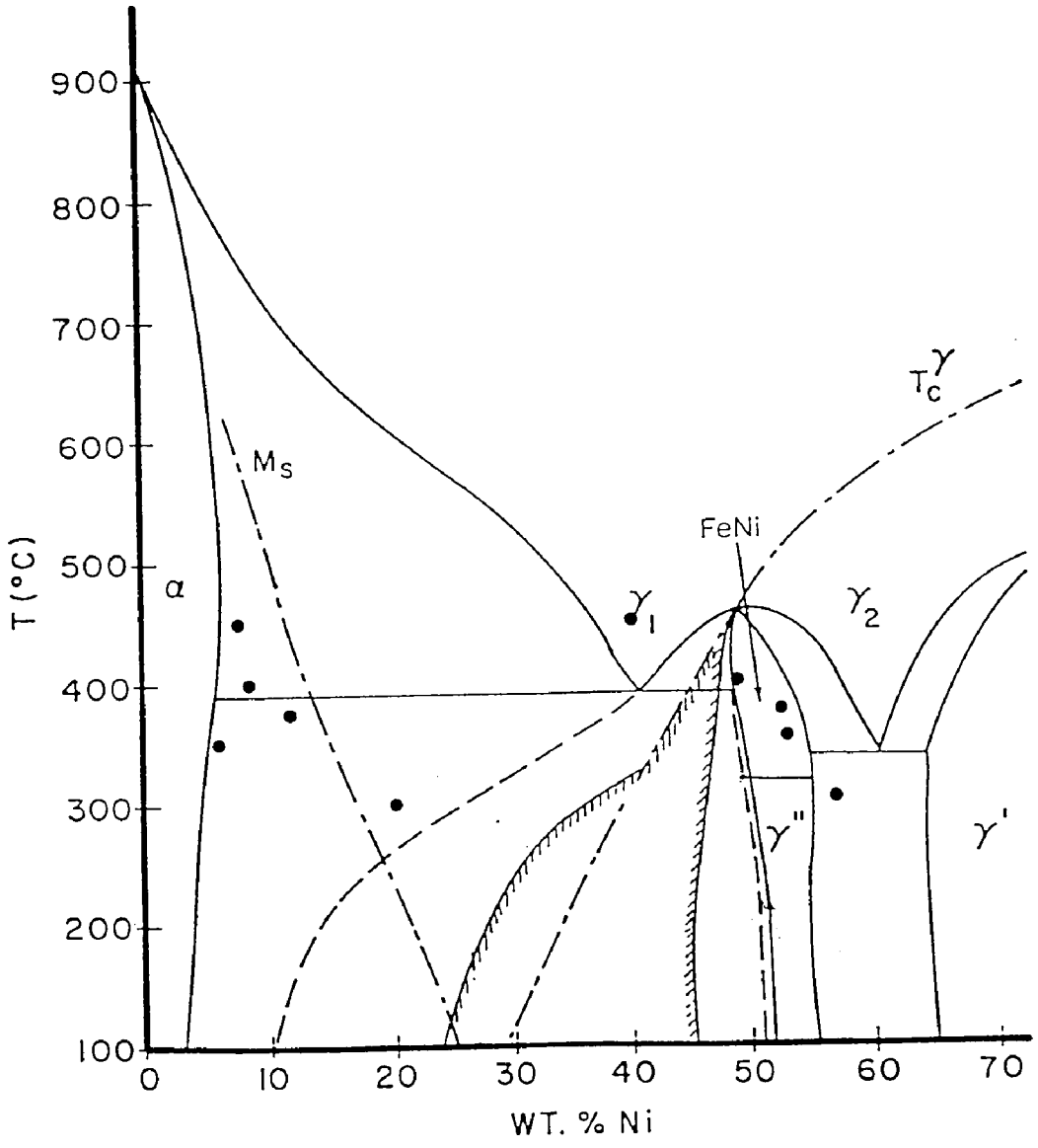

Fig. 5.11 Selected data from Table 4-2 (also shown in Fig. 5.7-5.9) plotted on the Fe-Ni phase diagram (Reuter et al., 1989).

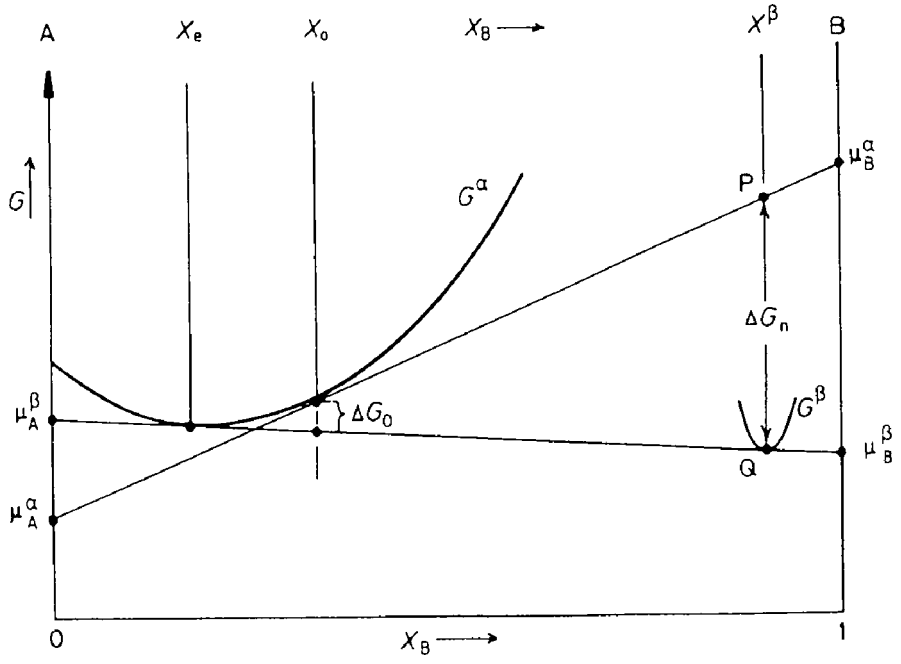

Fig. 5.12 Free energy vs composition diagram showing the driving force for the overall transformation (ΔG_0) and the driving force for the nucleation (ΔG_n). The precipitate phase is β with high solute (B) concentration, X_β. The matrix phase is α which supersaturated ($X_0 > X_e$). By the common tangent construction, it is shown that the driving force for the nucleation is higher for a larger X_0. (Porter and Eastling, 1981)

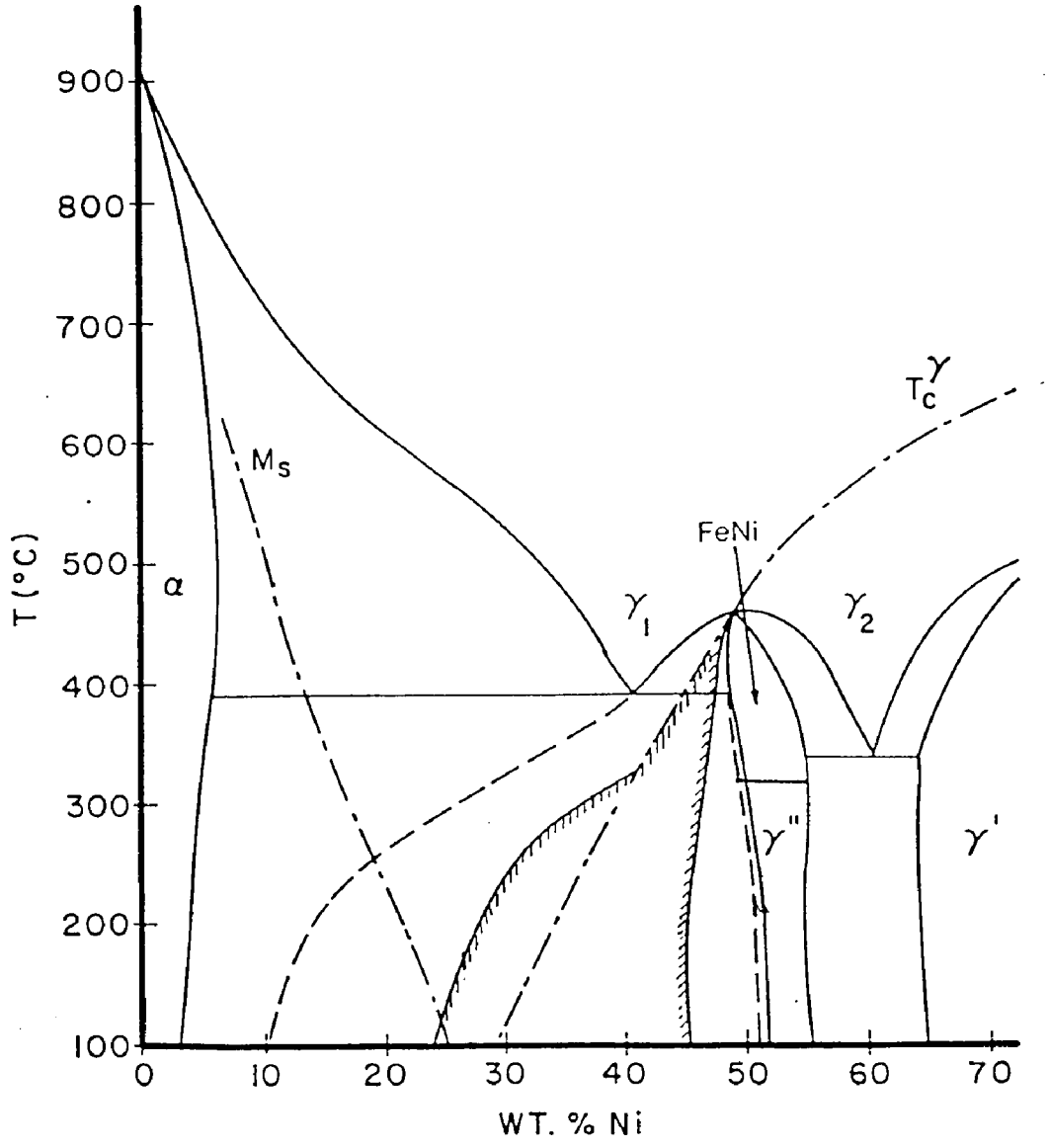

Fig. 5.13 Fe-Ni phase diagram (Reuter et al. 1989).

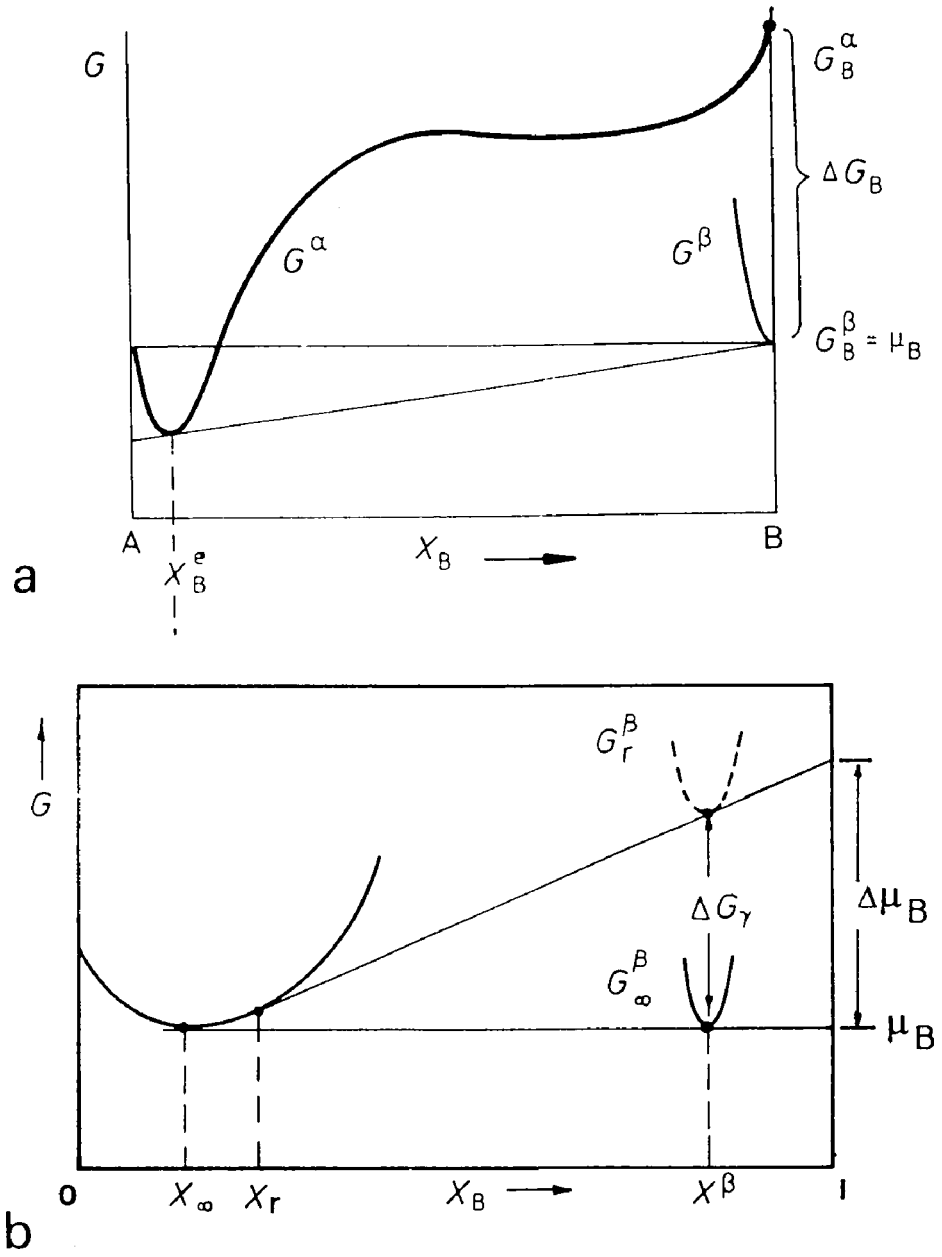

Fig. 5.14 Free energy vs composition diagrams which are used to derive the equilibrium solubility limit, X_β^e, in the α phase (5.14a) and higher solubility in the α phase due to the Gibbs-Thomson effect (5.14b). (Porter and Easterling, 1981).

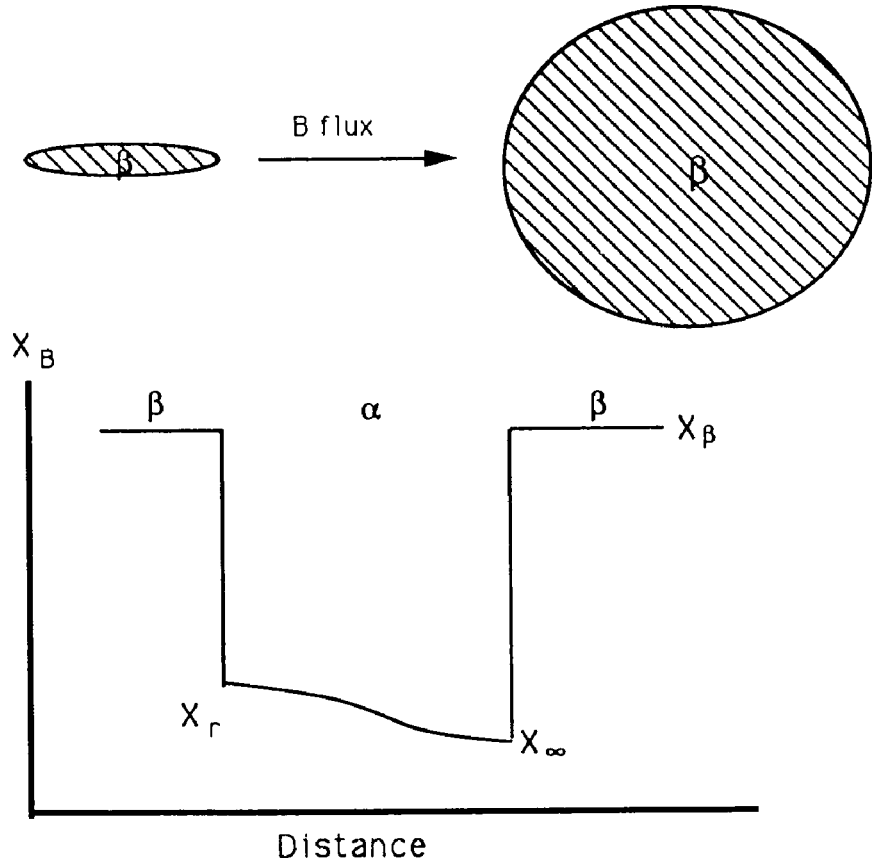

Fig. 5.15 Schematic diagram showing the driving force for the coarsening process, the composition gradient formed in the α matrix due to the different size of the β precipitate.

SUGGESTION FOR FUTURE WORK

(1) It has been shown in this study that the Fe-Ni martensite decomposition at low temperatures is not solely diffusion controlled. The precipitation process, during a heat treatment time of about one year, is not completed and the phase equilibria formed are metastable. Much work has yet to be done to understand more precisely the mechanism and the kinetics of the martensite decomposition in the Fe-Ni alloys.

First of all, it is still necessary to obtain the fully equilibrated alloys. While the use of significantly longer heat treatment time seems to be impractical, the alternative alloy preparation procedures aimed at increasing the growth rate of the precipitates should be used. The possible choices include: a) lower the homogenization temperature to obtain a smaller austenite grain size; b) mechanically deform the martensitic alloys before the heat treatment to introduce more defects into the martensite and to increase the strain energy stored in the martensite. Hopefully, these treatments will result in a higher diffusivity in the alloy due to a higher volume fraction of the large angle grain boundaries and a higher density of defects. During subsequent martensite decomposition process, the mobility of the precipitate/matrix interface will possibly be increased due to the increasing number of precipitates which are formed in large angle grain boundaries although the effect of the martensite structure on the precipitate/matrix interface mobility is not precisely known.

Secondly, the martensite structure formed using different alloy preparation parameters such as the homogenization temperature and quenching rate should be investigated in order to understand the effect of the martensite structure on the precipitate/matrix interface structure and the phase equilibria formed by the martensite decomposition. Since the diffusion coefficients reported in the previous study (Romig and Goldstein, 1981) were estimated under the assumption of the diffusion controlled growth, the diffusion coefficients may actually be larger if the effect of the interface reaction was properly accounted for. If an effective method to increase the precipitate/matrix interface mobility is found, a much shorter heat treatment time than that used in this study could be used and the precipitates formed may still be large enough for the current AEM instruments to analyze. Anyhow,

different from the experimental approach used in the previous and this study in which only the maximum heat treatment time was used, it is worth trying to use the heat treatment time as a variable in order to understand the kinetics of the Fe-Ni martensite decomposition.

(2) More information can be obtained from iron meteorites. Plessite structures of more octahedrites should be investigated to verify the scheme of the plessite formation proposed in this study including the reheating of the meteorites, the dependence of the matrix Ni composition on the precipitate size, etc.

A particular problem remaining in the investigation of the cloudy zone structure is the difference between the structure of the honeycomb phase of the octahedrites and stony iron meteorite (bcc) and that of the high Ni anomalous iron meteorite (fcc). The cloudy zone regions of the octahedrites and stony iron meteorite which have been analyzed all have a Ni composition of >40 wt% although the cloudy zone structure extended to much lower Ni composition regions (~30 wt%). This biased selection of the cloudy zone regions is partially because the high Ni cloudy zone regions have a coarser structure for which the EDS compositional analysis can be performed. Perhaps a more important reason is that, practically, the low Ni cloudy zone region close to the CT2 region is always very thick in the TEM specimen. It will be instructive to investigate the structure of the honeycomb phase in the 35 wt% cloudy zone region and compare it with the honeycomb phase in the Santa Catharina. An effort in the TEM specimen preparation is needed for this investigation.

The Fe-Ni particles in the stony iron meteorites, which have some similar structural regions to those in the retained taenite of the octahedrites, should be studied to provide more information about the phase transformations that occurred in Fe-Ni alloys. However, the interpretation of the analytical results of these particles might be difficult given the complexity of the meteorites. The effect of the presence of the silicate and different amounts of the trace elements may have to be considered if the comparison between the structures of the Fe-Ni phases in the octahedrites and in the stony iron meteorites is to be made.

(3) To compare the plessite structure of the octahedrites with the laboratory alloys, the role of the C and Co in the Fe-Ni martensite formation and decomposition needs to be investigated. It is suggested that the effect of a small addition of C, P and Co

on the M_S temperature and the martensite morphology is first investigated. The martensite decomposition in the Fe-Ni-C-Co-P alloys should then be studied using similar experimental approaches of this study.

Another heat treatment procedure which is more similar to that experienced by the meteorites should also be used to study the martensite decomposition in the Fe-Ni and the Fe-Ni based ternary alloys. This procedure is, instead of quenching the alloys to room temperature or LN_2 temperature and reheating them, to cool the alloys from the homogenization temperature directly to a temperature below the M_S and hold at this temperature for the martensite to decompose. This procedure is limited to low Ni alloys because the martensite has to be formed at the temperature at which the isothermal heat treatment is conducted. The heat treatment temperature cannot be too low so that the diffusivity is high enough for the decomposition to occur.

(4) The low diffusivity is the major problem to study spinodal decomposition in the austenite alloys below 400°C. For the thermally activated decomposition, using a higher homogenization temperature and a fast quenching rate is helpful to increase the vacancy concentration and the diffusivity. The Ni composition of the austenite alloys in this study may be too close to the high Ni miscibility boundary. A study of the 35 to 40 wt% Ni alloys is proposed. The scale of the decomposition is probably very close to the practical detection limit of the atom probe (atomic distance). Therefore, very diligent atom probe experiment is desired.

REFERENCES

Aaronson, H.I. (1962), Decomposition of Austenite by Diffusional Processes. Interscience, New York, p.387.

Aaronson, H.I., C. Laird and K.R. Kinsman (1970), Phase Transformations, ASM, p.313.

Abbott, K. and C.W. Howarth (1973), "Dissolution of γ phasse in Al-Ag alloys." Acta Met. 21,951-60.

Albertsen, J.F., G.B. Jensen and J.M. Knudsen (1978), "Structure of taenite in two meteorites." Nature 273,453-54.

Albertsen, J.F., J.M. Knudsen, N.O. Roy-Paulsen and L. Vistissen (1980), "Meteorites and thermodynamic equilibrium in fcc iron-nickel alloys (25-50% Ni)." Physica Scripta 22,171-75.

Albertsen, J.F., H.P. Nielsen and V.E. Buchwald (1983), "On the fine structure of meteoritical taenite/tetrataenite and its interpretation." Physica Scripta 27,314-20.

Anderson, R. and C.E. Lyman (1990) Lehigh University AEM Short Course.

Asano, H. (1969), "Magnetism of γ Fe-Ni invar alloys with low Ni concentration." J. Phys. Soc. Japan 27,542-53.

Bäro, G. and H. Gleiter (1974), "On the structure and migration of incoherent interphase boundaries between fcc and bcc crystals." Acta Met. 22,141-43.

Bastin, G.F., F.J.J. Van Loo and H.J.M. Heijligers (1984) "Evaluation of the use of gaussian $\Phi(\rho z)$ curve in quantitative electron probe microanalysis: A new optimization." X-ray Spectrometry 13,91-97.

Bleiberg, M.C. and J.W. Bennet (1977), Radiation Effects in Breeder Reactor Structural Materials. Met. Soc. AIME.

Bowles, J.S., M. Hatherly and A.S. Malin (1978), "FeNi superlattice formation by corrosion of Santa Catharina meteorite." Nature 276,168-69.

Brager, H.R. and F.A.Garner (1985), "Microsegregation observed in Fe-35.5Ni-7.5Cr irradiated in EBR-II." Effects of Radiation on Materials. 12th Int. Symp. v.1, F.A.Garner and J.S.Perrin eds. ASTM Philadelphia. pp.139-150.

Brofman, P.J. and G.S. Ansell (1982), "On the morphology of martensite in Fe-27Ni

alloys." Solid-Solid Phase Transformations. pp.1373-77.

Bryans, R.G., T. Bell and V.M. Thomas (1969), "The morphology and crystallography of massive martensite in iron-nickel alloys." The Mechanism of Phase Transformations in Crystalline Solids. Inst. of Metals, pp.181-88.

Buchwald, V.F. (1975a), Handbook of Iron Meteorites, Their History, Distribution and Structure. University of California Press.

Buchwald, V.F. (1975b), Handbook of Iron Meteorites, Their History, Distribution and Structure. v.1, pp.65-74. University of California Press.

Buchwald, V.F. (1975c), Handbook of Iron Meteorites, Their History, Distribution and Structure. v.3, pp.1068-73. University of California Press.

Buchwald, V.F. (1975d), Handbook of Iron Meteorites, Their History, Distribution and Structure. v.3, pp.1201-05. University of California Press.

Cahn, J. (1961), "On spinodal decomposition." Acta Met. 9,795-801.

Cahn, J. (1968), "Spinodal decomposition." Trans. TMS-AIME 242,166-80.

Chamberod, A, J. Laugier and J.M. Penisson (1979), "Electron irradiation effects on iron-nickel invar alloys." J. Magnetism and Magnetic Mater. 10,139-44.

Christian, J.W. (1965), The Theory of Transformations in Metals and Alloys. Pergamon Press, Oxford.

Chuang, Y.Y, Y.A. Chang, R. Schmid and J.C. Lin (1986), "Magnetic contributions to the thermodynamic functions of alloys and the phase equilibria of Fe-Ni system below 1200K." Met. Trans. A 16A,1361-72.

Clarke, R.S., Jr. and E.D.R. Scott (1980), "Tetrataenite-ordered FeNi, a new mineral in meteorites." American Mineralogist 65,624-30.

Cliff, G and G.W. Lorimer (1975), "The quantitative analysis of thin specimens." J. Microscopy 103,203-07.

Danon, J., R. Scorzelli, I. Souza Azevedo, W. Curvello, J.F. Albertsen and J.M. Knudsen (1977), "Iron-nickel 50-50 superstructure in the Santa Catharina meteorite." Nature 277,283-84.

Danon, J., R.B. Scorzelli, I. Souza-Azevedo, J. Laugier and A. Chamberod (1980), "Santa Catharina meteorite and phase composition of irradiated Fe-Ni Invar alloys." Nature 284,537-38.

Dean, D.C. and J.I. Goldstein (1986), "Determination of the interdiffusion coefficients in the Fe-Ni and Fe-Ni-P systems below 900°C." Met. Trans. A 17A,1131-38.

Doan, Jr., A.S. and J.I. Goldstein (1970), "The ternary phase diagram, Fe-Ni-P." Met. Trans. 1,1759-67.

Dodd, R.A., F.A. Garner, J. Kai, T. Lauritzen and W.G. Johnston (1986), Radiation-Induced Changes in Microstructure: 13th Int. Symp. part I, F.A.Garner, N.H.Packan and A.S.Kumar eds. ASTM Philadelphia, p.788.

Egerton, R.F. (1986) Electron Energy-Loss Spectroscopy in the Electron Microscope. Plenum Press.

Fraser, H.L. and J.P. McCathy (1982), "Specimen preparation limitations in quantitative thin foil microanalysis." Microbeam Analysis -- 1982, K.F.J. Heinrich ed., San Francisco Press, pp.93-96.

Ganessan, V., V.Seetharaman and V.S. Raghunathan (1984), "Interdiffusion in the Ni-Fe system." Mat. Letters 2,257-62.

Garner, F.A. and J.S. Perrin (1985), Effects of Radiation on Materials. ASTM.

Garner, F.A., H.B. Brager and J.M. McCarthy (1986), Radiation-Induced Changes in Microstructure: 13th Int. Symp. part I, F.A.Garner, N.H.Packan and A.S.Kumar eds. ASTM Philadelphia, pp.775-87.

Goldstein, J.I. and R.E.Ogilvie (1965a), "The growth of the Widmanstätten pattern in metallic meteorites." Geochim. et Cosmochim. Acta 29,893-920.

Goldstein, J.I. and R.E. Ogilvie (1965b), "A re-evaluation of the iron-rich portion of the Fe-Ni system." Trans. TMS-AIME 233,2083-87.

Goldstein, J.I., R.E. Hanneman and R.E. Ogilvie (1965), "Diffusion in the Fe-Ni system at 1 atm and 40 kbar pressure." Trans. TMS-AIME 233,812-20.

Goldstein, J.I. and J.M. Short (1967), "The iron meteorites, their thermal history and parent bodies." Geochim. et Cosmochim. Acta 31,1733-70.

Goldstein, J.I. (1969), "The classification of iron meteorites." Meteorite Research, P.M. Millman, ed. pp.721-37.

Goldstein, J.I. and A.S. Doan, Jr. (1972), "The effect of phosphorus on the formation of the Widmanstätten pattern in iron meteorites." Geochim. et Cosmochim. Acta 36,51-69.

Goldstein, J.I., J.L. Costley, G.W. Lorimer and S.J.B. Reed (1977), "Quantitative x-ray analysis in the electron microscope." Scanning Electron Microscopy v.1, IITRI, pp.315-23.

Goldstein, J.I., D.E. Newbury, P. Echlin, D.C. Joy, C. Fiori and E. Lifshin (1981),

Scanning Electron Microscopy and X-ray Microanalysis. Plenum Press.

Goldstein, J.I., D.B. Williams and G. Cliff (1986), "Quantitative x-ray analysis." Principles of Analytical Electron Microscopy, D.C. Joy, A.D. Romig and J.I. Goldstein eds. Plenum Press, pp.155-70.

Goldstein, J.I., C.E. Lyman and J. Zhang (1990), "Spatial resolution and detectability limits in thin film x-ray microanalysis." Microbeam Analysis -- 1990. in press.

Guillaume, C.E. (1897), CR Acad. Sci. 125,235.

Hausch, G. and H. Warlimont (1971), "Structural inhomogeneity in Fe-Ni invar alloys studied by electron diffraction." Phys. Lett. A36,415-16.

Hausch, G. and H. Warlimont (1973), "Single crystalline elastic constants of ferromagnetic fcc Fe-Ni invar alloys." Acta Met. 21,401-13.

Hetherington, M.G. and M.K. Miller (1988), "Statistical analysis of the early stages of phase decomposition by atom probe." J. de Physique, Colloque C6, 49,427-432.

Hetherington, M.G., J.M. Hyde, M.K. Miller and G.D.W. Smith (1991), "Measurement of the amplitude of a spinodal." Surf. Sci. in press.

Heumann, T. and G. Karsten (1963), "The carbonyl method and vapor deposition for determining equilibrium phases at low temperatures taking iron-nickel alloys as an example." Arch. furdas Eisenh. 34,781-86.

Heyward, T.R. and J.I. Goldstein (1973), "Ternary diffusion in the α and γ phases of the Fe-Ni-P system." Met. Trans. 4,2335-42.

Hillert, M. (1957), Jernkontorets Ann. 141,757.

Horita, Z., T. Sano and M. Nemoto (1987), "Simplicication of x-ray absorption correction in thin-sample quantitative microanalysis." Ultramicroscopy 21,271-76.

Ivey, D.G. and G.R.Piercy (1988), "Cross-sectional TEM specimens of metal contacts to semiconductors." J. Electron Microscopy Technique 8,233-35.

Ives, L.K., M.B. Kasen, R.E. Schramm, A.W. Ruff and R.P. Reed (1978), "A microstructural study of the Tishomingo meteorite." Geochim. et Cosmochim. Acta 42,1051-66.

Jago, R.A. (1979), "Santa Catharina and the origin of cloudy taenite in meteorites." Nature 279,413-15.

Jago, R.A., P.E. Clark and P.L. Rossiter (1982), "The Santa Catharina meteorite and the equilibrium state of Fe-Ni alloys." Physica Status Solidi (a) 74,247-53.

Joy, D.C., R.F. Egerton and D.M. Maher (1979), "Progress in the quantification of electron energy-loss spectra." Scanning Electron Microscopy. SEM Inc, v.2, pp.817-26.

Kachi, S. and H. Asano (1969), "Concentration fluctuations and anomalous properties of invar alloy." J. Phys. Soc. Japan 27,536-41.

Kaufman, L. and M. Cohen (1956), "The martensitic transformation in the iron-nickel system." Trans. AIME 206,1339-1401.

Kelly, P.M. and J. Nutting (1960), "The martensite transformation in carbon steels." Proc. Roy. Soc. A259,45-58.

Kondorsky, E.J. and V.L. Sedov (1960), "Antiferromagnetism of iron in face-centered crystalline lattice and the cause of anomalies in invar physical properties." J. Appl. Phys. **31**,331S-335S.

Krauss, G. and W. Pitsch (1965), "The fine structure and habit planes of martensite in an Fe-33wt%Ni single crystal." Trans. TMS-AIME 233,919-26.

Krauss, G. and A.R. Marder (1971), "The morphology of martensite in iron alloys." Met. Trans. 2,2343-57.

Kubaschewski, O. (1982), Iron Binary Phase Diagrams, Springer Verlag, p.73.

Leapman, R.D., C.E. Fiori and C.R. Swyt (1984), "Mass thickness determination by electron energy-loss for quantitative x-ray microanalysis in biology." J. Microscopy 133,239-53.

Leech, P and C. Sykes (1939), "The evidence for a superlattice in nickel-iron alloy Ni_3Fe." Philos. Mag. 27,742-53.

Lin, L.S., D.B. Williams and J.I. Goldstein (1977), "Analytical electron microscopy study of the plessite structure in the Carlton iron meteorite." Goechim. et Cosmochim. Acta 41,1861-74.

Lin, L.S., D.B. Williams and J.I. Goldstein (1979), "Analytical electron microscopy study of the plessite structure in four IIICD iron meteorites." Geochim. et Cosmochim. Acta 43,725-37.

Lovering, J.F. and L.G. Parry (1962), "Thermomagnetic analysis of co-existing nickel-iron metal phases in iron meteorites and the thermal histories of the meteorites." Geochim. et Cosmochim. Acta 26,361-81.

Lovering, J.F. and C.A. Andersen (1965), "Electron microprobe analysis of oxygen in an iron meteorite." Science 147,734-36.

Lyman, C.E. and J.R. Michael (1987), "A sensitivity test for energy-dispersive x-ray spectrometry in the analytical electron microscope." Analytical Electron Microscopy -

- 1987, D.C. Joy, ed. San Francisco Press, pp.231-34.

Lyman, C.E., D.W. Ackland, D.B. Williams and J.I. Goldstein (1989), "The hole count test revisited: effects of test specimen thickness." Microbeam Analysis--1989, P.E. Russell ed., pp.507-10.

Malis, T.F. (1989), "AEM specimen: staying one step ahead." Microbeam Analysis - - 1989, P.E. Russell ed., San Francisco Press, pp.487-91.

Malis, T. (1988), AEM Workshop, EMAG-87, p.127.

Malis, T., S.C. Cheng and R.F. Egerton (1988), "EELS log-ratio technique for specimen-thickness measurement in the TEM." J. Elect. Mic. Techn. 8,193-200.

Marder, J.M. and A.R. Marder (1969), "The morphology of iron-nickel massive martensite." Trans. ASM 62,1-10.

Massalski, T.B., F.R. Park and L.F. Vassamillet (1966), "Speculations about plessite." Geochim. et Cosmochim. Acta 30,649-62.

Matin, J.W. and R.D. Doherty (1976a), Stability of Microstructure in Metallic Systems. Cambridge University Press. pp.36-50.

Matin, J.W. and R.D. Doherty (1976b), Stability of Microstructure in Metallic Systems. Cambridge University Press. p.18.

Mehta, S., P.M. Novotny, D.B. Williams and J.I.Goldstein (1980), "Electron optical observation of ordered FeNi in Estherville." Nature 284,151-52.

Michael, J.R. (1988), "Probe size measurement in a field emission STEM," Microbeam Analysis--1988, D.E. Newbury ed., pp.60-64.

Michael, J.R. and D. B. Williams (1987), "A consistent definition of probe size and spatial resolution in the analytical electron microscope." J. Microscopy 147,289-303.

Michael, J.R., D.B. Williams, C.F. Klein and R. Ayer (1990), "The measurement and calculation of the x-ray spatial resolution obtained in the analytical electron microscope." J. Microscopy 160,41-53.

Miller, M.K. (1987), "Ultrahigh-resolution chemical analysis with the atom probe." Int. Mater. Rev. 32,221-40.

Miller, M.K. and K.C. Russell (1988), "An atom probe study of phase decomposition in the Cape York meteorite." J. de Physique 49-C6,397-402.

Miller, M.K. and G.D.W. Smith (1989), Atom Probe Microanalysis: Principles and Applications to Materials Problems. MRS, pp.199-226.

Miller, M.K. (1990), private communication.

Miller, M.K. and K.C. Russell (1990), "An atom probe study of phase separation in three iron meteorites." Physical Metallurgy of Controlled Expansion Invar-Type Alloys. K.C. Russell and D.F. Smith eds. TMS, pp.101-17.

Miller, M.K. and K.C. Russell (1991), "In-situ phase transformation in the field ion microscope." Surf. Sci. in press.

Morris, P.L., N.C. Davies and J.A. Treverton (1977), "Development in Electron Microscopy and Analysis." D.L. Misell ed. Inst. of Phys., p.377.

Morita, H., A. Chamberod and S. Steinemann (1984), "Electron irradiation effect on the curie temperature of Fe-Ni invar alloys." J. Phys. F: Met.Phys. 14,3053-59.

Murray, W.D. and F. Landis (1959), "Numerical and machine solutions of transient heat-conduction problems involving melting or freezing. part I -- method of analysis and sample solutions." Trans. ASME J. Heat Transfer, May, 106-12.

Narayan, C. and J.I. Goldstein (1984a), "Growth of intragranular ferrite in Fe-Ni-P alloys." Met. Trans. A 15A,867-74.

Narayan, C. and J.I. Goldstein (1984b), "Nucleation of intragranular ferrite in Fe-Ni-P alloys." Met. Trans. A 15A,861-65.

Nicholson, R.R. and J. Nutting (1961), "The metallography of precipitation in an Al-16%Ag alloy." Acta Met. 9,332-43.

Novotny, P.M., J.I. Goldstein and D.B. Williams (1982), "Analytical electron microscope study of eight ataxites." Geochim. et Cosmochim. Acta 46,2461-69.

Owen, E.A. and H. Sully (1939), "The equilibrium diagram of iron nickel alloys." Philos. Mag. 27,615-36.

Owen, E.A. and Y.H. Liu (1949), "Further x-ray study of the equilibrium diagram of the iron-nickel system." J. Iron Steel Inst. 163,132-37.

Ostwald, W. (1900) Z. Phys. Chem. 34,495.

Petersen, J.R., M. Aydin and J.M. Knudsen (1977), "Mössbauer spectroscopy of an ordered phase (superstructure) of FeNi in an iron meteorite." Phys. Lett. A62,192-94.

Peterson, N.L. and S.D. Harkness (1976), Radiation Damage in Metals. ASM.

Porter, D.A. and K.E. Easterling (1981), Phase Transformations in Metals and Alloys. VNM International.

Rasmussen, K.L. (1981), "The cooling rates of iron meteorites -- a new approach." Icarus 45,564-576.

Reed, S.J.B. (1982), "The single scattering model and spatial resolution in x-ray analysis of thin foils." Ultramicroscopy 7,405-09.

Reuter, K.B., D.B. Williams and J.I. Goldstein (1984), "Microanalysis and microdiffraction of two-phase regions in the metallic phase of the Estherville meteorite." Analytical Electron Microscopy--1984, D.B. Williams and D.C. Joy eds. San Francisco Press, pp.177-82.

Reuter, K.B. (1986), Ph.D dissertation Lehigh University.

Reuter, K.B., D.B. Williams, J.I. Goldstein and E.P. Butler (1986), "Surface oxide on fcc iron-nickel alloys." Met. Trans. A 17A,163-67.

Reuter, K.B., D.B.Williams and J.I.Goldstein (1988), "Low tenmperature phase transformations in the metallic phases of iron and stony-iron meteorites." Geochim. et Cosmochim. Acta 52,617-26.

Reuter, K.B., D.B. Williams and J.I. Goldstein (1989), "Determination of the Fe-Ni phase diagram below 400°C." Met. Trans. A 20A,719-25.

Romig, Jr., A.D. and J.I. Goldstein (1980), "Determination of Fe-Ni and Fe-Ni-P phase diagram at low temperatures (700 to 300°C)." Met. Trans.A 11A,1151-59.

Romig, Jr., A.D. and J.I. Goldstein (1981), "The diffusivity of Ni in Fe-Ni and Fe-Ni-P martensites." Met. Trans. A 12A,243-51.

Rossiter, P.L. and R.A. Jago (1984), "Toward a true Fe-Ni phase diagram." Phase Transformation in Solid: Symp. Proc. MRS v.21, T. Tsakakos ed., North-Holland, pp.407-11.

Russell, K.C. (1984), "Phase Stability under irradiation." Progress in Materials Science 28,229-434.

Russell, K.C. and D.F. Smith (1990), Physical Metallurgy of Controlled Expansion Invar-Type Alloys. TMS.

Russell, K.C. and F.A. Garner (1991), "Thermal and irradiation-induced phase separation in Fe-Ni based invar-type alloys." Met. Trans. A in press.

Russell, K.F., E.A. Kenik and M.K. Miller (1991), "Characterization of the Tishomingo meteorite." Surf. Sci. in press.

Saikumar, V. and J.I.Goldstein (1988), "An evaluation of the methods to determine the cooling rates of iron meteorites." Geochim. et Cosmochim. Acta 52,715-26.

Saito, J. and H. Takeda (1988), "Adsorbed oxygen in the Santa Catharina ataxite." Proc. 51st Annu. Meet. Meteo. Soc., 1988, Fayetteville, AK, P1.

Scorzelli, R.B. and J. Danon (1985), "Mössbauer spectroscopy and x-ray diffraction studies of Fe-Ni order-disorder processes in a 35% Ni meteorite (Santa Catharina)." Physica Scripta 32,143-48.

Scott, E.D.R. (1973), "The nature of dark ecthing rims in meteoritic taenite." Geochim. et Cosmochim. Acta 37,2283-94.

Scott, E.D.R. and J.T. Wasson (1975), "Classification and properties of iron meteorites." Rev. of Geophys. and Space Phys. 13,527-546.

Scott, E.D.R. and R.S. Clarke, Jr. (1979), "Identification of clear taenite in meteorites on ordered FeNi." Nature 281,360-62.

Tanji, Y., H. Moriya and Y. Nakagawa (1978), "Anomalous concentration dependence of thermoelectric power of Fe-Ni(fcc) alloys at high temperatures." J. Phys. Soc. Japan 45,1244-48.

Thompson, M.N., P. Doig, J.W. Edington and P.E.J. Flewitt (1977), "The influence of specimen thickness on x-ray count rates in STEM-microanalysis." Philo. Mag. 35,1537-42.

Ustad, T. and H. Sorum (1973), "Interdiffusion in Fe-Ni, Ni-Co, and Fe-Co systems." Phys. Stat. Soli. (a) 20,285-94.

Vandeen, J.K. and F. Van der Wounde (1981), "Phase diagram of the order-disorder transition in Ni_3Fe." Acta Met. 29,1255-62.

Wasson, J.T. (1967), "The chemical classification of iron meteorite: I: A study of iron meteorite with low concentrations Gallium and Germanium." Geochim. et Cosmochim. Acta 31,161-80.

Wasson, J.T., J. Willis, C.M. Wai and A. Kracher (1980), "Origin of iron meteorite groups IAB and IIICD." Z. Naturforsch. 35a,781-95.

Wasson, J.T. (1985), Meteorites, Their Record of Early Solar System History. W.H. Freeman and Co., New York.

Weatherly, G.C. (1971), "The structure of ledges at plate-shaped precipitates." Acta Met. 19,181-92.

Wells, C. and R.F. Mehl (1941), "Rate of diffusion of Ni in γ iron in low-carbon and high-carbon steels." Trans. TMS-AIME 145,329-39.

Williams, D.B. (1984), Practical Analytical Electron Microscopy in Materials Science. Philips Electronic Instruments, Inc.

Woodruff, D.P. (1973), The Solid-liquid Interface. Cambridge University Press, p.151.

Zhang, J. (1988), unpublished research.

Zhang, J., D.B. Williams, J.I. Goldstein and R.S. Clarke, Jr. (1990), "Electron microscopy study of the iorn meteorite Santa Catharina." Meteoritics 25,167-175.

VITA

Jing Zhang was born to Cheng-qian Zhang and Hui-wen Liu on October 16, 1958 in Beijing, China. He received his secondary education in a number of schools in a central province, Shanxi, while his family was moved around during those chaotic years of China. After graduating from high school in 1976, he was sent to the countryside as a farmer to be re-educated. In the winter of 1977, he survived the national entrance examination for colleges which had been interrupted for eleven years and became one of the first generation of the post-cultural-revolution college students in Shandong University, Jinan, China. He was awarded a Bachelor of Science Degree in Physics in January, 1982.

He was then admitted to a joint graduate program of General Research Institute for Non-ferrous Metals, Beijing, and Beijing University of Iron and Steel Technology. He was awarded a Master of Science Degree in Materials Science in December, 1984. His M.S thesis was entitled "Solid state reaction and silicide formation in Pd-Si system". He worked in the electron microscope laboratory in General Research Institute for Non-ferrous Metals as an assistant engineer from December, 1984 to June, 1986.

Since July, 1986, he has been pursuing his doctoral study in materials science at Lehigh University. While at Lehigh, he was elected to Sigma Xi, National Scientific Research Society. He has twice received the student award from The Meteoritical Society in 1988 and 1989, received a student award from Microbeam Analysis Society (MAS) in 1990, and the Irene Payne Award from the Metropolitan Chapter of MAS and EMSA (Electron Microscopy Society of America) in 1990. He is a member of EMSA, MAS, The Meteoritical Society, a joint member of TMS and ASM International. He has eleven technical publications in print and several others pending.